Substructures, accretion events, and surrounding diffuse intra-group light in bright early-type galaxies

Johanna Hartke

München 2018

Substructures, accretion events, and surrounding diffuse intra-group light in bright early-type galaxies

Johanna Hartke

Dissertation
an der Fakultät für Physik
der Ludwig–Maximilians–Universität
München

vorgelegt von
Johanna Hartke
aus Lohne (Oldenburg)

München, den 14. August 2018

Erstgutachter: Prof. Dr. Ortwin Gerhard
Zweitgutachter: Dr. Klaus Dolag
Tag der mündlichen Prüfung: 26. September 2018

"Hope" is the thing with feathers
That perches in the soul,
And sings the tune without the words,
And never stops at all,

And sweetest in the gale is heard;
And sore must be the storm
That could abash the little bird
That kept so many warm.

I've heard it in the chillest land,
And on the strangest sea;
Yet, never, in extremity,
It asked a crumb of me.

Emily Dickinson

Contents

List of Figures

List of Tables

Acronyms

2D two-dimensional

2MASS Two Micron All Sky Survey

AGB asymptotic giant branch

AGN active galactic nucleus

BCG brightest cluster galaxy

BGG brightest group galaxy

BIC Bayesian Information Criterion

cD central dominant

CDI counter-dispersed imaging

CDM cold dark matter

CLASH Cluster Lensing and Supernova Survey with Hubble

CMB cosmic microwave background

CMD colour-magnitude diagram

CSPN central star of the planetary nebula

dE dwarf elliptical

dIrr dwarf irregular

dSph dwarf spheroidal

DM dark matter

ePN.S extended Planetary Nebula Spectrograph

ETG early-type galaxy

FOV field of view

FWHM full width at half maximum

GC globular cluster

GMM Gaussian-mixture model

HST Hubble Space Telescope

ICL intra-cluster light

ICM intra-cluster medium

IFS integral-field spectroscopy

IGL intra-group light

IMF initial mass function

IR infrared

ISM interstellar medium

KPNO Kitt Peak National Observatory

K-S Kolmogorov-Smirnov

LF luminosity function

LG Local Group

LOS line-of-sight

LOSVD line-of-sight velocity distribution

LSB low surface brightness

MC Monte Carlo

MCMC Markov chain Monte Carlo

MS main sequence

MW Milky Way

MUSE Multi-Unit Spectroscopic Explorer

MZR mass-metallicity relation

NFW Navarro, Frenk, and White

NIR near-infrared

PDF probability distribution function

PNLF planetary nebula luminosity function

PN planetary nebula

PN.S Planetary Nebula Spectrograph

PSF point-spread function

RGB red giant branch

rms root mean square

SB surface brightness

SBF surface-brightness fluctuation

SDSS Sloan Digital Sky Survey

SN supernova

SSP single stellar population

S/N signal-to-noise ratio

TRGB tip of the red giant brach

UV ultraviolet

VLT Very Large Telescope

WHT William Herschel Telescope

Zusammenfassung

In dieser Arbeit beschäftige ich mich mit der Entstehung der ausgedehnten Halos von elliptischen Riesengalaxien und wie deren Evolution durch ihre Umgebung beinflusst wird. Insbesondere konzentriere ich mich auf die zwei Riesengalaxien M49 im Virgo Galaxienhaufen B und M105 in der Leo I Gruppe. Durch die Erforschung ihrer ausgedehnten Halos können Rückschlüsse auf vergangene Akkretionsereignisse gezogen werden. Akretionsereignisse hinterlassen sowohl langlebige Signaturen in den galaktischen Halos, können aber auch dazu beitragen, dass Sterne aus dem galaktischen Halo oder einfallenden Satelliten in das umliegende "intra-cluster" oder "intra-group light" (IGL) herausgelöst werden. Die Entstehung und Entwicklung von IGL und Galaxien in Haufen und Gruppen sind demnach eng verzahnt. Jedoch wird die Beobachtung dieser beider Komponenten durch ihre geringen Oberflächenhelligkeiten erschwert.

Planetäre Nebel (PN) sind wertvolle stellare Indikatoren für die IGL- und Haloentwicklung, da sie eine sehr starke [O III]λ5007Å Emission haben. Dies ermöglicht sowohl ihre Identifikation als auch die Messung ihrer Radialgeschwindigkeiten bis zu Entfernungen von 100 Mpc. In dieser Arbeit verbinde ich neue Photometriedaten der SuprimeCam am Subaruteleskop mit kinematischen Daten, die mit dem Planetary Nebula Spectrograph am William Herschel Teleskop aufgenommen wurden. Die räumliche Verteilung der planetären Nebel im Vergleich mit Breitbandphotometrie zeigt, dass sowohl M105 als auch M49 zwei photometrische Komponenten besitzen: Einen stellaren Halo und das umliegende IGL. In beiden Fällen ist das IGL durch eine höhere PN-spezifische Frequenz und eine unterschiedliche Steigung der PN-Leuchtkraftfunktion im Vergleich zum Halo gekennzeichnet.

Aufbau und Entwicklung von Halo und IGL können mithilfe von PN Geschwindigkeitsverteilungen nachvollzogen werden: Im Fall von M105 zeigt ein sich mit Distanz vom Zentrum abflachendes Geschwindigkeitsdispersionsprofil den Übergang vom Halo ins IGL an. Im Fall von M49 identifiziere ich drei stellare Populationen mit unterschiedlichen Geschwindigkeitsverteilungen: Den (gravitativ gebundenen) Halo von M49, eine Sternenpopulation, die mit der Akkretion der Zwerggalaxie VCC 1249 zusammenhängt, und das ausgedehnte IGL. Zum ersten Mal können wir den Übergang vom Halo ins IGL mittels einzelner Sterne beobachten. In Verbindung mit Breitbandphotometrie ergeben sich Hinweise darauf, dass das IGL im Virgo Galaxienhaufen B sich vor allem durch die frühe Akkretion von masse- ($10^7 - 10^8\ M_\odot$) und metallarmen ([Fe/H]≤ -1) Zwerggalaxien ausgebildet hat. Diese Ergebnisse liefern wichtige Randbedingungen für die Umsetzung des sogenannten "Feedbacks" in kosmologischen Simulationen, da in diesen der Beitrag von

massearmen Zwerggalaxien zum IGL- und Haloaufbau systematisch unterschätzt wird.

Abstract

In this thesis, I investigate how the extended halos of early-type galaxies are built up and which role the environment in which they reside plays in their evolution. In particular, I focus on two early-type galaxies in group and cluster environments, M49 in the Virgo Subcluster B and M105 in the Leo I Group. The study of their outermost regions, i.e. their halos, provides important insights into their accretion history as accretion and merging events leave behind long-lasting signatures. These accretion events also liberate stars into the intra-cluster or intra-group light (IGL), whose assembly is closely linked with the morphological transformation of galaxies in clusters. However, the extremely low surface brightness of both the extended halos as well as the diffuse IGL makes it challenging to observationally constrain their physical properties.

Planetary nebulae (PNe) are valuable stellar tracers of halo and IGL assembly as their strong [O III]λ5007Å emission line allows their detection and measurement of line-of-sight velocities even at distances of the Coma Cluster (100 Mpc). In this work, I combine new photometric surveys of PNe obtained with SuprimeCam@Subaru with PN kinematics from the Planetary Nebula Spectrograph at the William Herschel Telescope. The analysis of the PN number density profiles of the photometric PN sample in comparison with deep broad-band stellar photometry allows the identification of an IGL component in addition to the stellar halos in both M105 and M49. In both galaxies, the IGL PN population has a higher PN-luminosity specific frequency and a distinct PNLF slope from the halo PNe.

The PN kinematics provide constraints on the assembly of the extended halos and surrounding IGL: in the case of M105, there is evidence for transition into the IGL regime based on the flattening of the velocity dispersion profile with radius. In M49, I identify three stellar populations with distinct kinematics that are M49's main halo, stellar-kinematic substructure associated with the infall of the dwarf irregular galaxy VCC 1249, and the extended IGL characterised by a large velocity dispersion. For the first time, the kinematic transition from halo to IGL is observed based on the velocities of individual stars. Combining these measurements with the colour information from broad-band photometry, I infer that the IGL in the Virgo Subcluster B is consistent with the early accretion of a population of metal-poor ([Fe/H]≤ -1) stars formed in low-mass ($10^7 - 10^8\ M_\odot$) galaxies that has since evolved passively. These measurements put important constraints on feedback mechanisms in the current cosmological simulations, which underestimate the contribution of these low-mass and metal-poor systems.

Chapter 1

Introduction

1.1 Galaxy formation and evolution in the ΛCDM paradigm

In the current paradigm, a cosmological constant (Λ) dominated, cold dark matter (CDM) universe, only a small fraction of the total mass density in the universe is made up by ordinary matter as we observe in galaxies, stars, or planets (see Fig. 1.1). In fact, the most recent results from the Planck and WMAP missions constrain the baryonic matter content of our Universe to be 4.6% (Hinshaw et al. 2013; Planck Collaboration et al. 2016).

A significant fraction, 24% of the energy density budget, is composed of so-called dark matter (DM). The DM particles are described to be non-relativistic (cold) and non-interacting with electromagnetic radiation (dark). However, DM particles interact gravitationally, which lead to effects that cannot be explained based on the observed luminous matter alone (Zwicky 1937; Rubin et al. 1980). The remaining 71.4% are contributed by dark energy, which is a hypothetical form of energy introduced to reconcile the observations of the accelerating expansion of the Universe (Riess et al. 1998; Perlmutter et al. 1999).

The ΛCDM paradigm has been extremely successful to date in explaining the observed large-scale properties of the Universe as for example the structure of the cosmic microwave background (CMB) and the large-scale structure of galaxies, clusters of galaxies, and superclusters in the Universe. In the context of ΛCDM, structure forms hierarchically (Peebles 1978; White & Rees 1978; White & Frenk 1991), originating in small adiabatic density fluctuations, which, on the smallest scales, can be observed in the CMB (Peebles 1982). As gravity is the driving force in structure formation, overdensities become denser with time, attracting more matter from underdense regions, which in turn get even less dense. Once an overdense region reaches a critical density, it starts to collapse, forming a small halo. These halos are the building blocks of larger structures, like groups and clusters of galaxies, which then further grow through mergers and accretion.

By studying cosmological N-body simulations, Navarro et al. (1996, 1997) showed that DM halos that form in a ΛCDM cosmology follow a universal density profile, called the

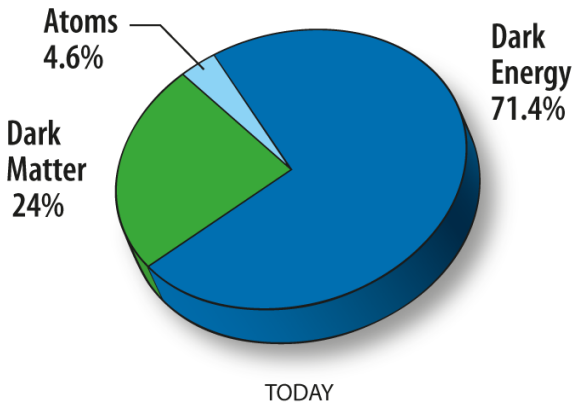

Figure 1.1: Matter content of the Universe based on WMAP 9-year data (Hinshaw et al. 2013). Credit: NASA/WMAP Science Team.

Navarro, Frenk, and White (NFW) profile, on all scales, from clusters of galaxies to dwarf galaxies:

$$\rho_{\rm NFW}(r) = \frac{\rho_0}{(r/r_s)(1+r/r_s)^2}. \tag{1.1}$$

The NFW profile is governed by the density parameter ρ_0 and the scale radius r_s. The density parameter ρ_0 is related to the NFW halo concentration c:

$$\frac{\rho_0}{\rho_{\rm crit}} = \frac{200}{3}\frac{c^3}{\ln(1+c) - c/(1+c)}, \tag{1.2}$$

where $\rho_{\rm crit} = 3H^2/8\pi G$ is the critical density of an Einstein-de Sitter Universe. The critical density is defined by the Hubble constant H and the gravitational constant G. The enclosed mass of the NFW profile within radius r can be obtained by integrating the density profile:

$$M_{\rm NFW}(r) = 4\pi\rho_0 r_s^3 \left(\ln(1+r/r_s) - \frac{r/r_s}{1+r/r_s}\right). \tag{1.3}$$

The enclosed mass profile expected from this theoretical profile compares well to these derived observationally in cluster and supercluster environments. Techniques to derive halo masses include weak and strong gravitational lensing (e.g. Broadhurst et al. 2005; Umetsu et al. 2005; Limousin et al. 2007; Gavazzi et al. 2007; Umetsu & Diemer 2017), as well as the observation of the hot, X-ray emitting gas – the intra-cluster medium (ICM) – that traces the gravitational cluster potential (e.g. Vikhlinin et al. 2005; Gitti et al. 2007; Zhang et al. 2007; Humphrey & Buote 2013).

While ΛCDM is in good agreement with observed large-scale structures, tension arises on the scales of individual galaxies. The galaxies that are observed today are the result of a complex evolutionary process that depends both on the cosmological paradigm as well as on the local environment(s) in which they were formed and where they subsequently evolved.

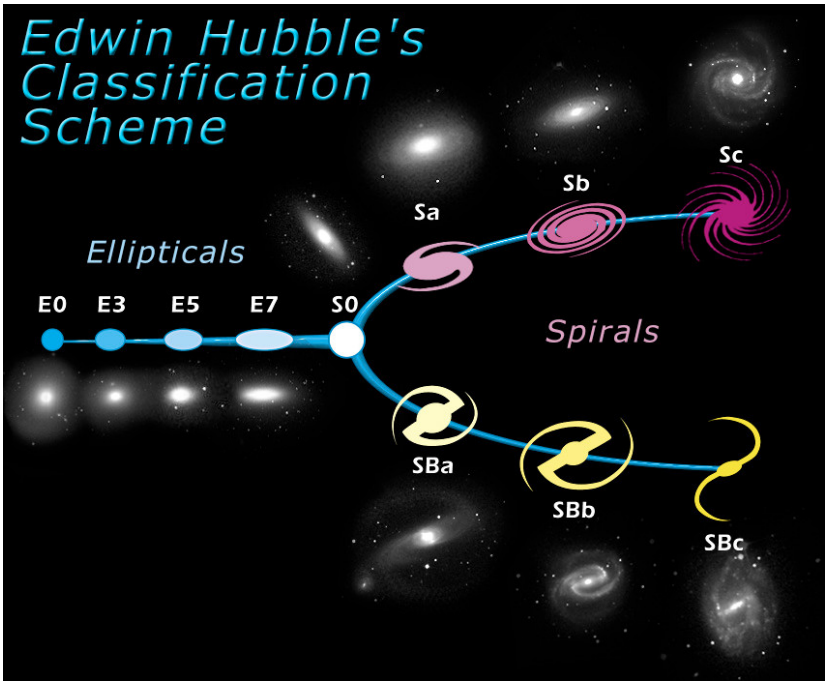

Figure 1.2: The Hubble galaxy classification scheme, also known as the Hubble tuning fork. Credit: ESA/Hubble.

1.2 Galaxies: an overview

Before diving into the properties of galaxies in group and cluster environments, I will first give a general overview on galaxy formation and evolution.

1.2.1 A census of morphological types

Galaxy classification

In general, galaxies in clusters, groups, and the field can be sorted into different classes. Figure 1.2 shows one of the first galaxy classification schemes, the so-called Hubble sequence. Hubble (1926) classified galaxies based on their colour and morphological properties. Galaxies are ordered in increasing morphological complexity ranging from featureless elliptical galaxies denoted with 'E' to spiral galaxies denoted by 'S'.

Elliptical galaxies are further divided into subclasses based on their ellipticity ϵ, denoted by $n = 10 \times \epsilon$, rounded to the nearest integer. Moving towards the right on the Hubble sequence, the ellipticity increases and the galaxies become more flattened. Their light distribution I as function of radius R can be well described by a Sérsic profile (Sérsic 1963):

$$I(R) = I_{\rm e} \exp\left((-R/R_{\rm e})^{1/n} - 1\right). \tag{1.4}$$

The Sérsic index n controls the concentration of the light, r_e is the effective radius at which half of the total light is contained, and I_e is the central surface brightness (SB). The de Vaucouleurs profile (1961) is a special case of the Sérsic profile with $n = 4$.

Moving further towards the right along the Hubble sequence, one reaches the bifurcation at the 'S0' galaxy type. S0 galaxies are a morphologically intermediate type between spiral and elliptical galaxies that contain large-scale disks but do not have prominent spiral arms. They are therefore also called lenticular galaxies.

Hubble divided spiral galaxies into barred 'SB'[1] and non-barred 'S' systems. In both sub-classes, letters from 'a' to 'c' indicate the prominence of the central bulge, the gas content, and the wrapping of the spiral arms as illustrated in Fig. 1.2. The light distribution of the bulge component, getting less prominent from 'a' to 'c', can also be described by a Sérsic profile (eq. (1.4)), while the light distribution of the disks can be approximated with an exponential profile

$$I(R) = I_0 \exp(-R/R_s), \tag{1.5}$$

where R_s is the disk scale length and I_0 again denotes the central SB.

In addition to the Hubble types identified above, there also exist dwarf counterparts. These are much smaller in size but with similar morphological appearance compared to the classical Hubble types. They are denoted with a 'd' prepended to the Hubble type as dwarf elliptical (dE), dwarf spheroidal (dSph), and dwarf irregular (dIrr) galaxies.

Initially, Hubble interpreted his classification as an evolutionary sequence and referred to galaxies classified 'E' as so-called early types and to 'S' and 'SB' galaxies as late-types. This terminology is still used to this day – 'E' and 'S0' galaxies are referred to as early-type galaxies (ETGs) – however, the assumption that galaxies along the Hubble tuning fork form in sequence has since been disproven. Ironically, the adjectives 'early' and 'late' chosen for the description of galaxies to the left and right of the sequence are diametrically opposed to the stellar spectral types observed in the respective galaxies: late-type galaxy spectra are dominated by (early-type) O+B stars, while early-type galaxy spectra are dominated by (late-type) K+M stars[2].

Observed colours of different galaxy types and the mass-metallicity relation

Due to the different stellar types dominating the stellar populations in early- and late-type galaxies, they have characteristically different integrated colours. The colour of a single star is directly related to its temperature and the colour of a stellar population depends on the evolutionary stage of the stars dominating its light distribution. Furthermore, the evolution and lifetime of single stars depend on their mass; high-mass stars have a shorter lifetime.

The stellar populations of late-type galaxies (irregulars and spirals) are dominated by many young stars. These high-mass stars have high temperatures and therefore emit in the

[1] Not to be confused with the commonly used abbreviation for surface brightness.

[2] For stars, the adjectives "early" and "late" indicate temperature instead of age, i.e. early-type stars are hotter and late-type stars are colder.

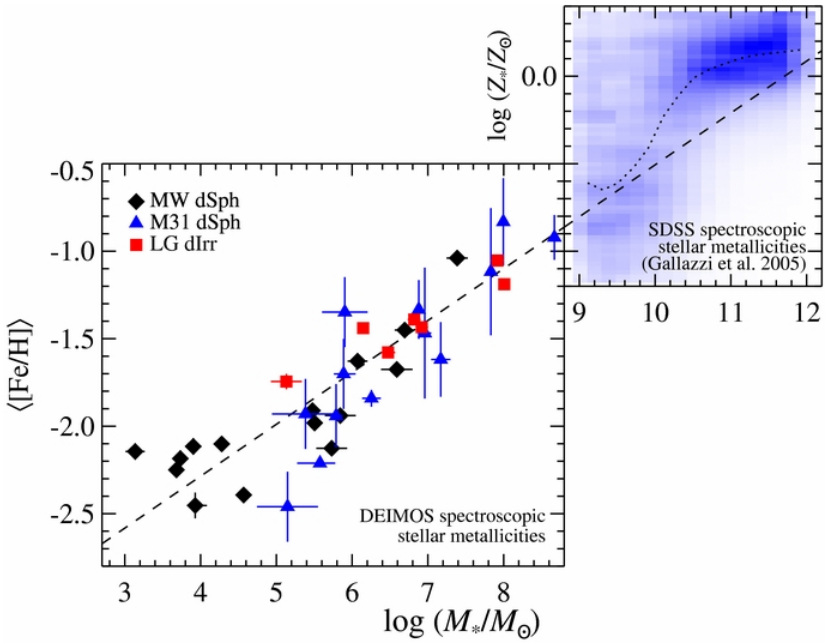

Figure 1.3: Stellar mass-metallicity relation (MZR) for Local Group galaxies (left) and more massive galaxies from the SDSS measured by Gallazzi et al. (2005). Note that the MZR is roughly continuous over nine orders of magnitude in stellar mass. Credit: Kirby et al. (2013)

blue wavelength range. In contrast to this, the star formation in ETGs has long ceased. The high-mass stars that dominated the blue colour of young stellar populations have since cooled. In addition, low-mass stars are generally colder, leading to an integrated galaxy colour in the red wavelength range.

However, the stellar population's colour is not only determined by its age but also by its metallicity[3]. It is hard to disentangle whether the spectrophotometric colours of an unresolved stellar population are due to its age or metallicity as these two quantities are *hopelessly* degenerate (Worthey 1994). For example, a single stellar population (SSP) with an age of 9 Gyr and solar metallicity ([Fe/H]$\approx$ 0) can hardly be distinguished from a 3 Gyr-old population with super-solar metallicity of [Fe/H]$\approx$ 0.3 (Chavez & Bertone 2011).

The metal content of a galaxy is correlated with its mass as the retention of metals depends on the depth of its gravitational potential well (Dekel & Silk 1986). The metallicity of a galaxy can be measured in the gas phase using emission line diagnostics of H II regions (e.g. Dopita & Evans 1986; Kewley & Dopita 2002). The gas-phase metallicity probes the present star-forming gas and is therefore a good diagnostic for star-forming, late-type galaxies. Tremonti et al. (2004) systematically measured the metallicities of thousands of galaxies in the Sloan Digital Sky Survey (SDSS), finding a strong correlation between gas-phase metallicity and stellar masses with an intrinsic scatter of only 0.1 dex. As shown

[3]The metallicity is the abundance of elements other than hydrogen and helium, measured with respect to the solar abundance.

in Fig. 1.3, the relation extends over nine magnitudes in stellar mass (Kirby et al. 2013).

1.2.2 Tidal interactions and the effect of environment

While interactions between galaxies are of course not limited to groups and cluster environments (our own galaxy the Milky Way (MW) will likely collide with Andromeda (M31) in about 3 Gyr), in these high-density environments, they happen more frequently than in the field. Besides galaxy-galaxy interactions, galaxy-cluster/group potential well, and galaxy-ICM interactions also play an important role in driving the formation and evolution of galaxies in group and cluster environments.

Galaxy mergers

Galaxy mergers are fundamental processes in the hierarchical structure formation scenario. Through galaxy mergers, two or more galaxies can be combined into a single larger galaxy. The process of galaxy merging lasts several billion years and the signatures of galaxy mergers change with merger stage.

Galaxy mergers can be divided into so-called *minor* and *major mergers*. In the latter case, the masses of the merging galaxies are similar and the merging process will result in a remnant with different morphological and dynamical properties from the progenitors, e.g. the merger of two similar-mass disk galaxies could produce a spheroidal galaxy (Toomre 1977). The ordered motions of the galaxy disks are turned into random motions due to the violent relaxation of stars in the rapidly changing gravitational field (Lynden-Bell 1967; Tremaine et al. 1986). While stellar-only[4] major mergers can produce spheroidal systems, their phase-space densities are too low when compared to elliptical galaxies, as the interaction of stellar-only system can be approximated to be collisionless (e.g. Toomre & Toomre 1972; Barnes 1992). The higher phase-space density of elliptical galaxies can however be reproduced with gas-rich (wet) mergers, as gas friction leads to energy dissipation (Hernquist et al. 1993; Lotz et al. 2008). A high gas fraction in the progenitor galaxies can lead to the increased star formation triggered by the merging process.

In *minor mergers*, one of the merging galaxies is much smaller and less massive than the other. In this case, the merger leaves the more massive galaxy relatively unchanged. Numerical simulations have shown that with increasing merger mass ratio (i.e. in major mergers) the probability that any disk-like structure gets transformed into a spheroidal one increases (Somerville et al. 2008), while the probability that a disk structure remains in place in the merger remnant is high for minor mergers.

Due to the long time scales of merging events, it is difficult to observationally constrain the galaxy merger rate. Especially in the case of minor mergers, the signatures left behind by the interaction are often low surface brightness (LSB) features like tidal tails, streams, fans, plumes, and shells. However, numerical simulations predict that very massive galaxies like the brightest cluster galaxies (BCGs) in groups and clusters can experience merger

[4]Due to the absence of gas that interacts hydrodynamically, this type of merger is also described as dry merger.

events multiple times during their dynamical evolution (De Lucia et al. 2006; De Lucia & Blaizot 2007; Stewart et al. 2008). Whether two galaxies engage in a merger depends on their relative velocity: if it is very high, the loss of orbital energy in a collision will be negligible and the galaxies pass through each other without strong changes to their internal kinematics or morphology (e.g Binney & Tremaine 1987).

Tidal destruction

As the name suggests, in a tidal destruction event, which can occur during galaxy-galaxy or galaxy-cluster interactions, the tidal forces exerted on a satellite are so strong that its outer regions are stripped (Gnedin 2003a,b) or even totally disrupted (Toomre & Toomre 1972; Toomre 1977).

Whether a galaxy gets totally disrupted during a merging event depends on the tidal radius, the orbital structure of the merging galaxies, and the infall orbit. The tidal radius is defined to be the radius at which the stars stripped from the satellite become bound to the host galaxy. Numerical simulations showed that it is hardest to strip satellites of their stars if they infall on retrograde orbits (orbits in the opposite direction to the motion of the main system), while satellites on radial and prograde orbits are more easily stripped (Read et al. 2006).

Harassment

Galaxy harassment happens as the effect of multiple encounters in dense environments such as galaxy clusters. These can be tidal interactions between an infalling galaxy and the global cluster potential as well as high-speed galaxy-galaxy encounters. Every interaction heats (increases the velocity dispersion of) the stellar component and decreases its angular momentum (Moore et al. 1996, 1998; Bialas et al. 2015). This process is more efficient in low-mass galaxies and might be responsible for the transformation of small disk galaxies into dwarf galaxies (Moore et al. 1999; Mayer et al. 2006).

Ram-pressure stripping

While the previous three interactions described above were purely gravitational effects, ram-pressure stripping is a hydrodynamical interaction. In clusters, ram pressure is experienced by galaxies moving through the hot x-ray emitting ICM, leading to the removal of cold gas from their disks and the shut-down of star formation (Gunn & Gott 1972). However, high ram pressure can also lead to the increase of star formation when galactic gas clouds are compressed to high enough densities (Dressler & Gunn 1983). The truncation of star-formation has for example been observed in the dIrr galaxy VCC 1249 due to its interaction with the BCG M49 of the Virgo Subcluster B (Arrigoni Battaia et al. 2012).

Figure 1.4: Elliptical galaxies from the Atlas3D survey with intricate LSB structures in their halos. Image by P.-A. Duc 2011 Credit: CEA/CFHT, images published in Duc et al. (2011).

1.2.3 The extended halos of early-type galaxies

In this thesis, a particular focus is set on accretion events and the related substructures that build the halos of bright ETGs.

Formation and evolution

In the hierarchical paradigm of galaxy formation, ETGs assemble in a two-phase formation scenario as identified in semi-analytic models of structure formation (Abadi et al. 2006) and hydrodynamical cosmological simulations (e.g. Naab et al. 2009; Oser et al. 2010). The two phases are closely related to the concept of the *in-situ*[5] and *accreted/ex-situ* halo. These terms were introduced by Abadi et al. (2006) in order to classify the luminous halos surrounding ETGs. The formation scenario of ETGs can be summarised as follows:

Phase I: At high redshifts ($6 < z < 2$) the inflow of cold gas leads to violent (in-situ) star formation building-up a massive and dense stellar core that has formed on a short timescale (~ 1 Gyr, Bernardi et al. 1998; Thomas et al. 2005, and references therein). At the present day, these stars are obviously old, as well as enriched in α-elements.

Phase II: From $z \sim 3$ until the present day, in-situ star formation does not play a significant role anymore. The strong size growth, that can be between a factor of two and four from $z \sim 2$ (e.g. Daddi et al. 2005; Thomas et al. 2005; van Dokkum et al. 2008), is due to accretion events (De Lucia et al. 2006; Oser et al. 2010; Pillepich et al. 2015).

[5] In situ: in the natural or original position or place (Merriam-Webster).

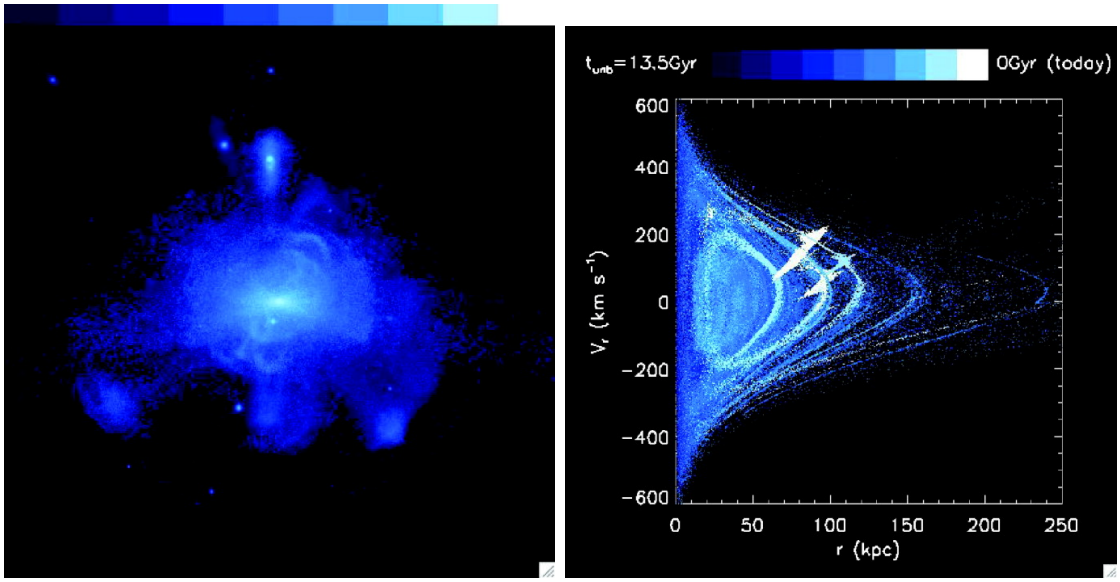

Figure 1.5: Halo assembly in cosmological simulations. *Left:* External view on a galaxy halo colour-coded by surface brightness (ranging from 38 mag arcsec^{-2} in dark blue to 23 mag arcsec^{-2} in white). *Right:* Corresponding radial phase-space diagram (V_r vs. r relative to the host halo center), colour-coded by the time each particle became unbound to its parent satellite. Credit: Bullock & Johnston (2005).

Metal-poor stars are accreted from smaller stellar systems, resulting in a metallicity gradient.

Substructure in galaxy halos

The extended stellar halos of galaxies are a gold mine for better understanding the second stage of the two-phase formation scenario as due to the long dynamical time scales in the halos, accretion events leave long-lasting imprints in their position-velocity phase-space[6].

Records of accretion events can manifest themselves as spatially extended LSB structures. Figure 1.4 shows deep images (Duc et al. 2011, 2015) of the extended halos of galaxies surveyed in the Atlas3D survey (Cappellari et al. 2011), illustrating both the diversity of extended halos in the LSB regime as well as the numerous features that are formed during mergers and accretion, such as tidal streams, shells, arcs, and plumes. These substructures can be well reproduced in numerical simulations of galaxy halos as shown in the left panel of Fig. 1.5 (e.g. Bullock & Johnston 2005). The right panel of this figure illustrates the imprints that accretion events can leave on the position-velocity phase space: satellite stars are not in equilibrium in the host galaxy potential and therefore occupy spatially coherent

[6]The term phase-space originates from statistical mechanics, where it denotes position-momentum space. In the theory of galaxy dynamics it is used to describe the six-dimensional space in position $\vec{x}$ and velocity $\vec{v}$ (see e.g Binney & Tremaine 1987, §3.1.1), however, for external galaxies only two positional coordinates and the line-of-sight (LOS) velocity are readily observable.

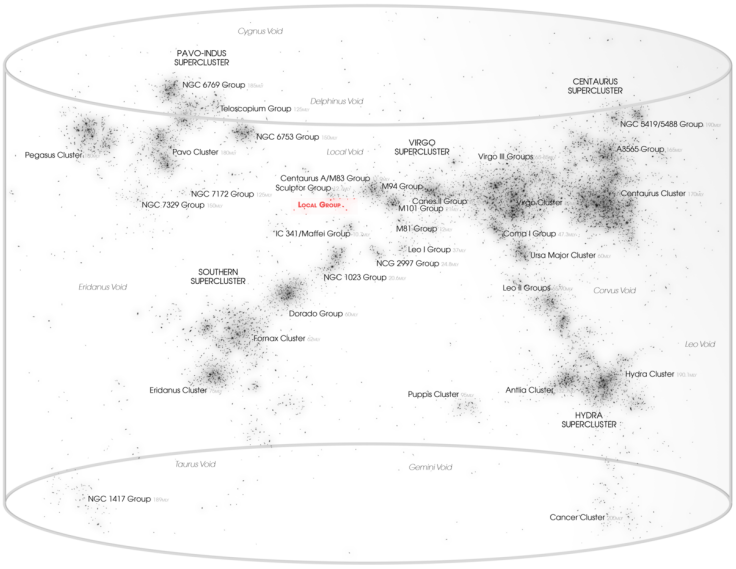

Figure 1.6: The Laniakea Supercluster containing more than 500 groups and clusters including our own Local Group marked in red. Credit: Andrew Z. Colvin.

regions (strips or chevrons) in this representation.

The luminance, coherence, and size of substructures can be used to infer the properties of its progenitor. For example, long and luminous tails are the results of major mergers (Toomre & Toomre 1972), while fainter streams can originate from the accretion of smaller systems through minor mergers (Bullock & Johnston 2005) or from material originating from a previous merging event that is falling back towards the merger remnant (Hibbard & Mihos 1995), and shells can be modelled to originate from minor mergers on very radial orbits (Quinn 1984; Dupraz & Combes 1986; Hernquist & Quinn 1988, 1989). Stellar substructure is thus an important probe for testing whether the hierarchical structure formation in the Concordance Cosmological model continues on the galaxy scale.

1.3 Galaxy clusters and their galaxy population

In the Concordance Cosmological model, galaxy clusters are the last structures to form in the Universe. As structures assemble in a hierarchical (bottom-up) way, they are thus the most massive virialized systems in the Universe. Figure 1.6 shows the structure of the groups and superclusters that surround us in our own Local Group (LG). This large-scale structure of more than 500 groups and clusters is also known as the Laniakea Supercluster (Tully et al. 2014). Clusters are vital probes both as physical laboratories to study the evolution of galaxies and as probes of cosmological models. In fact, galaxy clusters were one of the first probes that lead to the postulates on the existence of dark matter (Zwicky 1937).

1.3.1 Galaxies in clusters

Variation of the galaxy luminosity function for different galaxy types

In order to assess the large-scale distribution of galaxies in clusters, groups, or the field, their luminosity distribution can be determined. The galaxy luminosity function (LF) gives the number of galaxies per luminosity interval. The most commonly used galaxy LF is the empirically motivated Schechter function (Schechter 1976)

$$\Phi(L)\mathrm{d}L \propto L^{\alpha} \exp\left(\frac{L}{L^{\star}}\right) \mathrm{d}L, \tag{1.6}$$

where α denotes the faint-end slope and $L^{\star}$ is a characteristic luminosity describing the power-law cut-off of the LF. The parameters of the luminosity function are by no means universal and depend on environment and galaxy type studied.

Dressler (1978, 1980) observed a variation of the parameters α and $L^{\star}$ for different cluster morphologies, likely related to variations of the conditions at their formation. The LF parameters also vary for different galaxy types: Melnick & Sargent (1977) found that the inner regions of galaxy clusters are typically occupied by elliptical galaxies. This morphological segregation was corroborated by the work of Dressler (1980), who found an increase of the elliptical galaxy population with projected galaxy density and a corresponding decrease of the spiral galaxy population towards the high-density cluster centre.

1.3.2 The brightest cluster and group galaxies

The most luminous galaxies in clusters are often referred to as BCGs[7]. As already alluded to in Sect. 1.2.1, these galaxies are ellipticals/ETGs. They are often also referred to as central dominant (cD) galaxies[8] since their SB profile deviates from a single Sérsic or de Vaucouleurs profile at large radii due to the presence of an extended diffuse envelope contributing additional light. (Matthews et al. 1964; Binggeli et al. 1988). The non-BCG galaxies bound to the cluster potential are commonly denoted as *satellites*.

BCGs are located at the centre of galaxy clusters and thus at the bottom of the gravitational cluster potentials. Their location coincides with (or is close to) the peak of the X-ray emission from the hot ICM (Jones & Forman 1984; Beers & Tonry 1986; Sarazin 1986; Lauer et al. 2014). In velocity space, their location is close to the cluster rest frame (Zabludoff et al. 1990; Oegerle & Hill 2001); offsets with respect to the rest frame defined by the satellites are either due to the halo not being fully relaxed or to BCG oscillations within the cluster potential (van den Bosch et al. 2005).

[7]For simplicity, in this section, both brightest group galaxies (BGGs) and BCGs are referred to as BCGs.

[8]The nomenclature of the cD classification is ambiguous. In the Yerkes galaxy classification (Morgan 1958, 1959, 1961), the "D" denotes diffuse galaxies and the "c" can be interpreted as an adjective to describe the galaxies' large size. However, since then, the term cD has also been interchangeably used to abbreviate "central" or "cluster Dominant".

Morphologically, BCGs are very similar to ETGs, however, with effective radii of the order of 30 kpc and integrated luminosities ten times larger than the Schechter cut-off luminosity $L^\star$, they are bigger and brighter than ETGs in the field and non-BCG ETGs in clusters (Schombert 1986). Empirically, non-BCG galaxies show a tight correlation between luminosity L and the fourth power of the central velocity dispersion σ^4 (Faber & Jackson 1976) as well as between the effective radius $R_{\rm eff}$ and the enclosed SB $I_{\rm eff}$ (Kormendy 1977). BCGs, however, lie off these relations. Due to their luminosity, they are too bright to follow the same luminosity function as cluster ETGs (Dressler 1978) and lie on steeper Faber-Jackson and Kormendy relations (Von Der Linden et al. 2007; Bernardi et al. 2007).

Formation mechanisms

The fact that BCGs do not lie on the same relations as other ETGs indicates that their formation history may be different from 'classical' ETGs. Given their prominent location at the cluster centre, their evolution is likely tightly connected to the evolution of their host cluster (e.g. De Lucia & Blaizot 2007; Martel et al. 2014). Historically, three main channels have been proposed for BCG formation:

1. Due to dynamical friction, massive galaxies sink towards the cluster centre. The first galaxy to arrive becomes the BCG and grows in luminosity and mass by feeding (i.e. accreting) on late-coming infalling galaxies (Ostriker & Tremaine 1975). This process is called *galactic cannibalism*[9] (Hausman & Ostriker 1978).

2. The hot ICM loses energy by the emission of X-ray radiation, which leads to the formation of a *cooling flow*. In the densest regions of this flow cooled matter condensates onto inhomogeneities, forming cold clouds and eventually stars building up the BCG (Cowie & Binney 1977; O'Connell & McNamara 1989; McNamara & O'Connell 1989; Fabian 1994).

3. *Rapid mergers during cluster collapse* may also be responsible for the build-up of BCGs. In this scenario, BCGs form from a multitude of galaxy mergers in group or low-mass clusters (Merritt 1985).

1.3.3 The intra-cluster and intra-group light

The interactions of galaxies within cluster and group environments leads to the build-up of the so-called intra-cluster light (ICL) and intra-group light (IGL), a diffuse stellar component that is gravitationally bound to the cluster (or group) potential and not to the potential of individual galaxies. The term ICL was first introduced by Zwicky in 1937, and observationally confirmed in 1951 when he discovered stars *between* galaxies in the Coma Cluster. The formation of the ICL and IGL is closely linked to the processes of cluster and

[9]This term does not only apply to BCG formation, but can refer to the complete accretion of a satellite galaxy into any kind of host system.

group assembly. Therefore, the study of ICL and IGL can provide important constraints on the processes involved in the evolution of galaxies in dense environments.

Formation mechanisms and related IGL and ICL properties

After the discovery by Zwicky (1951), it was thought that the diffuse light originated from the tidal forces exerted on galaxies in the group or cluster potential. In the current understanding, the IGL and ICL are built by the interplay of different processes. The main channels that are proposed to majorly contribute to the build-up of the ICL are naturally related to the tidal effects experienced by galaxies in group and cluster environments that were described in the previous section (Sect. 1.2.2).

Due to the strong tidal forces in dense environments low-mass galaxies can be completely destroyed in tidal destruction events, leading to *complete dwarf disruption* (Toomre & Toomre 1972; Toomre 1977). Due to dynamical friction, the depth to which they can penetrate the cluster potential and thus the radial extent at which their debris is deposited depends on the mass of the dwarf galaxy: more massive galaxies reach closer to the cluster or group centre, while lower-mass galaxies are disrupted at larger cluster radii (Ostriker & Tremaine 1975; Rudick et al. 2006; Amorisco 2017). This leads to the build-up of a colour gradient ranging from red to blue colours as – due to the mass-metallicity relation (MZR) – lower-mass galaxies are more metal-poor and conversely bluer than their massive counterparts (Wechsler et al. 2006; Rudick et al. 2010; Melnick et al. 2012).

Partial tidal stripping feeds stars to the ICL and IGL that were liberated during merging events or galaxy flybys. This process also contributes to the ICL colour gradient. The deeper galaxies reach into the cluster potential, the stronger are the tidal forces that they experience. Therefore redder and more metal-rich stars can be stripped closer to the cluster centre.

Major mergers of satellites with the BCG can liberate a significant fraction of stars. Due to the violent nature of these events, any existing stellar population gradients are expected to be erased (Conroy et al. 2006; Murante et al. 2007; Lidman et al. 2013). This formation channel would therefore not result in significant ICL or IGL colour gradients.

In addition to that, a fraction of the ICL may be due to *in-situ star formation* that can be onset when cold gas clouds are stripped from infalling satellites (Puchwein et al. 2010).

Therefore, the detection of the ICL and the subsequent measurement of its spatial distribution and colours can put constraints on the different formation mechanisms and potentially their relative contribution to the ICL build-up.

Transition from the BCG halo into the ICL or IGL

The build-up of the ICL and IGL is closely related to the evolutionary processes involving the BCG. Many BCGs are characterised as cD galaxies due to an extended diffuse envelope contributing additional light at large radii. *Are the stars contributing to this additional light gravitationally bound to the galaxy and thus part of the BCG halo or are they largely unbound and 'live' in the cluster potential?*

Even though the existence of the ICL had been confirmed by Zwicky in the early 20th century, only the advent of powerful CCD cameras advanced its study to be more systematic, as the peak SB of ICL is about 1% of the night sky brightness (Vilchez-Gomez et al. 1994). In photometric observations, the ICL is usually identified either as all the light beyond a fixed SB limit (e.g. Feldmeier et al. 2004; Mihos et al. 2005; Zibetti et al. 2005; DeMaio et al. 2015; Montes & Trujillo 2018) or by separating the BCG from the ICL via multi-component SB profiles; the ICL is characterised by a shallower SB profile than the BCG (e.g. Gonzalez et al. 2005; Rudick et al. 2010; Iodice et al. 2016, 2017; Morishita et al. 2017a).

However, for some galaxies – e.g. NGC 6166 in Abell 2199 – the transition from BCG halo to ICL cannot be inferred from stellar surface photometry alone but is based on stellar dynamics (e.g. Dressler 1979; Bender et al. 2015). There the dynamical definition of the ICL on the basis of binding energy comes into play: stars associated with the ICL are not bound to the BCG or other satellite galaxies in the cluster (Murante et al. 2004). Observationally, this manifests itself in strongly winged line-of-sight velocity distributions (LOSVDs)(e.g Arnaboldi et al. 2004; Ventimiglia et al. 2011; Longobardi et al. 2015a; Veale et al. 2018; Barbosa et al. 2018) that can be well approximated by two Gaussians with different velocity dispersion (Dolag et al. 2010; Cui et al. 2014).

In addition to the information from integrated starlight, discrete tracers can also be used to determine the kinematics of the diffuse component. Bright individual stars in the ICL that have been used as tracers of its the distribution and kinematics are supernovae (SNe) (Gal-Yam et al. 2003), red giant branch (RGB) stars (Ferguson et al. 1998; Durrell et al. 2002), as well as planetary nebulae (PNe) that will be utilised as tracers in this thesis (Arnaboldi et al. 1996; Feldmeier et al. 2004; Arnaboldi et al. 2002, 2003; Aguerri et al. 2005; Gerhard et al. 2005; Ventimiglia et al. 2011; Longobardi et al. 2015a; Spiniello et al. 2018). There is also evidence that blue[10] GCs trace the ICL (Richtler et al. 2004; Durrell et al. 2014) with the cautionary remark that they do not always trace the light distribution of their parent stellar population well (Coccato et al. 2013). In a very recent study, Longobardi et al. (2018) find that both red and blue GCs trace the Virgo ICL. However, the fraction of blue GCs increases with increasing distance from the BCG M87 reaching up to 70%.

In cosmological simulations, where each star particle can be followed back to the galaxy in which it was born, it is of course possible to make use of the full dynamical information to separate the ICL from the BCG and to study their properties separately (Rudick et al. 2006; Murante et al. 2007; Dolag et al. 2010). This is both viable and valuable, as these results can then be compared to ICL selected using methods utilised by observers (e.g. Rudick et al. 2011; Cui et al. 2014).

The distribution of the ICL and the ICL fraction

Related to the ICL-BCG separation is the determination of the ICL fraction and distribution. The morphology of the ICL can range from a very smooth diffuse component to

[10]The adjective blue can be understood as a synonym to metal-poor. The globular cluster (GC) population in galaxies is observed to be bimodal in colour and divides into blue and red (metal-rich) GCs.

tidal features such as streams, fans, and plumes. This can be seen as a proxy for the timescale since the ICL material has been stripped from satellite galaxies (Gregg & West 1998; Feldmeier et al. 2004; Mihos et al. 2005, 2017): as time passes, phase-mixing and relaxation and potential further accretion events lead to a smoother ICL (Rudick et al. 2009).

The ICL luminosity fraction, i.e. the ratio between the ICL and the total luminosity of the cluster, can range from a few per cent to more than half of the optical light (Aguerri et al. 2005; Zibetti et al. 2005; Jiménez-Teja et al. 2018). Due to the different ICL classification methods, the measurement of the ICL fraction is not straightforward and the reported distribution of ICL fractions have a large scatter.

The relation of the ICL fraction with the cluster mass is unclear. While Lin & Mohr (2004) find a positive correlation between ICL fraction and halo mass for a sample of X-ray selected clusters with infrared (IR) colours from 2MASS, Krick & Bernstein (2007) find a large scatter in their measured ICL fractions and no dependence on halo mass. Cosmological simulations predict a growth of it with time (i.e. larger ICL fraction with decreasing redshift, Rudick et al. 2006, 2011), however due to the stochastic nature of merging events, the ICL fraction of clusters at the same redshift might drastically vary (Willman et al. 2004; Rudick et al. 2006). Nevertheless, even taking into account the different definitions of the ICL fraction, in an individual cluster it is predicted to rise during the evolution fuelled by the cumulative effect of accretion events over time (Rudick et al. 2011).

Using space telescopes, the ICL can now be observed up to redshift $z \approx 0.6$. Two notable surveys exploring redshifts in the range of $0.1 < z < 0.6$ are the Cluster Lensing and Supernova Survey with Hubble (CLASH; Postman et al. 2012) and the Hubble Space Telescope (HST) Frontier Fields (Lotz et al. 2017). The six clusters observed in the Frontier Fields show negative colour gradients with increasing distance from their BCG out to the ICL (Montes & Trujillo 2018; Morishita et al. 2017a; DeMaio et al. 2018). The consensus is that these strong colour gradients cannot be explained with metallicity gradients alone, but are a combination of metallicity and age gradients. Extending this analysis to even larger distances from the BCG centre, Morishita et al. (2017a) measure colours as blue as $B - V \approx 0.1$, at 300 kpc into the ICL. The observed colour gradients are in line with ICL formation through complete dwarf disruption as well as through partial tidal stripping of galaxy outskirts (Morishita et al. 2017a; DeMaio et al. 2018; Jiménez-Teja et al. 2018). Furthermore, Jiménez-Teja et al. (2018) find that the ICL fractions are on average higher for merging clusters.

1.4 Planetary nebulae as tracers of galaxy evolution

1.4.1 What are planetary nebulae?

Planetary nebulae (PNe) represent the very late stages of the evolution of low-mass stars, with initial masses between 1 and 8 $M_\odot$. In a 10^{10} $L_\odot$ population of stars as old as 1 Gyr,

Figure 1.7: The Saturn Nebula (NGC 7009) observed with MUSE at the VLT. The green hue is due to the λ4959/5007Å forbidden lines of the [O III] emission. The red colouration is due to Hα emission. Credit: ESO/J. Walsh.

there are thousands of stars that are in the PN phase. Fig. 1.7 shows the PN NGC 7009; the central star of the planetary nebula (CSPN) is surrounded by an intricate system of gaseous and dusty shells. This object was one of the first PNe ever discovered and was observed by William Herschel in 1782. It was Herschel who coined the term *planetary nebulae* as the objects he observed appeared to have disks like planets, but also the pale light of nebulae (Hoskin 2014). Many PNe are also included in the Messier Catalogue; the first PNe were catalogued by Messier in 1976. While earlier models suggested that PNe were formed by the ejection of the envelopes of RGB stars (Abell & Goldreich 1966), it is now widely accepted that PNe are the progeny of asymptotic giant branch (AGB) stars.

An AGB star has a degenerate carbon-oxygen core that is surrounded by helium- and hydrogen-fusion shells, and a convective hydrogen-rich envelope. Towards the end of the AGB phase, stars eject a high density superwind, expanding slowly with a speed of only $10-20$ km s^{-1} and a mass-loss rate of 10^{-4} $M_\odot$ yr^{-1} (Renzini 1983). Therefore, at the end of the AGB phase, the mass in the stellar H envelope has decreased so much (to about 10^{-2} to 10^{-3} $M_\odot$) that a fully developed convection zone can no longer be sustained. During the post-AGB phase, the envelope shrinks and becomes radiative rather than convective. Despite the ongoing mass loss in the envelope, the star's luminosity is still determined by the ongoing shell fusion around the degenerate stellar core and remains nearly constant.

During the post-AGB phase, the radius of the star decreases from 200 $R_\odot$ to about 3 $R_\odot$ and the temperature increases to $30,000$ K. The star develops a relatively fast (10^3 km s^{-1}) line-driven stellar wind. The interaction of the pre-existing AGB superwind

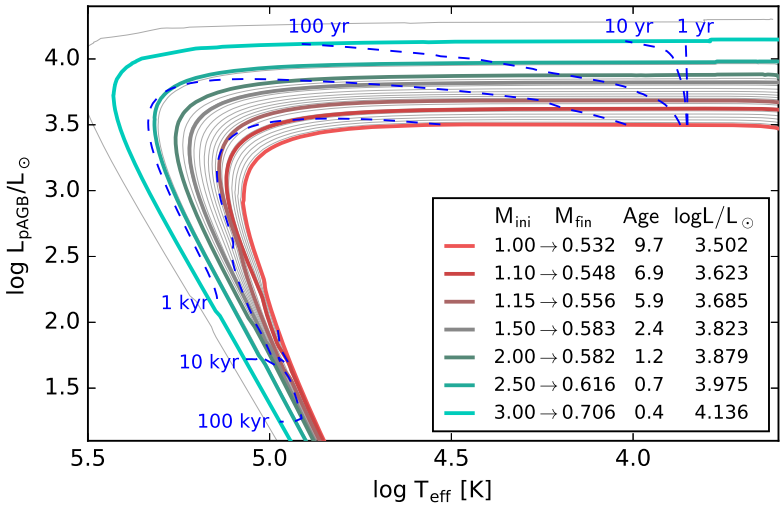

Figure 1.8: Post-AGB stellar evolution sequences from Miller Bertolami (2016) with colour coding according to the post-AGB model parameters defined in the inset. Blue dashed lines indicate isochrones at selected post-AGB ages. Credit: Gesicki et al. (2018).

with the fast wind from the CSPN produces a shell containing shock heated material from the fast wind and ejecta from the AGB star (Kwok et al. 1978). The material in the shell is photoionised by the ultraviolet (UV) radiation from the increasingly hot CSPN. The balance between recombinatation and photoionisation leads to the characteristic emission lines (Hα, [O III]) that dominate the observed PN spectra. The evolution of effective temperature and luminosity for different post-AGB models (Miller Bertolami 2016) is shown in Fig. 1.8.

1.4.2 Observational properties of PNe

As described in the previous section, PNe have characteristic spectra that are dominated by emission lines. An examplary PN spectrum is shown in Fig. 1.9. The defining features are immediately notable: the absence of a stellar continuum and the strong nebular emission lines from the UV to the near-infrared (NIR). The brightest emission is at the 5007Å forbidden[11] [O III] line. Theoretical predictions estimate that up to 15% of the UV radiation of the CSPN is re-emitted in the [O III] line (Dopita et al. 1992).

The width of the emission lines can be used to measure the expansion velocities of the PNe, which are typically of the order of $10 - 30$ km s^{-1} (e.g. Gesicki & Zijlstra 2000). The expansion velocity of a PN can be used to estimate its dynamical age using dynamically evolving nebular models (e.g McCarthy et al. 1990; Dopita et al. 1996; Gesicki & Zijlstra

[11]Forbidden lines are spectral lines that can only be generated in very low densities and are due to electrons that populate meta-stable energy levels in atoms or ions. In higher-density environments these meta-stable energy levels would be de-excited by collisions.

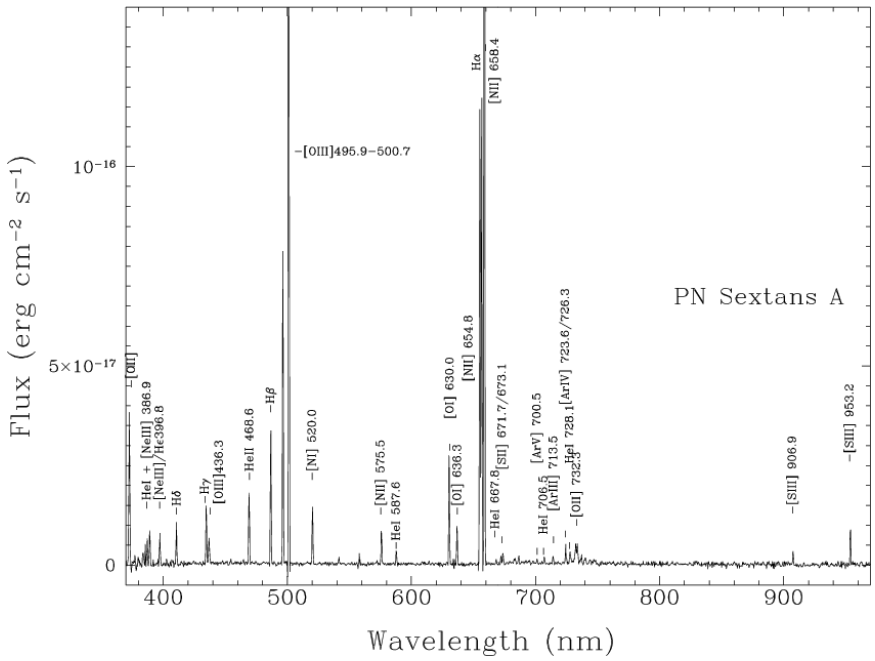

Figure 1.9: VLT Spectrum of a PN in the Sextans A dwarf galaxy in the Local Group. Note the absence of a stellar continuum and the strong [O III], Hα, and [N II] emission lines. Credit: Magrini et al. (2005).

2000; Schönberner et al. 2005). The visibility lifetime of a typical PN can vary between 1 000 and 30 000 years (Buzzoni et al. 2006; Jacob et al. 2013). Afterwards the PN shell will have dissipated into the interstellar medium, while the CSPN will evolve to be a white dwarf.

The typical diameter of PNe in the MW bulge is 0.3 pc, however, not all resolved PNe have a simple and symmetric round morphology. Many PNe have a bipolar structure or even more complex morphologies of shells, filaments, and knots. One example of a PN with a more complex morphology is the Saturn Nebula shown in Fig. 1.7. The difference in morphology may be due to the shell ejection mechanisms, the wind from the CSPN, binary central star systems, or magnetic fields (Balick & Frank 2002).

1.4.3 PNe as tracers of stellar populations at extragalactic distances

Motivation

In Sect. 1.2 I highlighted the importance of understanding the build-up of the halos of early-type galaxies in group and cluster environments. However, mapping the kinematics of these halos that can span several degrees on the sky at distances beyond 10 Mpc is observationally challenging. While the halos of nearby galaxies, as our own MW halo, M31, or Centaurus A can be mapped with absorption-line spectroscopy of single, resolved RGB

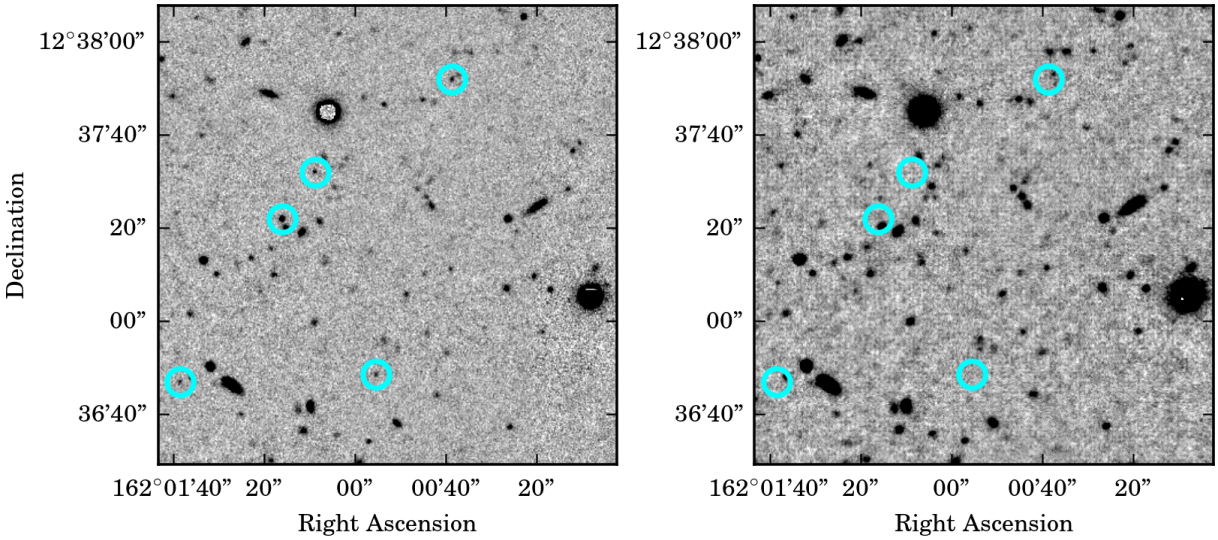

Figure 1.10: PN detections indicated by cyan circles on the on-band image (left) and corresponding non-detections on the off-band image (right) in the galaxy M105.

stars that provide both spatial and LOS distributions (Rejkuba et al. 2005; McConnachie et al. 2009; Rejkuba et al. 2009; Crnojević et al. 2013; Rejkuba et al. 2014; Crnojević et al. 2016), absorption-line spectroscopy of stars becomes increasingly difficult with ground-based facilities as halo stars can be fainter than the sky background at $m_V = 23.5$ mag. Space telescopes as the HST have greatly advanced our understanding of the evolution of galaxies and their halos, however, observations with space-based instruments are still costly and limited to a small field of view (FOV).

The advent of integral-field spectroscopy (IFS) has revolutionised the study of the central high-surface brightness regions of ETGs (e.g Emsellem & Sauron Team 2002; Ma et al. 2014; Cappellari 2016). However, the current generations of IFSs is also limited by their small FOV, making it increasingly costly to map extended halos at larger distances (beyond $2r_e$). The most extended surveys that use sparse sampling strategies do not reach galaxy coverages beyond $4r_e$.

In order to overcome these limitations, discrete tracers are used to map the extended halos of galaxies beyond the LG. The two most commonly used discrete tracers are PNe and GCs. Due to their strong [O III] emission and the absence of a stellar continuum, PNe can even be observed in galaxy clusters like Hydra I at 50 Mpc distance (Ventimiglia et al. 2008, 2011) and Coma at 100 Mpc distance (Gerhard et al. 2005; Arnaboldi et al. 2007).

Extragalactic PN survey strategies

Historically, different observational strategies for the detection of PNe and the measurement of their LOS velocities have been developed. All observational techniques make use of the strong [O III]λ5007Å emission and the absence of a stellar continuum. In imaging, the so-called *on-off band technique* is most commonly used: PNe are detected as point-like objects

in the on-band image taken through a narrow-band [O III] filter, and are not detected in the off-band continuum image taken through broad-band filters (Ford et al. 1973; Ford & Jenner 1975; Jacoby et al. 1992). Figure 1.10 shows exemplary detections of a PNe on the on-band [O III] image in the galaxy M105 and the corresponding non-detections on the off-band V-image. Arnaboldi et al. (2002, 2003) advanced this concept towards a colour-magnitude diagram (CMD)-based automated detection technique with which PNe are detected based on their [O III] vs. broad-band colour-excess as a function of [O III] magnitude. This technique has since been successfully applied to detect intra-cluster PN in the Virgo Cluster (Castro-Rodriguéz et al. 2009) and in its BCG M87 (Longobardi et al. 2013). In order to obtain the LOS velocities of PNe detected with the on-off band and CMD-based techniques, spectroscopic follow-up is required.

Counter-dispersed imaging (CDI), a technique first developed by Douglas & Taylor (1999), enables the measurement of PN LOS without a previous imaging run. As the name suggests, the field of interest is observed through a slitless spectrograph tuned to the [O III] line at the redshift of the galaxy. While any objects with continuum emission (i.e. foreground stars or background galaxies) appear as stripes on the image, the monochromatic emission from the [O III]λ5007Å line remains point-like. In order to measure the PN LOS velocity, two dispersed images with opposite dispersion vectors need to be observed. This can be achieved with conventional spectrographs, where the two images are taken after each other, the second rotated by 180° (e.g. McNeil et al. 2010; Spiniello et al. 2018). With the custom-built Planetary Nebula Spectrograph (PN.S, Douglas et al. 2002), both images can be taken simultaneously. Figure 1.11 illustrates how a section of the sky containing both continuum emitters and PNe (a) is dispersed in the two arms of the instrument (b,c). Since the image in the right arm is rotated by 180° compared the left arm, the dispersion vector has the opposite sign. After de-rotating the right-arm image and calibrating both images, a combined image can be generated (d), in which the PNe in the field appear as pairs with a distance offset Δx that is directly proportional to their LOS velocity (Douglas et al. 2002). The PN.S has been instrumental for surveys of the kinematics of ETGs (Douglas et al. 2007; Coccato et al. 2009, 2013; Pulsoni et al. 2017), S0 galaxies (Cortesi et al. 2013a,b), and disks (Aniyan et al. 2018).

Multi-slit imaging spectroscopy enables the detection of PNe at unprecedented distances beyond 25 Mpc. At these distances, the magnitude of the [O III] emission would be of the order as the sky noise in a narrow-band image taken through a typical filter with a full width at half maximum (FWHM) of $30 - 70$Å. This technique combines imaging through a narrow-band [O III]λ5007Å filter with multi-slit spectroscopy. As the PN emission is monochromatic, its entire flux is collected in a few pixels, whereas the continuum emission of the sky background gets dispersed over the whole spectral range, reducing the sky noise by a factor of $5 - 10$. Using this technique, the kinematics of the diffuse stellar light in Hydra I cluster at 50 Mpc distance (Ventimiglia et al. 2008, 2011) and in the Coma cluster at 100 Mpc distance (Gerhard et al. 2005, 2007; Arnaboldi et al. 2007) could be studied.

The three survey techniques presented above work well with imagers and spectrographs with a large FOV. However, they are "blind" in the central regions of galaxies due to the presence of strong stellar background continuum light and can therefore only detect very

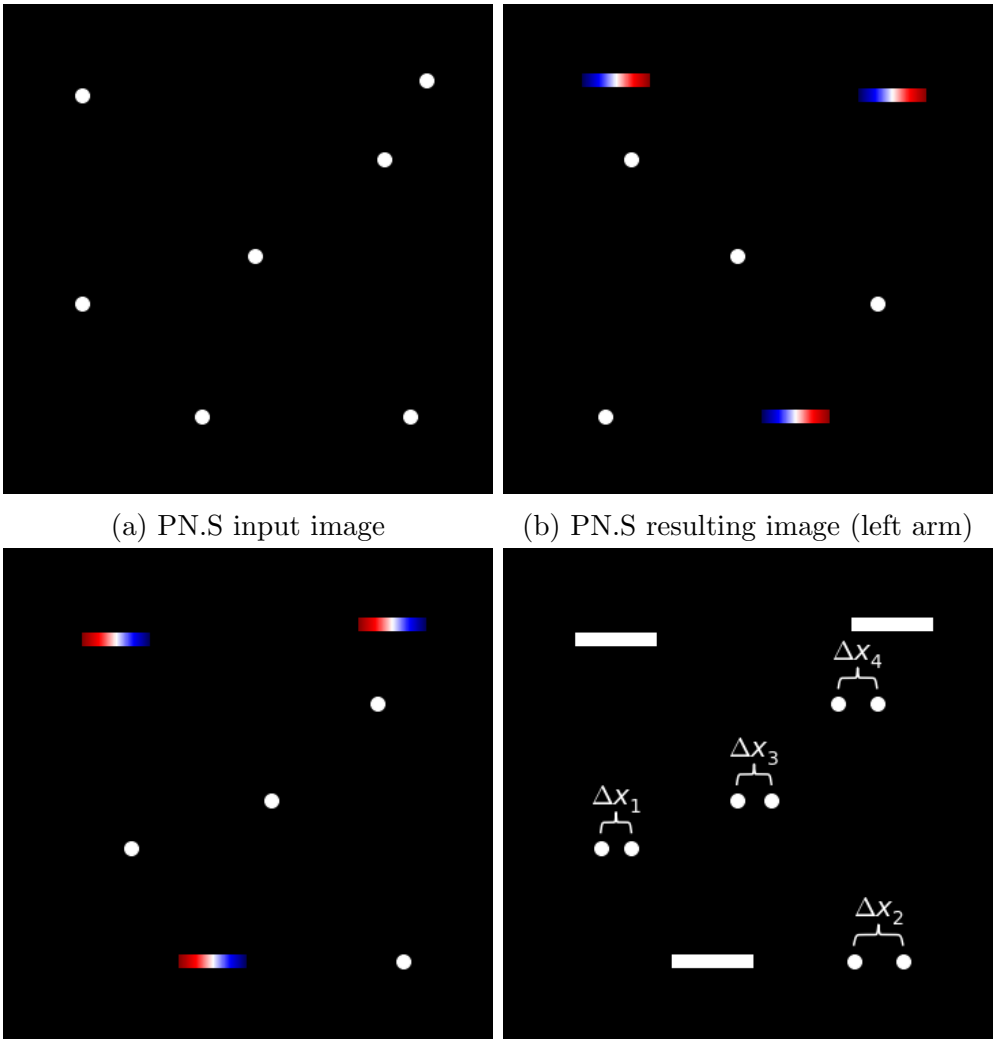

(a) PN.S input image (b) PN.S resulting image (left arm)

(c) PN.S resulting image (right arm) (d) PN.S combined image

Figure 1.11: Illustration of CDI as utilised with the PN.S. The input image (a) is dispersed in the left (b) and right (c) instrument arms that have opposite dispersion vectors. The distance Δx between the PN on the calibrated and registered combined image (d) is proportional to their LOS velocity.

bright PNe. The advance of *IFS* can overcome this limitation as the spectra in the bright central region can be decomposed into their respective stellar and nebular contribution (Sarzi et al. 2011).

The PN luminosity function

A defining characteristic of a PN sample is the shape of its planetary nebula luminosity function (PNLF). While PNe and their CSPNe are spatially resolved in our own galaxy, beyond a distance of 1 Mpc, PNe appear as unresolved sources with a light distribution that is dominated by the strong [O III]λ5007Å emission. In order to determine the apparent magnitude m_{5007} from the observed flux from this line F_{5007}, the Jacoby-relation (1989) can be used:

$$m_{5007} = -2.5 \log F_{5007} - 13.74. \tag{1.7}$$

From the magnitudes of all PNe in the sample, a luminosity function can then be calculated by simply counting the number of PNe in bins of magnitude m_{5007}. The first galaxy in which the PNLF was systematically studied is one of our nearest neighbours, the Andromeda galaxy, also known as M31. The analytic fit to the PNLF of M31 as function of absolute magnitude M_{5007} (Ciardullo et al. 1989) has become the benchmark for extragalactic PN studies:

$$N(M_{5007}) = c_1 \mathrm{e}^{0.307 M_{5007}} (1 - \mathrm{e}^{3(M^\star - M_{5007})}). \tag{1.8}$$

In the equation above, c_1 is a normalisation constant, and $M^\star$ is the absolute magnitude of the PNLF's bright cut-off. The first term describes the fading of the SB of a spherical gas cloud around a non-evolving central star expanding with a constant velocity (Henize & Westerlund 1963). More recent observations of galaxies beyond the LG motivated a generalisation of equation (1.8) with a faint-end slope c_2 that is allowed to vary (Longobardi et al. 2013):

$$N(M_{5007}) = c_1 \mathrm{e}^{c_2 M_{5007}} (1 - \mathrm{e}^{3(M^\star - M_{5007})}). \tag{1.9}$$

The Ciardullo et al. (1989) PNLF is thus a specific case of equation (1.9) with a faint-end slope of $c_2 = 0.307$. Empirically, steeper faint-end slopes are associated with older stellar populations while flatter slopes can be associated with younger stellar populations (Ciardullo et al. 2004; Ciardullo 2010; Longobardi et al. 2013, 2015a).

The bright cut-off $M^\star$ governs the second term of equation (1.8). Empirically, it has been found that the bright cut-off is invariant with galaxy type and nearly-constant at $M^\star = -4.51^{+0.02}_{0.04}$ (Ciardullo et al. 2002, 2004). By determining the apparent bright cut-off $m^\star$ of a galaxy one can thus calculate its distance modulus $\mu = m^\star - M^\star$, making the PNLF an important secondary distance indicator especially for ETGs where no Cepheid stars are observed[12].

[12]The pulsation period of Cepheid variable stars is directly related to their luminosity (Leavitt 1908), making them an important distance indicator for star-forming galaxies (e.g. Mould et al. 2000)

While the invariance of the bright cut-off with galaxy type and age and metallicity of the underlying stellar population is well established observationally, it has puzzled theoreticians in the field of stellar evolution. The invariance of the bright cut-off with metallicity could be explained with the small dependence of the [O III]λ5007 flux on PN metallicity (Jacoby 1989; Dopita et al. 1992), however, the age-invariance of the PNLF bright cut-off cannot be easily explained (Mendez & Soffner 1997; Jacoby 1997; Marigo et al. 2004). The magnitude of the PNe populating the bright cut-off strongly depends on the luminosity at which they enter the post-AGB phase.

The detailed models of Marigo et al. (2004) found a strong age dependence of the PNLF bright cut-off using the post-AGB isochrones of Vassiliadis & Wood (1994) leading to the conclusion that the bright cut-off of the PNLF is populated by stars with progenitor masses of about 2.5 $M_\odot$. However, stars with these masses are absent in galaxies that did not have a recent starburst. In this model, the bright cut-off of ETGs with old stellar populations would be expected to be fainter than $M_\star > -3$, which is 1.5 magnitudes fainter than the observed value.

An alternative hypothesis is that the PNLF bright cut-off is populated by PNe whose progenitors were close-binary blue straggler stars (Ciardullo et al. 2005). In this scenario, the combined mass in the binary system would have to be at least $2M_\odot$, a value that can also be reached in old stellar populations.

With the advent of improved models of post-AGB evolution (Miller Bertolami 2016), the invariance of the bright cut-off with metallicity *and* age could for the first time be reproduced for an intermediate-age population (Gesicki et al. 2018). In the Miller Bertolami (2016) models, post-AGB evolution is much faster and produces brighter PN progenitors, allowing older stellar populations to produce brighter PNe. However, these models cannot explain the high luminosities of the bright PNe in old stellar populations as for example in the bulge of M31 (Davis et al. 2018).

The luminosity-specific PN number

The total number of PNe $N_{\rm PN}$ can be related with the total bolometric luminosity $L_{\rm bol}$ of the parent stellar population via the luminosity-specific PN number α (Jacoby 1980):

$$N_{\rm PN} = \alpha L_{\rm bol}. \tag{1.10}$$

As PN surveys are always magnitude-limited, the α-parameter can only be determined within a magnitude range spanning Δm magnitudes from the bright cut-off $m^\star$. The α-parameter for a given magnitude range Δm is defined to be

$$N_{{\rm PN},\Delta m} = \int_{m^\star}^{m^\star+\Delta m} N(m){\rm d}m = \alpha_{\Delta m} L_{\rm bol}, \tag{1.11}$$

and depends on the PNLF $N(m)$ as defined in equation (1.9).

In the context of the SSPs theory, the total number of PNe expected in a chemically homogenous, coeval stellar population can be expressed in terms of the specific evolutionary

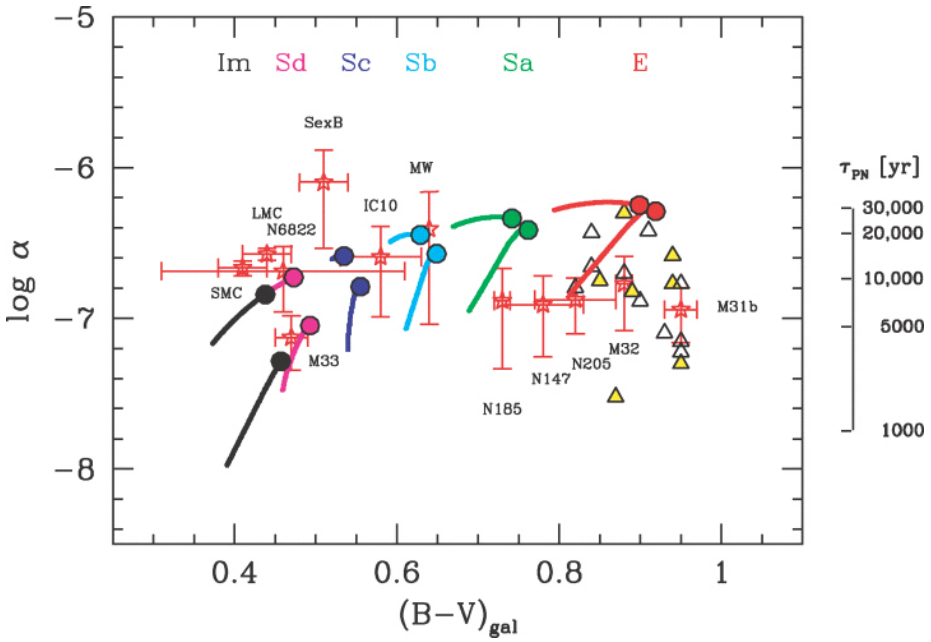

Figure 1.12: Correlation between α-parameter and $B-V$ galaxy colour for local-group galaxies (stars) and external ellipticals (triangles). The Buzzoni (2005) template galaxy models are superposed on the plot. Credit: Buzzoni et al. (2006)

flux $\mathcal{B}$ and the PN visibility lifetime $\tau_{\rm PN}$ (Renzini & Buzzoni 1986; Buzzoni 1989; Buzzoni et al. 2006):

$$N_{\rm PN} = \mathcal{B} L_{\rm bol} \tau_{\rm PN}. \tag{1.12}$$

The specific evolutionary flux $\mathcal{B}$ is defined as the evolutionary flux of a SSP normalised by the unit light, where the evolutionary flux is the rate of stars leaving the main sequence (MS) towards the post-MS evolutionary stages before turning into dead remnants (see e.g. Greggio & Renzini 2011). It therefore links the α-parameter to the evolutionary properties of the underlying SSP:

$$\alpha = \mathcal{B} \tau_{\rm PN}. \tag{1.13}$$

The PN visibility lifetime $\tau_{\rm PN}$, not to be confused with the time spent in the PN evolutionary phase, depends both on the chemical and dynamical properties of the material ejected by the AGB wind as well as the core-mass evolution of the CSPN, whose UV radiation photoionises the nebular gas. The visibility lifetime of PN populations in observed local-group and early-type galaxies ranges between 1 000 and 30 000 years.

As shown in Fig. 1.12, there is observational evidence for a correlation between a galaxy's α-parameter and its $B-V$ colour, with a large spread in α towards redder colours ($B-V > 0.8$, Buzzoni et al. 2006). This alludes to the value of α being dependent on the morphological type of the host galaxy and thus on the properties of the stellar populations therein.

PNe as kinematic tracers

The PNLF and α parameter provide valuable links between the observed PN population and the underlying stellar population(s). As detailed in the previous section, their strong [O III] emission also makes them valuable kinematic tracers, as PNe LOS-velocities can be measured out to several effective radii from a galaxy's centre – regions that cannot be probed with standard spectroscopy due to the decreasing low SB that is characteristic for the extended halos of ETGs and in the case of galaxies in group and cluster environments the IGL and ICL.

Multiple surveys have used PNe to trace the outer regions of ETGs (e.g. Hui et al. 1995; Arnaboldi et al. 1996, 1998, 2004; Douglas et al. 2007; Coccato et al. 2009; Doherty et al. 2009; McNeil et al. 2010; Cortesi et al. 2013a; Coccato et al. 2013; Arnaboldi et al. 2017; Pulsoni et al. 2017) and the ICL of nearby galaxy clusters (e.g. Gerhard et al. 2005; Ventimiglia et al. 2011; Longobardi et al. 2015a; Spiniello et al. 2018) and it is now unanimously accepted that the PN kinematics are in good agreement with those derived absorption-line studies in the region of overlap (e.g. Coccato et al. 2009). The large extent of these surveys has revealed that a majority of the ETGs show a kinematic transition from the inner to the outer halo and that the radius at which this transition happens anticorrelates with galaxy mass (Pulsoni et al. 2017).

1.5 This thesis

The aim of this thesis is to study the stellar populations in the halos of early-type galaxies living in the centres of nearby groups and clusters. The study of the outermost regions of galaxies provides insights into the accretion history of galaxies as galaxy halos contain fossil records of past accretion and merging events. By studying the BCGs of groups and clusters, it is furthermore possible to trace the transition from the halo under the influence of the BCG's potential to the ICL or IGL that is governed by the group or cluster potential.

In the past decade, the extended halos of nearby galaxies could be photometrically mapped in splendid detail and many LSB features were detected to date (see e.g. Martínez-Delgado et al. 2010; Rudick et al. 2010; Crnojević et al. 2016; Duc et al. 2015, 2011; Mihos et al. 2017; Iodice et al. 2017). Parallel to these developments, cosmological simulations have advanced from pure N-body treatment of gravitational interactions to the inclusion of hydrodynamical effects and the treatment of feedback from SNe and active galactic nuclei (AGN) (Crain et al. 2015; Schaye et al. 2015; Remus et al. 2017; Dolag et al. 2017; Pillepich et al. 2018; Vogelsberger et al. 2014). Cosmological magnetohydrodynamical simulations can be used to better understand the physical processes at play that drive the formation and evolution of galaxies in different environments.

The two galaxies studied in this thesis are M49 (NGC 4472), the brightest galaxy in the Virgo Cluster, centred on the Subcluster B, and M105 (NGC 3379), an ETG in the Leo I Group. While the two environments have very different halo masses, both galaxies are surrounded by very extended but blue halos. In the case of M105, the CMD of individual

stars from HST imaging indicates unambiguously that these stars are old (≈ 12 Gyr) and metal-poor ([Fe/H] ≈ -1.5 Lee & Jang 2016).

The blue colour ($B-V \simeq 0.6-0.7$), total luminosity (10% of the total) and size (50 to 100 kpc) of these halos are in conflict with conventional hierarchical assembly because they cannot be formed by the predicted late satellite accretion. The halos' blue colour matches that of dwarfs like Fornax or Phoenix in the LG. Hence their build-up by accretion of galaxies of this type would correspond to a $10^{-3}:1$ mass-merger ratio, yet requires that this inefficient channel contributes up to 10% of the light of the galaxy at $z = 0$. This scenario conflicts with the predictions of hydrodynamical cosmological simulations (e.g. Rodriguez-Gomez et al. 2016), which rule out a significant mass contribution from very minor mergers with mass ratios below $10^{-2}:1$. Higher-mass merging satellites would deposit stars with much higher metallicities of [Fe/H]~ -0.2 (Tremonti et al. 2004), and correspondingly redder colours. Conversely, if these metal-poor halos were to come from the rapid early assembly at $z \geq 3$, as indicated by the age of the metal-poor stars in M105, they would need to have reached a 50-100 kpc size then, which is at odds with the observed apparent slow growth of the stellar half-mass radius at those redshifts (van der Wel et al. 2008). Forming many low-mass, low-metallicity satellite galaxies early at these large radii would seem plausible, but it is also in contradiction with the results from recent cosmological simulations (Correa et al. 2015).

Thus, the properties of these blue halos represent a significant challenge to the current picture of galaxy formation. Its resolution requires developing new approaches to understanding the nature of these outer stellar components. In this thesis, I use extended samples of PNe in order to trace the transitions from the BCG halo to the surrounding ICL and IGL signalled by changes in the PN distribution, i.e. by the α-parameters and PNLF, as well as by their kinematics. In what follows, I will briefly describe the environments of the two galaxies studied in this thesis.

1.5.1 M49 in the Virgo Cluster

The Virgo Cluster is one of the closest cluster environments and therefore has been the target of numerous observational campaigns that revealed a complex dynamical history. It is not in dynamical equilibrium yet and is composed of multiple subgroups, labelled Virgo A, B, and C, that were first identified by Binggeli et al. (1987). The centres of the subgroups coincide with the location of the massive ETGs M87, M49, and M60. The X-ray emission of the hot and dense ICM is also highest at these centres (Schindler et al. 1999). In the image of the Virgo Cluster in the left panel of Fig. 1.13, the brightest galaxies in the subclusters A and B are annotated.

Colour segregation effects as described in Sect. 1.3.1 are also observed in the Virgo Cluster: in each subcluster, Boselli et al. (2014) observe that red galaxies are more abundant in high-density regions, while blue star-forming galaxies are more abundant in the outskirts of the cluster. This segregation is also observed on the scale of the entire cluster as galaxies in the most massive subcluster A are devoid of dusty and gaseous phases of the interstellar medium (ISM) while subcluster B hosts a large faction of blue, star-forming

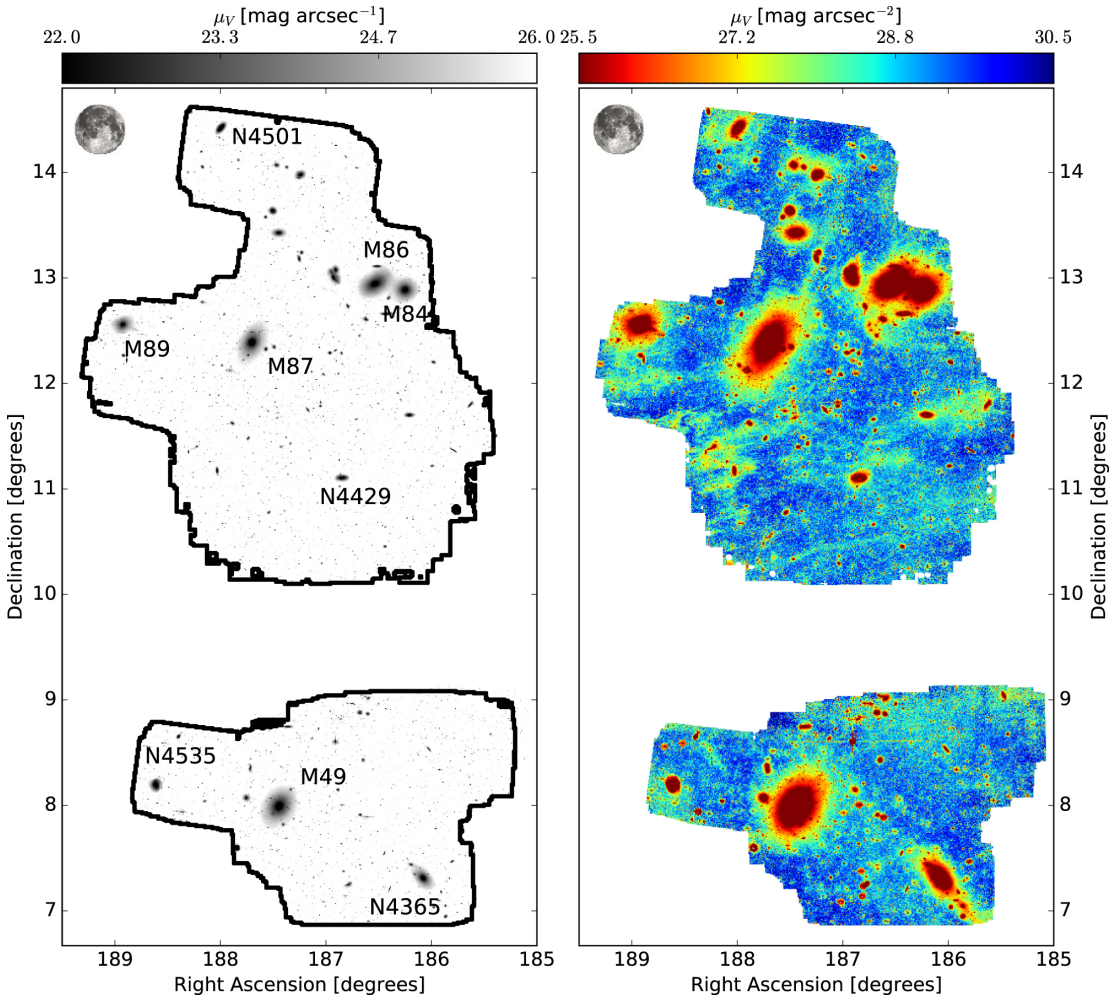

Figure 1.13: False-colour image of the Virgo Cluster. *Left:* V-band image of the Virgo Cluster *Right:* Same image with the magnitude-scale stretched to highlight the plethora of LSB features building up the ICL of the Virgo Cluster. Credit: Mihos et al. (2017).

galaxies.

As shown in the right panel of Fig. 1.13, the space between the bright galaxies is filled by intricate structures of diffuse ICL, which is indicative of its hierarchical assembly (Mihos et al. 2005, 2017). The ICL in the subcluster A has also been well traced by intra-cluster PNe (Feldmeier et al. 2004; Aguerri et al. 2005; Castro-Rodriguéz et al. 2009). Its BCG, M87 (NGC 4486), has been the target of a successful pilot PN survey that uncovered the transition from an inner PN-scarce galaxy to an outer PN-rich accretion driven component (Longobardi et al. 2013, 2015a,b).

In this thesis, I am extending this survey to M49 (NGC 4472), the brightest elliptical galaxy in the Virgo Cluster and the BCG of the Virgo Subcluster B. As there is an extended X-ray bow shock to the north of M49, Irwin & Sarazin (1996) suggested that the Subcluster B is falling into the centre of the Virgo Cluster. The Subcluster B therefore acts like an ICL pre-processing factory for diffuse light in the main cluster and is thus an ideal laboratory to better understand the processing contributing to ICL formation.

1.5.2 M105 in the Leo I Group

Compared to the Virgo Cluster, the Leo I group, a loose group containing a dozen of galaxies, is a very small – maybe even insignificant – association of galaxies. However, group environments are the most common environments for galaxies to reside in and, in the hierarchical paradigm, are the progenitors of larger structures such as clusters. *Loose groups*[13] are characterised by small number of luminous galaxies within a radius of 0.5 Mpc and a small velocity spread of 350 km s^{-1} and the Leo I group has been classified as such by several authors (de Vaucouleurs 1975a; Huchra & Geller 1982; Tully 1987). At just 10.3 Mpc (Tonry et al. 2001) it is the nearest loose group to contain both early- and late-type massive galaxies (de Vaucouleurs 1975b).

The left panel of Fig. 1.14 shows a false-colour image (Watkins et al. 2014) with the most luminous galaxies in the Leo I group highlighted along with contours of the so-called Leo Ring. The origin of this 200 kpc diameter broken ring of neutral hydrogen, first discovered by Schneider et al. (1983), is still highly debated. After its discovery, Schneider (1985) showed that the kinematics of the H I gas could be reconciled with an elliptical orbit centred at the luminosity-weighted centroid of M105 and the nearby NGC 3384 spiral galaxy. In their model, the ring rotates with a period of approximately 4 Gyr. However, the crossing times in the group are much shorter than this (Pierce & Tully 1985), which is problematic for the stability of the ring. Moreover, only the disk of NGC 3384 is aligned with the orientation of the ring, which is puzzling if M105, NGC 3384, and M96 formed from a single rotating cloud.

An alternative formation scenario to the primordial origin of the H I ring is the collision of two spiral galaxies (Rood & Williams 1984, 1985). A recent simulation of the collision of two gaseous disk galaxies reproduces both the shape and rotation of the H I ring as well

[13]Ironically, in this context, the term "Loose Group" can only be loosely defined due to the irregular nature of these systems.

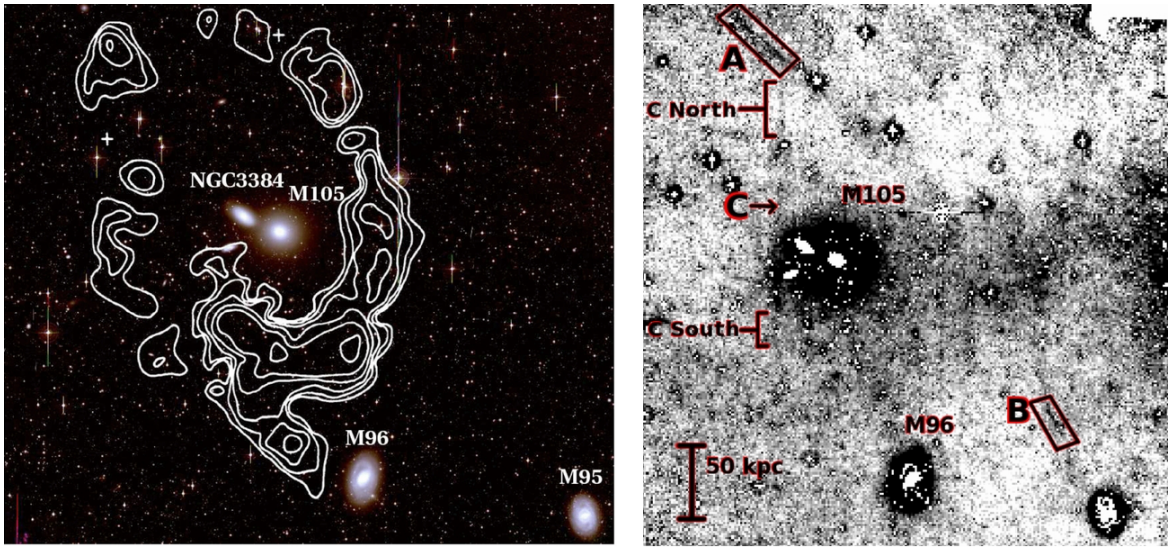

Figure 1.14: M105 at the centre of the Leo I Group. *Left:* False-colour $B-V$ image of the Leo I Group with contours of the H I ring superposed. *Right:* B-band image with pixels binned 18×18 to enhance LSB features. Credit: Watkins et al. (2014).

as the lack of a visible-light counterpart (Michel-Dansac et al. 2010). To date, neither of the two scenarios has been disproven or confirmed. Watkins et al. (2014) detected no LSB stellar counterpart to the H I ring, however, they find streamlike features that might be associated with it (see right panel of Fig. 1.14). Except for these streamlike features, the authors do not find extended diffuse IGL within the SB limit of $\mu_B = 30$ mag arcsec^{-2} and argue that the group might not be dynamically evolved enough to have generated a substantial amount of IGL.

1.5.3 Structure of this thesis

This thesis is organised as follows.

In Chapter 2, I will describe the results from our photometric PN survey of the halo of M49 and its immediate environment – the Virgo Subcluster B. This survey is the deepest and most extended PN survey of this galaxy to date. In this chapter, I first review the CMD-based PN detection technique used in this work and then determine the radial PN number density profile of PNe in M49's halo. Based on the flattening of the number density profile with respect to the stellar SB profile we identify an extended IGL component that is characterised by a three-times higher specific frequency α compared to the main halo, a very blue colour, and a constant SB profile. We also show that the variation of the α-parameter within M49 with galaxy colour agrees well with the α-colour relation for individual galaxies (Buzzoni et al. 2006). We find that M49's PNLF is steeper than the standard Ciardullo PNLF and that the distance determined from its bright cut-off agrees with M49's surface-brightness fluctuation (SBF) distance. The PNLF-slope varies within the inner halo; its steeper slope in the eastern quadrant is likely due to young PN associated

with the accretion of the dIrr galaxy VCC 1249. We then compare our findings on the IGL properties with those on M87's ICL properties from Longobardi et al. (2013): we find that their PN populations reflect the different environments in which they reside.

In Chapter 3 I continue our work on the ETG M49 and link the findings from Chapter 2 to the kinematic properties of M49 as traced by PNe. We find evidence for three dynamically distinct stellar populations, which are M49's main halo, stellar-kinematic substructure associated with the infall of the dIrr galaxy VCC 1249, and the extended IGL characterised by a large velocity dispersion. The dispersion of the PNe associated with the IGL joins onto that of the satellite galaxies in subcluster B; we thus observe the kinematic transition from halo to IGL and this is the first time that this transition is traced with *individual* stars. We conclude that M49's halo has undergone an extended parent group potential. The blue colours of the IGL component are consistent with a population of stars formed in low-mass galaxies at redshift $z \sim 0.5$ that has since evolved passively.

In Chapter 4 I present our recent study of the halo of the ETG M105 in the Leo I group based on new deep and extended narrow-band photometry and the extremely-extended PN.S ETG survey. I first review the different data sets and their reduction techniques, and then provide an overview on the current status of broad-band photometric surveys of the Leo I group. Based on the PN number density profile of our extended photometric survey we find evidence for a very faint, but PN-rich IGL population that would not have been detected based on broad-band photometry alone. The PNLF of M105 is characterised by a steeper faint-end slope than the standard Ciardullo PNLF. We observe a steepening of the PNLF slope from the inner to the outer halo. As M105 has a companion galaxy, NGC 3384, and the two galaxies overlap in velocity phase-space, I construct a Gaussian-mixture model (GMM) to decompose our kinematic sample into components associated with M105 and NGC 3384. Due to the sparser coverage at large radii in the kinematic sample, we can unfortunately not identify a kinematic counterpart to the IGL identified from the photometric sample. However, our kinematics provide first constraints on the much-debated matter content of M105.

In Chapter 5 I will summarise the main findings of this thesis and draw my conclusions. Finally, in Chapter 6 I will discuss the future perspectives of this work.

Chapter 2

The halo of M49 and its environment as traced by planetary nebulae populations[1]

This chapter is published as the paper Hartke et al. (2017) in Astronomy & Astrophysics.

2.1 Introduction

In the context of hierarchical structure formation, galaxies grow by mergers and accretion of smaller structures (e.g. White & Frenk 1991; Steinmetz & Navarro 2002; Oser et al. 2012) that leave long-lasting signatures in the galaxies' outermost regions, because of long dynamical timescales (of the order of a Gyr at 50 kpc). Early-type galaxies (ETGs) predominantly consist of a very old population of stars that are believed to have formed on a short timescale ($\sim$ 1 Gyr, Thomas et al. 2005, and references therein). The strong size evolution of massive early-type galaxies (ETGs), that is, of a factor of between two and four from $z \sim 2$ (e.g. Daddi et al. 2005; van Dokkum et al. 2008) can be explained with a two-phase formation scenario for which the initial phase of violent star formation is followed by accretion events (Oser et al. 2010; Pillepich et al. 2015), whose stellar populations are also old. Hence the distribution of stars and their dynamics at very large radii around massive ETGs should contain important evidence of their accretion histories (Cooper et al. 2013; Cook et al. 2016).

In nearby galaxies, the halos can be mapped with absorption-line spectroscopy of red giant branch (RGB) stars, providing spatial and line-of-sight (LOS) velocity distributions (e.g. McConnachie et al. 2009; Crnojević et al. 2013, 2016). While RGB stars are an excellent tracer to map the halos of the Milky Way (MW), M31, or Centaurus A, it becomes too costly to carry out absorption-line spectroscopy for faint sources with apparent

[1]Based on data collected at Subaru Telescope, which is operated by the National Astronomical Observatory of Japan under programme S14A-006. We thank S. Okamura and F. Nakata for carrying out the observations with SurpimeCam@Subaru. I subsequently reduced, calibrated, and analysed the data.

magnitudes $m_V > 23.5$ mag.

Integral-field spectroscopy (IFS) has played a pivotal role in characterising the two-dimensional kinematics of ETGs (Cappellari 2016) within the high surface brightness regions ($1 - 2r_e$). To reach larger distances, discrete tracers are needed to study the halos of bright ETGs. Two common discrete tracers at distances larger than $2r_e$ are planetary nebulae (PNe) and globular clusters (GCs). The latter can be separated into red (metal-rich) and blue (metal-poor) populations, which possess different spatial, velocity, and angular momentum distributions (Coccato et al. 2013; Pota et al. 2013; Hargis & Rhode 2014). The GC systems in nearby bright ETGs have been studied in multiple surveys (e.g. SLUGSS: Usher et al. (2012), NGVS: Durrell et al. (2014)).

PNe are a population of dying asymptotic giant branch (AGB) stars in the zero-age main sequence mass range of $1 - 8\,M_\odot$. The core star strongly emits in the UV. This radiation ionises the envelope of gas surrounding the core star, which re-emits 10% of the UV radiation in one optical line: the [O III]5007Å line. It can still be detected in distant galaxies and serves as an identifier of PNe (Dopita et al. 1992). Observational evidence suggests that PNe trace stellar light (e.g. Ciardullo et al. 1989; Coccato et al. 2009; Cortesi et al. 2013b) and that their angular momentum distribution is that of the stars (e.g. Hui et al. 1995; Arnaboldi et al. 1996, 1998; Méndez et al. 2001). As their luminosity-specific frequency does not vary much with galaxy type (Buzzoni et al. 2006), they are an effective tracer of substructures, which have not been detected in previous imaging or integrated absorption-line spectroscopy, as for example the stellar stream in the M31 disc (Merrett et al. 2006) and the crown in M87 (Longobardi et al. 2015b).

In order to relate the observed properties of the PN population in external galaxies with the properties of the stellar population (e.g. age and metallicity), one characterises the PN population by the luminosity-specific PN number (α-parameter) and the shape of the planetary nebula luminosity function (PNLF). Observational evidence suggests that the α-parameter, which relates the stellar luminosity with the number of PN, is further correlated with the integrated $(B-V)$ colour of the galaxy (Buzzoni et al. 2006). Ciardullo et al. (1989) analytically describe the shape of the PNLF based on the LF of PNe in M31. The shape of the PNLF is governed by a bright cut-off at $m^\star$. The absolute magnitude $M^\star$ of this cut-off is invariant with galaxy type and can therefore be used as a secondary distance indicator to the respective galaxy (Ciardullo et al. 2002).

The Virgo Cluster is an interesting target as there are many indicators for a complex dynamical history. It is one of the closest cluster environments and has already been targeted by a number of PN surveys (Ciardullo et al. 1998; Feldmeier et al. 1998, 2004; Arnaboldi et al. 2002, 2003; Aguerri et al. 2005; Castro-Rodriguéz et al. 2009). It is composed of multiple subgroups (Virgo A, B, and C), that were first identified by Binggeli et al. (1987, 1993), centred on the ETGs M87, M49, and M60. The X-ray emission of the hot and dense intergalactic medium is highest at the centres of the subclusters, where the concentration of quiescent galaxies peaks (Schindler et al. 1999). Boselli et al. (2014) observe a colour-segregation effect in the (sub)cluster: red galaxies are located in the high-density regions, whereas blue star-forming galaxies are found in the outskirts of the cluster. Galaxies at the centre of subcluster A are devoid of dusty and gaseous phases of the ISM,

while subcluster B mainly consists of star-forming galaxies.

Deep wide-field imaging reveals intricate structures of diffuse intra-cluster light (ICL) surrounding the bright ETGs, suggesting a hierarchical build-up (Mihos et al. 2005, 2017). This is also reflected in the distribution of intracluster PNe, which show field-to-field variations (Feldmeier et al. 2004; Aguerri et al. 2005; Castro-Rodriguéz et al. 2009). The colours of ICL features around the cluster core near the cD galaxy NGC 4486 (M87) are similar to those of M87's halo itself, suggesting that they may have formed from similar progenitors (Rudick et al. 2010).

The galaxy M87 has been the target of a successful pilot survey combining narrow-band photometry from Suprime-Cam at the Subaru telescope (Longobardi et al. 2013) with high-resolution spectroscopy with FLAMES at the VLT (Longobardi et al. 2015a), uncovering the transition from an inner PN-scarce (old and metal-rich) galaxy to an outer PN-rich, accretion-driven component (young and metal-poor). Longobardi et al. (2015b) identified a recent satellite accretion event through a chevron-like PN structure, that also manifests itself as excess light in the M87 outer halo.

We extended this survey to NGC 4472 (M49), the brightest elliptical galaxy in the Virgo Cluster, residing at the centre of subcluster B. The X-ray bow shock to the north of the galaxy suggests that it is falling into the centre of the Virgo Cluster (Irwin & Sarazin 1996). M49 possesses a system of shells along the major axis, suggestive of past accretion events of satellite galaxies (Janowiecki et al. 2010; Capaccioli et al. 2015). Further substructure is associated with the dwarf galaxy VCC 1249 (UGC 7636). Optical and infrared observations combined with Hα measurements show signs of a recent interaction between the dwarf and M49 (Arrigoni Battaia et al. 2012). Côté et al. (2003) mapped the dynamics of M49's GC system within 400″ (33 kpc), and a more extended photometric GC study mapped M49's halo in its entirety, finding a smooth GC density distribution with radius (Durrell et al. 2014).

This paper is organised as follows: in Sect. 2.2 we describe the photometric PN survey and the data reduction procedure. The selection and validation of PN candidates is described in Sect. 2.3. We then study the relation between the azimuthally averaged spatial distribution of the PN candidates and the stellar surface brightness of M49 in Sect. 2.4. In Sect. 2.5 we present the PNLF of M49 and the corresponding inferred distance. In Sect. 2.6 we trace variation of the PNLF in M49's halo with our PN catalogue and discuss whether these are signatures of substructure in Sect. 2.7. We summarise and conclude in Sect. 2.8. If not stated otherwise, we assume a distance of 17.1 Mpc (Mei et al. 2007) to M49 that corresponds to a physical scale of 82 pc per 1″.

2.2 The Suprime-Cam M49 PN survey

This survey expands the ongoing effort to study PNe as tracers in cluster and group environments. We use the same techniques as Longobardi et al. (2013), who observed M87 at the centre of Virgo's subcluster A using the same instrumental configuration. In order to detect PN candidates, we used a narrow-band filter centred on the [O III]5007Å-line and

measure the colour excess of spatially unresolved sources with respect to the continuum, measured in the broad V-band.

2.2.1 Imaging and observations

The observations were carried out with the Suprime-Cam at the prime focus of the 8.2 m Subaru telescope (Miyazaki et al. 2002) in May 2014. The 10k × 8k mosaic camera covers an area of $34' \times 27'$, corresponding to a scale of $0\farcs2$ per pixel. The halo of M49 can thus be observed out to a radial distance of 155 kpc with a single pointing.

As we identified PNe using the on-off-band technique (see Sect. 2.3 for further details), we observe M49 through a narrow-band [O III] filter ($\lambda_c = 5029$ Å, $\Delta\lambda = 74$ Å, on-band) and a broad-band V-filter ($\lambda_c = 5500$ Å, $\Delta\lambda = 956$ Å, off-band). The on-band image consists of 13 dithered exposures with a total exposure time of three hours and the off-band image of 14 dithered exposures with a total exposure time of 1.4 hours. The exposure time was chosen such that PNe with an apparent narrow-band magnitude of 2.5 mag from the bright cut-off $m^{\star}_{5007} = 26.79$ can still be detected assuming a distance modulus of 30.8 for Virgo. The observations were carried out in one night, with photometric conditions. Throughout the whole night, the seeing was better than $0''.7$ and the airmass of the observations varied between 1.1 and 1.5.

2.2.2 Data reduction, astrometry, and flux calibration

The data were reduced using the instrument pipeline SDFRED[2] for Subaru's Suprime-Cam. As this data set will be used to provide positions of PN candidates for a spectroscopic follow-up, accurate astrometry is needed. We improved the accuracy of the images using the IRAF[3] package `imcoords` with the 2MASS catalogue as an astrometric reference frame.

In order to flux calibrate the broad-band and narrow-band frames to the AB magnitude system, we observed standard stars through the same filters used for the survey, using the spectrophotometric HILT600 and BD332642 stars for the [O III]-band and Landolt stars for the V-band. The zero points for the [O III] and V-band frames normalised to a 1 second exposure are $Z_{[\mathrm{O\,III}]} = 24.51 \pm 0.04$ and $Z_{\mathrm{V}} = 27.48 \pm 0.01$. These values are consistent with those obtained by Longobardi et al. (2013), and Castro-Rodriguéz et al. (2009), who use the same filters for the Suprime Cam narrow-band photometry.

The integrated flux F_{5007} from the [O III] line can be related to the magnitude m_{5007} using the following relation (Jacoby 1989)

$$m_{5007} = -2.5 \log_{10} F_{5007} - 13.74, \tag{2.1}$$

[2] `http://www.naoj.org/Observing/Instruments/SCam/sdfred`

[3] IRAF is distributed by the National Optical Astronomy Observatories, which are operated by the Association of Universities for Research in Astronomy, Inc., under cooperative agreement with the National Science Foundation

where the flux is in units of ergs cm^{-2}s^{-1}. Arnaboldi et al. (2003) determine the relation between the AB and m_{5007} magnitudes to be

$$m_{5007} = m_{AB} + 2.49 \tag{2.2}$$

for the narrow-band filter in use.

The final images are the astrometrically and photometrically calibrated, stacked images in the [O III] and V-band. We fitted the point-spread function (PSF) using the IRAF task `psf`. The best-fit profile is a Gaussian analytical function with a radius $r = 2.36$ pixels and a standard deviation $\sigma = 2.35$ pixels. We also computed the PSF fit in four different image regions separately showing that the PSF does not vary across the image.

2.3 Selection of the PN candidates and catalogue extraction

PNe have a bright [O III]5007Å and no continuum emission.[4] Therefore extragalactic PNe can be identified as objects detected in the on-band [O III] image, which are not detected in the off-band continuum images, or in other words, which have an excess in [O III] - V colour. Furthermore PNe are unresolved at extragalactic distances, therefore we only considered point-like objects for analysis. We used the automatic selection procedure developed and validated in Arnaboldi et al. (2002, 2003), subsequently applied to studies of PN populations in Virgo's diffuse ICL (e.g. Castro-Rodriguéz et al. 2009) and in Virgo ellipticals. The selection procedure has been tailored to Suprime-Cam data by Longobardi et al. (2013). As the selection procedure is vital to the properties of the extracted catalogue we review the main steps in the following section and refer to Appendix 2.A for further information regarding the basic catalogue extraction.

2.3.1 Catalogue pre-processing

Throughout the following analysis, we used SExtractor (Bertin & Arnouts 1996) as a tool to detect and carry out photometry of the sources on the images. The narrow- and broad-band magnitudes $m_{\rm n}$ and $m_{\rm b}$ are measured in dual-image mode for sources detected on the narrow-band image. In order to determine the **limiting magnitude** of our survey, we populated the images with a synthetic PN population that follows a Ciardullo-like PNLF and determine the recovery fraction as a function of magnitude. The magnitude at which the recovery fraction drops below 50% is adopted as the limiting magnitude; on the narrow-band image it is $m_{\rm n,lim,cat} = 26.8$ (AB magnitude) or $m_{5007,\rm lim,cat} = 29.3$ (see Sect. 2.A.1).

There are different **image artefacts** that can lead to false detections of PNe. We therefore masked the pixel columns affected by dithering as well as regions with a high

[4] If a faint continuum emission is detected at the position of [O III] emission, it is likely to be caused by background residuals or crowding.

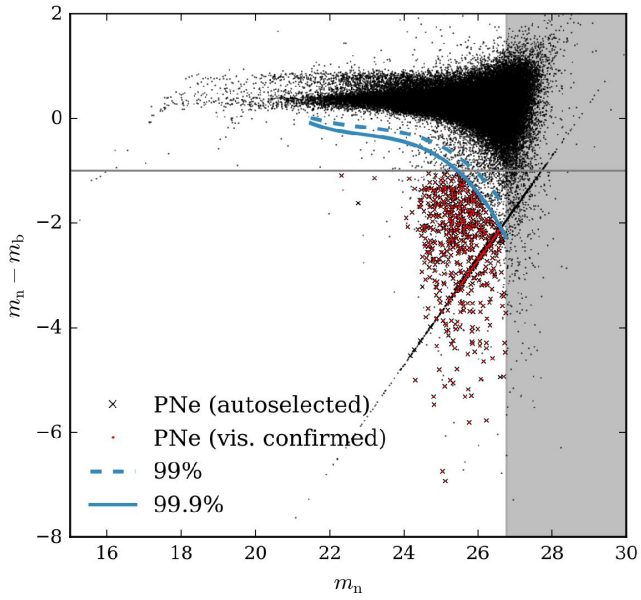

Figure 2.1: CMD for all sources in the M49 Suprime Cam field. Objects below the horizontal line are emission line objects with an $EW_{obs} \leq 110$ Å and colour excess. The solid (dashed) blue lines indicate the regions above which 99.9% (99%) of simulated continuum objects fall. Objects fainter than the limiting magnitude fall into the grey region. The candidate PNe from the automatic selection are denoted by crosses and those confirmed by visual inspection of the images by red dots.

background value (e.g. due to charge transfer or saturated stars). Due to the high contribution of diffuse galaxy light we furthermore excluded objects detected within a major-axis radius of $r_{major} = 159''$ (corresponding to 13 kpc) from the galaxy's centre.

2.3.2 Object selection

We selected objects as PN candidates based on their position on the colour-magnitude diagram (CMD) and their spatially unresolved light distribution. The CMD selection criteria are shown in Fig. 2.1. We selected objects with a colour excess of $m_n - m_b \leq -1$ that are brighter than the survey's limiting magnitude $m_{n,lim,cat} = 26.8$. In order to limit the contamination by foreground stars we then constrained our sample to those objects that fall below the 99.9% confidence limits of a simulated continuum population.

In Fig. 2.1 and Fig. 2.2 we show the CMD-selected sources that are classified as unresolved or point-like sources. Based on the light distribution of the simulated population, point-sources satisfy the following two criteria: these sources (i) have a half-light radius of $1 < R_h < 3.5$ pixel, where the upper limit corresponds to the 95%-percentile of the simulated population, and (ii) they fall in the region where the difference between m_n and m_{core} is within the 95%-limits of the simulated population (see Sect. 2.A.4).

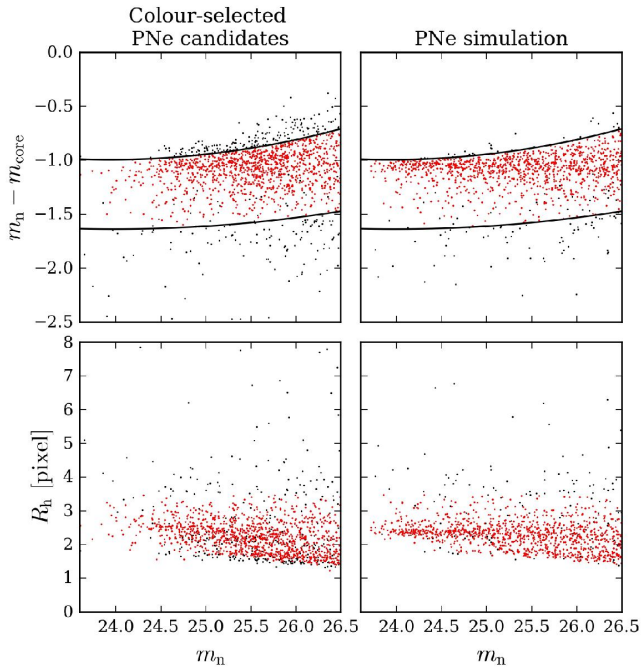

Figure 2.2: Point-source test: The left column shows the colour-selected PNe candidates and the right the simulated PN-population. The top row shows $m_\mathrm{n} - m_\mathrm{core}$ vs. m_n, the black lines indicate the region in which 95% of the simulated population fall. The bottom row shows R_h as a function of m_n. We impose a limit of 3.5 pixel on R_h, such that 95% of the simulated population is included. Objects which satisfy both criteria are plotted in red and are termed point-like.

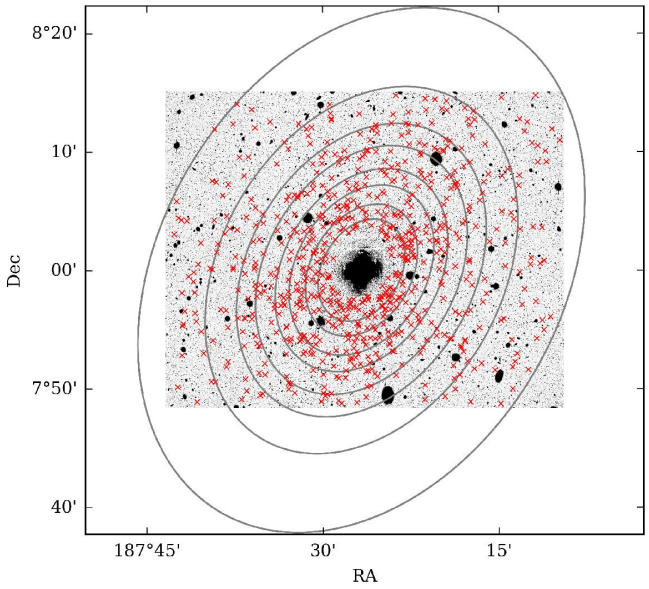

Figure 2.3: [O III] image of M49 with PN candidates overplotted in red. The elliptical bins have $PA = -31°$ and a constant ellipticity $\epsilon = 0.28$ (Kormendy et al. 2009) and were defined such that they contain the same number of objects. North is up, east is to the left.

2.3.3 Catalogue completeness

Evaluating the completeness of our catalogue is a critical step to be carried out before we can use it for further investigation (see Sect. 2.A.5 for further details). We again made use of our synthetic PN population and determined its recovery as a function of radius to assess its spatial completeness ($c_{\rm spatial}(r)$) and as a function of magnitude for the photometric completeness. For the latter, we independently determined the detection and colour completeness ($c_{\rm detection}(m_{5007})$ and $c_{\rm colour}(m_{5007})$ respectively).

2.3.4 Catalogue validation and visual inspection

The photometric catalogue obtained from the automatic selection was visually inspected and any remaining spurious detections were removed. Spurious detections amounted to $\sim$ 3% of the automatically extracted sources, the final catalogue contains 735 sources. The visually confirmed PN candidates are shown in Fig. 2.1. The spatial distribution of the extracted and visually confirmed objects is shown in Fig. 2.3, superposed on the continuum-subtracted mosaic image.

While the limiting magnitude based on completeness estimations is $m_{5007,\rm lim,cat} = 29.3$ (see Sect. 2.3.3), we introduce a more conservative limit of $m_{5007,\rm lim} = 28.8$ based on the morphology of M49's PNLF (see Sect. 2.5). At fainter magnitudes, the PN-number counts decline strongly (Fig. 2.4). Given that the number of PNe increases exponentially as a

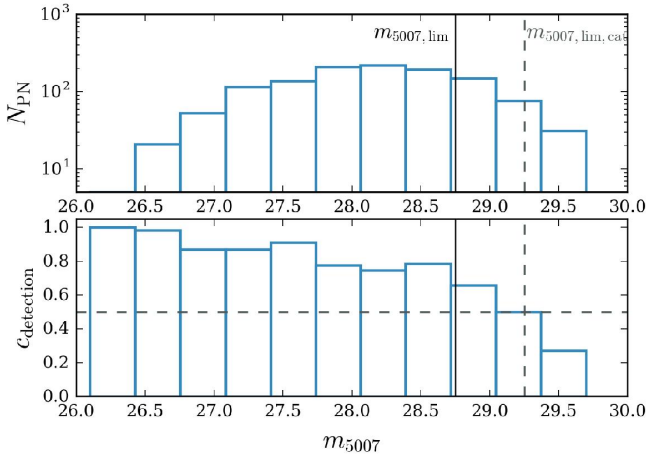

Figure 2.4: Observed number counts of PN as function of magnitude (top panel) and detection completeness of a simulated PN population (bottom panel). The dashed horizontal line denotes the 50% recovery limit that results in the limiting magnitude $m_{5007,\mathrm{lim,cat}} = 29.3$ indicated by the dashed vertical line. The solid vertical line denotes the conservative limiting magnitude $m_{5007,\mathrm{lim}} = 28.8$ based on the decrease of the observed PN-number counts.

function of magnitude beyond the cut-off in old stellar populations (Ciardullo et al. 1989; Longobardi et al. 2015b), such behaviour is indicative of photometric incompleteness. Our final complete sample within $m_{5007,\mathrm{lim}} = 28.8$ consists of 624 PNe.

2.3.5 Possible sources of contamination

Contamination by faint continuum objects

As we describe in Sect. 2.A.3, we limited our selection of objects to those that fall below the 99.9%-line of a simulated continuum population in order to minimise the contamination by foreground objects, for example, faint MW stars. However, some of these objects will be scattered below this line. We estimated the fraction of foreground contaminants in the colour-selected sample by determining the total number of observed foreground stars down to $m_{\mathrm{n,lim}}$ and assuming that 0.1% of these are scattered into the sample of colour-selected PNe. This results in 47 objects, which corresponds to a contribution of 8% of the extracted sample of 624 PNe.

Contamination by background galaxies

Another source of contamination are faint background Ly-α galaxies, that emit at the same wavelength as PNe in the Virgo Cluster, if at redshift $z = 3.1$. In order to quantify this effect, we use the Ly-α luminosity function (LF) determined by Gronwall et al. (2007), who carried out a deep survey for $z = 3.1$ Ly-α emission-line galaxies. The LF is characterised by

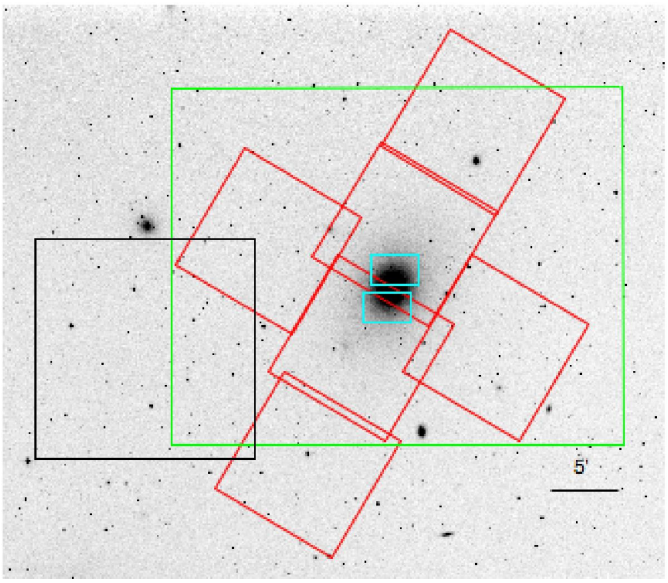

Figure 2.5: DSS image of M49 with PN survey fields overplotted. Green: this survey, cyan: Jacoby et al. (1990), black: Feldmeier et al. (2003), red: PN.S (Pulsoni et al. 2017)

a Schechter-function (Schechter 1976). More recent surveys (e.g. Ciardullo et al. 2012) agree with this LF within 0.1 mag. For a detailed description, we refer the reader to Longobardi et al. (2013) who estimated the number of background contaminants for two Suprime-Cam fields covering Virgo's central galaxy M87. An important validation of this approach is the confirmation of the number of estimated contaminants during the spectroscopic follow-up of PN candidates (Longobardi et al. 2015a). As our survey is half a magnitude deeper than that of Gronwall et al. (2007), we extrapolate the LF to a limiting magnitude of $m_{5007,\mathrm{lim}} = 28.8$. We expect 310 Ly-$\alpha$ emitters, which corresponds to $(29.8 \pm 6.0)\%$ of the completeness-corrected sample. The corresponding LF is shown in Fig. 2.10.

Another source of background contaminants are [O II]3727Å emitters at redshift $z = 0.345$. The colour-selection criterion $m_\mathrm{n} - m_\mathrm{b} < -1$ corresponds to an observed equivalent width of $EW_\mathrm{obs} > 110\,\text{Å}$, which reduces the contribution from [O II] emitters, as no [O II] emitters beyond $EW_\mathrm{obs} > 95\,\text{Å}$ have been observed (Colless et al. 1990; Hammer et al. 1997; Hogg et al. 1998). Gronwall et al. (2007) employ a similar colour-selection criterion ($\Delta m_\mathrm{G07} \lesssim -1$) and consider the fraction of [O II] contaminants at redshift $z = 0.345$ negligible. Therefore the contribution of background [O II] emitters with $EW_\mathrm{obs} > 110\,\text{Å}$ is accounted for when using the Gronwall et al. (2007) Ly-α LF.

2.3.6 Comparison with other PN-surveys of M49

The first survey of PNe in M49 was carried out by Jacoby et al. (1990). They detected 54 objects with [O III] excess, of which 27 belong to the statistically complete sample as defined by the authors. This survey consists of two $3.'5 \times 2.'2$ CFHT fields that cover the

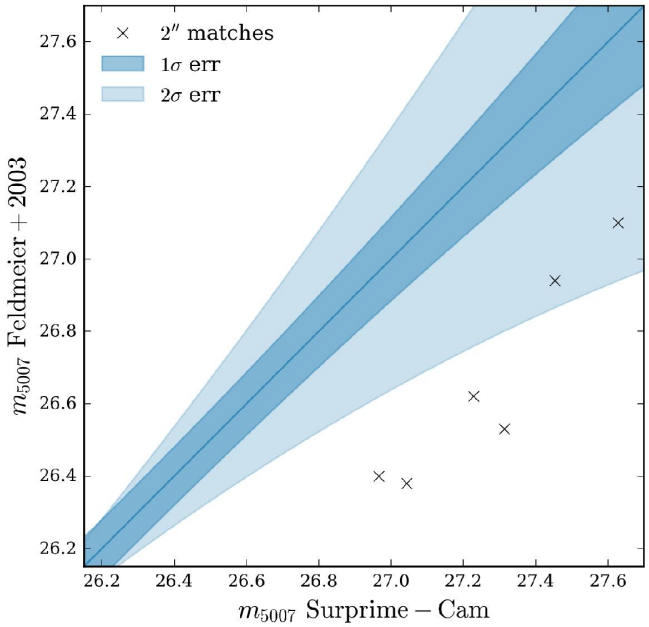

Figure 2.6: Magnitude comparison and photometric error of the matched emission-line objects between our catalogue and Feldmeier et al. (2003).

central region of M49 and are indicated in Fig. 2.5 (cyan rectangles). As the majority of this region is masked out in our deep images, only one common PN candidate is identified. We will discuss the comparison between our PNLF and that of Jacoby et al. (1990) in Sect. 2.5.

Our survey also overlaps with a previous photometric study of intra-cluster PNe (Feldmeier et al. 2003, 2004). The field that overlaps with our survey is denoted by a black rectangle in Fig. 2.5 and has been observed with the Prime Focus CCD camera at the Kitt Peak National Observatory (KPNO) 4m telescope. The survey depth in the [O III] is $m_{5007} = 28$ mag. A cross-matching of the survey with our catalogue identifies six common objects. The comparison of the [O III] magnitudes is shown in Fig. 2.6. An average zero-point offset of 0.5 mag is found. A previous comparison of M87's PN sample from from Suprime Cam photometry Longobardi et al. (2013) with PNe identified by Feldmeier et al. (2003) found an offset in magnitude zero-point that equalled to 0.3 mag.

Currently there is no published spectroscopic PNe data for M49 available. However, we have access to unpublished data from the Planetary Nebula Spectrograph (PN.S, Douglas et al. 2002) as part of a survey of ETGs (Pulsoni et al. 2017). Of the six PN.S fields ($10' \times 10'$, indicated in red in Fig. 2.5) four are aligned along the major axis and two along the minor axis, covering $18'$ and $15'$ along the respective axis, extending a little further along the major axis than our survey. In total, 465 PNe have been detected, of which 226 fall into the unmasked regions of our observations. The PN.S is capable of detecting PNe in the Virgo Cluster down to $\Delta m = 1.5$ from the bright cut-off. We therefore matched

only PNe in this magnitude range with the PN.S catalogue. There are 207 PNe in common within a matching radius of 5″, which serves as a first spectroscopic confirmation of these sources.

2.4 The radial PN number density profile and the PN luminosity-specific frequency

In the following section, we determine the radial PN number density profile and compare it to stellar surface brightness profiles derived from broad-band photometric studies of the M49 halo. Empirically, it has been shown that the PN number density profile follows the stellar light in elliptical (Coccato et al. 2009; Longobardi et al. 2013, 2015b) and S0 galaxies (Cortesi et al. 2013a,b). In the last decade, there have been a number of deep photometric surveys of the Virgo cluster. In this section, we will discuss the surface brightness profile and the two-dimensional (2D) properties of the stellar light in M49's extended halo. In a cluster environment, surface brightness and colour profiles do not only provide important evidence about the galaxy halo but also about its environment, the ICL. Our goal is to link the structural components in the light, which are signalled by a change of slope in the radial gradients of the SB profile, isophotal twists, and different colour gradients, with variations in the PN population parameters as the number density profile, PNLF slopes and the α-parameter.

2.4.1 Stellar surface photometry of M49

The stellar surface brightness profile of ETGs is well-described by a Sérsic function (Sérsic 1963) of the form

$$I(r) = 10^{-0.4\mu_e} 10^{-b((r/r_e)^{1/n}-1)}, \tag{2.3}$$

with $b = 0.868n_V - 0.142$. For M49, Kormendy et al. (2009) determine the major-axis fit parameters in the V-band to be $\mu_{e,V} = 23.371^{+0.171}_{-0.144}$ mag arcsec^{-2}, $r_{e,V} = 269.291^{+23.634}_{-18.570}$ arcsec, and $n_V = 5.992^{+0.314}_{-0.292}$. The Sérsic profile is also fit to data from a deep V-band imaging survey of diffuse light in the Virgo Cluster (Janowiecki et al. 2010), the fit-parameters agreeing within $1-2\sigma$ with Kormendy et al. (2009). The effective radius derived from integration of the 2D profile is $r_e = 194\farcs44 \pm 17\farcs0$.

More extended photometry from the VEGAS survey (Capaccioli et al. 2015) is also well-fit by a Sérsic profile with an effective radius of $r_e = 152'' \pm 7''$ in both the g- and i-bands.[5] The g-band profile changes slope beyond a major-axis distance of $r \sim 915''$. A hint of this flattening at large radii can also be seen in the i-band and was also already observed in the surface brightness profile derived from photographic plates by Caon et al. (1994). Figure 2.4 shows the V- and g-band stellar surface brightness profiles of Kormendy

[5]In order to match the g-band photometry to the V-band photometry of Kormendy et al. (2009), we adopted a constant offset of -0.35 as determined by Capaccioli et al. (2015).

et al. (2009) and Capaccioli et al. (2015) as well as the Sérsic fit determined by Kormendy et al. (2009) .

Beyond a major-axis distance of $r \sim 250''$ the orientation and morphology of the isophotes change. The position angle, which is at constant $-20°$ for the main galaxy halo, rapidly decreases from $-20°$ to $-40°$ in the g- and V-band and rapidly increases from $-20°$ to $-5°$ in the i-band. Furthermore, the isophotal ellipticity ϵ changes: the g- and V-band isophotes become more elongated, reaching a maximum ellipticity of $\epsilon \approx 0.3$, while the i-band isophotes become nearly round ($\epsilon \approx 0$, Capaccioli et al. 2015, see Fig. 7 therein).

Gonzalez et al. (2005) suggest that the rapid variation of the isophotes' parameters as well as the flattening of the surface brightness profile at large radii is likely due to a population of ICL. The flattening of the surface brightness profile occurs at a surface brightness level of $\mu_g \sim 27\,\mathrm{mag\,arcsec^{-2}}$ (Capaccioli et al. 2015), which is compatible with the surface brightness where a ICL-induced change of slope is observed in a sample of stacked SDSS galaxy clusters between redshift $z = 0.2$ and 0.3. (Zibetti et al. 2005). In the case of M49, which is located at the heart of the Virgo Subcluster B, this extra light is probably not ICL from the main Virgo Cluster, but rather intra-group light (IGL, Rudick et al. 2006; Gonzalez et al. 2005) of the subcluster B.

The colour profile of M49 has a clear gradient that is shallow in the red, inner regions and steepens towards the bluer outskirts (Mihos et al. 2013; Capaccioli et al. 2015). The transition from shallow to steep gradient occurs at $r \sim 200''$, similar to where the isophotes start to change ellipticity and orientation. There are at least two causes for such a colour gradient, which might be interlinked. It can be interpreted as a metallicity gradient from a metal-rich to a metal-poor component, but also as an age gradient from an older to a younger population. This supports the assumption of a two-component galaxy halo with a change of halo composition in the outer part. When comparing the results of the VEGAS survey (Capaccioli et al. 2015) with the ones of Mihos et al. (2013, 2017), the VST broadband images show an extended outer envelope that is responsible for the change of slope in the surface brightness profile beyond $r^{1/4} = 5.5$. The most reliable measurement of the envelope's colour is that of Mihos et al. (2013) of $(B-V) = 0.66 \pm 0.02$ at $r^{1/4} = 6.0$.

In the remainder of this section, we wish to investigate whether we observe similar trends in our PN sample. Signatures are expected to be found in the radial PN number density profile and the α-parameters.

2.4.2 The radial PN number density profile

Figure 2.3 shows the distribution of PNe on the sky together with elliptical bins, aligned with the photometric major axis with a $PA = -31°$ and a constant ellipticity $\epsilon = 0.28$ as measured from isophotes (Kormendy et al. 2009). The binning has been chosen such that every bin contains the same number of objects (~ 70). The PN logarithmic number density profile is defined as

$$\mu_{\mathrm{PN}}(r) = -2.5 \log_{10} \Sigma_{\mathrm{PN}}(r) + \mu_0, \tag{2.4}$$

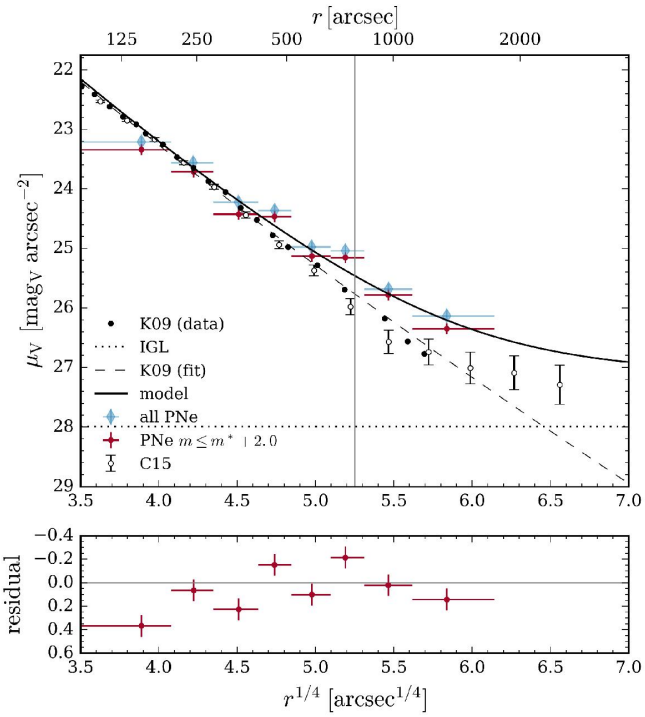

Figure 2.7: Top panel shows the radial surface brightness profiles in M49: the filled circles denote the surface brightness profile observed by Kormendy et al. (2009) and the open circles are from Capaccioli et al. (2015). The Sérsic fit (Kormendy et al. 2009) is indicated by the dashed line. The dotted horizontal line shows the expected contribution of the IGL. The PN number density profile is denoted with blue diamonds and red circles, where the latter sample has a magnitude limit of $m^\star + 2.0$ mag. The two-component model fit to the PN number density profile is shown with the solid black line. The vertical line denotes the transition radius from the inner PN-scarce to the outer PN-rich halo based on the change in the PN number density slope. The bottom panel shows the residuals of the fit.

where μ_0 is a constant in order to match the PN number density profile with the stellar surface brightness profile and $\Sigma_{\rm PN}$ is the completeness-corrected PN number density. As detailed in Sect. 2.3.3 we have to account for colour and spatial incompleteness ($c_{\rm colour}$ and $c_{\rm spatial}$ respectively) that have been determined in Sect. 2.3.3 and detailed values are given in Appendix 2.A, Table 2.1 and Table 2.2. The total number of expected PNe is thus

$$N_{\rm PN,corr}(r) = \frac{N_{\rm PN,obs}(r)}{c_{\rm spatial}(r) c_{\rm colour}}, \tag{2.5}$$

and the number density is

$$\Sigma_{\rm PN}(r) = \frac{N_{\rm PN,corr}(r)}{A(r)}. \tag{2.6}$$

The area $A(r)$ is the area of intersection of the elliptical annulus with the field of view of the observation, accounting for the regions that have been masked, which was computed using Monte Carlo (MC) integration techniques.

As explained in Sect. 2.3.5, we also need to account for background galaxies at $z = 3.1$ emitting Ly-α radiation redshifted to our narrow-band filter range. We therefore statistically subtracted the contribution of Ly-α emitters from the completeness corrected number of PNe $N_{\rm PN,corr}$. We assume a homogeneous distribution in the surveyed area, accounting for a 20% variation in the Ly-α LF due to large-scale cosmic variance (cf. App. 2.B). We calculated the number density profile adopting a limiting magnitude of $m_{5007,\rm lim} = 28.8$ (see Sect. 2.3.4). Given that the PNLF bright cut-off is at $m^*_{5007} = 26.8$ (see Sect. 2.5), we span a magnitude range of $\Delta m = 2$.

The resulting density profile matched to the V-band surface brightness profile (Kormendy et al. 2009) is shown in Fig. 2.7. We also computed the number density profile for all PNe down to the automatically determined limiting magnitude $m_{5007,\rm lim} = 29.3$ and only find a constant offset to the magnitude-limited sample which does not depend on radius. We cover a radial range of 250″ to 1785″, corresponding to 20 to 155 kpc, spanning $9r_e$.[6] The error bars account for the counting statistics and the uncertainty on the Ly-α LF.

The PN number density profile follows the stellar light closely out to a radius of $r \sim 730''$. At larger radii, it starts to flatten and diverges from the Sérsic profile. We note that the flattening occurs much earlier than for the stellar surface brightness profile, but seems to have a steeper slope compared to the flattened part of the stellar profile. As we statistically subtracted the contribution from Ly-α background galaxies, we do not expect the flattening to be due to Ly-α emitters (see also Longobardi et al. 2013, Sect. 4.1). The origin of the flattening of the logarithmic PN number density is investigated in the following.

[6] assuming the effective radius from the 2D profile integration of Kormendy et al. (2009)

2.4.3 The PN luminosity-specific number – the α-parameter

Before we fit a model to the PN number density profile, we need to establish the connection between the PN population and the underlying stellar population. The total number of PNe can be directly related with the total bolometric luminosity $L_{\rm bol}$ of the parent stellar population via the so-called α-parameter:

$$N_{\rm PN} = \alpha L_{\rm bol} \tag{2.7}$$

As our survey is magnitude-limited to $\Delta m = 2$ magnitudes from the bright cut-off, we first determined the α-parameter for that magnitude range, which is defined to be

$$N_{\rm PN,\Delta m} = \int_{m^*}^{m^*+\Delta m} {\rm N}(m)\ {\rm d}m = \alpha_{\Delta m} L_{\rm bol}, \tag{2.8}$$

where $N(m)$ is the PNLF and $m^{\star}_{5007} = 26.8$ its apparent bright cut-off magnitude.

If we sample the entire stellar population, we can determine the total number of PNe associated to a parent stellar population with total bolometric luminosity $L_{\rm bol}$ under the assumption that the luminosity-specific stellar death rate is approximately independent of its parent population's age, metallicity, and initial mass function (IMF, Renzini & Buzzoni 1986):

$$N_{\rm PN} = \mathcal{B} L_{\rm bol} \tau_{\rm PN}, \tag{2.9}$$

where $\tau_{\rm PN}$ is the PN visibility lifetime and $\mathcal{B}$ is the specific evolutionary flux.[7] Combining Eqs. (2.7) and (2.9) one can determine the luminosity-specific PN number:

$$\alpha = \frac{N_{\rm PN}}{L_{\rm bol}} = \mathcal{B}\tau_{\rm PN} \tag{2.10}$$

Simulations of single stellar populations (SSPs) predict that the variations of $\mathcal{B}$ with metallicity or IMF are small – values of B are in the range of $1-2\times10^{-11}$ ${\rm L}_{\odot}^{-1}$ ${\rm yr}^{-1}$ for simulated SSPs (Renzini & Buzzoni 1986) – thus one can understand the observed values of the α-parameter as a proxy for the visibility lifetime $\tau_{\rm PN}$ of the PNe associated with the parent stellar populations. For PN-surveys that do not have the sensitivity to span the entire PNLF, the luminosity specific alpha-parameter provides an estimate of the PN visibility lifetime within the limiting magnitude of the survey.

2.4.4 A two-component photometric model for M49

The flattening of the PN number density profile at large radii might be due to an additional outer component. This can be a secondary component of M49's halo, or the diffuse light

[7] The evolutionary flux quantifies the stellar death rate based on the flow of stars through post-main sequence evolutionary stages. Normalising this quantity by the unit light of the stellar population one gets the specific evolutionary flux (see e.g. Greggio & Renzini 2011).

component of the Virgo Subcluster B (IGL), at whose centre M49 resides (Binggeli et al. 1987, 1993). We therefore constructed a two-component photometric model in order to reproduce the flattening at large radii. A change of slope is also observed in the stellar surface brightness profile, but at larger radii (Capaccioli et al. 2015).

The inner component is dominated by a Sérsic profile. As the slope of the outer stellar surface brightness profile has not been fitted to date, we followed the suggestion of Longobardi et al. (2013) to use a constant surface brightness for the IGL component. We determined this component's value by determining the differential surface brightness between the last measured value of the flattened stellar profile (Capaccioli et al. 2015) and the extrapolated Sérsic fit at that radius and find $\mu_{\rm outer} = 28.0\,{\rm mag\,arcsec^{-2}}$.

The photometric model for the predicted PN surface density is then

$$\tilde{\Sigma}(r) = (\alpha_{\Delta m,{\rm inner}} I_{\rm inner,bol}(r) + \alpha_{\Delta m,{\rm outer}} I_{\rm outer,bol}(r)) s^2 \tag{2.11}$$

$$= \alpha_{\Delta m,{\rm inner}} \left(I_{\rm inner,bol}(r) + \left(\frac{\alpha_{\Delta m,{\rm outer}}}{\alpha_{\Delta {\rm m,inner}}} - 1 \right) I_{\Delta {\rm m,outer,bol}}(r) \right) s^2. \tag{2.12}$$

The two components $I_{\rm inner,bol}(r)$ and $I_{\rm outer,bol}(r)$ are the bolometric surface brightness profiles related by the α-parameters of the respective populations and $s = D/206265$ is a scale factor related to the galaxy's distance D. The bolometric correction is done via

$$I = 10^{-0.4({\rm BC}_V - {\rm BC}_\odot)} 10^{-0.4(\mu - K)}, \tag{2.13}$$

with the solar bolometric correction ${\rm BC}_\odot = -0.07$, and $K = 26.4\,{\rm mag\,arcsec^{-2}}$ is the V-band conversion factor to physical units $L_\odot\,{\rm pc^{-2}}$. One can assume a fixed value of ${\rm BC}_V = -0.85$ with 10% accuracy based on the study of stellar population models for different galaxy types (irregular to elliptical, see Buzzoni et al. 2006).

In order to determine the α-parameter of the inner component, we matched PN surface density (Eq. (2.4)) to the stellar surface brightness profile in the V-band (Kormendy et al. 2009) in the inner region, where the two profiles follow each other closely. The α-parameter can then be determined from the offset μ_0 between the two profiles and applying the bolometric correction:

$$\alpha_{\rm inner} = \frac{10^{-0.4(\mu_0 - K - ({\rm BC}_\odot - {\rm BC}_V))}}{s^2} \tag{2.14}$$

Within the chosen magnitude range ($\Delta m = 2$), we determined an offset of $\mu_0 = 15.0 \pm 0.1\,{\rm mag\,arcsec^{-2}}$, corresponding to $\alpha_{2,{\rm inner}} = (1.99 \pm 0.27) \times 10^{-9}\,{\rm PN}\,L^{-1}_{\odot,{\rm bol}}$.

We then fitted the two-component model to the observed PN number density profile over the whole radial range. As we have already determined $\alpha_{2,{\rm inner}}$, the only free parameter is the ratio of the two parameters $\alpha_{\Delta {\rm m,outer}}/\alpha_{\Delta {\rm m,inner}}$, which is determined using the fit algorithm `lmfit` (Newville et al. 2014). The best-fit ratio is $\alpha_{2,{\rm outer}}/\alpha_{2,{\rm inner}} = 3.21 \pm 0.54$ with $\chi^2_{\rm red} = 2.9$ and the resulting best-fit model is denoted by the black line in Fig. 2.7.

A common magnitude range in which α-parameters are evaluated is within $\Delta m = 2.5$ magnitudes from the bright cut-off. We can extrapolate $\alpha_{2.5}$ to from a sample that is only complete to a magnitude $m_c < m^\star + 2.5$ using the following relation

$$\alpha_{2.5} = \Delta m_c \times \alpha_{m_c} \tag{2.15}$$

with

$$\Delta m_c = \frac{\int_{m^\star}^{m^\star+2.5} N(m)\mathrm{d}m}{\int_{m^\star}^{m_c} N(m)\mathrm{d}m}, \tag{2.16}$$

derived from Eq. (2.8).

In Sect. 2.5 we derive the PNLF of M49, which we use here as $N(m)$. For $m_c = m^\star + 2 = m_2$, the extrapolation factor to $\alpha_{2.5}$ is $\Delta_2 = 1.6$, which results in the following parameters:

- $\alpha^{\mathrm{M49}}_{2.5,\mathrm{inner}} = (3.20 \pm 0.43) \times 10^{-9}\,\mathrm{PN}\,L^{-1}_{\odot,\mathrm{bol}}$ for the inner component, and
- $\alpha^{\mathrm{M49}}_{2.5,\mathrm{outer}} = (1.03 \pm 0.22) \times 10^{-8}\,\mathrm{PN}\,L^{-1}_{\odot,\mathrm{bol}}$ for the outer component.

For comparison, Jacoby et al. (1990) determine $\alpha_{2.5} = (6.5 \pm 1.4) \times 10^{-9}\,\mathrm{PN}\,L^{-1}_{\odot,\mathrm{bol}}$ for the very inner regions of M49.

We find that the outer halo has a α-parameter that is 3.2 times higher compared to the inner halo. This is suggestive of a change of the parent stellar population with radius. This might be due to a contribution of intra-group PNe from the subcluster B to the outer halo, as was observed for M87 in Virgo's subcluster A (Longobardi et al. (2013); Longobardi et al. 2015a).

Combining the two-component PN number density model with the colour profile from Mihos et al. (2013), we were able to evaluate the relation between α-parameter and $(B-V)$ colour continuously for the entire galaxy. Motivated by the two-component photometric model described earlier in this section, we extended this approach to the colour profile. At each radius the colour was calculated as the luminosity-weighted average from each component, whose spatial distribution is given by the PN surface-density decomposition. We allowed for a radially dependent colour profile in the inner halo that has the form

$$(B-V)_{\mathrm{inner}}(r) = \Delta_{\mathrm{i}} r + (B-V)_{\mathrm{i}}, \tag{2.17}$$

where the best fit results in a colour gradient of $\Delta_{\mathrm{i}} = (-1.0 \pm 0.4) \times 10^{-4}$ mag arcsec^{-1} and $(B-V)_{\mathrm{i}} = (B-V)_{\mathrm{inner}}(r=0) = 0.96 \pm 0.01$ with a constant outer colour of $(B-V)_{\mathrm{outer}} = 0.25 \pm 0.11$. The resulting total colour profile is in agreement with the new extended photometry of Mihos et al. (2017). The bluer colour of the IGL is in line with younger, more metal-poor IGL components identified in cosmological simulations (Cui et al. 2014).

Figure 2.8 shows the relation for the modelled α-parameter as a function of galaxy colour computed from the above model compared to data points of individual galaxies from previous PN surveys of early-type and Local Group (LG) galaxies collected by Buzzoni et al. (2006, and references therein). We scale our α-parameters from $\alpha_{2.5}$ to α_8 using Eq. 2.16 based on the best-fit PNLF (Sect. 2.5) in order to use the same reference system as Buzzoni et al. (2006). As our survey spans a radial range that is $\sim 500''$ larger compared to Mihos et al. (2013), the colour profile has been extrapolated from $1260''$ to $1785''$ based

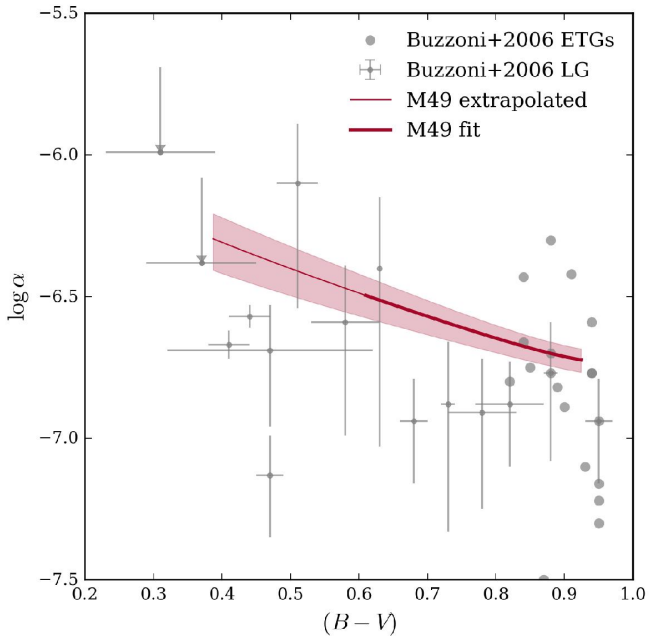

Figure 2.8: Variation of the α-parameter in M49 with colour (red line, colour data from Mihos et al. 2013) compared to data from previous PN surveys in Local Group galaxies (grey error bars) and ETGs (grey circles) based on Buzzoni et al. (2006) and references therein. The result for M49 is based on the two-component model presented in Sect. 2.4.4. The thinner line denotes data exceeding the radial range of the colours measured by Mihos et al. (2013) where the colours have been extrapolated based on the model in Sect. 2.4.4.

on our best-fit model. The relation between α and $(B-V)$ colour can be approximated with the following second order polynomial:

$$\alpha(B-V) = 0.34(B-V)^2 - 1.25(B-V) - 5.86 \tag{2.18}$$

The α-parameter is lowest in the inner, red, metal-rich halo, as it would be empirically expected from bright ETGs. It increases with decreasing colour and is highest in the metal-poor, blue, outer halo, similar to the star-forming LG galaxies with this colour.

2.4.5 Comparison to GCs in M49's halo

GCs are another tracer of faint extended galaxy halos. The Next Generation Virgo Survey (NGVS, Ferrarese et al. 2012) covers the subclusters A and B out to their virial radii, being sufficiently deep to detect GCs (Durrell et al. 2014). The GC density profiles shown in Fig. 2.9 are obtained through isophote-fitting of the smoothed red (RGC) and blue (BGC) distributions. In order to compare with the PN number density, we match the distribution of the RGCs to the stellar light in the inner halo (Kormendy et al. 2009). The number

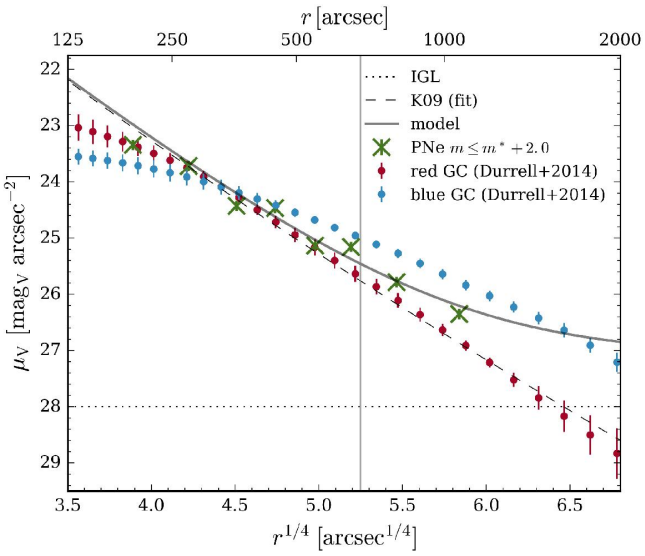

Figure 2.9: Comparison of the PN number density profile with that of red and blue GCs. The Sérsic fit to broad-band photometry (Kormendy et al. 2009) is indicated by the dashed line. The dotted line shows expected contribution of the IGL. The PN number density profile is shown with green crosses and the two-component model fit to it is denoted with the solid grey line. The density profile from red and blue globular clusters are indicated by filled circles in the respective colours. The vertical line denotes the transition radius from the inner to the outer halo based on the change in the PN number density slope.

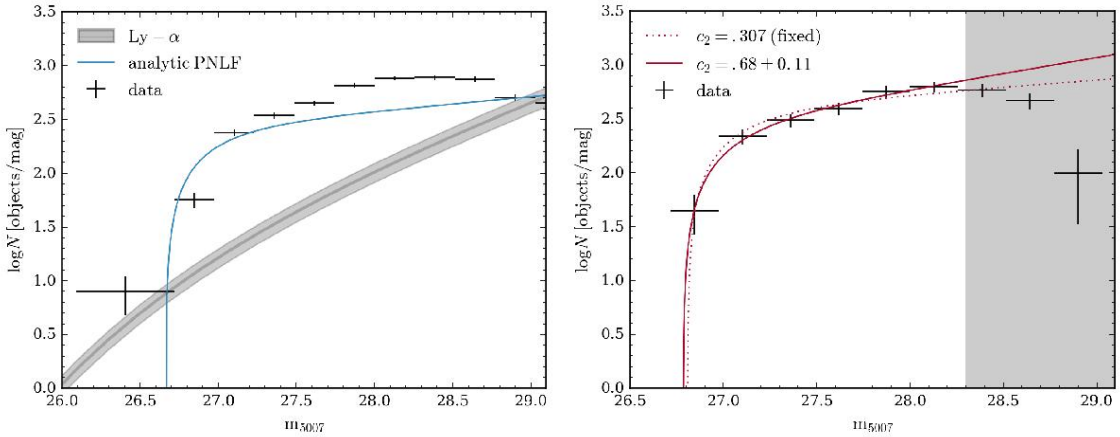

Figure 2.10: *Left:* PNLF of the completeness-corrected PN sample (without accounting for contamination by Ly-α-emitting background galaxies). The error bars along the y-axis account for the Poissonian error and the x-errors for the bin width. The solid blue line shows the analytical PNLF at a distance modulus $\mu = 31.3$ with $c_2 = 0.307$ (Ciardullo et al. 1989). The solid grey line shows the Ly-α LF (Gronwall et al. 2007) and its variance due to density fluctuations is represented by the shaded region. *Right:* PNLF of the completeness-corrected PN sample after statistical subtraction of the estimated Ly-α LF. The grey region denotes the magnitude range in which the PNLF might be affected by incompleteness that could not be corrected for. The error bars along the y-axis account for the Poissonian error and the x-errors for the bin width. The solid red line shows the fit of the generalised PNLF, with the best-fit parameters $c_2 = 0.69 \pm 0.12$ and $\mu = 31.29 \pm 0.05$. The dotted line shows the fit to the PNLF for $c_2 = 0.307$ (Ciardullo et al. 1989).

density of the PNe and the RGCs agree out to a radius $r^{1/4} = 5.5$, which is where the PNe also start to deviate from the stellar light. The density profile of the BGCs is flatter than both the stellar light and the PN density over the entire radial range covered by both surveys.

2.5 The planetary nebula luminosity function of M49

Another characteristic of a PN sample is the shape of its PNLF. As there is empirical evidence for a bright cut-off of the luminosity function, which is consistent with a nearly constant absolute magnitude, the PNLF can be used as a secondary distance indicator (Ciardullo et al. 2002). This cut-off is found to be invariant between different Hubble types (Ciardullo et al. 2004). We compared the PNLF of our completeness-corrected PN sample to the generalised analytical formula introduced by Longobardi et al. (2013)

$$N(M) = c_1 e^{c_2 M}(1 - e^{3(M^\star - M)}), \tag{2.19}$$

where c_1 is a normalisation constant, c_2 is the slope at the faint end, and $M^\star$ is the absolute magnitude of the LF's bright cut-off. The Ciardullo et al. (1989) analytical LF is then a specific case of Eq. (2.19) with $c_2 = 0.307$ that reproduces the best fit to the PNLF of M31. It describes the exponential envelope expansion (Henize & Westerlund 1963) combined with a sharp exponential truncation at the bright end. Observations also suggest that the slope described by the parameter c_2 is correlated with the star formation history of the parent stellar population. Steeper slopes are associated with older stellar populations and conversely flatter slopes with younger populations (Longobardi et al. (2013); Ciardullo et al. 2004; Ciardullo 2010).

The left panel of Fig. 2.10 shows the PNLF of the data corrected for detection and colour incompleteness before having subtracted the contribution from Ly-α emitting galaxies together with the expected LF of these objects (Gronwall et al. 2007). The panel also shows the PNLF expected for a galaxy at the distance of M49 (Mei et al. 2007) based on Eq. (2.19), with $c_2 = 0.307$, normalised to the number of objects in our sample. Furthermore, compared to the bright cut-off of the expected PNLF, there are a number of overluminous objects, whose nature we will discuss in the next section.

We calculated the PNLF of our PN catalogue, corrected it for detection and colour incompleteness as a function of magnitude (see Sect. 2.3.3 for details), and statistically subtracted the expected number of Ly-α emitters in each magnitude bin based on the Gronwall et al. (2007) LF. The right panel of Fig. 2.10 shows the resulting PNLF with black crosses indicating the bin width, and the errors due to counting statistics and the uncertainty of the Ly-α LF. Due to the sharp decrease of the PNLF beyond $m_{5007} = 28.8$, we adjust our limiting accordingly, as discussed in Sect. 2.3.4. As the generalised function does not account for a decrease of the PNLF with magnitude, we fitted the PNLF to a maximal magnitude of $m_{\max} = 28.3$.

For a fixed parameter c_2, we determined a distance modulus $\mu = 31.34 \pm 0.04$ with $\chi^2_{\rm red} = 1.3$. Allowing for a variation of the slope we fit $c_2 = 0.69 \pm 0.12$ and $\mu = 31.29 \pm 0.05$ with $\chi^2_{\rm red} = 0.4$. A PNLF with a steeper slope compared to M31 (Ciardullo et al. 1989) is clearly favoured, but the distance modulus determined in the two fits is similar. Besides of the error in the best-fit, we also needed to account for further sources of error. The random uncertainty in the determination of the photometric zero-point is $\Delta Z_{[\rm O\,III]} = 0.04$. The absolute bright cut-off of the PNLF is $M^\star = -4.51^{+0.02}_{-0.04}$ (Ciardullo et al. 2002). Our final distance to M49 is thus $\mu_{\rm PNLF} = 31.29^{+0.07}_{-0.08}$, which is in agreement with the distance modulus determined from surface-brightness fluctuations (SBFs), which is $\mu_{\rm SBF} = 31.17 \pm 0.07$ (Mei et al. 2007). However, it does not agree with an earlier study of PNe in the centre of M49, which determines the distance modulus to be $\mu_{\rm PNLF} = 30.70 \pm 0.14$ (Jacoby et al. 1990). As there is only a very small overlap between this survey and ours, we are not able to conclude whether this difference in distance modulus is to be ascribed to a zero-point offset between the two photometric systems.

This leads us to the discrepancy between SBF and PNLF distances. Previous studies have generally found a discrepancy between SBF and PNLF distances, which amounts to a mean difference of $\Delta\mu(\rm PNLF - SBF) \approx -0.3$ (Ciardullo et al. 2002; Ciardullo 2012; Mendez 2016). SBF, as the PNLF, is a secondary distance indicator that makes use of luminosity

fluctuations due to counting statistics in the individual pixels of CCDs whose amplitude is inversely proportional to the galaxy's distance (Tonry & Schneider 1988). Both SBF and PNLF distances are calibrated based on Cepheid distances (Ciardullo et al. 2002; Tonry et al. 2001). Several explanations for the discrepancy are discussed in Ciardullo (2012), arguing that it is likely a combination of multiple small effects like zero-point offsets of the two methods and different extinction due to dust in different galaxy types.

The offsets in distance moduli neither correlate with absolute galaxy magnitude nor with galaxy colour, however, a small correlation is found between offset and SBF distance modulus (Ciardullo et al. 2002). There are multiple factors that could be responsible for this correlation. It could be due to uncertainties in the measurement in relatively nearby spirals ($\mu_{\rm SBF} \sim 29 - 30$, Ciardullo 2012), or to contamination by foreground intracluster stars or background galaxies (Ciardullo et al. 2002). As we detail in Sect. 2.3.5, Ly-α emitters at redshift $z = 3.1$ can mimic the unresolved [O III] emission of PNe and cannot be distinguished from PNe solely based on photometric surveys. This contamination affects galaxies with distances moduli larger than $\mu_{5007} \geq 30.5$, and can bias the empirical PNLF towards brighter magnitudes due to the presence of Ly-α emitters brighter than the PNLF cut-off. By comparing the empirical PNLF with the contribution of the Ly-α LF scaled by filter area and depth, the overluminous sources in the left panel of Fig. 2.10 are clearly consistent with Ly-α-emitting background galaxies. Further validation must await the spectroscopic follow-up of these objects.

A recent MUSE study of the star-forming disc galaxy NGC 628 drew the attention to another source of contamination: supernova remnants, that also appear as unresolved [O III]-emitting objects (Kreckel et al. 2017). However, these objects are predominantly expected in star-forming galaxies as the [O III] emission from these SN remnants comes from the interaction of the SN blast wave with the circumstellar medium of the progenitor. This is relevant for core-collapse SNe in spiral galaxies which do not occur in ETG-like galaxies like M49 (e.g. Cappellaro et al. 1999).

We are aware that the PNLF distance determination in M87 (Longobardi et al. 2013) still finds a 0.3 magnitude discrepancy between the PNLF and SBF distance moduli of M87, also for spectroscopically confirmed PN sample (Longobardi et al. 2015a). As Ly-α emitters were identified in the spectroscopic follow-up, any overluminous Ly-α emitter biasing the PNLF cut-off to brighter magnitudes is expected to have been removed from the PN sample.

2.6 Tracing halo variation with PNe

In Sect. 2.4 we found evidence for two different PN populations in the inner and outer halo based on a variation of the α-parameter. We want to investigate whether these differences are also reflected in the PNLF. The PNLF does not only serve as a distance indicator, but furthermore provides insights into the underlying stellar populations, which influence its morphology at fainter magnitudes than the bright cut-off.

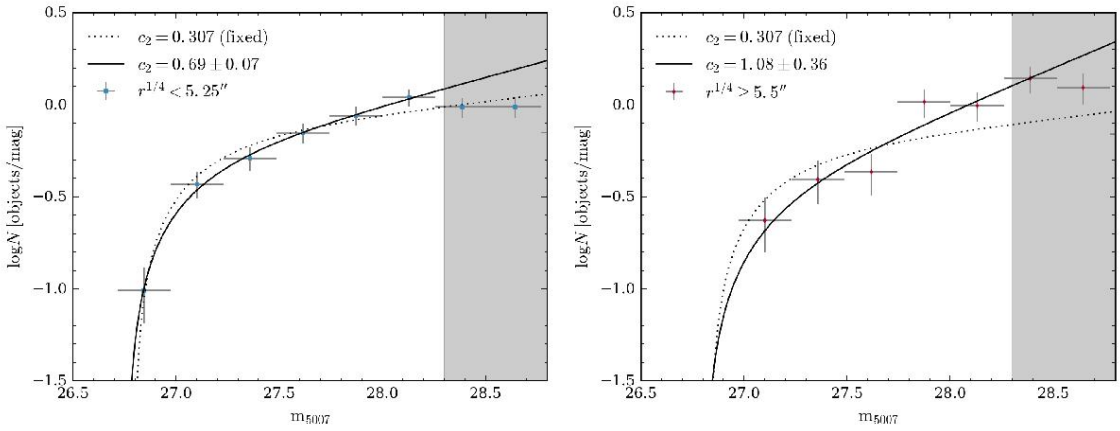

Figure 2.11: PNLF of the completeness-corrected PN sample in two radial bins. The left panel shows the PN sample in the inner halo ($r^{1/4} < 5.25$) and the right one the sample in the outer halo ($r^{1/4} \geq 5.25$). The error bars along the y-axis account for the Poissonian error and the x-errors for the bin width. The solid lines show the fits to the PNLF allowing for variation in the parameter c_2 while the dashed lines show the fits with a fixed $c_2 = 0.307$ (Ciardullo et al. 1989). As in Fig. 2.10, the grey region denotes the magnitude range in which the PNLF might be affected by incompleteness.

2.6.1 The PNLF morphology in the inner and outer halo

We first divided the PN sample into two concentric elliptical bins, indicated by the grey line in Fig. 2.7 at $r^{1/4} = 5.25$. The inner sample is characterised by a density profile that decreases steeply with radius, and contains 517 PNe, whereas the outer sample has a shallower number density profile and contains 197 objects (see also Sect. 2.4). We computed the completeness-corrected PNLF in each bin, normalising by the total number of objects for better comparison and again fit the generalised PNLF. The resulting profiles are shown in Fig. 2.11. For comparison we also show the PNLF with a fixed $c_2 = 0.307$, which is clearly disfavoured in both bins. The PNLF in the outer bin is less well fit by the generalised function than the one in the inner bin. The fitted distance moduli are $\mu_{\mathrm{PNLF,inner}} = 31.27 \pm 0.02$ and $\mu_{\mathrm{PNLF,outer}} = 31.31 \pm 0.05$, which agree with the distance modulus determined in the previous section.

In the outer regions of the halo, the slope of the PNLF is steeper ($c_{2,\mathrm{outer}} = 1.08 \pm 0.36$) than in the inner region ($c_{2,\mathrm{inner}} = 0.69 \pm 0.07$). Empirically, one would thus expect an older underlying stellar population in the outer halo compared to the inner halo. This seems counterintuitive, given the colour gradient towards bluer colour and the general understanding of halo growth through the accretion of smaller, younger systems (Oser et al. 2012; Cooper et al. 2013). In the following section, we investigate the properties of the PNLF in the inner halo.

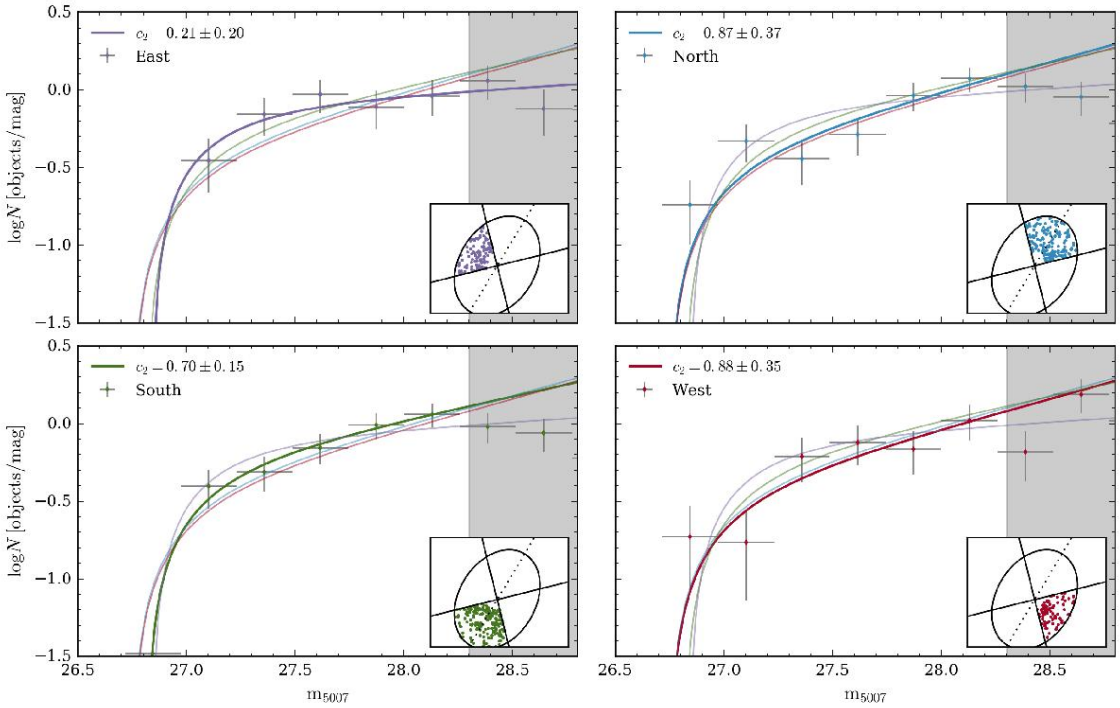

Figure 2.12: PNLF variation in the inner bin in four quadrants. Each panel shows the observed PNLF (data points and error bars) and the corresponding fit for the quadrant indicated in the inset.

2.6.2 PNLF variation in the inner halo

As M49's halo is rich in substructure (Janowiecki et al. 2010, Capaccioli et al. (2015)), we next investigate the azimuthal variation of the PNLF in the inner halo. We therefore divide the halo into four quadrants, such that the positive and negative minor and major axes are enclosed respectively, as shown in Fig. 2.13. The quadrants are denominated by their position with respect to M49's centre (north, west, east, south). We calculate the completeness-corrected PNLF in each quadrant and normalise it by the total number of PN in that quadrant. The resulting profiles are shown in Fig. 2.12. We again fitted the generalised PNLF to each profile.

While the PNLF in the northern, southern, and western quadrants have similar slopes ranging from $c_2 = 0.87 \pm 0.37$ in the north to $c_2 = 0.70 \pm 0.15$ in the south, the slope of the PNLF in the eastern quadrant is significantly flatter, being $c_2 = 0.21 \pm 0.20$, even shallower than the slope of the Ciardullo-PNLF. Compared to the other quadrants, the bright end of the PNLF in the east is populated by more objects. This drives the flattening of the PNLF in the inner halo, which we described in the previous section. If this flattening is related to a younger stellar population, it likely points towards an accretion event. No substructure is found in deep broad-band photometric studies (Janowiecki et al. 2010) in

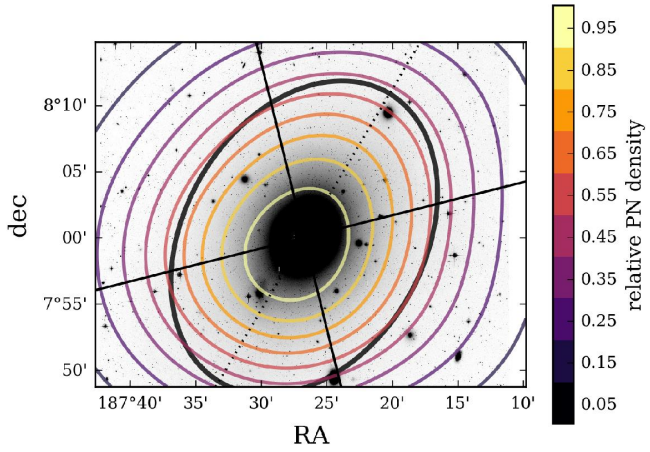

Figure 2.13: NGVS g-band image of M49 (from Arrigoni Battaia et al. 2012) with 2D contours of the relative PN density superimposed. The black ellipse denotes the major-axis transition radius from the inner to the outer halo at 730″ as defined in Sect. 2.4, the dashed line indicates the major axis and the solid lines the borders of the quadrants as defined in Sect. 2.6.

this quadrant, which could be associated to the PNLF variation. However, the spatial proximity to the trail of the accreted dwarf irregular (dIrr) galaxy VCC 1249, which could well extend further into the eastern quadrant, argues for a relation between the flat PNLF and this accretion event.

2.6.3 2D number density map

We next evaluated whether we can identify any substructure in the 2D PNe density distribution. We therefore performed a kernel density estimate (KDE) with a Gaussian kernel using `scikit-learn` (Pedregosa et al. 2011). The kernel bandwidth was chosen such that no artificial overdensities are introduced due to the masked regions in the centre. The resulting density contours overplotted on the NGVS g-band image are shown in Fig. 2.13. This Fig. also shows the borders of the quadrants defined in the previous Sect., as well as the boundary between the inner and outer halo. Due to the large bandwidth we were not able to resolve individual structures. The PN-contours along the north of the major axis have a similar position angle and ellipticity as the isophotes from broadband studies, in the south are flattened and denser. This spatial squashing coincides with the region of interaction with VCC 1249.

2.7 Discussion

Hydrodynamical cosmological simulations such as the Illustris simulations (Vogelsberger et al. 2014) predict that accretion and mergers will deposit significant amounts of tidally stripped stars in the outer regions of galaxies (Pillepich et al. 2015). Because the dynamical timescales in galaxy outskirts, at 50 – 150 kpc radii, are of the order of 2 Gyr, this predictions can be tested by looking observationally for unrelaxed dynamical structures at these radii. This motivates the investigation in this paper of the observational evidence for substructures, environmental effects and intra-group light around the giant Virgo galaxy M49.

2.7.1 Substructure in M49

Recent deep broad-band photometric studies have revealed an intricate system of stellar substructure in M49's halo. Janowiecki et al. (2010) fit Sérsic and double-deVaucouleurs profiles to their V-band photometry and subtract the resulting galaxy model from the images in order to identify substructures. They find a system of diffuse shells, mainly along the major axis of the galaxy. Furthermore, there are two plumes to the south and in the north-east of the galaxy, the latter running through the dwarf galaxy VCC 1254. There might be a connection between the south plume and the inner shell system. This plume is also closely located to the dIrr galaxy VCC 1249, whose properties will be discussed later in this section. The colours of the substructures that were identified by Janowiecki et al. (2010) were measured by Mihos et al. (2013). Their measurement of the global colour trend in the halo of M49 was already discussed in Sect. 2.4. The starforming companions of M49 (VCC 1249 and VCC 1205) clearly stand out due to their bluer $B-V$ colour. The inner shells cannot be identified in the colour map, as they are too close to the bright and red main halo of the galaxy. However, the extended debris shell in the north-west can be identified in the colour map. It is ~ 0.07 mag redder than the remainder of the halo at this radius, indicating that the shell is a remnant of a disruptive accretion event.

The interaction between the dIrr galaxy VCC 1249 and M49 has come to the attention after the detection of an H I cloud displaced from the dwarf towards M49 (Krishna Kumar & Thonnard 1983). Follow-up VLA observations of this cloud by McNamara et al. (1994) revealed a debris trail between the dIrr and M49. A multi-wavelength analysis of this region (Arrigoni Battaia et al. 2012) including near-UV data as well as optical imaging, Hα and spectroscopy comes to the conclusion that star formation in VCC 1249 has been quenched. Due to ram pressure stripping and tidal interaction H I gas has been removed from the dIrr core. Star formation remains active in the H I cloud.

Spatially coinciding with this accretion event, we observe denser PN contours south-east of M49's centre (Sect. 2.6.3). Having evaluated the PNLF in different quadrants, we however do not find a significant change in the PNLF morphology in this region (Sect. 2.6.2). A significant difference in the PNLF slope is indeed found in the adjacent eastern quadrant. The flattening of the PNLF slope can have multiple origins, being driven by either an overabundance of bright to medium luminosity PNe or a lack of fainter PNe.

Based on Fig. 2.12 we assume that the presence of additional medium luminosity PNe ($27.2 \leq m_{5007} \leq 27.7$) compared to the general halo population is driving the flattening of the PNLF. The presence of these bright objects could very well be related to the accretion of VCC 1249, as the shedding of tidal debris after its pericentre passage can lead to a wider distribution of stars (and therefore PNe) than inferred from the distribution of the light (e.g., Amorisco 2015). The validation of this claim will be one of the aims of the spectroscopic follow-up survey of this data, with which we expect to be able to identify accretion events based on their signatures in the kinematic phase-space.

2.7.2 The effect of environment: a comparison to M87

M87 has been a milestone for this type of PN-surveys in the Virgo cluster. With the spectroscopic follow-up of the deep photometric PN-survey (Longobardi et al. 2013), Longobardi et al. (2015a) were able to kinematically separate the stellar halo and intracluster light and furthermore found evidence for a late accretion event in M87's velocity phase-space (Longobardi et al. 2015b).

We first compared the properties of the PN number density profiles in the two galaxies. The morphology of the number density profiles is very similar, both closely following the stellar light (Kormendy et al. 2009) in the inner galaxy halos and then flattens at larger radii. In both galaxies, a two-component model is fit that allows for different α-parameters of the galaxy PN and the PN associated with the ICL/IGL. We scaled M87's α-parameters by a factor of 0.54, as they were calculated assuming a distance modulus of $\mu_{5007} = 30.8$ (Longobardi et al. 2013) instead of $\mu_{\rm SBF} = 31.17$ (Mei et al. 2007), resulting in

- $\alpha^{\rm M87}_{2.5,\rm halo} = (5.94^{+0.17}_{-0.21}) \times 10^{-9}\,{\rm PN}\,L^{-1}_{\odot,\rm bol}$ for the halo component, and
- $\alpha^{\rm M87}_{2.5,\rm ICL} = (1.78^{+0.60}_{-0.72}) \times 10^{-8}\,{\rm PN}\,L^{-1}_{\odot,\rm bol}$ for the ICL component (Longobardi et al. 2013).

The ratio between the two parameters is $\alpha_{2.5,\rm ICL}/\alpha_{2.5,\rm halo} = 3$. In the photometric study, the contribution of the ICL was expected to be constant $\mu_{\rm V} = 27.7$ mag arcsec^{-2}. In M49, we assume that the contribution from the IGL is $\mu_{\rm V} = 28.0$ mag arcsec^{-2}. For reference M49's α-parameters as determined in Sect. 2.4 of this paper are

- $\alpha^{\rm M49}_{2.5,\rm inner} = (3.20 \pm 0.43) \times 10^{-9}\,{\rm PN}\,L^{-1}_{\odot,\rm bol}$ for the inner component (halo), and
- $\alpha^{\rm M49}_{2.5,\rm outer} = (1.03 \pm 0.22) \times 10^{-8}\,{\rm PN}\,L^{-1}_{\odot,\rm bol}$ for the outer component (IGL).

The α-parameter in the main halo of M87 is higher compared to the one in M49, while the ICL and IGL have consistent α-values within the errors.

The halo PNLF of M87 is steeper than what is expected based on the analytic PNLF from Ciardullo et al. (1989), which motivated the introduction of the generalised analytic PNLF in Longobardi et al. (2013). The distance modulus and the slope are fit to be $\mu = 30.73$ and $c_2 = 1.17$. The determined distance modulus is ~ 0.4 mag brighter than the one determined using SBFs (Mei et al. 2007). In Longobardi et al. (2015a), the slope of the halo and ICL PNLFs were determined based on the kinematically separated populations,

leading to $c_{2,\mathrm{halo}} = 0.72$ and $c_{2,\mathrm{ICL}} = 0.66$. The PNLF of the ICL shows a dip 1 - 1.5 mag from the bright cut-off, which is seen in star-forming systems. There is little variation of the PNLF with radius. In contrast to this, we find differences in the PNLF slope in different regions of M49's halo. The slope of the PNLF in the entire sample is also steeper ($c_2 = 0.69 \pm 0.12$) than the analytic PNLF from Ciardullo et al. (1989), which further corroborates the empirical trend of steepening PNLFs from star-forming to old metal-rich populations (Longobardi et al. (2013); Ciardullo et al. 2004; Ciardullo 2010). We believe that the flat PNLF in the inner halo of M49 is driven by the excess of bright to medium-luminosity planetaries in the eastern quadrant.

We spatially associate this excess with the tail of the accretion event of VCC 1249, but note that there is no overdensity that can be related with it in the broad-band photometric surveys of M49's halo (Janowiecki et al. 2010; Capaccioli et al. 2015). As identified in Longobardi et al. (2015b), M87's kinematic PN phase-space reveals signatures of a recent accretion event, also termed as M87's crown. However, the PNLF of the crown in M87 does not show signs of variation from the halo PNLF. The nature of the accreted system is very different from what is observed for the VCC 1249 - M49 interaction. Reflecting the environment of Virgo's subcluster A, the infalling system was devoid of gas. The subcluster B at whose centre M49 resides mainly consists of star-forming galaxies. Thus the infall of a gas-rich, star-forming galaxy is more likely to be observed in the subcluster B.

2.7.3 M49 and its environment: the intra-group light in the Virgo Subcluster B

Combining our study of individual tracers (PNe) with broad-band photometric observations of M49 and its environment allows us to model the PN populations in M49's halo as a two-component system that consists of an inner Sérsic-like halo and a flat outer component with a constant surface brightness (see Sect. 2.4.4). Our best-fit model is characterised by the α-parameters of the respective components, which we re-stated in Sect. 2.7.2 above.

By applying the same concept to the colour profile (Mihos et al. 2013), we are able to derive a relation between the α-parameter and the $(B-V)$ colour at each radius: M49's α-parameter increases with decreasing colour. The best-fit colour model consists of an inner component with a radially dependent colour profile with gradient $\Delta_\mathrm{i} = (-1.0 \pm 0.4) \times 10^{-4}$ mag arcsec^{-1} and $(B-V)_\mathrm{i} = (B-V)_\mathrm{inner}(r=0) = 0.96 \pm 0.01$ and an outer component of constant colour $(B-V)_\mathrm{outer} = 0.25 \pm 0.11$. The comparison with the most recent hydrodynamical cosmological simulations, shows that the Sérsic component and its mild colour gradient of $\nabla(B-V)_{2-4r_e} = -0.13$ mag dex^{-1} are consistent with the hierarchical assembly of early-type galaxies (Cook et al. 2016). In fact, the colour profiles measured in the Illustris simulation have an average $(g-r)$ colour gradient of $\nabla(g-r)_{2-4r_e} \approx -0.1$ mag dex^{-1} (Cook et al. 2016) with a scatter of $\sigma \approx 0.08$ mag dex^{-1}. This is much shallower than the global gradient observed in M49 that ranges from $\nabla(B-V)_{2-4r_e} = -0.3$ mag dex^{-1} in the inner halo to $\nabla(B-V)_{4-8r_e} = -0.8$ mag dex^{-1} in the outer halo, thus supporting the presence of an additional component.

The shallow, blue, outer component is likely due to a contribution of a smooth IGL that is superposed onto the Sérsic galaxy halo. This result is consistent with the extended photometry from the Burrell Schmidt deep Virgo survey (Mihos et al. 2017) and the VEGAS survey (Capaccioli et al. 2015). Because Mihos et al. (2017)'s morphological classification of ICL/IGL is based on the luminosity fraction that is either in filamentary or in clumpy structures, in addition to an azimuthally smooth spheroid, the smooth blue IGL around M49 would not fall in this classification and hence their different conclusion on the presence of IGL around M49. We also note that the footprint of the Burrell Schmidt survey does not extend to the south of M49, where the outer boundary of the external envelope is most elongated (see Fig. 6 in Capaccioli et al. 2015).

As the outer halo of M49 is observed to be smooth (Capaccioli et al. (2015), Mihos et al. 2017) we would expect the component to have already started to relax. As the precession time at these radii is about 5 Gyr, following the SSP models of Bruzual & Charlot (2003) applied to M49 in Mihos et al. (2013), we expect this population to be quite metal-poor ([Fe/H] ≤ -2). Similar to the analysis in M87 by Longobardi et al. (2015a), we are planning to carry out a spectroscopic follow-up of the PN-survey presented in this paper. This will enable us to assess the degree of relaxation of the outer component, which points towards its evolutionary history. Based on their velocity phase-space properties we will also be able to kinematically disentangle the halo and IGL populations.

2.8 Summary and conclusions

We present a deep narrow-band survey of the bright ETG M49 using Subaru's Suprime-Cam in order to identify and analyse the PN population therein. The survey's extent and depth is unprecedented for M49. Down to a limiting magnitude of $m_{5007,\mathrm{lim}} = 28.8$ and covering a radial range of 155 kpc from the galaxy's centre, we identify a PNLF-complete sample of 624 PNe using automated detection techniques. The selection criteria are based on the fact the PNe have a bright [O III] and no continuum emission and that they appear as point-like at extragalactic distances. Using a simulated PN population, we are able to account for detection and colour incompleteness.

The radial PN number density profile follows the broad-band surface brightness distribution to a radius of $r = 730''$, equivalent to $r = 60$ kpc and then shows flattening with respect to the stellar surface brightness profile. This is consistent with a two-component model that accounts for a Sérsic distribution of halo PNe in the inner region and a shallower population of IGL PNe at larger radii. The α-parameter of this IGL population signifies a 3.2 times higher specific frequency of PNe in the IGL compared to the main galaxy halo, which is similar to what was observed in Virgo's BCG M87 (Longobardi et al. 2013).

The PNLF is as an important diagnostic tool for the properties of the global PN population of M49's halo as well as for variation therein. First, due to accurately accounting for contamination by Ly-α emitting background galaxies at $z = 3.1$, we are able to determine a PNLF distance modulus that agrees with the one determined using the SBF technique, which is a first for a galaxy at this distance. Second, the PNLF slope varies in the inner

halo of M49, due to additional bright PNe in one quadrant. Whether these PNe are related to the accretion of VCC 1249 will be one of the aims of the planned spectroscopic follow-up. We will also be able to disentangle the halo and intra-group populations by studying their kinematics separately.

While both M49 and M87 are massive and bright early-type galaxies in the Virgo cluster, their PN populations have different properties, reflecting the different environments in which they reside. M87 in Virgo's most dense environment, the subcluster A, is surrounded by ICL with a higher specific frequency compared to the IGL around M49 in Virgo's subcluster B. Both galaxies are undergoing or have undergone recent accretion. The fact that M87's accreted companion did not contain any gas, while M49 has multiple star-forming companions reflects the different environments in which the halos of these ETGs grew.

Appendix

2.A Catalogue extraction

2.A.1 Extraction of point-like emission-line objects

We extracted emission-line objects using the object detection algorithm SExtractor (Bertin & Arnouts 1996) in dual-image mode. Objects were detected if the flux value in at least 20 adjacent pixels is higher than $1.2 \times \sigma_{\rm rms}$ in the on-band image. We chose an aperture radius of 12 pixels, since this is the smallest aperture in which we can recover the magnitudes of a simulated emission-line population (see Fig. 2.14). The detection in dual-image mode was carried out on the on-band image and the extracted aperture magnitudes are denoted with $m_{\rm n}$. In order to determine the colour of the emission-line objects, the broadband magnitudes $m_{\rm b}$ were extracted in the same apertures as on the narrow-band image. The colour is defined as $m_{\rm n} - m_{\rm b}$.

In order to determine the limiting magnitude of our sample, we simulated a synthetic point-like population onto the on-band image using the IRAF task `mkobjects`. The synthetic population follows a Planetary Nebula Luminosity Function (PNLF) as detailed in Ciardullo et al. (1989, see also Sect. 2.5) and the objects have a Gaussian PSF profile as detailed in Sect. 2.2.2. The limiting magnitude is defined as the magnitude at which the recovery fraction of the simulated objects drops below 50%. The limiting AB magnitude of the on-band image is $m_{\rm n,lim} = 26.8$ or $m_{5007,\rm lim} = 29.3$ (see also column 3 of Table 2.1).

2.A.2 Masking of bad or noisy regions

After identifying emission-line objects on the images, the image regions which were affected by dithering or saturation are masked on the on- and off-band images. Dithering leads to different exposure depths at the image edges. Due to the combination of the 10 Suprime Cam CCDs, the same effect also affects columns at the borders of the individual CCDs. In order to mask regions with a high background value (e.g. due to charge transfer or saturated stars) we used the rms-background map created by SExtractor and create a pixel-mask with all values higher than 1.5 times the median background. We also excluded objects within a major-axis radius of $r_{\rm major} = 159''$, corresponding to a physical distance of 13 kpc from the galaxy's centre, where the background due to the galaxy's light is higher than the threshold defined above. This reduces the survey area by 4% to 0.244 deg^2.

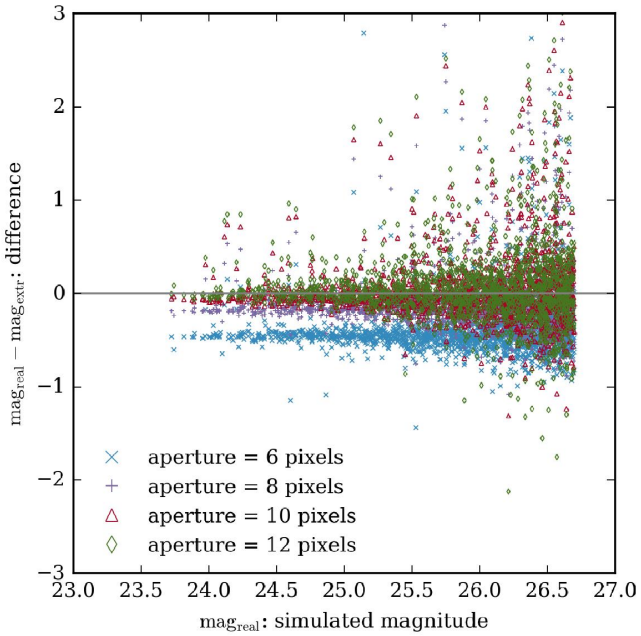

Figure 2.14: Recovery of the input magnitudes of a simulated emission-line population using different SExtractor aperture sizes.

2.A.3 Colour selection

We selected PN candidates based on their position on the $m_{\rm n}$ versus $m_{\rm n} - m_{\rm b}$ CMD. Candidates were objects with a colour excess $m_{\rm n} - m_{\rm b} < -1$ that are brighter than the limiting AB magnitude in the narrow band $m_{\rm n,lim} = 26.8$, which corresponds to $m_{5007,\rm lim} = 29.3$. The colour excess corresponds to an equivalent width $EW_{\rm obs} = 110\,$Å (Teplitz et al. 2000) and was chosen in order to limit contamination from background galaxies (see discussion in Sect. 2.3.5).

To evaluate the contamination by faint stellar sources that fall below the adopted colour excess due to photometric errors, we simulated a continuum population onto the on- and off-band images and calculate the 99% and 99.9% limits based on the extracted CMD of the population. Below these limits, the probability of detecting stars was reduced to the 1% and 0.1% level respectively. Objects with colour-excess above the 99.9% limit are not considered for further analysis. The CMD with the selection criteria overplotted is shown in Fig. 2.1. [O III] sources for which no broad-band magnitude can be measured are assigned a magnitude of $m_{\rm b} = 28.7$, which corresponds to the flux from an [O III] emission of $m_{\rm n} = m_{\rm n,lim}$ observed through a broadband V filter (Theuns & Warren 1997). These sources are located on the diagonal line in Fig. 2.1.

2.A.4 Point-like versus extended sources

In order to distinguish point-like sources from extended ones (e.g. background galaxies or other extended objects with strong [O III] emission), we again first considered the simulation of the PNe on the on-band image and analyse their light distribution. Based on the simulated population, we considered sources as point-like if they satisfied the following two criteria: these sources (i) have a half-light radius of $1 < R_{\rm h} < 3.5$ pixel, where the upper limit corresponds to the 95%-percentile of the simulated population, and (ii) they fall in the region where the difference between $m_{\rm n}$ and $m_{\rm core}$ is within the 95%-limits of the simulated population. The core magnitude $m_{\rm core}$ was measured in a fixed circular aperture with a radius of four pixels at the same position as the main detection. For point-like objects, the difference between the two magnitudes is expected to be constant as a function of magnitude, for extended sources it varies. The results of this test are shown in Fig. 2.2. The objects which fulfil these criteria along with the ones detailed in the previous section are indicated in the CMD of Fig. 2.1.

2.A.5 Catalogue completeness

As we selected PN-candidates on flux-ratio-based criteria, we might not have detected PNe that fell below the flux-threshold due to photometric errors. In order to quantify the detection incompleteness, we simulated a PN-population onto the unmasked regions of the on-band image and determined how many sources we retrieved as a function of magnitude. For sources brighter than the limiting magnitude, the average detection completeness was 80%. The detection completeness as a function of magnitude is displayed in Table 2.1. We then used the simulated population brighter than the limiting magnitude to determine the colour completeness of our selected sample. This is needed, as there will be genuine PNe which lie in CMD regions outside of the colour-selection criteria because of photometric errors. The average colour completeness of our selected sample from 23.5 to 26.8 *AB* magnitudes was 81% and the magnitude-binned values are presented in Table 2.1.

Similarly, we determined the spatial completeness by determining the recovery fraction of the simulated population within the limiting magnitude as a function of major-axis radius (see Table 2.2).

2.B The $z = 3.1$ Ly-α luminosity function

Gronwall et al. (2007) carried out a deep survey for $z = 3.1$ Ly-α emission-line galaxies. The LF is characterised by a Schechter-function (Schechter 1976)

$$\phi(L/L^\star)\,{\rm d}(L/L^\star) \propto (L/L^\star)^\alpha \exp(-L/L^\star)\,{\rm d}(L/L^\star), \tag{2.20}$$

with parameters $\log L^\star = 42.66\,{\rm erg\,s^{-1}}$, $\alpha = -1.36$ and normalisation $\phi^\star = 1.28 \times 10^{-3}$. The survey has a limiting magnitude of $m_{5007,{\rm lim}} = 28.3$, which is somewhat brighter than the limiting magnitude of our study. We extrapolated the LF down to the depth of our survey, which is $m_{5007,{\rm lim}} = 28.8$ (cf. Sect. 2.3.4).

Table 2.1: Photometric completeness: colour completeness c_{colour} and detection completeness $c_{\mathrm{detection}}$ for a range of narrow-band magnitudes m_{n}

m_{n} [mag]	c_{colour}	$c_{\mathrm{detection}}$
23.97	0.80	0.92
24.23	0.87	1.00
24.48	0.84	0.83
24.74	0.84	0.90
25.00	0.86	0.82
25.25	0.84	0.82
25.51	0.82	0.77
25.77	0.81	0.77
26.03	0.78	0.67
26.28	0.74	0.61
26.54	0.70	0.65

Table 2.2: Spatial completeness c_{spatial} for a range of major-axis radii r_{major}. A denotes the un-masked bin area and a_{frac} the unmasked fraction of a complete elliptical bin.

r_{major} [°]	A [°^{2}]	c_{spatial}	a_{frac}
0.08	0.0069	0.69	0.04
0.10	0.0084	0.79	0.94
0.13	0.0140	0.83	0.98
0.15	0.0160	0.88	0.98
0.19	0.0260	0.93	0.99
0.22	0.0290	0.86	0.95
0.28	0.0500	0.93	0.80
0.40	0.0790	0.88	0.44

The survey area of $0.244\,\mathrm{deg}^2$ corresponds to a comoving volume of $1.84 \times 10^5\,\mathrm{Mpc}$. However, as Gronwall et al. (2007) state, the effective survey volume is roughly 25% smaller when taken through a non-square filter bandpass. Taking this into account, the total number of Ly-α emitters that we expect in our survey area is 310.

The clustering correlation length is $r_0 = 3.6$ Mpc, which corresponds to $r_0' = 7.9'$ at the distance of the Virgo cluster. We can thus expect about 20% variation in the LF due to large-scale cosmic variance (Gawiser et al. 2007; Somerville et al. 2004). Accounting for this variation, $(29.8 \pm 6.0)\%$ of the objects in the completeness-corrected sample are predicted to be Ly-α emitting background galaxies. Fig. 2.10 shows the Gronwall et al. (2007) Ly-α LF alongside with the LF of the selected PNe.

Chapter 3

Three dynamically distinct stellar populations in the halo of M49[1]

This chapter is published as the paper Hartke et al. (2018) in Astronomy & Astrophysics.

3.1 Introduction

In the current hierarchical paradigm, early-type galaxies (ETGs) grow with time. The initial phase of strong in-situ star formation is followed by growth through minor mergers and accretion at large radii (White & Frenk 1991; Steinmetz & Navarro 2002; Oser et al. 2010). This scenario reproduces the morphology, metallicity, and the kinematics of the inner halos at $30 - 50$ kpc radius – see, for example, evidence for recent accretion events at these radii in M87 (Longobardi et al. 2015b) and M49 (Arrigoni Battaia et al. 2012).

As more effort is put into understanding the mass-assembly history, reaching higher sensitivity and larger radii in these galaxies, recent extended photometry and detection of individual stars provide evidence for very extended, blue halos around nearby ETGs at the centre of their groups. M49, the brightest galaxy in the Virgo Cluster, is surrounded by such an extended envelope that is characterised by a strong blueward colour gradient beyond two effective radii (Mihos et al. 2013, 2017). If this strong colour gradient, reaching from $B-V = 0.92$ at 25 kpc to $B-V = 0.65$ at 100 kpc, were due to a strong metallicity gradient, the corresponding stellar populations would have to have metallicities below [Fe/H] ≤ -0.2 and ≤ -1, respectively, at these radii (Mihos et al. 2013)[2].

[1]Based on data collected at Subaru Telescope, which is operated by the National Astronomical Observatory of Japan under programme S14A-006 and with the William Herschel Telescope operated on the island of La Palma by the Isaac Newton Group of Telescopes in the Spanish Observatorio del Roque de los Muchachos of the Instituto de Astrofísica de Canarias. We thank S. Okamura and F. Nakata for carrying out the observations with SurpimeCam@Subaru. I described the reduction and calibration of these data in the previous chapter. The PN.S data used in this work are part of the ePN.S survey (see Sect. 4.2 for details) and I could make use of the fully reduced data set.

[2]Mihos et al. (2013) assume Bruzual & Charlot (2003) single stellar population models for a range of ages. The values quoted here assume an age of at least 5 Gyr.

Within the cosmological framework, simulations predict that the mergers building up M49's halo would have typical mass ratios of 0.2 ± 0.1 (1:5, Oser et al. 2012). However, according to the stellar mass-metallicity relation (Zahid et al. 2017), such merging satellites would deposit stars with much larger metallicities ([Fe/H] $\approx -0.1 \pm 0.1$), which would be redder in colour. If the bulk of the metal-poor stars in the outer halo instead originated from the formation of many low-mass, low-metallicity objects at high redshift, this would be in tension with recent cosmological simulations (Rodriguez-Gomez et al. 2016), which predict that satellites with mass ratios less than $10^{-2} : 1$ do not contribute significantly to the mass of the stellar halo. Finally, if the halo had been made by the more recent accretion of relatively massive (1:5 merger-mass ratio) star-forming galaxies, these would have left behind long-lasting dynamical signatures like asymmetric velocity fields or substructures in the velocity phase-space (Bullock & Johnston 2005).

Therefore, a possible way to address the tension between the size and the colour of these halos at 100 kpc radial distance, and to discriminate between the different formation channels of these extended blue halos, is to measure the kinematics of the associated stars. If the halo formed from many small, metal-poor objects, its phase-space would be characteristically smooth and point symmetric. On the other hand, if it had been built relatively recently from more massive, star-forming satellites, we would detect dynamical signatures in the velocity phase-space.

While the dynamics of the halos of local group galaxies like M31 can be mapped by absorption-line spectroscopy of individual red giant branch (RGB) stars at the distance of the Virgo Cluster, these stars would have apparent magnitudes $m_V > 23.5$, which is fainter than the sky background. Integral-field spectrographs are ideally suited for mapping the central high-surface-brightness regions of ETGs (see e.g. Emsellem & Sauron Team 2002; Ma et al. 2014; Cappellari 2016), but due to their small field of view it becomes increasingly costly to map the extended halos at larger distances (beyond $2r_{\rm e}$). Even with sparse sampling, the coverage does not extend beyond $4r_{\rm e}$ (e.g. Weijmans et al. 2009; Ma et al. 2014; Boardman et al. 2017).

Beyond these distances, discrete tracers like globular clusters (GCs) or planetary nebulae (PNe) are needed. The latter are the progeny of asymptotic giant branch (AGB) stars and can be easily identified due to their relatively strong [OIII]5007Å emission lines, and the absence of a continuum. With multi-slit imaging techniques PNe can even be detected in galaxy clusters like Hydra I (Ventimiglia et al. 2008) at 50 Mpc distance and Coma (Gerhard et al. 2005) at 100 Mpc distance. Within 20 Mpc distance, common techniques for PNe identification are the on-off band technique (Arnaboldi et al. 2002, 2003) and counter-dispersed imaging (Douglas et al. 2002; McNeil et al. 2010).

Empirically, it has been found that PNe are about three times more abundant in the outer bluer halos around M87 and M49, compared to the inner redder galaxy (Longobardi et al. 2013, 2015a; Hartke et al. 2017, hereafter L13; L15a; H17). This difference is also present in the morphology of the planetary nebula luminosity function (PNLF), as it has been found that PNLFs steepen from recent star-forming to old parent stellar populations (e.g. Ciardullo 2010, L15a; H17), thus making PNe ideal single stellar tracers to map the transition from the inner galaxy halo to the outer blue envelope in bright cluster galaxies.

In addition to PNe tracers being relatively abundant in blue outer halos, a series of studies indicate that PNe in different magnitude bins of the PNLF have distinct kinematics. For example, the study of the kinematics of the PN population in NGC 4697, an ETG located in the Virgo southern extension, showed that PNe in different magnitude intervals of the PNLF exhibited different kinematics and spatial distributions (Sambhus et al. 2006). A very recent study of PN populations in the face-on disk galaxy NGC 628 showed that PNe within 0.5 mag from the bright cut-off of the PNLF are dynamically colder with respect to PNe at fainter magnitudes (Aniyan et al. 2018, Arnaboldi et al. 2018, in prep.). The correlation between the magnitude of the [OIII]5007Å emission and kinematics may be understood in the framework given by the recent models of post-AGB evolution (Miller Bertolami 2016), which link the total luminosity of the PN core stars to the age and metallicity of the parent stellar population (Zijlstra et al. 2016).

In light of these empirical and theoretical results, we may expect the accretion events of satellites with different ages, masses, and metallicities, which build the extended halos of ETGs, to leave different imprints in the magnitude-position-velocity space traced by PN populations. Therefore, by studying correlations in this space, we may be able to identify substructures and assign them to different progenitors.

The aim of this work is to understand the build-up of M49's halo and the surrounding intra-group light (IGL) by a synergy of accurate photometry (H17) from Suprime-Cam at Subaru Telescope (Miyazaki et al. 2002) with line-of-sight (LOS) velocities from the extended Planetary Nebula Spectrograph (ePN.S) ETG survey (Arnaboldi et al. 2017; Pulsoni et al. 2017). The Planetary Nebula Spectrograph (PN.S) at the William Herschel Telescope (WHT) is a double-arm slitless spectrograph that facilitates the identification of PNe and the measurement of their LOS velocities in a single observation (Douglas et al. 2002).

This paper is organised as follows: in Sect. 3.2, we describe the synergy of photometric and spectroscopic surveys of PNe in the halo of M49. Section 3.3 summarises the methods used for the analysis of the LOS velocity distribution (LOSVD). We present our results in Sect. 3.4 and subsequently discuss them in Sect. 3.5. For the remainder of this paper we adopt a distance to M49 of 16.7 Mpc (Blakeslee et al. 2009), corresponding to a physical scale of 81 pc per $1''$ and an effective radius of $r_{\rm e} = 194\farcs4 \pm 17\farcs0$ (Kormendy et al. 2009, corresponding to 15.7 ± 1.4 kpc).

3.2 Matching photometric and kinematic data of PNe in M49

We aim to investigate whether there are correlations between substructures in distance-velocity phase-space with [OIII]5007Å magnitudes for a large sample of PNe. We therefore combine accurate photometry from a narrow-band survey with LOS velocities obtained with the PN.S. The complete photometric survey from H17 consists of 624 PNe within a limiting magnitude of $m_{5007,\rm lim} = 28.8$, covering a major-axis distance of 155 kpc (equivalent

to $9r_{\rm e}$) from the centre of M49, excluding the central 13 kpc due to the high background from M49's light. For a detailed discussion of the survey's completeness and photometric accuracy, we refer to H17.

The ePN.S ETG survey (Pulsoni et al. 2017) provides positions (RA, dec), LOS velocities (v) and magnitudes ($m_{5007,\rm PN.S}$) for 465 PNe in the halo of M49, covering a major-axis distance of 95 kpc (equivalent to $6r_{\rm e}$). We remove all measurements with a signal-to-noise ratio $S/N < 2.5$ in either of the two dispersed arms from the PN.S dataset. The median error on velocities measured with the PN.S is $\delta v = 20$ km s^{-1}. We refer the reader to Douglas et al. (2007) for a detailed description of the data reduction procedures for the PN.S. We then calculate the velocity dispersion $\sigma = 363 \pm 17$ km s^{-1} using a robust-fitting technique (McNeil et al. 2010) and remove all PNe with velocities outside a velocity range of 3σ about the mean velocity $\bar{v} = 935 \pm 17$ km s^{-1}. We remove one high-velocity outlier that is likely not a PNe but a foreground object as its magnitude is much brighter than M49's bright cut-off $m^{\star}_{5007} = 26.8$, and 13 low-velocity outliers that are all located at the field edges and thus likely affected by degrading image quality. After the removal of low signal-to-noise ratio (S/N) measurements and 3σ-clipping, the cleaned catalogue contains 436 PNe.

From the cleaned catalogue, 226 PN.S-PNe fall into the unmasked regions of the photometric survey. We cross-correlate their positions with those of the PNe from the photometric survey with a tolerance of $5''$, resulting in 215 common objects. The resulting catalogue, containing positions (RA, dec), LOS velocities (v), and magnitudes ($m_{5007,\rm Sub}$) of 215 PNe, is referred to as *matched catalogue*. The combination of the two surveys allows us to assess the accuracy of the magnitudes measured with the PN.S in comparison to the excellent Suprime-Cam photometry. We find an offset in magnitudes that is governed by a linear relation of the form

$$m_{5007,\rm PN.S} = a m_{5007,\rm Sub} + b, \tag{3.1}$$

with $a = 0.704 \pm 0.084$ and $b = 8.78 \pm 2.29$. We correct for the magnitude offset by inverting this relation. There is a residual ± 0.7 mag scatter of the PN.S magnitudes with respect to the Suprime-Cam photometry, which is likely due to instrumental effects as the PN.S has been optimised for kinematic measurements only. We apply the magnitude correction to all PN.S PNe in the cleaned catalogue, resulting in the *magnitude-corrected PN.S catalogue*, which contains positions (RA, dec), LOS velocities (v), and magnitudes ($m_{5007,\rm PN.S_{-corr}}$) of 441 PNe.

3.3 Methods for LOSVD decomposition

In this section, we briefly describe the methods used to analyse the closer velocity distribution (line-of-sight velocity distribution (LOSVD)) of PNe in the halo of M49.

3.3.1 First and second moments of the LOSVD

Following the procedure outlined in Sambhus et al. (2006), we calculate the reduced velocity U for each PNe with velocity v:

$$U(x) = (v - v_{\rm sys}) \cdot \mathrm{sgn}(x). \tag{3.2}$$

M49's systemic velocity as computed from the ePN.S velocity fields is $v_{\rm sys} = 960 \pm 24$ km s^{-1} (Pulsoni et al. 2017) and x is the position along the galaxy's photometric major axis ($PA = -31^{\circ}$, Kormendy et al. 2009). PNe with $U > 0$ are denoted as co-rotating and with $U < 0$ as counter-rotating, respectively. The mean reduced velocity is calculated in magnitude bins to evaluate how the kinematics of M49 change as a function of magnitude.

We then calculate the LOS velocity dispersion profile as a function of radius, using the robust-fitting technique described in McNeil et al. (2010). As galaxies in group and clusters often have a LOSVD with strong wings due to the presence of intra-cluster or intra-group light (IGL, e.g. Arnaboldi et al. 2012; Veale et al. 2018; Barbosa et al. 2018, L15a), we estimate the dispersion within three standard deviations from the mean velocity. The error on the velocity dispersion is calculated using Monte Carlo (MC) techniques (see McNeil et al. 2010, eq. (2)).

3.3.2 Adaptive-kernel smoothing

Smoothed velocity and velocity dispersion fields are calculated using the adaptive-kernel-smoothing technique of Coccato et al. (2009). For a sample of N PNe, the smoothed velocity $\tilde{v}$ and $\tilde{\sigma}$ at every position on the sky (x, y) are

$$\tilde{v}(x,y) = \frac{\sum_{i=0}^{N} v_i w_i}{\sum_{i=0}^{N} w_i} \tag{3.3}$$

$$\tilde{\sigma}(x,y) = \left(\frac{\sum_{i=0}^{N} v_i^2 w_i}{\sum_{i=0}^{N} w_i} - \tilde{v}(x,y)^2 - \delta v^2 \right)^{1/2}, \tag{3.4}$$

where v_i is the observed ith tracer velocity and δv is the corresponding measurement error. Following Coccato et al. (2009), we use a distance-dependent Gaussian kernel for the ith tracer

$$w_i = \exp \frac{-D_i^2}{2k(x,y)^2}, \tag{3.5}$$

where D_i are the distances of the ith tracer from the remainder of the sample. The kernel width k is defined to be proportional to the distance $R_{i,M}$ to the Mth closest tracers:

$$k(x_i, y_i) = A R_{i,M}(x_M, y_M) + B, \tag{3.6}$$

where x_M and y_M are the coordinates of the Mth closest PN to the ith tracer (x_i, y_i). Pulsoni et al. (2017) optimised the kernel parameters A and B for the best compromise

between spatial resolution and noise smoothing through MC simulations of discrete velocity fields extracted from cosmological simulations (see Sect 3.1.1 therein). For M49, they determine $A = 0.73$ and $B = 11.3$ as kernel parameters. We use these parameters to calculate the two-dimensional (2D) smoothed velocity and velocity dispersion fields presented in Sect. 3.4.

3.3.3 A multi-Gaussian model for LOSVD decomposition

The information of the velocity and velocity dispersion fields is contained in the LOSVD. We model the LOSVD as the sum of individual Gaussians to evaluate whether it is consistent with a single or multiple components. In order to assign PNe to the kinematic components, we use a Gaussian-mixture model (acsgmm, see e.g. Walker & Peñarrubia 2011; Amorisco & Evans 2012; Watkins et al. 2013; Agnello et al. 2014, L15b). We decompose the LOSVD profiles into multiple independent Gaussian components. Each Gaussian G_i can be described by its central value μ_i and dispersion σ_i. For a PN k with measured velocity $v_k \pm \delta v_k$ this is

$$G_i(v_k, \delta v_k; \mu_i, \sigma_i) = \frac{1}{\sqrt{2\pi}\sigma_i} \exp\left(\frac{(v_k - \mu_i)^2}{2(\sigma_i^2 + \delta v_k^2)}\right). \tag{3.7}$$

In the simple case of a two-component system, the likelihood would be

$$\mathcal{L}_k = \frac{G_1(v_k, \delta v_k; \mu_1, \sigma_1) + a_2/a_1 G_2(v_k, \delta v_k; \mu_2, \sigma_2)}{1 + a_2/a_1}, \tag{3.8}$$

with a_1 and a_2 being the amplitudes of the respective Gaussians. The total likelihood is the product of the individual likelihoods that are calculated for each *individual* PN. This method allows us to exploit the information of every PN without the need for binning.

We assume flat priors on the model parameters and calculate their posterior probability distribution functions (PDFs) using the ensemble-based MCMC sampler EMCEE (Foreman-Mackey et al. 2013).

3.4 Results

3.4.1 Distinct kinematics of bright and faint PNe

We want to investigate whether the kinematics of PNe correlate with magnitude as possible correlations or anti-correlations could point to different stellar populations with distinct kinematics. We therefore calculate the reduced velocity for PNe from the matched catalogue using eq. (3.2), as these have the most accurate magnitude measurements. As Fig. 3.1 illustrates, we find no significant correlation between reduced velocity and magnitude, however, the entire sample (black circles) shows an excess of co-rotating PNe brighter than $m_{5007} < 27.5$ mag. This excess is driven by PNe localised in the northern (blue squares) and southern (red diamonds) quadrants, as illustrated in the top panel of Fig. 3.1. The PNe

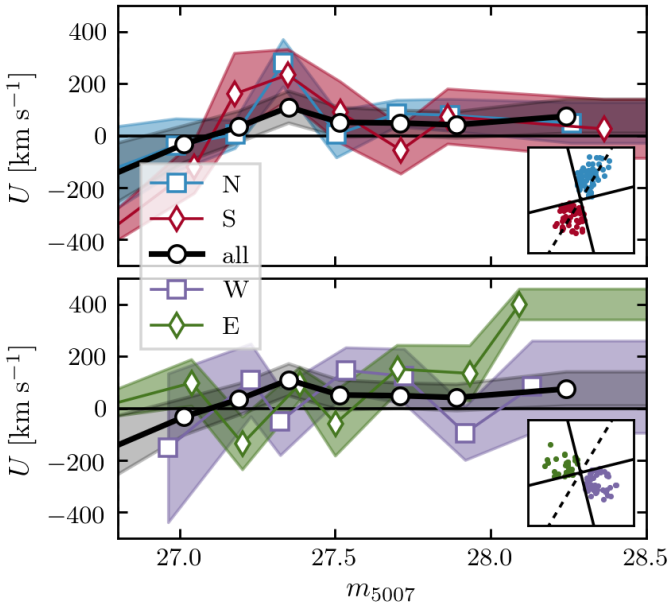

Figure 3.1: Mean reduced velocity U vs. magnitude m_{5007} of PNe in the matched catalogue. *Top:* Northern (blue squares) and Southern (red diamonds) quadrants. *Bottom:* Western (purple squares) and Eastern (green diamonds) quadrants. In both panels, the black open symbols denote the entire sample and the respective colour bands the 1σ-error on the reduced velocity. The insets highlight the respective quadrants on the sky, with M49's photometric major axis denoted by a dashed line. The excess of bright PNe with positive reduced velocity in the Northern and Southern quadrants motivates the division into a bright and a faint PN sample.

in the western (purple squares) and eastern (green diamonds) quadrants do not show such an excess; see bottom panel in Fig. 3.1. A 2D Kolmogorov-Smirnov (K-S) test (Peacock 1983; Fasano & Franceschini 1987) investigating whether the northern and southern samples could be drawn from the same U-magnitude distributions as the western and eastern samples results in a p-value of $p = 0.17$, thus rejecting this hypothesis (Press et al. 2007). Based on the behaviour of the mean reduced velocity as a function of magnitude, we divide the magnitude-corrected PN.S-sample into a *bright* ($m_{5007} < 27.5$, 258 PNe) sample that is governed by an excess reduced velocity in the fields along the major axis, and a *faint* ($m_{5007} > 27.5$, 178 PNe) sample, where this excess is absent.

The comparison of the LOS velocity dispersion profile, calculated in seven elliptical bins, of the magnitude-corrected sample with that of stellar tracers from integral-field spectroscopy (IFS, Veale et al. 2017, hereafter V17b) shows that the PN kinematics agree well with those of the integrated light in the region of overlap; see solid and dashed black lines in Fig. 3.2. We then calculate the velocity dispersion profiles for the bright (open green diamonds) and faint (filled red squares) samples separately.

We also construct smoothed velocity and velocity dispersion fields for the total PN-sample as well as for the bright and faint samples, using the adaptive kernel-smoothing

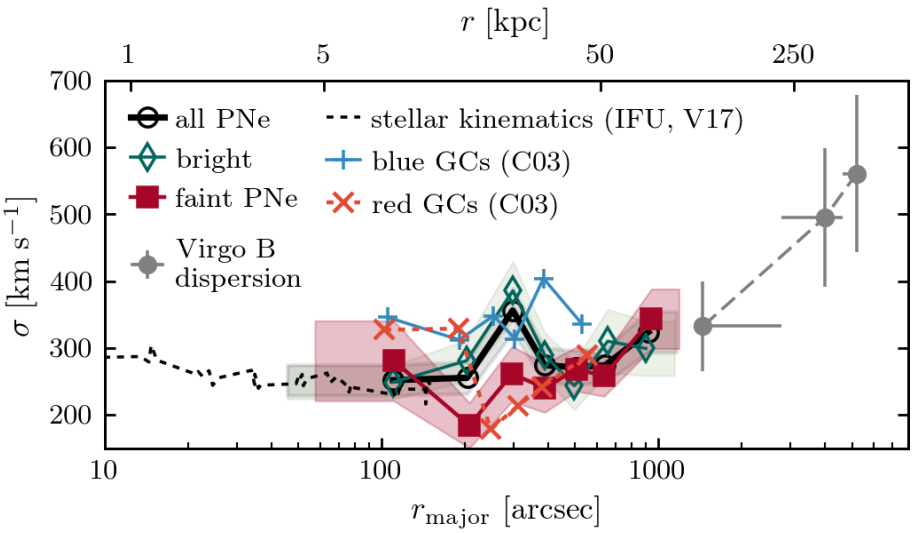

Figure 3.2: LOS velocity dispersion profile as a function of major-axis radius of the total (open black circles), bright (open green diamonds), and faint (filled red squares) magnitude-corrected PNe in the halo of M49. The coloured bands denote the 1σ errors. The stellar velocity dispersion profile is indicated by the dashed black line (V17b) and the dispersions of metal-poor and metal-rich GCs are indicated by the solid blue and dashed red line respectively (C03). The grey error bars connected with dashes denote the velocity dispersion of galaxies in the Virgo Subcluster B. The velocity dispersion of the faint PN-sample reaches that of the Subcluster B at large radii, which indicates that these PNe are tracing the underlying IGL.

Table 3.1: Maximum likelihood and BIC of single- and double-Gaussian models of the LOSVD in the respective PN-samples. $N_{\rm Gauss}$ denotes the number of Gaussians and $N_{\rm fit}$ the number of fitted parameters.

Sample	$N_{\rm Gauss}$	$N_{\rm fit}$	$\log(\mathcal{L}_{\rm max})$	BIC
Faint	1	2	−1352	2714
Faint	2	5	−1258	2543
Bright-North	1	2	−834	1678
Bright-North	2	5	−835	1694
Bright-South	1	2	−1009	2028
Bright-South	2	2	−1005	2020

technique (Coccato et al. 2009; Pulsoni et al. 2017) that is described in Sect. 3.3.2. The resulting fields are shown in Fig. 3.3, where the smoothed values $\tilde{v}$ and $\tilde{\sigma}$ are plotted at the position of the observed PNe. The bright and faint samples have distinct features, which we discuss in turn below. It is apparent that the velocity and velocity dispersion of the bright sample that are shown in panels (a) and (b) of Fig. 3.3 differ significantly from those of the faint sample shown in panels (c) and (d).

3.4.2 Faint sample: separation of halo and intra-group light

The velocity field of the faint sample (Fig. 3.3c) is dominated by a rotation of $v_{\rm rot} = 120$ km s^{-1} about the minor axis. The velocity dispersion (Fig. 3.3d) is $\sigma = 270$ km s^{-1} along the major axis and increases up to $\sigma = 320$ km s^{-1} along the minor axis. Comparing the spatial density of tracers, the faint component (see Fig. 3.3c) is less centrally concentrated compared to the bright one (Fig. 3.3a), which allows us to study the kinematics of the extended outer halo.

The smoothed velocity (Fig. 3.3c) and velocity dispersion (Fig. 3.3d) fields do not immediately suggest multiple velocity components due to their smooth and symmetric appearance. However, inspecting the LOS velocity dispersion profile shown with red squares in Fig. 3.2, the rising dispersion at large radii – even reaching the velocity dispersion of the Virgo Subcluster B (grey error bars, derived from Binggeli et al. 1993) – indicates a smooth transition that might be driven by an additional component with larger velocity dispersion.

We therefore constructed the LOSVD for the PNe in the faint sample. As shown by the histogram in the left panel of Fig. 3.4, it has strong wings. If we characterise the overall LOSVD of the faint component in terms of Gauss-Hermite polynomials (van der Marel & Franx 1993; Gerhard 1993) with moments μ, σ, h_3, and h_4, we obtain a high h_4 value, that is, $h_4 = 0.11 \pm 0.03$, and a much smaller $h_3 = 0.01 \pm 0.03$ (dashed green line in Fig. 3.4). This is in contrast to observations of ETGs in equilibrium, where the asymmetric deviations of the LOSVD from Gaussianity (characterised by h_3) are more prominent than the symmetric deviations (characterised by h_4), with the latter being a few percent at most

(Gerhard 1993; Bender et al. 1994).

In order to illustrate the uncommonly large value of h_4 with respect to galaxies in equilibrium, we compare our derived value to the distribution of luminosity-averaged h_4 values of ETGs in the SAURON (Emsellem et al. 2004) and MASSIVE (Veale et al. 2017) surveys. As shown in Fig. 3.5, the error-band of our best-fit value of h_4 (indicated by the red shaded region) overlaps with the tails of the histograms from the SAURON (grey) and MASSIVE (blue) surveys and is larger than any of the measured h_4 values based on integral-field spectroscopy (IFS) data. It shows that the radially extended LOSVD of the faint PN sample cannot be reproduced by the LOSVDs found in most ETGs within a few effective radii ($0.5 - 4.0\,r_\mathrm{e}$). The large h_4 value measured for M49 is more extreme than any of the 41 values measured for the MASSIVE galaxies, which demonstrates that it has not been drawn from the same distribution at the 97.5% confidence level.

We note that M49 is part of the MASSIVE sample and that the h_4 value measured here is larger than the luminosity-averaged value determined by Veale et al. (2017). However, our best-fit value agrees with their h_4 value at the largest radii within the errors (see Veale et al. 2017, Fig D8), continuing the trend of rising h_4 values with increasing radius observed in the MASSIVE survey. This positive gradient of h_4 values with radius present in the MASSIVE survey is also illustrated by the offset between the mean h_4 values between the SAURON and MASSIVE surveys. The SAURON survey covers the central $0.5 - 1\,r_\mathrm{e}$, where the h_4 values are generally small or even slightly negative (see also Bender et al. 1994). The radial coverage of the MASSIVE survey extends to $2.0 - 4.0\,r_\mathrm{e}$. Due to this larger coverage, the transition to a core-wing structure of the LOSVD as signalled by an increase in h_4 value can be observed. Our measurement that includes data out to $6\,r_\mathrm{e}$ shows that this positive gradient of h_4 values extends to larger radii than those sampled in the MASSIVE survey.

Strongly winged LOSVDs such as the one observed in M49 are also observed in other galaxies in group and cluster environments (e.g. Ventimiglia et al. 2011; Veale et al. 2018; Barbosa et al. 2018, L15a). Hydrodynamical cosmological simulations of galaxies at the centre of clusters find that the strongly winged LOSVDs of star particles are well described by two Gaussians with different dispersion (Cui et al. 2014; Dolag et al. 2010) and centred on different mean velocities (van den Bosch et al. 2005). The Gaussian with the largest velocity dispersion indicates the presence of a population of intra-group (or intra-cluster) stars at large radii, which do not trace the halo but the group (or cluster) potential.

Using the method described in Sect. 3.3.3, we fit a single- and a double-Gaussian model to the data, with the latter being clearly favoured, with a lower Bayesian Information Criterion (BIC, cf. Table 3.1). If we were to fit a single Gaussian to the LOSVD for the entire faint sample, its velocity dispersion would be $\sigma_\mathrm{faint,single} = 290^{+17}_{-16}$ km s^{-1} and it would be centred on M49's systemic velocity. A K-S test whether the faint LOSVD can be drawn from a single Gaussian with these parameters results in $p = 0.08$. This model is denoted by the orange line in the left panel of Fig. 4, while the best-fit two-component model scaled to the binned LOSVD is denoted by the solid black line. For comparison, we also carry out a K-S test between the observed faint LOSVD and our best-fit two-component model, resulting in $p = 0.64$.

The first component of the model (dashed blue line), which we associate with M49's halo, is centred on $\mu_{\rm halo} = -27.1^{+26.8}_{-24.5}$ km s^{-1} (with respect to the systemic velocity of M49) and has a velocity dispersion of $\sigma_{\rm halo} = 169 \pm 27$ km s^{-1}. The second component (dotted red line), which we associate with the IGL, has a central velocity of $\mu_{\rm IGL} = 54.0^{+54.0}_{-55.0}$ km s^{-1} that is marginally offset from the halo one and its velocity dispersion $\sigma_{\rm IGL} = 397^{+38}_{-36}$ km s^{-1}, which is more than twice as large as that of the halo component, or, phrased differently, is 5.9σ away. The difference between the central velocities of the IGL and main halo indicates a velocity bias that is consistent with that observed in several central dominant (cD) galaxies (e.g. van den Bosch et al. 2005; Barbosa et al. 2018, L15a).

In order to quantify the contribution of the second Gaussian with respect to the main one, we statistically associate each PN to either one of the two Gaussians based on its LOS velocity. To determine the mean fraction and its error as a function of radius, we calculate 10 000 realisations. On average, we associate 81 PNe with the second, broader Gaussian. These PNe have a uniform spatial distribution in M49's halo. The right panel of Fig. 3.4 shows the increasing relative contribution of PNe associated to the second Gaussian as a function of major-axis radius. The fraction of PNe associated with the second Gaussian, which is already 30% in the innermost elliptical bin, rises with increasing radius and reaches above 50% beyond 50 kpc.

3.4.3 Bright sample: kinematic signature of the accretion of VCC 1249

We now investigate the presence of a kinematically distinct component in the bright sample. North of the minor axis, the velocity dispersion is $\sigma = 230$ km s^{-1} and the velocity field is featureless, with the majority of the PNe moving with velocities close to M49's systemic velocity (see Fig. 3.3a). The velocity field south of the minor axis shows a multi-peaked distribution. There is an approaching component $5'$ along the major axis with a $\sigma = 400$ km s^{-1} peak in the velocity dispersion field. This peak is centred on the position of the dwarf irregular (dIrr) galaxy VCC 1249 (black cross), which is currently interacting with M49 (e.g. Arrigoni Battaia et al. 2012). VCC 1249 has a systemic velocity of $v_{\rm VCC1249,sys} = 390 \pm 30$ km s^{-1} (SDSS), therefore the superposition of the LOS velocities of PNe originating from this galaxy and halo PNe results in a high-velocity dispersion in the kernel smoothing (recall $v_{\rm M49,sys} = 960 \pm 24$ km s^{-1}, Pulsoni et al. 2017).

We therefore divide the bright population along the major axis into two subsamples. The southern subsample contains signatures of the accretion of VCC 1249. Based on the featureless appearance of the smoothed velocity and velocity dispersion fields north of the minor axis (see Fig. 3.3), we assume that the PN-kinematics in the northern subsample are unaffected by the accretion of VCC 1249. We again fit single- and double-Gaussian models to the data and find that the best-fit model for the bright northern subsample is a single Gaussian with $\mu = -2.7^{+25.1}_{-24.8}$ km s^{-1} and $\sigma = 270^{+19}_{-51}$ km s^{-1}. Adding a second Gaussian to the model only marginally increases the maximum likelihood and is penalised with a higher Bayesian Information Criterion (BIC) (see Table 3.1). A K-S test remains inconclusive as

to whether the northern subsample is drawn from a single or a double Gaussian model.

Assuming that the underlying halo population of bright PNe in M49 is symmetric, we expect the LOSVD of halo PNe[3] in the southern subsample to have the same mean velocity and velocity dispersion that we fit in the northern subsample. However, when comparing the LOSVD of PNe in the northern subsample with that of the southern sample (grey histograms in the top and bottom panel of Fig. 3.6), it is apparent that the LOSVD of the southern subsample cannot be described by a single Gaussian. This is further corroborated by Pulsoni et al. (2017), who cannot reconcile the asymmetric LOSVD of M49 at the position of VCC 1249 with simulated galaxies in equilibrium.

In order to account for the contribution of PNe from the accretion of VCC 1249, we fit a double-Gaussian model: the first Gaussian is fixed by the Gaussian fit to the LOSVD of PNe from the northern sample and the second Gaussian is free to vary. We find that the second component is centred on $\mu_{\rm VCC1249} = -512 \pm 30$ km s^{-1} relative to the systemic velocity of M49 and has a velocity dispersion of $\sigma_{\rm VCC1249} = 40^{+28}_{-19}$ km s^{-1}. The maximum likelihood and BIC for this model in comparison to a single Gaussian are shown in Table 3.1, with the two-component model being preferred with a lower BIC. If we add M49's systemic velocity to the centre of the secondary component, it results in $v_{\rm VCC1249,LOS} = 412 \pm 30$ km s^{-1}, which agrees with VCC 1249's systemic velocity from SDSS within the errors. As illustrated in Fig. 3.7, PNe associated with this secondary peak cluster around the position of VCC 1249, which further supports the association of these PNe with VCC 1249.

3.5 Discussion and conclusions

In this work, we found that the PNe in the halo of M49 divide in subpopulations in a position-velocity-magnitude space. The three subpopulations correspond to the main halo, the intra-group light, and the accreted satellite VCC 1249. We investigated the bright and the faint samples and identified the main halo in both. In the faint sample, we find evidence for two kinematic components: the M49 halo and the IGL with velocity dispersions $\sigma_{\rm faint,M49} = 169 \pm 27$ km s^{-1} and $\sigma_{\rm faint,IGL} = 397^{+38}_{-36}$ km s^{-1}, respectively. If only a single Gaussian is fit, the resulting velocity dispersion is $\sigma_{\rm faint,single} = 298^{+17}_{-16}$ km s^{-1}. In the bright component, where a single Gaussian fit is preferred based on a lower BIC, the velocity dispersion is $\sigma_{\rm bright} = 270^{+19}_{-51}$ km s^{-1}, which is in agreement with the estimate for the faint component, obtained with the same method, within the errors. Therefore the absence of two distinct IGL and halo model components in the bright sample is likely due to the smaller sample size.

The fit of a two-component LOSVD for the bright sample, with contribution from a high-dispersion IGL component and a halo with velocity dispersion similar to the one measured in the faint component, is impeded by the kinematic signature of the dIrr galaxy VCC 1249 in the low-velocity tail of the LOSVD. We therefore first discuss the accretion

[3]PNe not associated to the accretion of VCC 1249

of VCC 1249 in Sect. 3.5.1 and then the implications on IGL detection in the bright component in Sect. 3.5.2.

3.5.1 Accretion of VCC 1249

We can clearly detect the kinematic signature of the dIrr galaxy VCC 1249 in the bright PN sample. The interaction between M49 and VCC 1249 led to the formation of stellar tidal tails and to the removal of gas from the dwarf (Arrigoni Battaia et al. 2012). Our best-fit velocity for the VCC 1249 PNe (412 ± 30 km s^{-1}) falls in between the systemic velocity derived from SDSS $v_{\rm sys} = 390 \pm 30$ km s^{-1} and the peak velocity of the H I removed from it, which is $v_{\rm HI} = 469$ km s^{-1} (McNamara et al. 1994), suggesting that the PNe trace both the dwarf and the stripped stars as their average velocity is between the H I and VCC 1249 systemic velocities. PNe associated with the interaction of VCC 1249 and M49 are clustered around the position of the dIrr galaxy with a loose association of PNe appearing to stream towards or away from the centre of M49 (see Fig. 3.7). They broadly overlap in space with the H I tail associated with VCC 1249 (McNamara et al. 1994, blue contours). The interaction also triggered the formation of H II regions, which also emit at 5007Å. However, as they are extended, they should not be contaminating our PNe sample. A cross-correlation of our catalogue with the positions of H II regions from Arrigoni Battaia et al. (2012) did not yield any matches. Therefore our detections are not H II regions, but PNe associated with this accretion event. Our findings will be the basis for a more in-depth dynamical model of the dynamics of M49's halo and its recent interaction with VCC 1249.

3.5.2 M49 halo and the IGL in the Virgo Subcluster B

We find evidence for an extended population of PNe that are kinematically associated with the IGL. Based on their LOS velocities, we statistically associate 81 PNe in the faint sample with the IGL population, which are uniformly distributed in M49's halo. This PN subsample has a velocity dispersion more than twice that of the halo ($\sigma_{\rm IGL} = 397^{+38}_{-36}$ km s^{-1}) and traces the IGL out to 95 kpc along the major axis, much further than any X-ray observations of M49 to date. It is therefore difficult to assess the dynamical state of the IGL based on the X-ray potential. If we however assumed that the circular velocity profiles derived by Das et al. (2010) remained flat beyond their maximum radius of 30 kpc, the circular velocity would be $v_{\rm c} \approx 500$ km s^{-1}. Churazov et al. (2010) derive a number of relations to calculate the circular velocity from the velocity dispersion for a given surface brightness profile and orbital configuration. Inverting their eq. (24) for an isotropic system, assuming a flat rotation curve, and the surface brightness profile from Kormendy et al. (2009), the corresponding dispersion at 80 kpc would therefore be $\sigma \approx 300$ km s^{-1}, similar to the combined velocity dispersion of the halo and IGL traced by the PNe at large radii (see Fig. 3.2). This suggests that the circular velocity inferred from X-ray observations within 30 kpc is indeed constant out to ~ 80 kpc, and that the transition to the group structure takes place at larger radii, as also shown in Fig. 3.2.

In order to trace the transition from halo to IGL, we consider the velocity dispersion profile. In the decomposition of the LOSVD of the faint sample, we approximate the velocity dispersion profile of the IGL as constant, resulting in with a value of $\sigma_{\rm IGL} = 397^{+38}_{-36}$ km s^{-1}. However, the velocity dispersion profile of the total faint sample (indicated by red squares in Fig. 3.2) increases with radius, reaching the velocity dispersion of galaxies in the Subcluster B (grey error bars). The subcluster velocity dispersion was calculated from the velocities of individual galaxies (Kim et al. 2014) within $1.^{\circ}6$ from the subcluster centre based on their membership classification by Binggeli et al. (1993). The characteristic increase in velocity dispersion is also observed in the bright sample. A similar increase in velocity dispersion is seen in the metal-rich (red) GCs, however, as their data have a smaller radial extent, Côté et al. (2003) did not attribute this rise to an IGL contribution. The right panel of Fig. 3.4 illustrates that the rise in velocity dispersion is due to the increased fraction of PNe associated with the IGL at larger radii.

The fact that the velocity dispersion of the faint sample reaches that of the Subcluster B indicates that M49's outermost halo is dynamically controlled by the subcluster's gravity. This is one of the defining features of a cD, or in this case group dominant galaxy. Early attempts to measure the velocity dispersion out to radii where the halo is dynamically controlled by cluster gravity were made by Dressler (1979). In the case of NGC 6166 in Abell 2199, where a velocity dispersion profile reaching the cluster dispersion was already observed by Kelson et al. (2002), the cD halo would not have been recognisable based of surface photometry alone (Bender et al. 2015). *M49 is the first galaxy where the transition from galaxy to cluster velocity dispersion has been measured from the velocities of individual stars (PNe).*

In the case of M49, deep broad-band photometry from the VEGAS survey (Capaccioli et al. 2015; Spavone et al. 2017) and Mihos et al. (2013, 2017) already indicated the presence of an extended, blue outer halo, characterised by a steep colour gradient and a shallower surface-brightness profile. Based on their narrow-band PN survey, H17 argue for the presence of IGL, that is traced by a PN population with a PN-specific frequency of $\alpha_{\rm IGL} = (1.03 \pm 0.22) \times 10^{-8}$ PN $L^{-1}_{\odot,\rm bol}$, three times higher than the specific frequency of M49's halo, and an underlying stellar population that contributes 10% of the total luminosity in the surveyed area. The PN kinematics presented here corroborate their result of an extended PN population associated with the IGL. The blueward colour gradient measured by Mihos et al. (2013) constrains the IGL colour to $B - V \leq 0.65$.

In addition to the smooth blue halo, Janowiecki et al. (2010) observe a number of shells surrounding M49. However, these shells are significantly redder than the underlying smooth blue halo and are therefore clearly of distinct origin. Mihos et al. (2013) argue that the colour of these shells ($B - V \approx 0.85$) is in agreement with the accretion of a single dwarf elliptical (dE) galaxy from the dE population surrounding the Virgo Cluster, which have a mean colour of $B - V \approx 0.77$ (van Zee et al. 2004).

3.5.3 Origin of the IGL in the Virgo Subcluster B

In addition to the photometric properties discussed in the previous subsection, we would like to derive constraints on the dynamical age of the IGL, on the basis of its smooth appearance in photometry (Mihos et al. 2013; Capaccioli et al. 2015) and regular velocity field and LOSVDs (see Fig. 3.3 and Fig. 3.4). The smooth appearance suggests that the IGL has a dynamical age that is older than the orbital precession time, that is, at least 5 Gyr, thereby ruling out the accretion of a moderately massive (1:5 merger-mass ratio), young star-forming galaxy as the origin of the extremely blue IGL. As the LOSVD is smooth and the velocity field is point-symmetric, this is consistent with the accretion of many low-mass systems. Due to the constraint on the dynamical age (> 5 Gyr) and the observed $B-V$ colour (0.6), these systems must have metallicities lower than [Fe/H] $< -1 \pm 0.5$ (Mihos et al. 2013). According to the low-mass end of the mass-metallicity relation (Kirby et al. 2013), galaxies with these low metallicities would have stellar masses of at most a few times $10^8\ M_\odot$.

Independent constraints on the age and metallicity of intra-cluster stellar populations in the Virgo Cluster were derived from HST-ACS observations of ~ 5300 stars in a single pointing located between M87, M86, and M84 at 190 kpc distance from M87 (Williams et al. 2007). The theoretical stellar evolution models suggest that this intracluster population is dominated by stars with old ages (≥ 10 Gyr) with a significant number of very metal-poor stars ([Fe/H] < -1.5). If the IGL is as blue as the last measured point at 100 kpc by Mihos et al. (2013, $B-V \approx 0.6$), for a 10-Gyr old stellar population the corresponding metallicity is [Fe/H] < -1.5, leading to even stronger constraints on the stellar masses of the satellites that built the IGL: these would have to be less than $M_\star \leq 10^7\ M_\odot$ (Kirby et al. 2013).

We now put these measurements into the context of galaxy clusters observed at slightly larger redshift ($0.3 \leq z < 0.6$). Recent studies on six clusters in the Hubble Frontier Fields (Lotz et al. 2017) measured negative colour gradients with increasing distance from the brightest cluster galaxy (BCG) out to the intra-cluster light (ICL, Montes & Trujillo 2018; Morishita et al. 2017a; DeMaio et al. 2018). The three different studies agree that these strong colour gradients cannot be explained with metallicity gradients alone, but are a combination of metallicity and age gradients.

Morishita et al. (2017a) extend these measurements out to 300 kpc from the central BCG and measure colours as blue as $B-V \approx 0.1$. They estimate that $10-15\%$ of the intra-cluster light (ICL) mass beyond 150 kpc was contributed by (post-) star-forming populations with young ages (~ 1 Gyr) at $z \approx 0.5$ and low stellar mass ($M_\star < 3 \times 10^9\ M_\odot$). However, the total ICL mass in the six Hubble Frontier Field clusters is similar to the mass of all existing red satellites with stellar masses below $10^{10}\ M_\odot$ as estimated from the combination of the Frontier Field data with the GLASS survey (Morishita et al. 2017b), which suggests that tidally stripped stars from higher-mass systems likely also contribute some of the mass of the ICL (Morishita et al. 2017a). Due to dynamical friction, low-mass systems will stay roughly at the radius at which they were disrupted, while the more massive (and therefore metal-rich and red) satellites would sink towards the BCG centre

(e.g. Ostriker & Tremaine 1975; Amorisco 2017).

An evolutionary path for the formation of a blue, smooth, and extended IGL around M49 may come from the early (before $z \sim 0.5$) accretion of a number of low-mass satellites with young (~ 1 Gyr) and blue ($B - V = 0.1$) stellar populations at that redshift. Since their accretion more than 5 Gyr ago, their stars would have evolved passively and would now have reached a colour of $B - V = 0.65$ at $z = 0$. If applicable, the constraints on the age from the resolved stellar populations in the ICL in Virgo (Williams et al. 2007) would set the time of accretion at even higher redshift and the stellar mass of the satellites to lower masses (e.g. $10^7\ M_\odot$)

The formation of a smooth IGL by the accretion of low-mass satellites at intermediate redshift can be well reproduced in N-body simulations combined with particle tagging (e.g. Amorisco 2017), where it is assumed that any low-mass halo forms stars according to the cosmological baryon fraction. The contribution of such low-mass systems with low merger-mass ratios is lower in current hydrodynamical cosmological simulations: while being able to resolve mergers with mass ratios below $10^{-4} : 1$, the cumulative effect from mergers with stellar mass ratios below $10^{-2} : 1$ is found to be negligible with respect to stellar halo growth (see Fig. 1 in Rodriguez-Gomez et al. 2016). As more massive satellites form sufficient stars in these hydrodynamical simulations, these satellites can now well reproduce the build-up of the halo closer to M49; see, for example, Pop et al. (2017), who reproduce shells that are distinctly redder than the underlying galaxy halo, like the ones observed in M49 (Janowiecki et al. 2010; Mihos et al. 2013).

Our observations suggest that the IGL formed early from the accretion of many low-mass satellites. This scenario is also in line with the observations of GC colours in ETGs; blue, metal-poor GCs are attributed to accretion from satellite galaxies, while red, metal-rich GCs are thought to have been formed in-situ (Côté et al. 2003; Peng et al. 2006; Li & Gnedin 2014; Renaud et al. 2017; Forbes et al. 2016). Our robust results on the mass of the satellites ($M_\star \lesssim 10^8\ M_\odot$), which were accreted at redshift $z \approx 0.5$, imply that the feedback in the current cosmological simulations is too strong for low-mass satellites to form sufficient stars. As these satellites need to contribute significantly to the growth of the IGL, the feedback would have to be reduced early in their lifetimes.

Understanding the build-up of the IGL in low-mass subclusters is important because they will eventually contribute to the overall ICL in their parent cluster. Our results corroborate the existence of multiple channels contributing to the ICL and IGL build-up at different cluster mass scales and distances to the cluster centre. In order to constrain the masses of the IGL and halo progenitor galaxies, we are planning to obtain more accurate LOS velocity measurements, as they would allow us to detect also substructures with lower velocity dispersion and therefore lower masses, which will set important constraints on the feedback mechanisms in the current cosmological simulations.

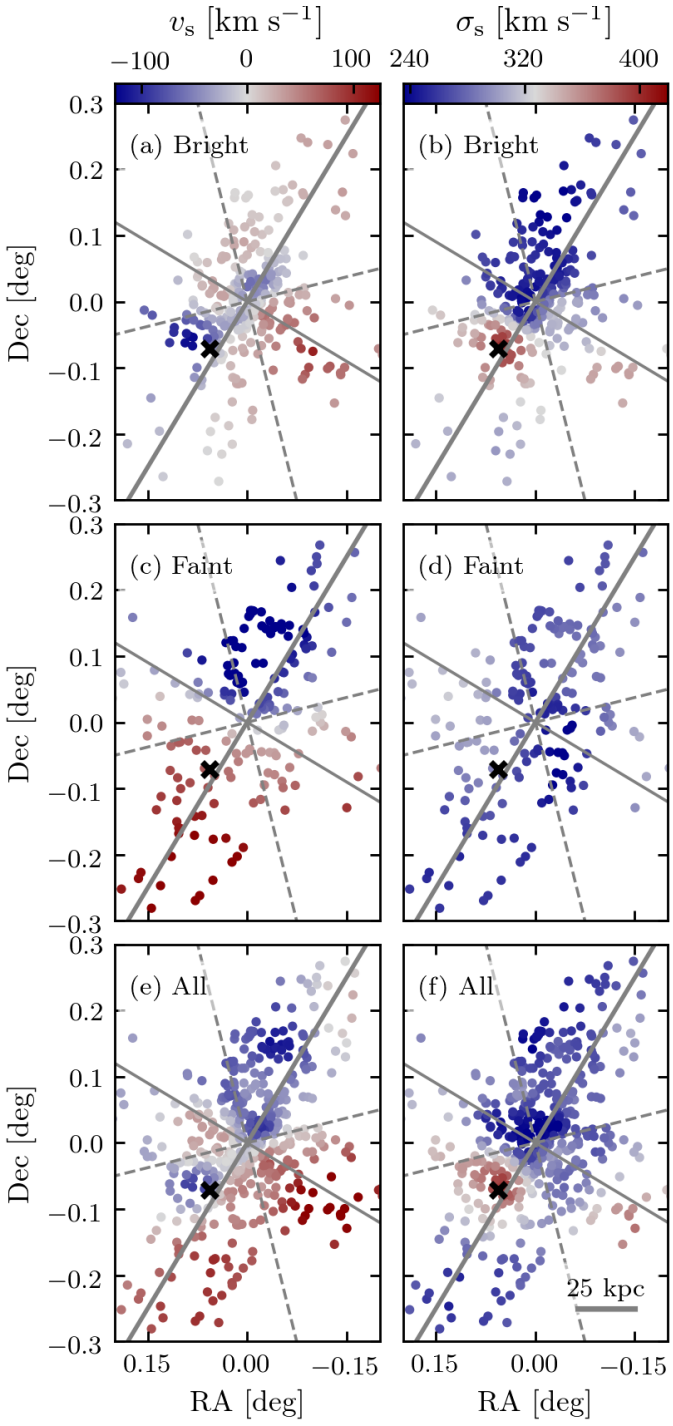

Figure 3.3: Smoothed velocity (left column) and velocity dispersion (right column) fields for the bright (top row) and faint (middle row) magnitude-corrected PN-samples. For comparison, the bottom row shows the smoothed fields for the total sample from Pulsoni et al. (2017). The solid grey lines denote the photometric major and minor axes of M49. The dashed lines divide the sample into four quadrants. The black cross denotes the position of the dIrr galaxy VCC 1249. The mean errors on the smoothed fields are $\Delta v_{\rm bright} = 39$ km s^{-1}, $\Delta v_{\rm faint} = 43$ km s^{-1}, $\Delta \sigma_{\rm bright} = 34$ km s^{-1}, and $\Delta \sigma_{\rm faint} = 38$ km s^{-1} respectively. The bar in the lower-left corner of panel (f) corresponds to 25 kpc. North is up, east is to the left.

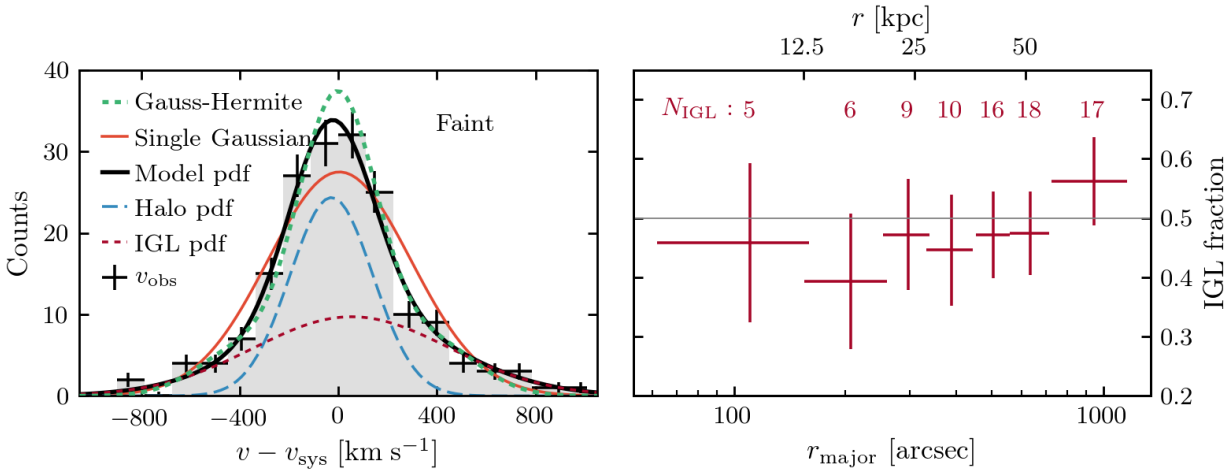

Figure 3.4: *Left:* LOSVD of the faint component (grey histogram with errorbars) and best-fit model PDF (black line), consisting of the halo (dashed blue line) and IGL (dotted red line), and scaled to the observed LOSVD. While the likelihood is fit with a bin-free method, we bin the LOSVD for visual convenience. For comparison, the best-fit single-Gaussian model is shown in orange. The dashed green line denotes the best-fit Gauss-Hermite expansion. *Right:* Fraction of faint PNe associated with the IGL as a function of major-axis radius, based on the probabilities derived from the LOSVD decomposition. The number of PNe associated with the IGL is given on top of each bin.

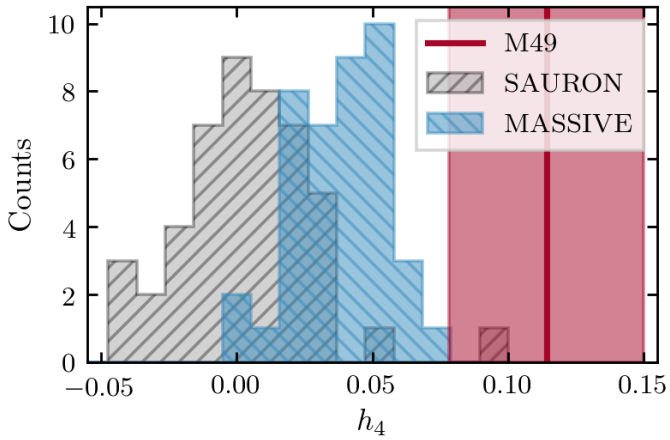

Figure 3.5: Best-fit h_4 value and error band (red vertical line and shaded region) derived from the LOSVD of the faint sample compared to the h_4 distribution of 47 and 41 ETGs from the SAURON (Emsellem et al. 2004) and MASSIVE (Veale et al. 2017) surveys (grey and blue histograms).

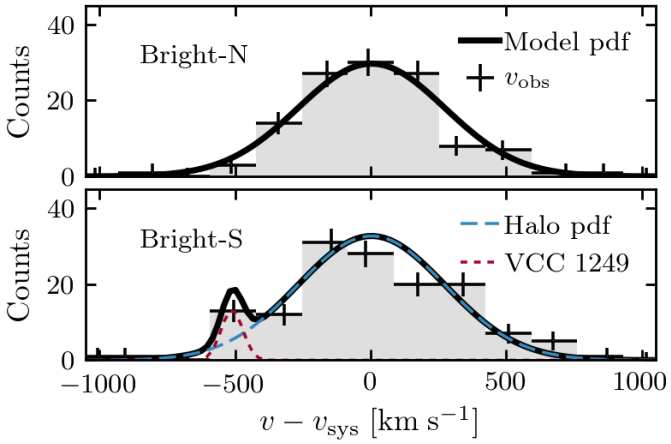

Figure 3.6: LOSVD of the bright component (grey histogram with error bars) in the north (top) and south (bottom) of the galaxy. The northern component is best-fit by a single Gaussian (solid black line). The substructure of VCC 1249 in the southern part is fit by a Gaussian (dotted red line) in addition to the halo (dashed blue line). While the likelihood is fit with a bin-free method, we bin the LOSVDs for visual convenience.

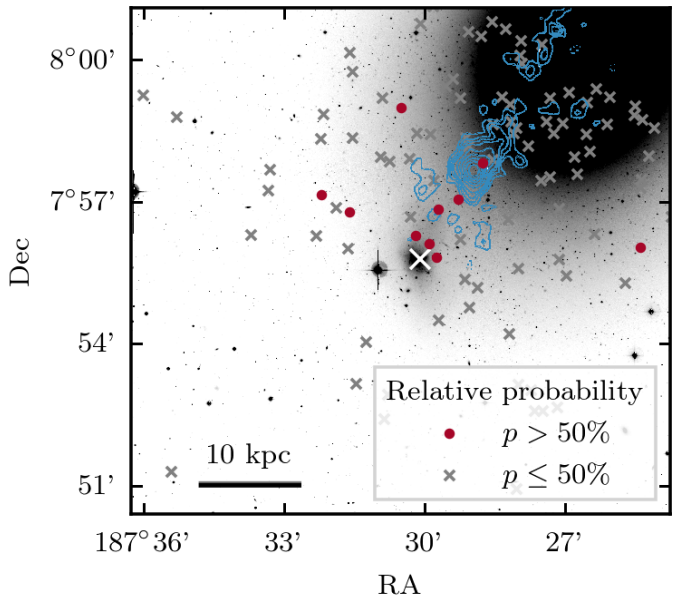

Figure 3.7: NGVS g-band image of M49 (from Arrigoni Battaia et al. 2012). PNe from the southern bright PN sample are colour-coded by their relative probability to be associated with VCC 1249. The white cross denotes the centre of VCC 1249. The H I contours from McNamara et al. (1994, precessed to from B1950 to J2000) are superposed in blue. The bar in the lower-right corner corresponds to 10 kpc. North is up, east is to the left.

Chapter 4

The halo of M105 and its group environment as traced by planetary nebulae populations[1]

4.1 Introduction

In a cold dark matter (CDM) dominated Universe with a cosmological constant (ΛCDM) structure forms hierarchically (White & Rees 1978; Peebles 1980). In this paradigm, the favoured formation scenario for early-type galaxies (ETGs) is a two-phase process: the initial phase of strong in-situ star formation (e.g. Thomas et al. 2005, and references therein) is followed by growth through mergers and accretion (White & Frenk 1991; Steinmetz & Navarro 2002; Oser et al. 2010). Therefore, the study of the distribution and kinematics of stars in their extended halos can provide important constraints on the late galaxy growth, as accretion events leave behind long-lasting dynamical signatures in the velocity phase-space (e.g. Bullock & Johnston 2005; Richardson et al. 2008; Starkenburg et al. 2009; Helmi et al. 2011; Crnojević et al. 2016) as well as low-surface brightness features like stellar streams, fans, and plumes (e.g. Ferguson et al. 2002; Mihos et al. 2005; Belokurov et al. 2007; Janowiecki et al. 2010; Mihos et al. 2017).

The galaxy M105 in the Leo I group has been at the centre of a long-standing debate on the dark matter (DM) content of ETGs and is one of the poster children of the Planetary

[1]Based on data collected at Subaru Telescope, which is operated by the National Astronomical Observatory of Japan under programme S14A-006 and with the William Herschel Telescope operated on the island of La Palma by the Isaac Newton Group of Telescopes in the Spanish Observatorio del Roque de los Muchachos of the Instituto de Astrofísica de Canarias. We thank S. Okamura and F. Nakata for carrying out the observations with SurpimeCam@Subaru. I reduced and calibrated the SurpimeCam data. Two of the four PN.S fields used in this work are part of the ePN.S survey (see Sect. 4.2 for details) and I could make use of the fully reduced data set. I lead the effort for the two additional fields (the e^{2}PN.S survey) observed in March 2017. This included the preparation of the proposal (PI: Merrifield) and the preparation of the observing run. I was in charge of the observations at the WHT during the seven-night run after two nights of training. I carried out the data reduction with the PN.S pipeline for these two fields.

Nebula Spectrograph (PN.S) ETG survey (Douglas et al. 2007). Using data obtained with the PN.S, Romanowsky et al. (2003) and Douglas et al. (2007) found that several intermediate luminosity elliptical galaxies – one of them being M105 – appeared to only have low-mass and low-concentration DM halos, if any, based on their rapidly falling velocity dispersion profiles. This is in stark contrast to the inferences made on the massive dark halos of giant elliptical galaxies from multiple tracers such as spectra of the integrated light, X-ray profiles of the hot gas atmospheres, as well as gravitational lensing (Awaki et al. 1994; Loewenstein 1999; Kronawitter et al. 2000; Gerhard et al. 2001; Hoekstra et al. 2004; Cappellari et al. 2006; Mandelbaum et al. 2006; Wilson et al. 2001; Treu & Koopmans 2004; Koopmans et al. 2006; Tortora et al. 2010, 2014).

Following the results of Romanowsky et al. (2003), Dekel et al. (2005) remarked that the apparent dearth of dark matter in the galaxies studied might have been due to not correctly accounting for the mass-anisotropy degeneracy. The authors argue that under some viewing angles, the triaxial nature of elliptical galaxies can cause low line-of-sight (LOS) velocity dispersions as the ones observed in M105, thus due to the mass-anisotropy degeneracy Romanowsky et al. (2003) might have underestimated the halo masses. In a follow-up paper (Douglas et al. 2007), it was however argued that the initial analysis by Romanowsky et al. (2003) correctly took into account the orbital anisotropies and that the probability of observing three triaxial galaxies at such particular viewing angles would be low.

In order to address these tensions, de Lorenzi et al. (2009) constructed dynamical models using the flexible χ^2-made-to-measure method implemented in the NMagic code (de Lorenzi et al. 2007), that allows for fitting spherical, axisymmetric, as well as triaxial models. Using a combination of ground- and spaced based photometric data (Gebhardt et al. 2000; Capaccioli et al. 1990), and kinematic data from long-slit spectroscopy (Statler & Smecker-Hane 1999; Kronawitter et al. 2000), integral-field spectroscopy (IFS) obtained with the Sauron instrument (Shapiro et al. 2006), as well as the discrete kinematics from the PN.S (Douglas et al. 2007), de Lorenzi et al. (2009) conclude that the kinematic data for M105 do not give strong constraints on the mass distribution in this galaxy. Consistent models include both near-isotropic systems with little DM as well as models with moderately massive DM halos such as the one proposed by Dekel et al. (2005), provided M105's outer envelope is strongly radially anisotropic.

The stellar kinematics are not the only interesting aspect about M105. Lee & Jang (2016) obtained deep Hubble Space Telescope (HST) photometry of resolved red giant branch (RGB) stars in two fields in the halo of M105 covering a galactocentric distance from $3R_{\rm eff}$ to $13R_{\rm eff}$. They fix the age of the stellar population to be 12 Gyr (Weijmans et al. 2009) and derive a metallicity for each star in M105 from the comparison of the observed colour-magnitude diagrams (CMDs) with the Darthmouth isochrones (Dotter et al. 2008). Both in colour and metallicity, the bright RGB stars show the existence of two distinct subpopulations: a dominant, red, metal-rich population with an approximately solar peak metallicity as well as a much weaker blue, metal-poor population whose peak metallicity is [Fe/H] ≈ -1.1, and which has a flattened radial number density profile in the outer halo.

Like the ETG M49 that was discussed in the previous two chapters, M105 does not live in isolation, but in a group environment. The Leo I Group, originally named G11

or M96 (NGC 3368) group, in which M105 resides, is the nearest loose group to contain both early- and late-type massive galaxies (de Vaucouleurs 1975a). The group contains at least 11 galaxies and has an on-sky extent of 1.6×1.0 Mpc (de Vaucouleurs 1975a). It is surrounded by a 200 kpc diameter broken ring of neutral hydrogen (Schneider et al. 1983) whose origin has been debated to be either due to the collision of two spiral galaxies (Rood & Williams 1984, 1985; Michel-Dansac et al. 2010) or due to the primordial formation of the galaxies M96, M105, and NGC 3384 from the same primordial gas cloud (Schneider 1985). There is no evidence for low surface brightness (LSB) features associated with the H I ring and no extended diffuse intra-group light (IGL) within a surface brightness (SB) limit of $\mu_B = 30$ mag arcsec (Watkins et al. 2014). In addition to that, Castro-Rodríguez et al. (2003) do not detect any planetary nebulae (PNe) associated with the H I ring and place an upper limit of $1.6^{+3.4}_{-1.0}$% on the IGL fraction. These findings are surprising, given that numerical simulations predict galaxy groups should have IGL fractions between 12% and 45% (Sommer-Larsen 2006; Rudick et al. 2006).

Using an extended photometric and kinematic samples of PNe, our aim is to place better constraints on the assembly history of M105 and its group environment. Our new kinematic data spans a three-times-larger minor-axis distance than Douglas et al. (2007), which will give important new constraints on the shape of the LOS dispersion profile of M105 at large radii as well as on the stellar populations in the outer halo as traced by PNe.

This Chapter is organised as follows. In Sect. 4.2 we present the photometric and kinematic surveys of PNe in the Leo I Group. In Sect. 4.3 we review broad-band photometric surveys of the group. We then study the relation between the azimuthally averaged distribution of the PNe and said SB photometry in Sect. 4.4. Section 4.5 is about the PNLF of M105 and its variation with radius. In Sect. 4.6 we present our novel photo-kinematic decomposition of our sample into two subcomponents associated with NGC 3384 and M105 and discuss M105's halo kinematics in Sect. 4.7. We conclude this Chapter with a discussion in Sect. 4.8.

4.2 Photometric and kinematic surveys of PNe in the Leo I Group

The photometric and kinematic surveys in this work expand our ongoing effort to study PNe as tracers in group and cluster environments. We combine kinematic data from the ePN.S survey (Arnaboldi et al. 2017; Pulsoni et al. 2017), including two additional, newly acquired fields, with accurate narrow- and broadband photometry obtained with Suprime-Cam mounted at the prime focus of the 8.2 m Subaru telescope. (Miyazaki et al. 2002).

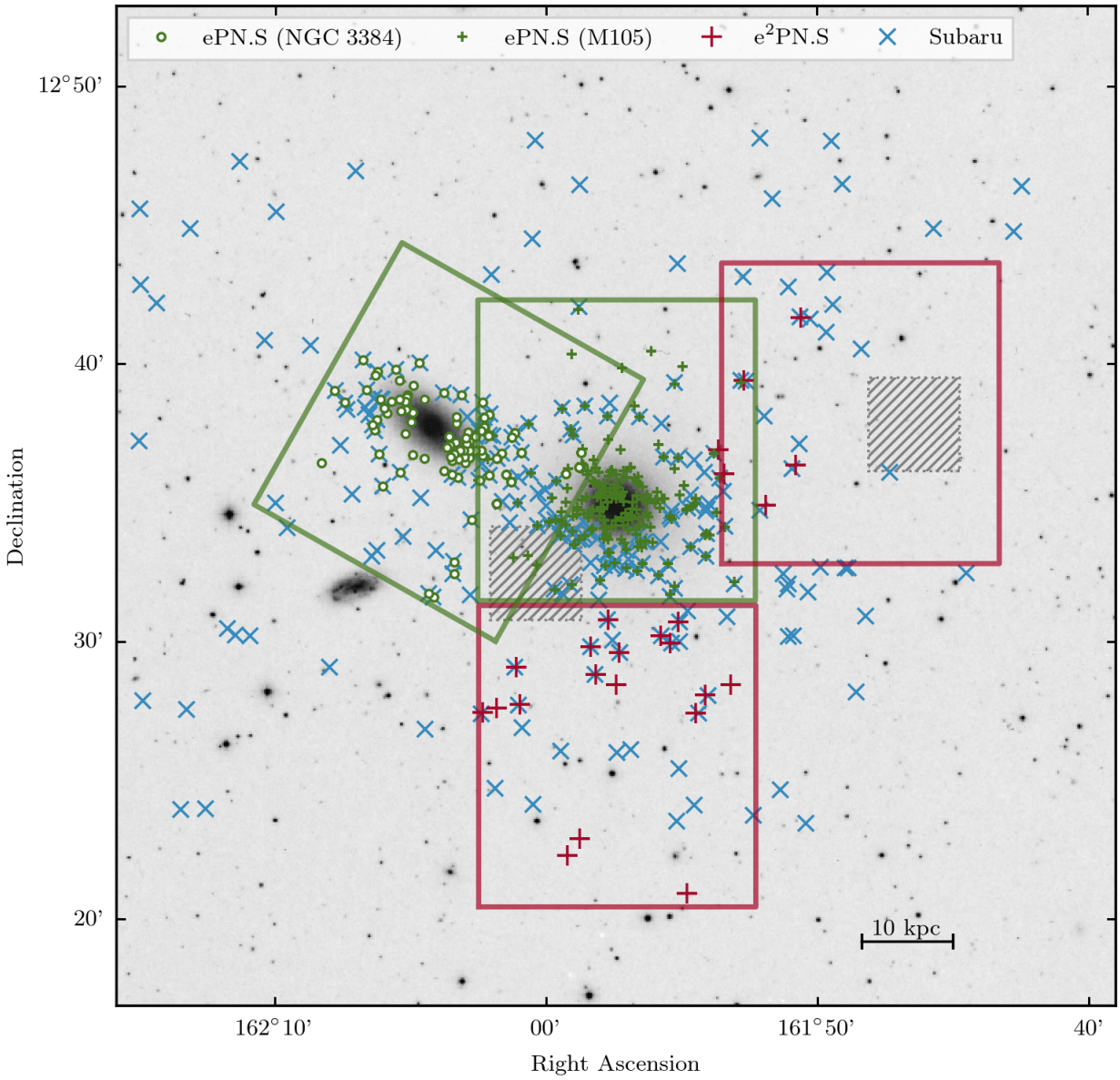

Figure 4.1: DSS image of M105. Overplotted are the PN-candidates from the Subaru survey (blue crosses), the ePN.S survey (Pulsoni et al. 2017, green plus signs), and the e^{2}PN.S survey (this work, red plus signs). The red and green rectangles denote the ePN.S and e^{2}PN.S fields. The grey hatched regions indicate the two HST fields analysed in Lee & Jang (2016). The scale bar in the lower-left corner denotes 10 kpc. North is up, East is to the left.

4.2.1 Subaru Suprime-Cam photometry

Survey description and data reduction

We used the on-off band technique to detect PNe candidates. M105 was observed through a narrow-band [O III] filter ($\lambda_{\rm c,on} = 5500\,$Å, $\Delta\lambda_{\rm on} = 74\,$Å) and a broad-band V-filter ($\lambda_{\rm c,off} = 5029\,$Å, $\Delta\lambda_{\rm off} = 956\,$Å), using the same observational strategy as Longobardi et al. (2013), who observed M87 in the Virgo Cluster. The observations were taken in the same night as Hartke et al.'s (2017) survey of M49 (Chapter 2 in this thesis). We therefore only briefly re-capitulate the data reduction steps and refer the reader to Chapter 2 for further details.

In order to reach down to two magnitudes from the planetary nebula luminosity function (PNLF) bright cut-off of the ($m^{\star}_{5007} = 25.7$, corresponding to a distance of 10.3 Mpc), six dithered exposures with a total exposure time of 1.8 h through the on-band and six dithered exposures with a total exposure time of 0.6 h through the on-band filter were observed. The observing conditions were photometric, with seeing better than 0.″7. The photometric zero points were calculated to be $Z_{[\rm O\,III],AB} = 24.51 \pm 0.04$ and $Z_{V,AB} = 27.48 \pm 0.01$ by Hartke et al. (2017). In order to convert the AB magnitudes to the m_{5007} from the [O III] line we use the relation by Arnaboldi et al. (2003) for the narrow-band filter in use:

$$m_{5007} = m_{AB} + 2.49. \tag{4.1}$$

The relation between integrated flux F_{5007} and magnitude m_{5007} is given by the Jacoby relation (Jacoby 1989):

$$m_{5007} = -2.5\log_{10}(F_{5007}) - 13.74. \tag{4.2}$$

The data were reduced using the instrument pipeline SDFRED2[2]. As the field is dominated by the three bright and extended galaxies M105, NGC 3384, and NGC 3398, the final images were astrometrised and stacked using the Astromatic tools Weight Watcher (Marmo & Bertin 2008), SCAMP (Bertin 2006), and SWARP (Bertin et al. 2002), using the UCAC-4 catalogue (Zacharias et al. 2012) as an astrometric reference (see Appendix A for details). In order to determine the images' point-spread function (PSF), we used the `psf` task of the IRAF-`daophot`[3] package. The best-fit profile is a Moffat analytical function with $\tilde{\alpha} = 2.5$, seeing radius $r_{\rm FWHM} = 2.35\,$pix, and axial ratio $b/a = 0.96$.

Selection of PN candidates and catalogue extraction

We make use of the characteristic spectral features of PNe: a bright [O III]5007Å emission and no continuum emission. Observed through an on-band filter, PNe appear as unresolved sources at extragalactic distances, while they are are not detected in the off-band image.

[2] `https://www.naoj.org/Observing/Instruments/SCam/sdfred/sdfred2.html.en`

[3] IRAF is distributed by the National Optical Astronomy Observatories, which are operated by the Association of Universities for Research in Astronomy, Inc., under cooperative agreement with the National Science Foundation.

Arnaboldi et al. (2002, 2003) developed a CMD-based automatic selection procedure that selects PNe based on their excess in [O III] − V colour and their point-like appearance. This technique has since been tailored to Suprime-Cam data by Longobardi et al. (2013) and Hartke et al. (2017, Chapter 2 in this thesis). For reference, the detailed catalogue extraction procedure for M105 can be found in Appendix 4.A.

We extract 226 objects within a limiting magnitude of $m_{5007} = 28.1$ and therefore cover 2.4 magnitudes from the bright cut-off of the PNLF. Our survey covers 67.6 kpc along M105's major axis and also covers the halos of NGC 3384 and NGC 3398. The selected PN candidates are denoted as blue crosses in Fig. 4.1.

4.2.2 The extended Planetary Nebula Spectrograph (ePN.S) ETG survey

The PN.S is a custom-built double-arm slitless spectrograph at the William Herschel Telescope (Douglas et al. 2002). Its design enables the identification of PNe and the measurement of their LOS velocities in a single observation (Douglas et al. 2002). The ePN.S ETG survey (Arnaboldi et al. 2017; Pulsoni et al. 2017) provides positions (RA, dec), LOS velocities (v) and magnitudes ($m_{5007,\mathrm{PN.S}}$) for spatially extended samples of PNe in 33 ETGs. The survey typically extends out to 6 effective radii (R_{eff}).

M105 (NGC 3379)

M105, was one of the first ETGs observed with the PN.S and was a milestone for the development of the PN.S data reduction pipeline (Douglas et al. 2007). As part of the PN.S ETG survey (Douglas et al. 2007), 214 PNe were observed, covering a major-axis distance of 5.3 R_{eff}. These are indicated by green plus signs in Fig. 4.1.

NGC 3384

As the on-sky distance between M105 and the SB0-galaxy NGC 3384 is only 435″ and the difference in distance modulus between the galaxies is only 0.2 mag, their PN populations will appear superimposed. An immediate separation in velocity space is not possible due to the small difference in systemic velocity ($\Delta v_{\mathrm{sys}} < 200$ km s^{-1}). At the time of publication of the data (2007), Douglas et al. addressed this by dividing the sample into two components on a probabilistic basis assuming that the distributions of PNe in the two galaxies directly follow the diffuse starlight.

However, the PN.S survey of S0 galaxy kinematics Cortesi et al. (2013a), also a subsample of the ePN.S ETG survey, contains 101 PNe observed within major-axis radius of 6.8 R_{eff} from the centre of NGC 3384. These are denoted by open green circles on Fig. 4.1. The availability of these data will enable an improved photo-kinematic decomposition of the PN.S sample (see Sect. 4.6).

4.2.3 The extremely extended Planetary Nebula Spectrograph (e^2PN.S) ETG survey in M105 and NGC 3384

In addition to the data from the ePN.S survey, we acquired two additional fields with the PN.S located east and south of M105 in March 2017. This extension of the ePN.S survey is named the *extremely* extended (e^2)PN.S ETG survey given its unprecedented coverage. The western field was positioned such that it encompasses the HST field observed by Lee & Jang (2016). The southern field was positioned such that the coverage along M105's minor axis was maximised. We observed the western field for 4.5 hours (in 9 dithered exposures) and the southern field for 3.5 hours (in 7 dithered exposures). The data reduction, entailing PNe detection and LOS velocity and magnitude measurements, was carried out using the procedures described in Douglas et al. (2007). The 21 newly detected PNe are denoted as red crosses on Fig. 4.1. In addition to that, we observed 3 PNe that are also part of the ePN.S survey and provide calibration for any velocity zero-point offset. The e^2PN.S survey reaches down to 1.5 mag from M105's PNLF bright cut-off, which is similar to the limiting magnitude of two the ePN.S fields discussed previously.

4.2.4 Catalogue matching

We first identify which PNe have been observed multiple times in the regions of overlap of the PN.S fields (cf. Fig 4.1). The largest overlap exists between the fields centred on M105 and NGC 3384, where 30 matching PNe were identified within a matching radius of $5''$[4]. We also identified 3 PNe that were observed both in the ePN.S and the e^2PN.S survey. Figure 4.2 shows the good agreement between the velocity measurements in the different fields. The 13 measurements that lie outside of the grey shaded region that indicates the nominal PN.S velocity error of 20 km s^{-1} all belong to PNe that were observed close to one of the field edges in either of the two fields. For these PNe, we only considered the measurement taken closer to the respective field centre. For any other PNe with two velocity measurements, we use the mean of these two measurements. The resulting combined catalogue (hereafter the *kinematic* catalogue) contains 307 PNe.

We then match the kinematic catalogue with the photometric catalogue, again using a matching radius of $5''$. Figure 4.3 shows the comparison of magnitudes measured from the [O III] image obtained with SuprimeCam and from the counter-dispersed images of the PN.S. The grey shaded region indicates the photometric error of the SuprimeCam photometry as a function of magnitude (see also Appendix 4.A.2 for details.)

4.3 Stellar surface photometry of the Leo I Group

Before the analysis of the PN populations in the Leo I Group, this section will provide an overview on the stellar surface photometry of the two brightest galaxies in the field-of-view

[4]This seemingly large matching radius is chosen due to the larger positional uncertainties of the PN.S compared to conventional imaging.

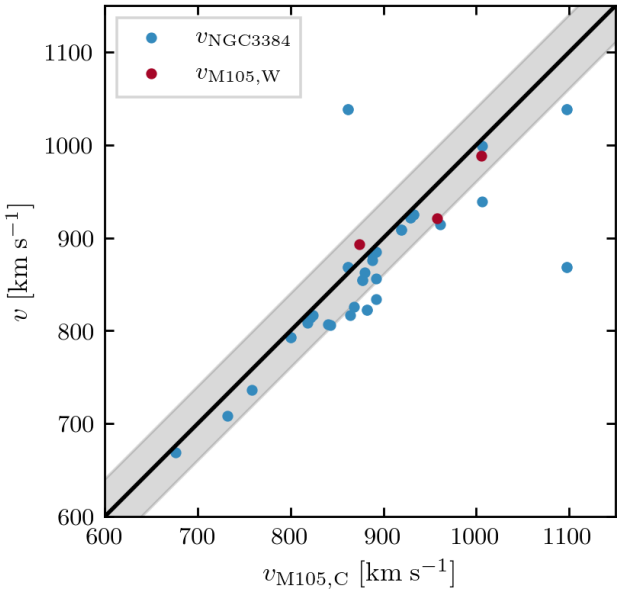

Figure 4.2: Velocity measurements of PNe observed in the central field of M105 compared to those observed in the field centred on NGC 3384 (blue) and the western e^{2}PN.S field (red). The grey shaded region indicates the PN.S velocity error of 20 km s^{-1} .

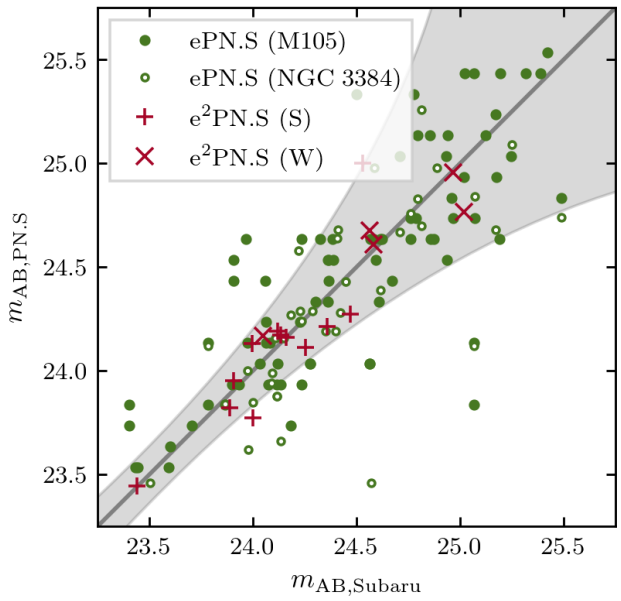

Figure 4.3: Comparison of magnitudes of PNe measured with Subaru's SuprimeCam and the PN.S. The colour coding is the same as in Fig. 4.1 and the grey shaded region indicates the photometric error of our SuprimeCam observations.

of our PN surveys: M105 and NGC 3384.

4.3.1 M105

M105 has been the target of numerous photometric studies. The light distribution of M105 was first analytically described by de Vaucouleurs (1948), and it was one of the galaxies that were used to define the de Vaucouleurs law (see also de Vaucouleurs & Capaccioli 1979). We use the relation determined by Capaccioli et al. (1990) based on B-band imaging:

$$\mu_{\mathrm{M105}}(r_{\mathrm{M105}}) = 3.0083 r_{\mathrm{M105}}^{1/4} + 14.076, \tag{4.3}$$

where r_{M105} is major-axis radius measured from the centre of M105. They furthermore determined the mean ellipticity to be $\epsilon_{\mathrm{M105}} = 0.111 \pm 0.005$ and the mean position angle to be $PA = 70\overset{\circ}{.}0 \pm 1\overset{\circ}{.}0$. These parameters are summarised in Table 4.1 and the corresponding profiles as a function of radius are shown in Fig. 4.4a.

4.3.2 NGC 3384

For completeness, we also briefly discuss the photometric properties of M105's closest neighbouring galaxy, NGC 3384, whose isophotes overlap with those of M105. As NGC 3384 is an S0 galaxy viewed edge-on, its light can be decomposed into a contribution from its bulge (spheroid) and a contribution from its disk. Cortesi et al. (2013b) carried out a photometric disk-spheroid decomposition with GALFIT (Peng et al. 2010) based on Two Micron All Sky Survey (2MASS) K-band images (Skrutskie et al. 2006). They found that the spheroid's light distribution is best described by a Sérsic profile

$$\Sigma_{\mathrm{spheroid}}(r_{3384}) = \Sigma_{\mathrm{e}} \exp\left(-\kappa\left(\left(\frac{r_{3384}}{r_{\mathrm{e}}}\right)^{1/n} - 1\right)\right), \tag{4.4}$$

with $\Sigma_{\mathrm{e}} = 4.09 \times 10^{-7}$, $n = 4$, $\kappa = 7.67$, $r_{\mathrm{e}} = 15\overset{''}{.}2$, ellipticity $\epsilon_{\mathrm{spheroid}} = 0.17$, and position angle $PA_{\mathrm{spheroid}} = 60\overset{\circ}{.}51$. The disk's light distribution is described by

$$\Sigma_{\mathrm{disk}}(r_{3384}) = \Sigma_{\mathrm{d}} \exp\left(-\frac{r_{3384}}{r_{\mathrm{d}}}\right), \tag{4.5}$$

with $\Sigma_{\mathrm{d}} = 5.01 \times 10^{-8}$, $r_{\mathrm{d}} = 63\overset{''}{.}73$, $\epsilon_{\mathrm{disk}} = 0.66$, inclination $i = 70^{\circ}$, and $PA = 52\overset{\circ}{.}5$. These parameters are summarised in Table 4.1.

4.3.3 A holistic view from a deep, extended multi-band survey

As the photometric data described above have been taken at different telescopes and through different filters, we needed to bring the to the same zero-point before using them jointly. We therefore used the deep wide-field data, encompassing both galaxies, and resulting SB profiles from Watkins et al. (2014). We determined a colour correction of

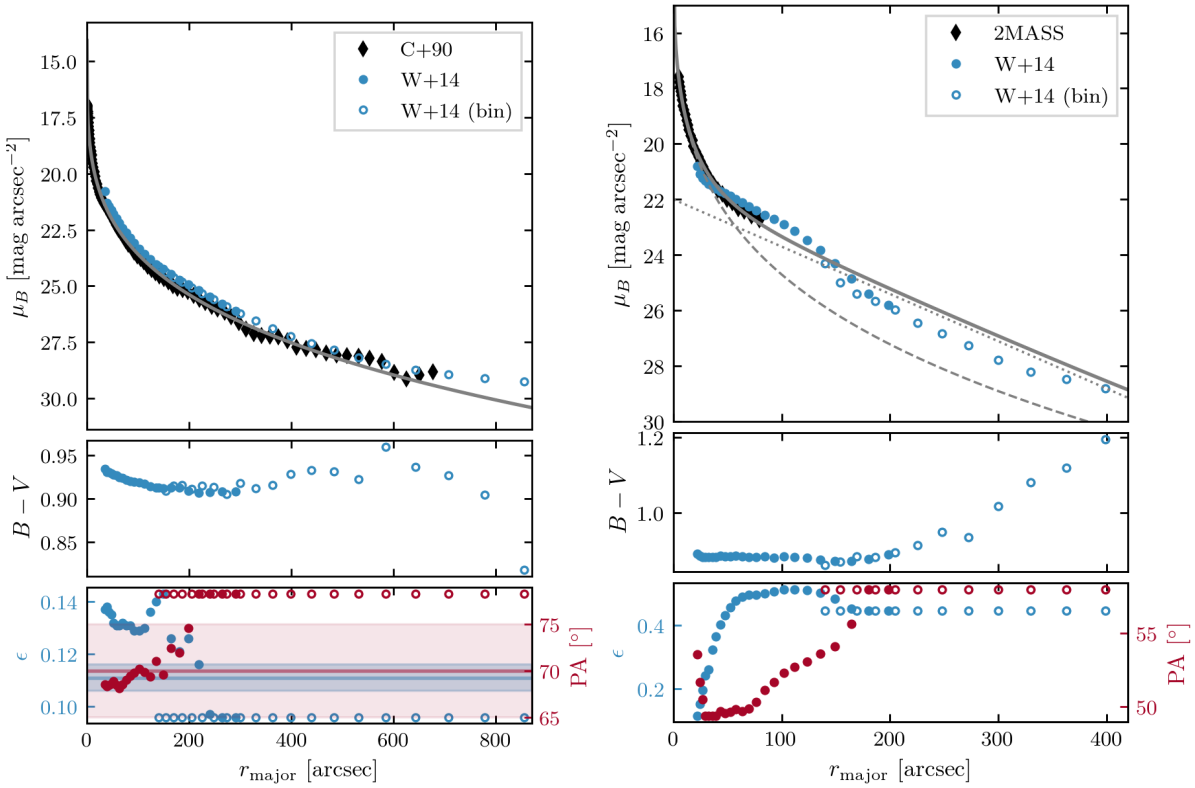

(a) M105 (b) NGC 3384

Figure 4.4: Broad-band photometry of the galaxies in the Leo I Group from Watkins et al. (2014, W14). The top panel shows the B-band surface brightness profile, the middle panel shows the $B-V$ colour profile, and the bottom panel shows the ellipticity (blue) and position angle (red), all as a function of major-axis radius. Open circles denote quantities measured on the 9×9 binned image. Panel (a) also shows the data from Capaccioli et al. (1990, black diamonds) and their best-fit de Vaucouleurs profile (grey line) in the top figure, their mean ellipticity and position angle are indicated by shaded bands in the bottom figure. In panel (b) the colour-corrected 2MASS profile Skrutskie et al. (2006, black diamonds) and the corresponding disk-spheroid decomposition (dotted, dashed, and solid grey lines) by Cortesi et al. (2013b) are shown in the top figure.

$B - K = -3.75$ for the profiles derived from the 2MASS data by Cortesi et al. (2013b). We furthermore determined a shift of -0.36 mag between the B-band profiles derived from Watkins et al. (2014) and Capaccioli et al. (1990) and corrected for it accordingly. The colour-corrected B-band SB profiles are shown in Figure 4.4.

Having a closer look at Fig. 4.4a, we note a flattening of the deep extended SB profile of M105 as observed by Watkins et al. (2014, blue circles) with respect to the analytic de Vaucouleurs profile fit by Capaccioli et al. (1990) at large radii, starting at approximately $750''$. We return to the implications of this observation in Sect. 4.4.2.

4.4 The radial PN number density profile and the luminosity-specific PN number

The connection between a PN population and the parent stars is given by the luminosity-specific PN number, α-parameter for short, that relates the total number of PNe $N_{\rm PN}$ to the total bolometric luminosity $L_{\rm bol}$ of the parent stellar population:

$$N_{\rm PN} = \alpha L_{\rm bol}. \tag{4.6}$$

The relation of the α-parameter with the underlying stellar population from the standpoint of single stellar populations (SSPs) has already been extensively discussed in Chapters 1.4.3 and 2.4. We therefore refrain from further discussing it here and continue directly with its determination.

4.4.1 The radial PN number density profile of M105

In the following sections, we only considered PNe from the photometric catalogue, as we have robust estimates on the catalogues spatial and photometric completeness. Furthermore, in order to limit the contamination from PNe associated with the S0 galaxy NGC 3384, we only considered PNe that are geometrically clearly associated with M105. As illustrated in Fig. 4.5, we defined two dividing lines (shown in blue), both enclosing 110° from M105's negative major axis and only considered PNe that lie to the west of these lines (selected PNe are highlighted in blue).

In total, 101 PN were selected for further analysis and were then binned into 8 elliptical bins (grey ellipses in Fig. 4.5), whose geometry is defined by the isophotal parameters of M105 as summarised in Table 4.1. The bin spacing was chosen such that each bin contains at least 12 PNe. In each bin, we determined the completeness-corrected number of PNe

$$N_{\rm PN,corr}(r) = \frac{N_{\rm PN,obs}(r) \cdot (1 - f_{\rm Ly\alpha})}{c_{\rm s}(r) c_{\rm c}}, \tag{4.7}$$

where $c_{\rm s}$ and $c_{\rm c}$ denote the spatial and colour incompleteness, as detailed in Appendix 4.A.5 and $f_{\rm Ly\alpha} = 24.9 \pm 5.0\%$ is the luminosity averaged expected fraction of Ly-α emitters at redshift $z = 3.1$ (see Appendix 4.A.6). The spatial completeness varies with radius

Table 4.1: Properties of M105 and NGC 3384 based on broad-band photometry.

Parameter	Symbol	Value	Ref.
	M105		
Distance[(a)]	$D_{\rm M105}$	10.3 Mpc	1
Effective radius	$r_{\rm e,M105}$	$54\farcs8 \pm 3\farcs5$	2
Mean ellipticity	$\epsilon_{\rm M105}$	0.111 ± 0.005	2
Mean position angle	$PA_{\rm M105}$	$70^\circ \pm 1^\circ$	2
Mean colour	$(B-V)_{\rm M105}$	0.92 mag	3
Sérsic index	n	4	2
	NGC 3384		
Distance	D_{3384}	11.3 Mpc	1
Mean colour	$(B-V)_{3384}$	0.88 mag	3
		Spheroid	
Sérsic index	n	4	4
Effective radius	$r_{\rm e}$	$15\farcs2$	4
Mean ellipticity	$\epsilon_{\rm spheroid}$	0.17	4
Mean position angle	$PA_{\rm spheroid}$	$60\fdg51$	4
		Disk	
Disk radius	$r_{\rm d}$	$63\farcs73$	4
Mean ellipticity	$\epsilon_{\rm disk}$	0.66	4
Mean position angle	$PA_{\rm disk}$	$52\fdg5$	4
Inclination	i	70°	4

References: (1) Tonry et al. (2001); (2) Capaccioli et al. (1990); (3) Watkins et al. (2014); (4) Cortesi et al. (2013b).

Notes: (a) This distance corresponds to a distance modulus of $\mu_{\rm SBF} = 30.049$, which is in excellent agreement with the distance determined from TRGB magnitudes by Lee & Jang (2016) that is $\mu_{\rm TRGB} = 30.05 \pm 0.02$ (random) $\pm\, 0.12$ (systematic).

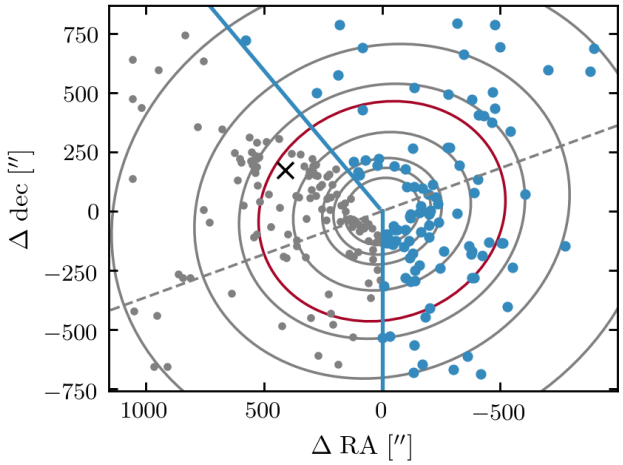

Figure 4.5: On-sky PN distribution for the PN density and PNLF calculation in M105. Only PNe from the photometric survey care considered. The PN density of M105 is calculated in 8 elliptical bins denoted in grey. In order to limit the contamination from NGC 3384, only PNe west of the blue lines are considered (see text). The dashed line indicates M105's photometric major axis. The red contour corresponds to the vertical dashed line in Fig. 4.6. The black cross denotes the centre of NGC 3384. North is up, East is to the left.

and ranges from 77% to 98% and the average colour completeness of our field is 87%. The observed number of PNe $N_{\rm PN,obs}$ is determined within the limiting magnitude of $m_{5007,\rm lim} = 28.1$, the number density profile thus spans a magnitude range of $\Delta m = 2.4$ mag from the bright cut-off.

The PN logarithmic number density profile is then

$$\mu_{\rm PN}(r) = -2.5 \log_{10} \left(\frac{N_{\rm PN,corr}(r)}{A(r)} \right) + \mu_0, \tag{4.8}$$

where $A(r)$ is the area of intersection of the elliptical annulus with the field of view (FOV) of the observation. The FOV corresponds to the dimensions of Fig. 4.5. From the offset μ_0 to the observed stellar SB profile, the α-parameter can be determined.

The PN number density profile shown in Fig. 4.6 was matched to the B-band surface brightness profile from Watkins et al. (2014). Within $\sim 530''(\approx 10 r_{\rm e})$ from the centre of M105, PN number density and stellar SB agree very well with each other, but beyond this transition radius the PN number density profile significantly flattens with respect to the stellar SB profile. We note that the flattening occurs nearly $250''$ further inward compared to the flattening of the SB profile that is observed beyond $\sim 750''$. As already discussed in Chapter 2 of this thesis, as well as in Longobardi et al. (2013, 2015a), we do not expect the flattening to be due to contaminants such as Ly-α-emitting galaxies, as their contribution is statistically subtracted. The origin of the flattening of the PN number density is investigated in the following.

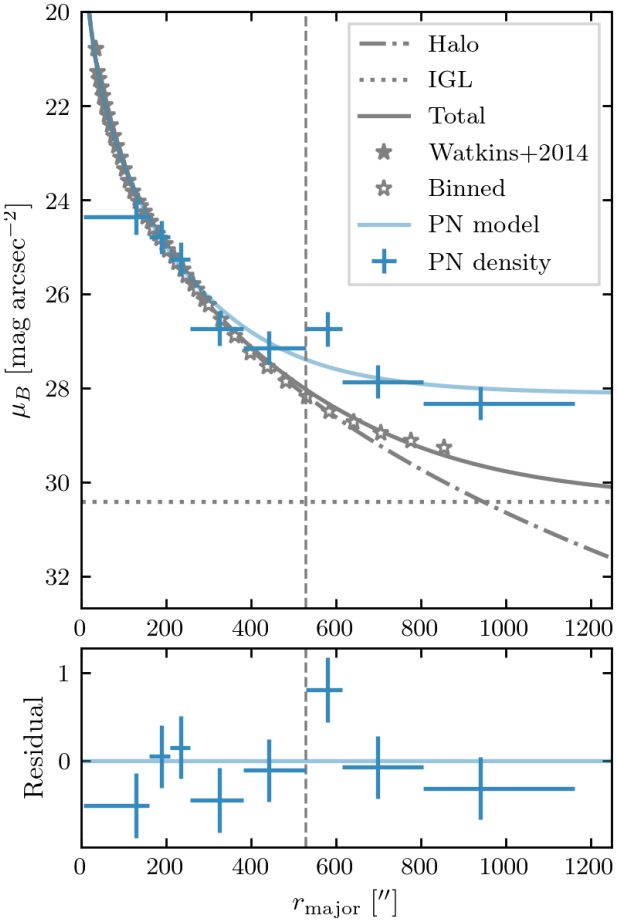

Figure 4.6: PN number density profile calculated from the PN sample defined in Fig. 4.5 (101 PNe) as function of major-axis radius (blue error bars) compared to the B-band SB profile (gray stars, Watkins et al. 2014). The stellar SB profile (solid grey line) can be approximated by a halo-component following a de Vaucouleurs law (dash-dotted grey line) and a constant IGL component (dotted grey line). The best-fit model for the PN number density is denoted by the blue solid line. The bottom panel shows its residuals. In both panels the vertical line denotes the transition from the inner PN-scarce to the outer PN-rich halo based on the change in the PN number density slope.

4.4.2 A two-component photometric model for the extended halo of M105

Similar to our findings regarding the PN number density profile of M49 in the Virgo Cluster (Chapter 2), the flattening of the PN number density profile at large radii might be due to the presence of a diffuse outer component. The presence of a second component, be it an additional component of the extended halo or in the form of diffuse IGL, is corroborated by the flattening of the stellar SB profile observed by Watkins et al. (2014).

We therefore again constructed a two-component photometric model to reproduce the flattening at large radii. In this case, the stellar light of the inner halo was modelled with a de Vaucouleurs profile as fitted by Capaccioli et al. (1990) and for simplicity, the outer component was approximated by a constant flat SB profile. The value of this component was determined from the mean differential SB between the last measured values of the flattened stellar profile (Watkins et al. 2014) and the extrapolated de Vaucouleurs fit at these radii ($530'' \leq r_{\rm major} < 900''$). We determined it to be $\mu_{\rm outer} = 30.40 \pm 0.15$ mag arcsec^{-2}. This value is a lower limit on the SB of the IGL – if it was increasing inwards as for example found in the Virgo Cluster (Longobardi et al. 2015a), the contribution of the IGL could be larger at smaller radii. The resulting composite stellar SB profile reproduces the flattening present in the data by Watkins et al. (2014) and is denoted by the solid grey line in Fig. 4.6.

However, while this model reproduces the flattening of the stellar SB well, it would not resolve the discrepancy between the observed PN number density and stellar SB profiles at large radii beyond $530''$. In order to do so, another assumption is needed, namely that the two components have different α-parameters (Longobardi et al. 2013). The photometric model for the predicted PN surface density is thus similar to the one presented in Chapter 2 (eqs. (2.11 - 2.12)):

$$\begin{aligned}\tilde{\Sigma}(r) &= (\alpha_{\Delta m,\rm inner} I_{\rm inner,bol}(r) + \alpha_{\Delta m,\rm outer} I_{\rm outer,bol}(r)) s^2 \\ &= \alpha_{\Delta m,\rm inner} \left(I_{\rm inner,bol}(r) + \left(\frac{\alpha_{\Delta m,\rm outer}}{\alpha_{\Delta \rm m,inner}} - 1 \right) I_{\Delta \rm m,outer,bol}(r) \right) s^2. \end{aligned} \tag{4.9}$$

Again, the two components $I_{\rm inner,bol}(r)$ and $I_{\rm outer,bol}(r)$ are the bolometric SB profiles weighted by the α-parameters of the respective populations and $s = D/206265$ is a scale factor related to the galaxy's distance D.

The bolometric SB profiles $I_{\rm bol}$ were obtained from the observed SB profiles μ:

$$I = 10^{-0.4(\mathrm{BC}_B - \mathrm{BC}_\odot)} 10^{-0.4(\mu - K)}, \tag{4.10}$$

with the solar bolometric correction $\mathrm{BC}_\odot = -0.69$, and $K = 26.98\,\mathrm{mag\,arcsec^{-2}}$ is the B-band conversion factor to physical units $L_\odot\,\mathrm{pc}^{-2}$. While one can assume a fixed value of $\mathrm{BC}_V = -0.85$ with 10% accuracy based on the study of stellar population models for different galaxy types, the bolometric correction in the B-band depends on galaxy colour (Buzzoni et al. 2006):

$$\mathrm{BC}_B = \mathrm{BC}_V - (B - V)_{\rm gal}. \tag{4.11}$$

Assuming a colour of $B-V=0.92$ (cf. middle panel of Fig. 4.4a), we used a value of $\mathrm{BC}_B=-1.76$.

Instead of fitting α_{inner} and α_{outer} simultaneously, we first determined the well-constrained α-parameter of the inner component from its offset to the stellar SB profile, which we find to be $\mu_0=16.5\pm0.2$ mag arcsec^{-2}. Applying the bolometric correction as defined in eq. (4.11), this offset translates to an α-parameter of $\alpha_{2.4,\mathrm{inner}}=(1.02\pm0.21)\times10^{-8}$ PN L_{bol}^{-1}.

We then determined the α-parameter of the outer component by fitting the two-component model defined in eq. (4.9) to the observed PN number density profile. We fitted the ratio of the two α-parameters $\alpha_{\mathrm{inner}}/\alpha_{\mathrm{outer}}=9.10\pm2.2$, which is the only free parameter. The resulting best-fit model is denoted by the blue line in Fig. 4.6.

In the literature, α-parameters are commonly stated for a magnitude interval of $\Delta m=2.5$ mag. We therefore extrapolate the previously calculated $\alpha_{2.4}$-parameters using the standard Ciardullo PNLF with a slope of $c_2=0.307$ and determine

- $\alpha_{2.5,\mathrm{inner}}=(1.08\pm0.22)\times10^{-8}$ PN L_{bol}^{-1} for the inner component, and
- $\alpha_{2.5,\mathrm{outer}}=(9.87\pm2.38)\times10^{-8}$ PN L_{bol}^{-1} for the outer component.

The α-parameter value for the outer component may be correlated with a radial gradient of the IGL SB profile. Hence the value quoted above represents an upper limit to the α value for the outer component. The stark – nearly order-of-magnitude – increase of the α-parameter from the inner to the outer halo is suggestive of a change of the parent stellar population with radius. As discussed in Chapters 2 and 3, in the case of M49 the increase of the α-parameter was one of many indicators signalling the presence of an extended population of PNe associated with the IGL.

The α-colour relation

In Chapter 2, we for the first time continuously evaluated a galaxy's α-parameter as function of radius and colour by combining the PN number density profile with the colour information from broadband photometric studies. In order to continuously evaluate M105's $B-V$ colour profile, we fit a cubic spline to the colour data from Watkins et al. (2014, see also middle panel Fig. 4.4a). The bluer colour at large radii is in line with a more metal-poor population identified by Lee & Jang (2016).

In order to assess the variation of the α-parameter as a function of major-axis radius, we determined the offset between the modelled PN number density profile and the two-component stellar SB profile. Figure 4.7 shows the resulting curve as a function of galaxy colour. In order to directly compare with the α-parameter values of Local Group (LG) galaxies and ETGs presented in Buzzoni et al. (2006), we scale our α-parameters from $\alpha_{2.5}$ to α_8 assuming a standard Ciardullo et al. (1989) PNLF. We find that the α-parameter in the inner halo agrees well with that quoted in Buzzoni et al. (2006), determined by Romanowsky et al. (2003) and labelled with a blue cross. We again find that the α-parameter is lowest in the inner, red halo and then increases with decreasing (i.e. bluer) galaxy colour and increasing distance from the galaxy centre. Compared to the α-colour

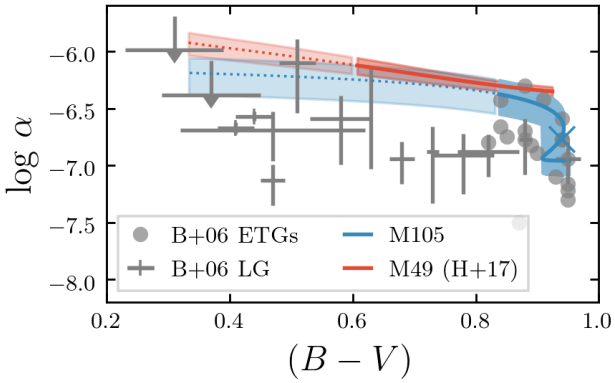

Figure 4.7: Variation of the α-parameter in M105 with $B-V$ colour (dark blue line, colour data from Watkins et al. 2014) compared to data from previous PN surveys in Local Group galaxies (grey error bars) and ETGs (grey circles) based on Buzzoni et al. (2006) and references therein. The dashed blue line and light blue band denotes data exceeding the radial range of colours measured by Watkins et al. (2014); in this range colours were extrapolated based on the cubic spline fit. The blue cross denotes the datapoint for M105 from Buzzoni et al. (2006). For comparison, we also show the α-colour relation for M49 (orange).

relation that we determined for M49 shown in orange, there is a much stronger increase of the α-parameter from $B-V \approx 1$ to $B-V \approx 0.8$, while for very blue colours the α-parameters of both galaxies asymptote towards similar values.

4.5 The planetary nebula luminosity function of M105

Besides of the PN number density profile, the PNLF is an important characteristic of a PN sample. One physical parameter, the bright cut-off, is an important secondary distance indicator. In this section, however, we will focus on the variation of the faint-end PNLF slope, as there has been empirical evidence for a variation of PNLF slope with stellar population properties (Ciardullo et al. 2004; Ciardullo 2010; Longobardi et al. 2013, 2015a, Chapter 2). We therefore compared the observed PNLF to the generalised analytical formula introduced by Longobardi et al. (2013):

$$N(M) = c_1 \mathrm{e}^{c_2 M}(1 - \mathrm{e}^{3(M^\star - M)}) \tag{4.12}$$

In the equation above, c_2 is the sought after faint-end slope and c_1 is a normalisation factor.

We calculated the PNLF from the same sample that was used to determine the PN number density profile in order to limit contamination from PN associated with NGC 3384 (see Fig. 4.5). The left panel of Fig. 4.8 shows the corresponding observed (gray error bars) and completeness-corrected PNLFs (blue error bars) as well as the estimated contribution from Ly-α emitting galaxies (red solid line) and its expected 20% variation (red shaded

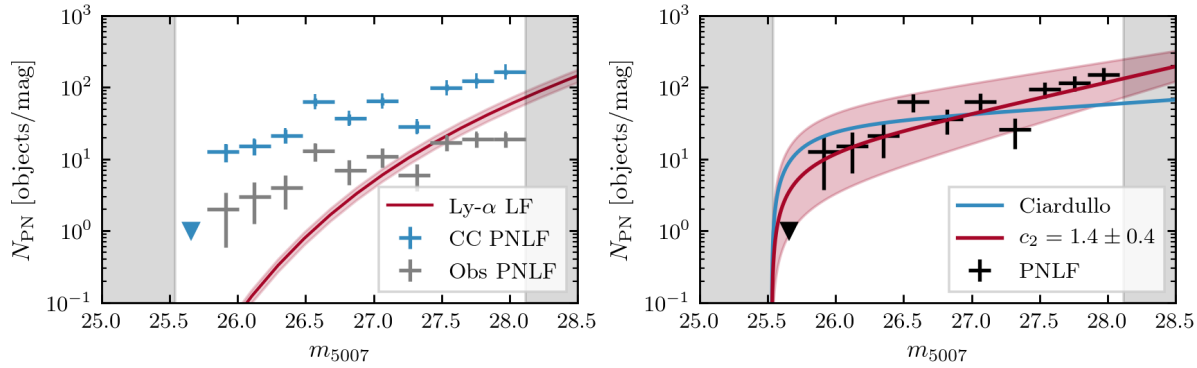

Figure 4.8: PNLF in M105. *Left:* Observed PNLF (gray errorbars) and PNLF of the completeness-corrected (CC) sample as defined in Fig. 4.5 (101 PNe) without accounting for contamination by Ly-α emitting background galaxies (blue error bars). Triangles denote upper limits. The solid red line shows the Ly-α LF and its variance due to density fluctuations indicated by the shaded regions (Gronwall et al. 2007). *Right:* PNLF of the completeness-corrected PN sample after statistical subtraction of the Ly-α LF (black error bars). Triangles denote upper limits. The solid blue curve denotes the standard Ciardullo PNLF with $c_2 = 0.307$. The red line and shaded region denote our best-fit PNLF with $c_2 = 1.5 \pm 0.4$ In both panels, magnitudes fainter than the limiting magnitude and brighter than the bright cut-off are shaded in gray.

region Gronwall et al. 2007). The completeness-corrected number of PNe in our survey is larger than the estimated number of Ly-α contaminants in every magnitude bin.

After statistically subtracting the estimated number of contaminants, we obtained the PNLF shown in the right panel of Fig. 4.8. The black error bars denote the magnitude bin width and the expected errors due to counting statistics and the uncertainty of the Ly-α luminosity function (LF). For the brightest magnitude bin, the completeness-corrected number of PNe is smaller than one – we therefore only show an upper limit.

A standard Ciardullo PNLF with a fixed $c_2 = 0.307$, as indicated by the solid blue line, is not a good representation of the data as it overestimates the number of bright PNe and underestimates the amount of faint PNe. We therefore fit the generalised PNLF as defined in eq. (4.12) to the observed PNLF. Given that the distance to M105 is well determined from surface-brightness fluctuation (SBF) measurements, $D = 10.3$ Mpc (Tonry et al. 2001), the only free parameters are the normalisation c_1 and the faint-end slope that we determine to be $c_2 = 1.5 \pm 0.4$. The resulting analytic PNLF (denoted by the red line in the right panel of Fig. 4.8) reproduces the behaviour of the observed PNLF well. A PNLF with a steeper slope compared to M31 (Ciardullo et al. 1989) is clearly favoured.

4.5.1 PNLF variation with radius

Motivated by the evidence of two different PN populations in the inner and outer halo based on the PN number density profile and the inferred α-parameters in Sect. 4.4, we

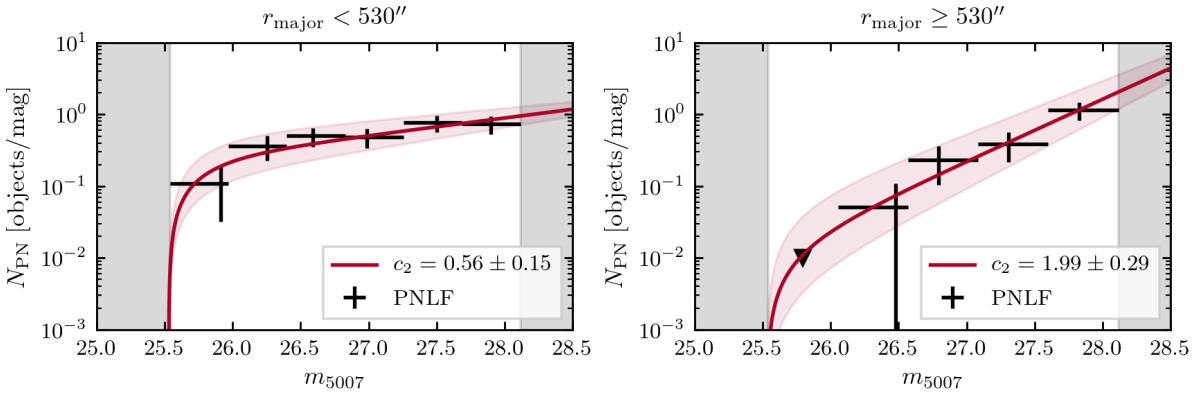

Figure 4.9: Radial variation of the PNLF in M105. *Left*: Observed PNLF in the inner halo (black error bars) and best-fit generalised PNLF with $c_2 = 0.56 \pm 0.15$ (red line and shaded region). *Right*: Observed PNLF in the outer halo (black error bars) and best-fit generalised PNLF with $c_2 = 1.99 \pm 0.29$ (red line and shaded region).

investigated whether this difference also manifests itself in the PNLF morphology. We therefore divided our sample into two concentric elliptical bins and calculated the PNLF for each sample individually. The dividing major-axis radius of $530''$ is indicated as the red ellipse in Fig. 4.5 and by the dashed vertical line in Fig. 4.6.

The *inner sample* is characterised by a density profile that decreases steeply with radius and contains 63 PNe. Its PNLF is shown in the left panel of Fig. 4.9. A fit of the generalised PNLF (solid red line and shaded region) results in a value of $c_2 = 0.56 \pm 0.15$, which is shallower than the slope of the total PN sample. The *outer sample* is characterised by a flattened density profile and contains 38 PNe. Its PNLF is shown in the right panel of Fig. 4.9. A fit of the generalised PNLF (solid red line and shaded region) results in a slope of $c_2 = 1.99 \pm 0.29$, which is steeper than the slope of the total and inner PN samples.

This steeper PNLF in the outer sample can be interpreted as an overabundance of faint PNe with respect to the inner sample, which may be the driving factor behind the flattening of the observed PN number density profile at large radii. Given that M105's halo only shows a slight colour gradient (Watkins et al. 2014), it is difficult to assess whether the increased PNLF slope of the outer sample is correlated with a change of the underlying stellar population. If at all, we may relate the change in PNLF morphology with the higher abundance of old and metal-poor stars in the outer halo observed by Lee & Jang (2016): in the inner halo ($240'' < R < 360''$) the fraction of metal-poor stars [Fe/H]< -0.7 is $\sim 27\%$, while in the outer halo ($540'' < R < 780''$) it increases to $\sim 41\%$.

4.6 Photo-kinematic decomposition of M105 and NGC 3394

The PN kinematics can contribute important indications of the dynamical status of the halo of M105. However, due to the proximity of M105 and NGC 3384 both in position and velocity space, we cannot immediately assign PN to either one of the two galaxies in the regions of overlap. In order to decompose the kinematic PN sample into subcomponents associated to M105 and NGC 3384, we model the observed PN in position-velocity space using a luminosity-weighted Gaussian-mixture model (GMM). GMMs are widespread in the astronomical literature to disentangle multi-component line-of-sight velocity distributions (LOSVDs) (see e.g. Walker & Peñarrubia 2011; Amorisco & Evans 2012; Watkins et al. 2013; Agnello et al. 2014; Hartke et al. 2018, Chapter 3 of this thesis).

4.6.1 Disk-spheroid decomposition of NGC 3384

In order to model the kinematics of NGC 3384, we used the disk-spheroid decomposition method developed by Cortesi et al. (2011) and subsequently applied to the PN.S survey of S0 galaxy kinematics (Cortesi et al. 2013b), including the decomposition of NGC 3384 into its disk and spheroid components.

The LOS velocity of the disk as function of azimuthal angle ϕ_{3384} and major-axis radius r_{3384} measured with respect to the centre of NGC 3384 can be expressed as

$$v_{\rm LOS}(r_{3384}, \phi_{3384}; V) = v_{\rm sys,3384} + V \sin(i) \cos(\phi_{3384}), \tag{4.13}$$

where V is the galaxy's mean rotation velocity, i the inclination at which the disk is observed, and $v_{\rm sys,3384} = 722 \pm 9$ km s^{-1} (Pulsoni et al. 2017) its systemic velocity. The corresponding velocity dispersion is

$$\begin{aligned}\sigma^2_{\rm LOS}(r_{3384}, \phi_{3384}; V, \sigma_r, \sigma_{\phi_{3384}}) = \sigma_r^2 \sin^2(i) \sin^2(\phi_{3384}) + \\ + \sigma^2_{\phi_{3384}} \sin^2(i) \cos^2(\phi_{3384}) + \sigma_z^2 \cos^2(i),\end{aligned} \tag{4.14}$$

where σ_r, σ_ϕ, and σ_z are its components in cylindrical coordinates. In edge-on galaxies the contribution along the z-axis is small and in the following the term $\sigma_z^2 \cos^2(i)$ will therefore be dropped. Assuming a Gaussian LOSVD, the contribution of the disk kinematics of a PN k with observed LOS velocity v_k can be described as

$$\mathcal{V}_{\rm disk}(v_k, r_{3384,k}, \phi_{3384,k}; V, \sigma_r, \sigma_\phi) = \frac{1}{\sqrt{2\pi}\sigma_{\rm LOS}} \exp\left(-\frac{(v_k - v_{\rm LOS})^2}{2\sigma^2_{\rm LOS}}\right). \tag{4.15}$$

Following Cortesi et al. (2011, 2013b), we can reduce the parameter space by using the epicycle approximation that holds for disk galaxies with approximately flat rotation curves (see e.g. Binney & Tremaine 1987) and links the radial velocity dispersion with the tangential one: $\sigma_\phi = \sigma_r/\sqrt{2}$.

The contribution from the spheroid is described as a Gaussian centred on the systemic velocity of NGC 3384 with velocity dispersion $\sigma_{\rm sph}$:

$$\mathcal{V}_{\rm spheroid}(v_k, r_{3384,k}, \phi_{3384,k}; \sigma_{\rm sph}) = \frac{1}{\sqrt{2\pi}\sigma_{\rm sph}} \exp\left(\frac{(v_k - v_{\rm sys,3384})^2}{2\sigma^2_{\rm sph}}\right). \tag{4.16}$$

The two kinematic components of the LOSVD of NGC 3384 were weighted by the SB profiles as will be futher detailed in in Sect. 4.6.3.

4.6.2 Kinematic model of M105

We describe M105's contribution to the LOSVD with a single Gaussian centred on the galaxy's systemic velocity $v_{\rm sys,M105} = 934 \pm 17$ km s^{-1} (Pulsoni et al. 2017) and with velocity dispersion $\sigma_{\rm M105}$:

$$\mathcal{V}_{\rm M105}(v_k, r_{\rm M105,k}; \sigma_{\rm M105}) = \frac{1}{\sqrt{2\pi}\sigma_{\rm M105}} \exp\left(-\frac{(v_k - v_{\rm sys,M105})^2}{2\sigma^2_{\rm M105}}\right). \tag{4.17}$$

For simplicity, we modelled M105 with a single parameter for the LOS velocity dispersion. However, in order to take into account the strong decrease of the radial LOS velocity dispersion that was observed by Romanowsky et al. (2003) a future model may allow for a radial variation of $\sigma_{\rm M105}$.

4.6.3 Priors on galaxy membership from broad-band photometry

We described the photometric surveys of NGC 3384 and M105 in Sect. 4.3. Our model will be weighted with the following three SB profiles:

- The light distribution of M105 is modelled with a deVaucoleurs profile $\Sigma_{\rm M105}(r_{\rm M105}) \propto \exp\left(-r^{1/4}\right)$.
- NGC 3384's disk SB distribution is a simple exponential disk: $\Sigma_{\rm disk}(r_{\rm disk}) \propto \exp\left(-r\right)$,
- and NGC 3384's bulge also follows a de Vaucouleurs profile as Cortesi et al. (2013b) determine a Sérsic index of $n = 4$: $\Sigma_{\rm spheroid}(r_{\rm spheroid}) \propto \exp\left(-r^{1/4}\right)$.

Taking into account the variation of PN-specific frequency α for different stellar populations

Since the number of PNe per unit light has been shown to slightly vary with galaxy type (Buzzoni et al. 2006; Hartke et al. 2017, Chapter 2), we need to take this into account when using SB profiles derived from integrated starlight as weights for our kinematic model. As the e^{2}PN.S survey is shallower than the SuprimeCam photometry and has a different spatial coverage, we re-calculated the α-parameters directly from e^{2}PN.S survey.

We determined the α-parameter of each galaxy by comparing its stellar SB profile with the PN-number density profile. In order to estimate the α-parameters of M105 and NGC 3384, we first used the priors on galaxy membership from the broad-band photometry described in Sect. 4.6.3 to select samples of PNe centred on M105 and NGC 3384 for which the contamination of the respective other galaxy is less than 10% based on the galaxy light distribution. We then calculated the PN-number density for each sample within one magnitude[5] from the respective PNLF bright cut-off. We used a magnitude-limited sample in order to reduce potential inhomogeneous effects due to survey incompleteness at fainter magnitudes. Due to the strong contribution from galaxy light in the spheroid region of NGC 3384 we cannot fit separate α-parameters for disk and spheroid, but assume $\alpha_{3384} = \alpha_{\rm disk} = \alpha_{\rm sph}$. This assumption was also made by Cortesi et al. (2013b).

We determined the following α-parameters

- $\alpha_{1,\rm M105} = (6.41 \pm 1.41) \times 10^{-9}$ PN $L_{\rm bol}^{-1}$ for M105 and
- $\alpha_{1,3384} = (3.35 \pm 0.04) \times 10^{-9}$ PN $L_{\rm bol}^{-1}$ for NGC 3384.

For convenience, we defined the parameter $\tilde{\alpha} = \alpha_{1,3384}/\alpha_{1,\rm M105}$. We also extrapolated the α-parameters from α_1 to $\alpha_{2.5}$ to facilitate the comparison with those determined in Sect. 4.4 and find

- $\alpha_{2.5,\rm M105} = (2.63 \pm 0.58) \times 10^{-8}$ PN $L_{\rm bol}^{-1}$ for M105 and
- $\alpha_{2.5,3384} = (1.38 \pm 0.02) \times 10^{-8}$ PN $L_{\rm bol}^{-1}$ for NGC 3384.

The α-parameter determined from the e^{2}PN.S survey is slightly higher than the one determined from the photometric sample. This discrepancy might be due to the different assessment of survey completeness for the photometric and kinematic surveys.

4.6.4 Likelihood analysis

The likelihood of a PN k with observed position RA, dec and velocity $v_k \pm \delta v_k$ can be expressed in terms of the velocity and SB distributions that we defined in the previous three sections. The model component weights are defined as follows:

$$w_{\rm sph} = \frac{\tilde{\alpha}\Sigma_{\rm sph}}{\tilde{\alpha}\Sigma_{\rm sph} + \tilde{\alpha}\Sigma_{\rm disk} + \Sigma_{\rm M105}}, \tag{4.18a}$$

$$w_{\rm disk} = \frac{\tilde{\alpha}\Sigma_{\rm disk}}{\tilde{\alpha}\Sigma_{\rm sph} + \tilde{\alpha}\Sigma_{\rm disk} + \Sigma_{\rm M105}}, \tag{4.18b}$$

$$w_{\rm M105} = \frac{\Sigma_{\rm M105}}{\tilde{\alpha}\Sigma_{\rm sph} + \tilde{\alpha}\Sigma_{\rm disk} + \Sigma_{\rm M105}}, \tag{4.18c}$$

[5]This magnitude limit is more conservative than the limiting magnitude of $m^\star + 1.5$ stated in Sect. 4.2. It was chosen because of a decline of the observed PNLF of NGC 3384 for magnitudes fainter than $m^\star + 1.0$.

where $\tilde{\alpha}$ is fixed to the value determined in the previous section and the SB profiles Σ are completely determined by the broad-band photometry as described in Sect. 4.6.3. The corresponding likelihood is then

$$\mathcal{L}_k = w_{\rm sph}\mathcal{V}_{\rm sph} + w_{\rm disk}\mathcal{V}_{\rm disk} + w_{\rm M105}\mathcal{V}_{\rm M105}. \tag{4.19}$$

The total likelihood is the product of the individual likelihoods that is calculated for each *individual* PN:

$$\mathcal{L}(RA, dec, v, \delta v; V, \sigma_r, \sigma_\phi, \sigma_{\rm sph}, \sigma_{\rm M105}) = \prod_{k=0}^{N} \mathcal{L}_k. \tag{4.20}$$

This method allows us to exploit the information of every PN without the explicit need for binning in velocity space. The model parameters are $V, \sigma_r, \sigma_{\rm sph}$, which describe the kinematics of NGC 3384, and $\sigma_{\rm M105}$. The resulting 4-dimensional parameter space was explored using the ensemble-based Markov chain Monte Carlo (MCMC) sampler EMCEE (Foreman-Mackey et al. 2013).

4.6.5 Best-fit model and decomposition

Figure 4.10 shows the joint posterior distributions of the model parameters. The best-fit parameters are stated on top of each histogram. We recover the spheroid velocity dispersion $\sigma_{\rm sph} = 135.84^{+12.53}_{-9.76}$ km s^{-1} and mean rotation velocity $V = 103.98^{+52.11}_{-54.17}$ km s^{-1}, which are in agreement with the model parameters of Cortesi et al. (2013b), while the coupled radial and azimuthal velocity dispersions of NGC 3384 are poorly constrained ($\sigma_r = 169.19^{+22.25}_{-44.40}$ km s^{-1}). The velocity dispersion of M105 is determined to be $\sigma_{\rm M105} = 125.89^{+7.27}_{-6.46}$ km s^{-1}, which is in line with previous measurements by Romanowsky et al. (2003), Douglas et al. (2007), and de Lorenzi et al. (2009).

After determining the best-fit model parameters, we evaluated the relative probability of each PNe to be associated with M105 or NGC 3384. Figure 4.11 shows the spatial distribution of PNe from the kinematic catalogue colour-coded by the relative probability to be associated with M105. PNe associated with M105 are denoted by blue colours and PNe associated with NGC 3384 are denoted by red colours. The association agrees well with the underlying light distribution: 193 PNe are associated with M105 with a probability greater than 90%. Similarly, 79 PNe are associated with NGC 3384. Only 30 PNe have relative probabilities between 10% and 90%. In the following, the relative membership probabilities will be used as weights to determine the line-of-sight velocity distribution (LOSVD) of M105.

4.7 Kinematic properties of the halo of M105

As the kinematics of the PNe in NGC 3384 are already well understood (Cortesi et al. 2013a,b), the following section will focus on the much-debated kinematics of M105. With

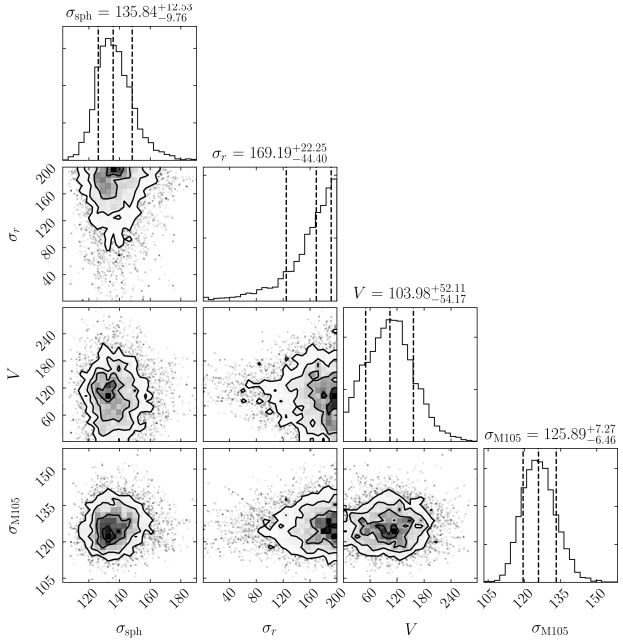

Figure 4.10: Corner plot of the joint posterior distributions of the model parameters. All parameters are in units of km s^{-1}. The best-fit parameters and their 1σ uncertainties are denoted on the top of each histogram and indicated by the vertical dashed lines.

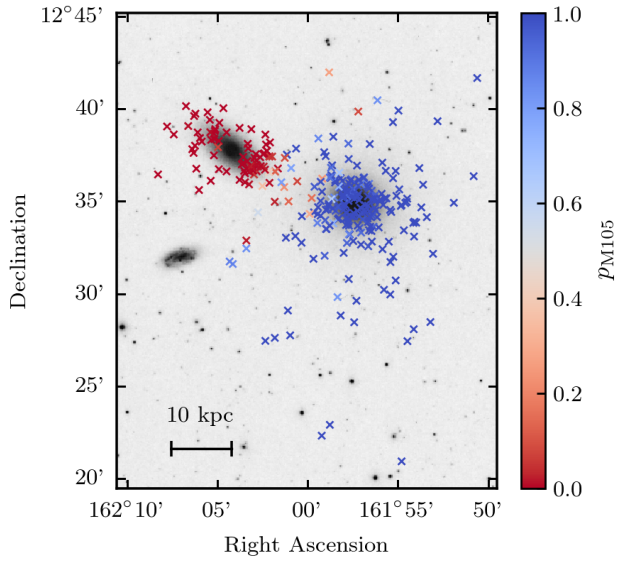

Figure 4.11: DSS image of M105 and NGC 3384 with PNe from the kinematic catalogue colour-coded by the relative probability to be associated with M105. The scale bar in the lower-left corner denotes 10 kpc. North is up, East is to the left.

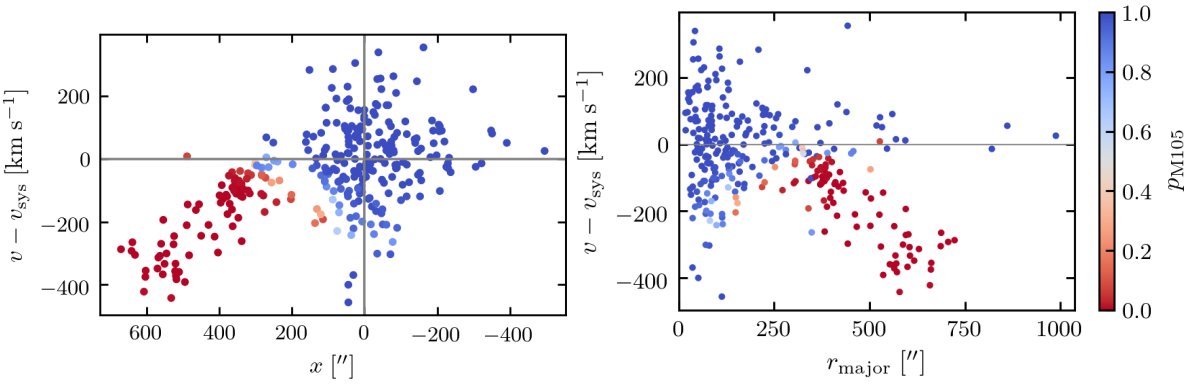

Figure 4.12: Position velocity phase-space of PNe in M105 and NGC 3384 colour coded by their relative probability to be associated with M105. *Left:* Phase-space along the axis connecting the centres of NGC 3394 and M105 centred on M105's position and systemic velocity (grey reticle). *Right:* Phase-space along M105's photometric major axis.

the data from Cortesi et al. (2013a) and Watkins et al. (2014), we are able to better constrain galaxy membership using the model described in Sect. 4.6. The additional coverage from our recent observational campaign with the PN.S extends the spatial coverage along the galaxy's minor axis by a factor of two.

Before we evaluated the LOSVD of M105, we first investigated the joint phase-space of M105 and NGC 3384 as seen through our photo-kinematic decomposition. Figure 4.12 shows the position-velocity phase-space of all PNe along the axis connecting the centres of NGC 3384 (left panel) and as function of the major-axis of M105 (right panel). In both panels, it can be seen that PNe associated with M105 and NGC 3384 occupy distinct regions in the diagram. The separation is clearest when the phase-space is visualised along the axis connecting the centres of the two galaxies. The more traditional phase-space, i.e. the LOS velocity as function of major-axis radius of M105 could not be unambiguously geometrically divided into regions with PNe solely associated with either M105 or NGC 3384.

4.7.1 Line-of-sight velocity distribution of PNe in M105

The LOSVD for one-dimensional velocity data is basically the phase-space presented above collapsed along the radial direction. As a first quality check of the model described in Sect. 4.6 we therefore calculated the LOSVD of all PNe in the kinematic catalogue. Figure 4.13 illustrates that the non-weighted LOSVD (grey histogram) clearly deviates from Gaussianity. When applying the relative membership probabilities as weights, the resulting distribution (hashed blue histogram) agrees well with the model LOSVD (red line and error bands) centred on M105's systemic velocity and with the best-fit velocity dispersion.

However, as we illustrated in Fig. 4.12, depending on the coordinate axis chosen, there may still be some ambiguity when deriving kinematic profiles as function of radius. For the following analysis, we therefore only considered PNe with relative membership probabilities larger than $p_{\rm M105} > 0.5$. The resulting LOSVD for this subsample is presented in

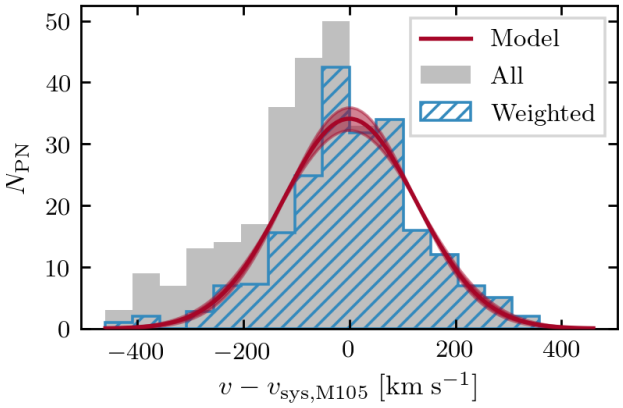

Figure 4.13: LOSVD of PNe in M105 and NGC 3384 (grey histogram). The hashed blue histogram has been weighted with the M105 relative membership probabilities. The red line denotes the model LOSVD determined in Sect. 4.6 and the shaded band the 1σ uncertainties.

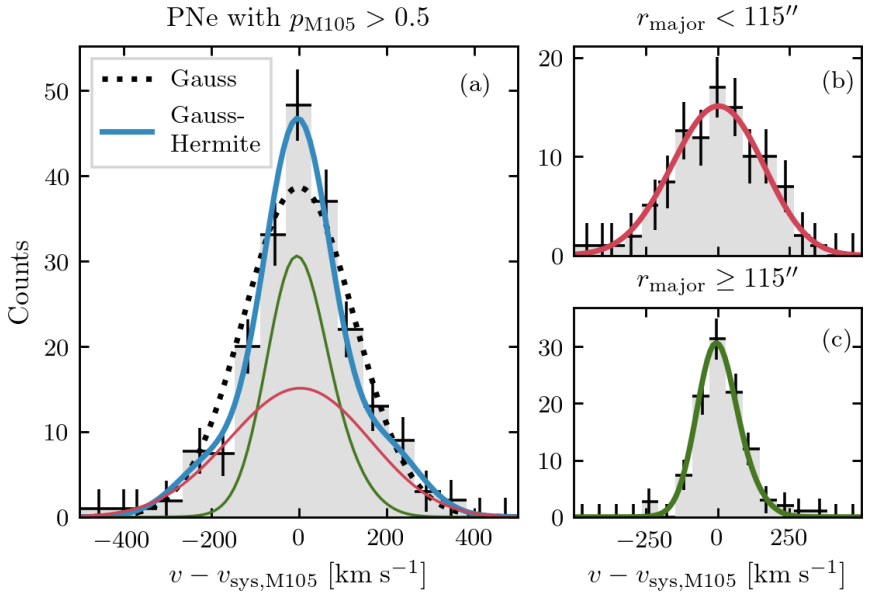

Figure 4.14: LOSVD of PNe in the halo of M105. *Panel (a):* histogram of LOS velocities for PNe in M105 (grey) with Gauss (black dotted line) and Gauss-Hermite (blue line) profiles fitted to the data. The thin orange and green lines correspond to the best-fit Gauss-Hermite profiles fit to the data displayed in panels (b) and (c). *Panel (b):* histogram of LOS velocities of PNe within a major-axis distance of 113″ (gray). The orange line denotes the best-fit Gauss-Hermite profile that is also shown in panel (a). *Panel (c)*: histogram of LOS velocities of PNe beyond a major-axis distance of 113″ (gray). The green line denotes the best-fit Gauss-Hermite profile that is also shown in panel (a).

Fig. 4.14(a). The model Gaussian (dotted black line) that was also shown in Fig. 4.13 is a good first approximation of the observed LOSVD, however, it underestimates the core of the distribution and overfits its wings. We therefore re-fitted the observed LOSVD in terms of Gauss-Hermite polynomials (van der Marel & Franx 1993; Gerhard 1993). In this representation, asymmetric deviations are characterised by the third moment h_3 and symmetric deviations by the fourth moment h_4. Empirically it has been found that for ETGs in equilibrium asymmetric deviations of the LOSVD are larger than the symmetric ones, with the latter being at most a few per cent (Gerhard 1993; Bender et al. 1994). This is however not always true for galaxies in group and cluster environments, e.g. as we showed in Chapter 3; the transition from M49's halo to IGL is signalled by a large value of h_4.

Our best-fit Gauss-Hermite profile is indicated by the solid blue line in Fig. 4.14(a) and is characterised by a velocity dispersion of $\sigma_{\rm M105} = 101.1 \pm 4.2$ km s^{-1}, asymmetric deviations of $h_3 = 0.02 \pm 0.02$, and symmetric deviations of $h_4 = 0.12 \pm 0.02$. The large value of h_4 is similar to the one determined in Chapter 3 for the faint PN population that has been shown to trace the IGL, however, as we detail in the remainder of this Sect., it is of different origin.

To further investigate the nature of the core-wing structure of the LOSVD, we divided the kinematic PN sample into two elliptical bins. We identified a transition from a PN-scarce inner halo to a PN-rich outer halo at a major-axis distance of $\approx 530''$ (cf. Sect. 4.4), however, we cannot use this dividing radius for the kinematic sample as the number of PNe in the outer bin would be too small. We therefore divided the sample at a major-axis radius of $115''$, resulting in two equally populated bins. The corresponding LOSVDs are shown in Fig. 4.14(b) and (c). The best-fit parameters for the inner bin are $\sigma_{\rm inner} = 157.8 \pm 8.5$ km s^{-1}, $h_3 = -0.01 \pm 0.04$ (orange solid line in panel (b)), and $h_4 = -0.005 \pm 0.037$ and for the outer bin we find $\sigma_{\rm inner} = 76.2 \pm 3.7$ km s^{-1}, $h_3 = 0.04 \pm 0.04$, and $h_4 = 0.02 \pm 0.03$ (green solid line in panel (c)). For comparison, we also show both fits in Fig. 4.14(a).

The core-wing structure can be interpreted as the superposition of two near- Gaussian velocity distributions: the high-dispersion centre of the galaxy that dominates the wings of the LOSVD and the low-dispersion halo that mostly contribute to the core of the distribution. We further evaluate the LOS dispersion profile as a function of radius in the following section.

4.7.2 The extended radial velocity dispersion profile of M105

We present M105's LOS velocity dispersion profile as function of minor-axis[6] radius in Fig. 4.15. We determined the velocity dispersion in each elliptical bin using the robust measurement technique described in McNeil et al. (2010) with a clipping tolerance of 2.5σ (blue error bars). For comparison, we also calculated the membership-weighted straight root mean square (rms) measurements (light blue error bars), that can be interpreted as

[6]We chose to evaluate the dispersion along the minor axis rather than the major axis because of the larger spatial coverage along this axis.

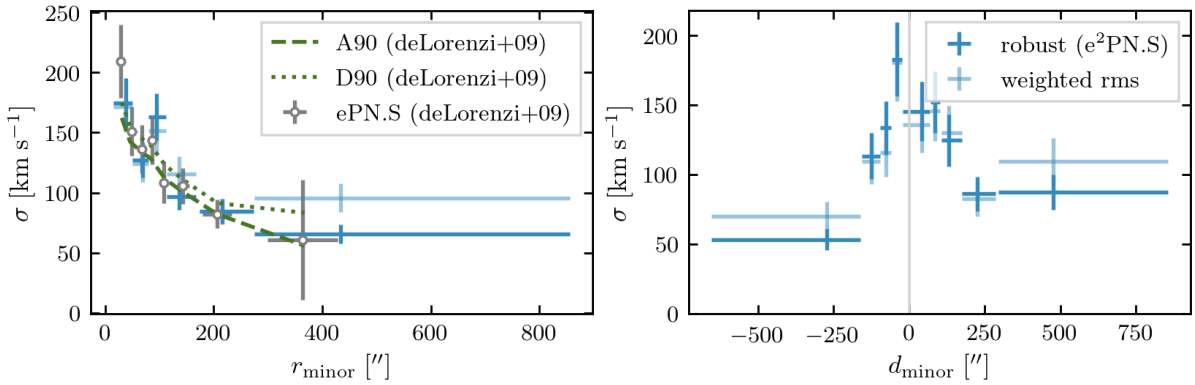

Figure 4.15: LOS velocity dispersion of PNe in M105 as function of minor-axis radius (*left*) and distance along the minor axis (*right*). The blue error bars denote a robust estimate of the velocity dispersion and the light blue error bars indicate a membership-weighted rms velocity dispersion. In both cases, the vertical error bars are derived from MCMC estimates and the horizontal error bars indicate the bin width. In the left panel, grey symbols denote the radial PN.S velocity dispersion profile presented in de Lorenzi et al. (2009). For comparison, we also show the models A90 (stellar halo only, dashed green line) and D90 ($M/L = 7.3$, dotted green line) from de Lorenzi et al. (2009) in the left panel. Negative distances in the right panel correspond to the northern minor axis and positive to the southern major axis.

upper limits on the velocity dispersion. Where the data overlap with the one presented in de Lorenzi et al. (2009) they agree well. The minor-axis LOS velocity dispersion profile is monotonically decreasing with magnitude and covers 860″ in the northern and 650″ southern direction. We do not find a significant variation of the LOS velocity dispersion between the two sides of the galaxy, except for in the very last bin where the LOS velocity dispersion remains constant at about 85 km s^{-1} in the southern half while it further decreases to about 50 km s^{-1} in the northern half.

From the analysis presented in this section, we conclude that we did not detect any kinematic signature of an extended IGL population. We, however, note that this might well be due to the smaller and sparser coverage of the extended halo compared to our photometric PN survey and that we cannot exclude the presence of kinematic signatures of a transition at larger radii. We furthermore compared our extended LOS velocity dispersion profile with the best-fit stellar-only and DM models from de Lorenzi et al. (2009, Fig. 20 therein). Model A90 (dotted green line in Fig. 4.15), the model with the overall lowest velocity dispersion is a spherical stellar-only model, while model D90 (dashed green line) is the most massive oblate model that still fits the data, characterised by a mass-to-light ratio of $M/L = 7.3$. Given the current radial coverage of the NMAGIC model, we cannot rule out either of the limiting cases presented in de Lorenzi et al. (2009). However, given that the velocity dispersion of the stellar-only model is expected to monotonically fall with radius, we hypothesise that a more extended dynamical model would favour a model with DM in order to reconcile the flattened velocity dispersion observed at large radii.

4.8 Discussion and Conclusion

4.8.1 The IGL content of the Leo I Group

In Sect. 4.4 we have contrasted our study of individual tracers (PNe) with deep broad-band photometry from Watkins et al. (2014) and have found a strong flattening of the PN number density profile with respect to the stellar SB profile at large radii ($\gtrsim 9.8 r_{\rm e}$). This flattening can be well reproduced with a two-component photometric model that consists of an inner de Vaucouleurs-like halo and a flat outer component with a constant surface brightness, that we determine to be $\mu_{\rm outer} = 30.40 \pm 0.15$ mag arcsec^{-2}. The inner and outer components are weighted by their α-parameters, which are

- $\alpha_{2.5,\rm inner} = (1.08 \pm 0.22) \times 10^{-8}$ PN $L_{\rm bol}^{-1}$ for the inner component, and
- $\alpha_{2.5,\rm outer} = (9.87 \pm 2.38) \times 10^{-8}$ PN $L_{\rm bol}^{-1}$ for the outer component.

We find a nearly one-magnitude difference in α for the inner and outer component, implying that the outer component has a nearly ten times larger specific PN frequency. Can this be interpreted as a dominant IGL contribution and how does this compare with the findings of Watkins et al. (2014)?

From their deep imaging Watkins et al. (2014) conclude that there is no evidence for extended group light down to a SB limit of $\mu_B = 30$ mag arcsec^{-2} except for a small number of LSB tidal features that they associate with tidally disrupted dwarfs and place an upper limit of 0.01% on the IGL fraction. This is in contrast with the predictions of cosmological simulations, which predict IGL fractions between 12% and 45%, with the fraction increasing as the group evolves and as the IGL is processed through numerous interactions (Sommer-Larsen 2006). Alternative models predict that the IGL content of groups should decrease with time due to the lower frequency of interactions with cosmic time, but even in these models the IGL fraction is predicted to be between 3% to 30% of the total stellar mass (Kapferer et al. 2010).

Watkins et al. (2014) hypothesise whether the apparent lack of IGL implies that the group is not dynamically evolved enough to have accumulated a significant amount of IGL, however they remark that this is at odds with the very regular photometry of M105's extended halo. Ongoing interactions would be signalled by irregular isophotal behaviour such as changing ellipticities or twists in their position angles, but neither are observed.

The results from our PN photometry point towards an extended, but very faint additional PN population that dominates the observed PN number density at large radii. Our inferred SB lies below the limit of Watkins et al. (2014), it is therefore not surprising that this diffuse component has not been identified in their work. If we assume that PNe associated with this component have the same density distribution as our model component in the stellar light, we can estimate their number. The bolometric luminosity of the diffuse component integrated over the total area of our SuprimeCam survey amounts to $L_{\rm bol,outer} = 9.05 \times 10^8\ L_\odot$. Within the limiting magnitude of our survey, we would hence expect 89 PNe to be associated with the diffuse light. For comparison, the

total bolometric luminosity associated with the main halo within our survey of M105 is $L_{\rm bol,inner} = 7.07 \times 10^{11}\ L_{\odot}$, which would correspond to over 7600 PNe[7]. We hence determine the IGL-to-halo PN fraction to be 1.2%. The IGL fraction based on the SB distribution of the inner and outer components corresponds to 0.1%, which is significantly larger than the upper limit of 0.01% predicted by Watkins et al. (2014). PNe.

The high α-parameter and steep faint-end PNLF slope may be interpreted as indicators for a very blue, old and metal-poor stellar population that dominates the IGL, which would be in line with the identification of a metal-poor ([Fe/H]≈ -1.1) stellar population in the outer halo on the basis of HST photometry by Lee & Jang (2016). Similar to the flattening of the stellar SB profile at large radii, Lee & Jang (2016), find that at large radii ($R > 600''$), the metal-poor RGB stars have a flatter number density profile compared to the metal-rich ones. The slope of the metal-poor RGB number density profile is similar to that of Watkins et al.'s (2014) ground-based observations (see Lee & Jang 2016, Fig. 8).

However, the question whether this diffuse component is dynamically bound to M105's halo or to the group potential cannot be answered based on photometric surveys alone. Unfortunately, due to the sparser coverage of our kinematic survey, we cannot provide conclusive evidence on the dynamical status of PNe at the large radii at which the PN-rich component dominates the observed PN number density profile.

4.8.2 The LOS velocity dispersion profile of M105 and implications on the galaxy's dark matter content

The LOS velocity dispersion profile has been at the centre of a long-standing debate on M105's (dark) matter content (Romanowsky et al. 2003; Douglas et al. 2007; Dekel et al. 2005; de Lorenzi et al. 2009). The new data presented in this Chapter, in combination with the photo-kinematic decomposition detailed in Section 4.6 to limit contamination from PNe associated with NGC 3384, allowed us to extend the coverage of M105's extended halo by a factor of two. However, as we effectively only sample 30% of the outer halo, our analysis is limited by low-number statistics at large radii. Our results show neither an increase nor a decrease of the LOS velocity dispersion at large radii, but a flattening at a value of 60 km s^{-1}. At a first glance, these results do not rule out any of the models presented in de Lorenzi et al. (2009). However, we hypothesise that a NMAGIC model fit to the extended data would need to contain DM in order to reproduce the flattened LOS velocity dispersion profile that we observe, that could not be reconciled with a stellar-only halo.

4.8.3 Outlook

The work presented in this chapter shows the promising synergy of photometric and kinematic PN surveys with deep and extended broad-band photometry. However, this work also illustrates the limitations when working in the low-SB regime and with sparsely sampled tracers. We are therefore planning to obtain more accurate and more extended LOS

[7]Due to incompleteness, especially in the bright galaxy centre, we observed significantly less PNe.

velocity measurements through multi-object spectroscopic follow-up campaign of our extended photometric survey. These new data would likely provide conclusive evidence on the dynamical state of the extended halo or IGL and could be the empirical basis for a more extended NMAGIC model to finally firmly constrain the DM content of M105.

Appendix

4.A Extraction of the photometric PN catalogue

We used Source Extractor (SExtractor, Bertin & Arnouts 1996) to detect objects, measure their photometric properties, and to calculate background maps of our mosaic on- and off-band images. We denote the measured narrow- and broadband magnitudes with $m_{\rm n}$ and $m_{\rm b}$ respectively. The extracted magnitudes are in the AB magnitude system.

SExtractor detected and analysed objects for which the flux value in at least 9 adjacent pixels was higher than $1.1 \times \sigma_{\rm rms}$ on the on-band image. As our aim was to measure the colour $m_{\rm n} - m_{\rm b}$ of each emission-line object, we chose an aperture radius of 13 pixels and subsequently extracted the broad-band magnitude $m_{\rm b}$ on the off-band image in dual-image mode, i.e. in the same aperture as in the on-band image. Following Theuns & Warren (1997), we assigned a magnitude of $m_{\rm b} = 28.7$ to [O III] emitters for which no V-band magnitude could be measured on the off-band image. This corresponds to the flux of an [O III] emitter at the limiting magnitude $m_{\rm n,lim}$ observed through a broadband V filter.

4.A.1 Catalogue pre-processing

In order to prevent false detections of PNe due to image artefacts, we masked the pixel columns affected by dithering as well as regions with a high background value (e.g. due to charge transfer or saturated stars). We calculated the rms-background maps of the on- and off-band images using SExtractor and masked all pixels with values higher than 1.5 times the median background. Furthermore, we masked the central regions of the three bright galaxies M105, NGC 3384, and NGC 3398 due to high background counts from diffuse galaxy light. The masked regions account for 2.3% of the total survey area, resulting in an unmasked survey area covering $0.2365\,\mathrm{deg}^2$.

4.A.2 Limiting magnitude and photometric error

We determined the limiting magnitude of our survey by populating the on-band image with a synthetic PN population and determining its recovery fraction as a function of magnitude. The simulated PNe have a Moffat-shaped PSF profile as measured on the image (see Sect. 4.2.1) and follow the "standard" PNLF (Ciardullo et al. 1989) scaled to the distance of M105. The synthetic population was added to the on-band image using

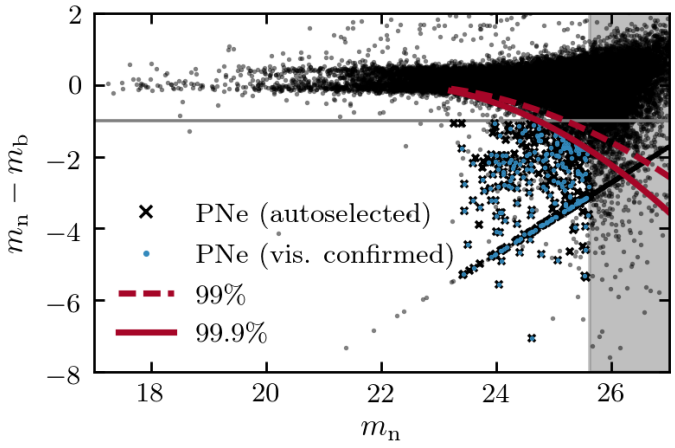

Figure 4.16: CMD for all sources (black dots) in the M105 Suprime Cam field. Obects that lay below the grey horizontal line at $m_n - m_b = -1$ are emission-line objects with an equivalent width $EW_{obs} \geq 110$ Å. The magnitude range fainter than the limiting magnitude is denoted by the shaded grey region. The dashed (solid) red lines denote the 99.9% (99.9%) limits of the simulated foreground population. Black crosses denote the PNe candidates that were automatically selected and blue dots denote those confirmed by visual inspection.

the IRAF task `mkobjects`. The limiting magnitude m_{lim} is defined as the magnitude at which the recovery fraction of the simulated population falls below 50%. We determine a limiting magnitude of $m_{lim,n} = 25.6$, which corresponds to $m_{lim,5007} = 28.1$.

We also used the synthetic population to determine the error on the extracted magnitudes by determining the difference between the simulated magnitudes and those extracted using SExtractor. We estimate the photometric error to be one standard deviation about the mean in ten magnitude bins. The resulting error bands are shown in Fig. 4.3.

4.A.3 Object selection

PN candidates are selected based on their position on the CMD and their unresolved light distribution.

CMD selection

Figure 4.16 shows the m_n versus $m_n - m_b$ CMD of all extracted sources in the M105 Suprime Cam field. In order to limit the contamination by [O II]3727 Å emitters at redshift $z = 0.345$, we imposed a colour-selection criterion of $m_n - m_b < -1$. This corresponds to an observed equivalent width of $EW_{obs} > 110$ Å (Teplitz et al. 2000)[8]. PNe candidates are thus objects that have a colour excess $m_n - m_b$ and are brighter than the limiting magnitude $m_{lim,n} = 25.6$.

[8]No [O II] emitters with $EW_{obs} > 110$ Å have been observed to date (Colless et al. 1990; Hammer et al. 1997; Hogg et al. 1998).

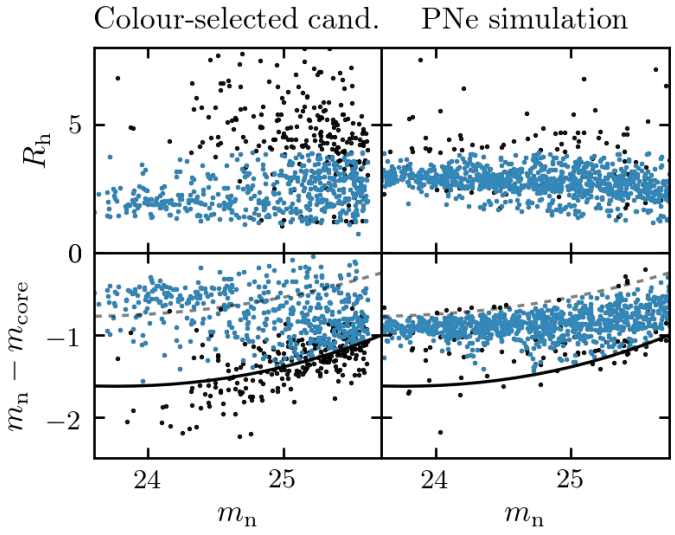

Figure 4.17: Point-source test for PN candidates in M105. *Left column:* colour-selected PNe, *right column:* simulated PNe. *Top row:* Half-light radius R_h as function of magnitude m_n, *bottom row:* $m_n - m_{core}$ as function of magnitude m_n

Another source of possible contaminants are faint stellar sources (e.g Milky Way (MW) stars) that are scattered below the adopted colour excess due to the increasingly large photometric errors are faint magnitudes. We therefore simulated a continuum population onto the on- and off-band images. The red dashed and solid lines in Fig. 4.16 denote the 99% and 99.9% limits calculated from the extracted CMD of the simulated population. In order to limit the probability of including foreground stars to the 0.1% level, we only considered objects below the 99.9% limit for further analysis.

Point-like versus extended sources

At extragalactic distances, PNe appear as unresolved, point-like sources. In order to limit contamination from extended sources (e.g. background galaxies or other objects with strong [O III] emission), we analysed the light distribution of the simulated PN population. We derived the following criteria for point-like sources:

1. The sources have half-light radii in the range $1 < R_h < 3.9$ pix (top panels of Fig. 4.17). This upper limit corresponds to the 95%-percentile of the simulated population.

2. The sources lie above the 95%-limit derived from the m_n vs $m_n - m_{core}$ distribution of the simulated population (solid black line in the bottom panels of Fig. 4.17). The core magnitude m_{core} is measured within a 5 pix aperture. Sources that fulfil both criteria are denoted in blue in Fig. 4.17 and as black crosses on the CMD in Fig. 4.16.

4.A.4 Catalogue validation and visual inspection

The automatically selected photometric catalogue was visually inspected and any remaining spurious detections were removed, resulting in the final catalogue of 226 sources within the limiting magnitude of $m_{\mathrm{lim},n} = 25.6$. These sources are highlighted with blue dots on the CMD in Fig. 4.16. Their spatial distribution is shown in Fig. 4.1, superposed on the DSS image, in which they are denoted by blue crosses.

4.A.5 Catalogue completeness

The evaluation of the completeness of our catalogue is a vital step preceding any further scientific analysis. Due to the selection of PN-candidates based on flux-ratio criteria, PNe that fell below the flux-threshold due to photometric errors would not have been detected. We used the synthetic PN population to determine is recovery fraction as function of radius (spatial completeness) and magnitude (photometric completeness). The spatial completeness of our survey within the limiting magnitude as function of major-axis radius is tabulated in Table 4.2. The detection completeness, encompassing both colour and detection completeness as function of magnitude is tabulated in Table 4.3.

4.A.6 Possible sources of contamination

Faint continuum objects

As we described earlier in this section (c.f. Sect. 4.A.3), we limited our selection of objects to those that fall below the 99.9%-line of a simulated continuum population in order to minimise the contamination by foreground objects like faint MW stars. However, some of these objects will be scattered below this line. We estimated the fraction of foreground contaminants in the colour-selected sample by determining the total number of observed foreground stars down to $m_{\mathrm{n,lim}}$ and assuming that 0.1% of these are scattered into the sample of colour-selected PNe. This results in 23 objects, which corresponds to a contribution of 10% of the extracted sample of 226 PNe.

Background galaxies

Another source of contamination are faint background Ly-α galaxies, that emit at the same wavelength as PNe in the Leo I Group, if at redshift $z = 3.1$. In order to quantify this effect, we used the Ly-α luminosity function (LF) determined by Gronwall et al. (2007), who carried out a deep survey for $z = 3.1$ Ly-α emission-line galaxies. The LF is characterised by a Schechter-function (Schechter 1976). More recent surveys (e.g. Ciardullo et al. 2012) agree with this LF within 0.1 mag. Within the limiting magnitude of our survey, we expect 56 Ly-α emitters, which corresponds to (24.9 ± 5.0)% of the completeness-corrected sample. The corresponding LF is shown in Fig. 4.8. The contribution from [O II]3727Å emitters at redshift $z = 0.345$ is already accounted for when using the Gronwall et al. (2007) Ly-α LF (cf. Chapter 2.3).

Table 4.2: Spatial completeness and unmasked survey area as function of major-axis radius.

r_{major} [$^\circ$]	A [$^{\circ 2}$]	c_{spatial}
0.0469	0.00277	0.77
0.0730	0.00817	0.98
0.1077	0.01682	0.98
0.1592	0.03577	0.79
0.2016	0.04074	0.82
0.3787	0.13114	0.86

Table 4.3: Colour and detection completeness as function of magnitude.

m_{n} [mag]	c_{colour}	$c_{\mathrm{detection}}$
23.265	0.66	0.64
23.565	0.94	1.00
23.738	0.94	0.72
23.897	0.87	0.96
24.031	0.89	1.00
24.146	0.87	1.00
24.260	0.91	0.83
24.376	0.89	0.96
24.476	0.87	0.96
24.594	0.96	0.72
24.714	0.83	0.96
24.808	0.91	1.00
24.894	0.89	0.96
24.989	0.85	0.87
25.087	0.87	0.83
25.182	0.81	0.81
25.277	0.76	0.86
25.363	0.85	1.00
25.450	0.72	0.74
25.561	0.70	0.56

Chapter 5

Summary and Conclusion

In this thesis, I have investigated the build-up of the extended halos of galaxies in group and cluster environments. Using the deepest and most-extended photometric and kinematic surveys of individual stars – planetary nebulae (PNe) – at these distances to date, I have been able to address some of the outstanding questions regarding the assembly of two galaxies, M49 and M105, as well as to contribute to a better understanding of halo assembly and intra-group light (IGL) build-up in group and cluster environments in general. In this chapter, I will highlight the main findings and implications of my research. I would like to preface this summary and conclusion with the following statement:

The concept of galaxies being built from composite single stellar populations (SSPs) has been widely accepted. It has now become evident that the same holds on the level of PN populations.

In the past decades, the majority of PN surveys of nearby galaxies were limited to the brightest magnitudes and a field of view (FOV) limited to the central 1-2 effective radii. Therefore, these surveys only probed the relatively uniform stellar population at the galaxy centres. In the last decade, however, PN surveys reached higher sensitivity and larger galaxy coverage. In this work, in conjunction with other studies (Longobardi et al. 2013, 2015a), we find that the assumption of the invariance of the describing parameters such as the luminosity-specific PN number α or the faint-end planetary nebula luminosity function (PNLF) slope does not hold on the level of galaxies, but rather on the level of the stellar populations that contribute to them. In this thesis, this finding is exemplified in Fig. 2.8, where we, for the first time, describe the α versus $B-V$ colour relation *within* a galaxy. Similar to comparing the abundance gradient in the outer halo of the Milky Way (MW) with the integrated-light properties of the present-day MW satellites (e.g. Venn et al. 2004; Tolstoy et al. 2009), the comparison of the α-colour relation within a galaxy with the integrated-light values of individual galaxies may provide important constraints on the galaxy's build-up.

PNe are excellent tracers of the diffuse IGL and can facilitate the detection of the IGL even down to magnitude levels where the current state-of-the-art broad-band photometric surveys cannot reach.

In Chapter 2 I found evidence for an extended population of PNe that is associated with the IGL of the Virgo Subcluster B. The combination of our study of PNe as individual tracers with broadband photometric observations allowed the modelling of M49's halo as a two-component system with an inner halo whose stellar surface brightness (SB) is described with a Sérsic profile and a flat outer component that we associate with the IGL. This component has a three-times higher α-parameter compared to M49's main halo and the corresponding stellar population is characterised by a constant SB of $\mu_{\rm IGL} = 28$ mag arcsec^{-2}, as well as by a very blue colour ranging from $B - V = 0.25$ to $B - V = 0.6$, which will be further discussed later in this chapter.

This result is consistent with deep extended photometry (Capaccioli et al. 2015; Mihos et al. 2017), where the change in isophote morphology as well as the strong colour gradient point towards an accreted component. However, Mihos et al. (2017)'s morphological classification of the IGL based on filamentary or clumpy structure would not have lead to the identification of IGL in the Virgo Subcluster B: my research has shown that the IGL in the Virgo Subcluster B is smooth and relatively featureless.

Similarly, in Chapter 4 I have reported the tentative detection of a very faint, but PN-rich IGL component based on the flattening of the photometric PN number density profile. In this case, the inferred broad-band SB of the IGL is $\mu_{\rm IGL} = 30.4$ mag arcsec, which is nearly half a magnitude fainter than the deepest broadband survey of the Leo I Group to date (Watkins et al. 2014). However, this detection still awaits confirmation based on PN-kinematics, as our current e^{2}PN.S survey is not quite extended enough to trace the transition from the PN-scarce to the PN-rich components identified from our photometric survey. This motivates a spectroscopic follow-up of our deep and uniform photometric sample.

For the first time we have observed the kinematic transition from the halo of brightest cluster galaxy (BCG) to the IGL based on the velocities of *individual stars*.

The detection PNe associated with an extended IGL component reported in Chapter 2 has been corroborated by the extended PN kinematics presented in Chapter 3. The 81 PNe associated with the IGL are uniformly distributed in M49's halo and have a velocity dispersion that is more than twice that of the halo, which is in line with predictions from numerical simulations (Cui et al. 2014; Dolag et al. 2010). The increase of the line-of-sight (LOS) velocity dispersion, reaching the velocity dispersion of satellite galaxies in the Subcluster B, is a strong indication that M49's outermost halo is dynamically controlled by the subcluster's gravity.

The very blue colour of M49's extended halo and IGL is at odds with predictions on merger-mass fractions from hydrodynamical cosmological simulations.

The smooth appearance in photometry (Mihos et al. 2013; Capaccioli et al. 2015) and the regular PN velocity field discussed in Chapter 3 provide important constraints on the dynamical age of the IGL, namely that its dynamical age is older than the orbital precession time and thus older than 5 Gyr. Hence the accretion of a moderately massive young star-forming galaxy, which would correspond to a merger-mass ratio of 1:5, cannot be the origin of the extremely blue IGL. Instead, we propose that the systems that built M49's outer halo and contributed to the IGL must have been many low-mass galaxies with metallicities below [Fe/H] $< -1 \pm 0.5$ (see also Mihos et al. 2013). Via the mass-metallicity relation (Kirby et al. 2013), we infer corresponding mass-merger ratios below 1:100. However, in the current hydrodynamical cosmological simulations, the cumulative effect from mergers with these merger-mass ratios is found to be negligible (Rodriguez-Gomez et al. 2016). Our findings thus put important constraints on the feedback mechanisms in cosmological simulations: currently they do not form sufficient low-mass low-metallicity galaxies that would be needed to build the very blue halo of galaxies such as M49. Even better constraints on the IGL progenitor masses could be obtained through more accurate and extended LOS velocity measurements.

The intra-cluster light (ICL) and IGL PN populations reflect the effect of environment on ICL and IGL build-up.

We first compare the ICL and IGL of M49 and M87, which are the two most massive and brightest early-type galaxies in the Virgo cluster. However, their stellar and PN populations have very different properties, which reflects the different environments in which they reside. M87 in Virgo's most dense environment, the Subcluster A, is surrounded by ICL with a higher specific frequency compared to the IGL around M49 in the Virgo Subcluster B. Both galaxies are undergoing or have undergone recent accretion. The fact that M87's accreted companion did not contain any gas, while M49 has multiple star-forming companions reflects the different environments in which the halos of these ETGs grew.

Furthermore, we can also compare the IGL fractions derived in this work. For the Leo I Group, we estimate the PN-based IGL-to-halo fraction to be 1%, while the same quantity in M49 ranges from 40% to 60% and its halo is nearly 100 times as massive as that of M105. It would however be presumptuous to draw conclusions from these two data points on the nature of ICL and IGL build-up. However, facilitated by the upcoming generation of extremely large telescopes, we will be able to bridge the gap between the current ground-based study of very nearby clusters such as Virgo and Fornax and the space-based study of intermediate-redshift clusters.

Chapter 6

Prospects and future work

This thesis has paved the way for future work in several directions. First and foremost, as already alluded to in the previous chapter, our understanding of the extended halos of M49 and M105 would significantly increase if we obtained higher-resolution spectroscopic data. A spectroscopic follow-up of our uniform, extended and deep surveys would allow us to detect also substructures with lower velocity dispersion and therefore lower masses, which could set important constraints on the feedback mechanisms in the current cosmological simulations. In the case of M105, we could achieve a larger and more uniform coverage of the intra-group light (IGL), nearly reaching the Leo H I ring (see Fig. 6.1). Furthermore, at these large radii, the models of de Lorenzi et al. (2009) show the largest variation, allowing us to better constrain the matter content of M105's extended halo and environment. In addition to this immediate continuation of the thesis project, there are three related projects that I outline in the following.

6.1 Early-type galaxy halo survey

M49 and M105 are not the only galaxies that are surrounded by unusually blue and metal-poor halos. I am planning to extend the work presented in this thesis into a survey of early-type galaxies (ETGs) in group and cluster environments with different dark-matter halo masses (see Fig. 6.2). To begin with, the most massive environment in the survey will be probed by M87 in the centre of the Virgo Cluster and build on the seminal work of Longobardi et al. (2013, 2015a). As a probe intermediate-mass environment, we also include the ETG Centaurus A (NGC 5128, Walsh et al. 2015). Where available, we will combine these data with globular cluster (GC) kinematics. As merger histories, relative velocities between merging subsystems, and feedback effects all depend on mass and environment it is important to understand what happens in the different steps of the hierarchical mass assembly from ETGs in less massive or loose groups to dense galaxy groups and clusters.

With these data, I aim to investigate which of the different proposed channels have been dominant in the build-up of the extended blue halos. For each of the galaxies in our sample, we aim to investigate whether the transition from the inner red, metal-rich, to the outer

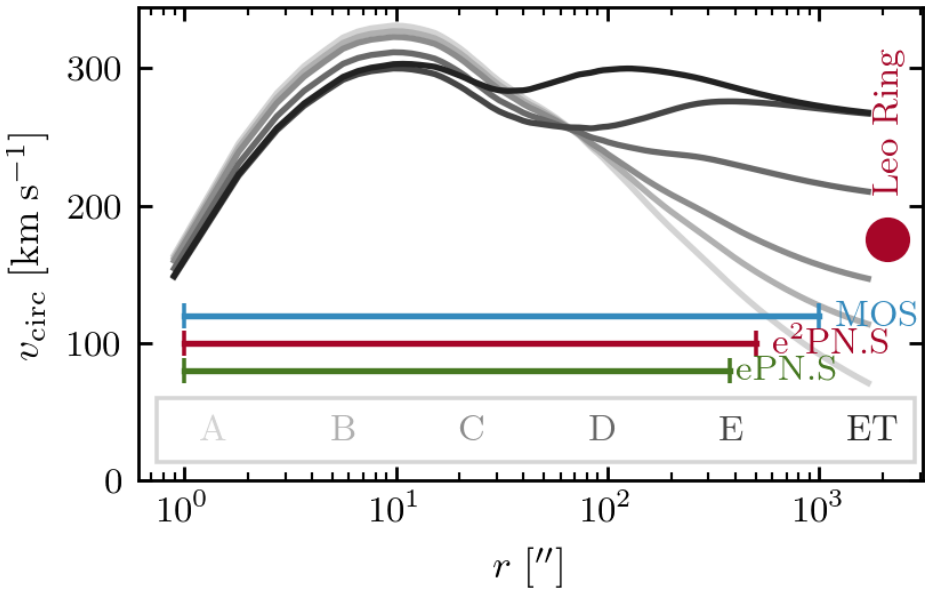

Figure 6.1: Circular velocity profiles of the Leo I group from de Lorenzi et al. (2009) ranging from stellar-only (A, light grey) to dark-matter dominated models (B to ET, gray to black). The green and red bars show the radial extent of the e- and e^{2}PN.S surveys and the blue bar the extent of our proposed spectroscopic follow-up observations. The red circle denotes the circular velocity of the Leo H I ring derived from Schneider (1985).

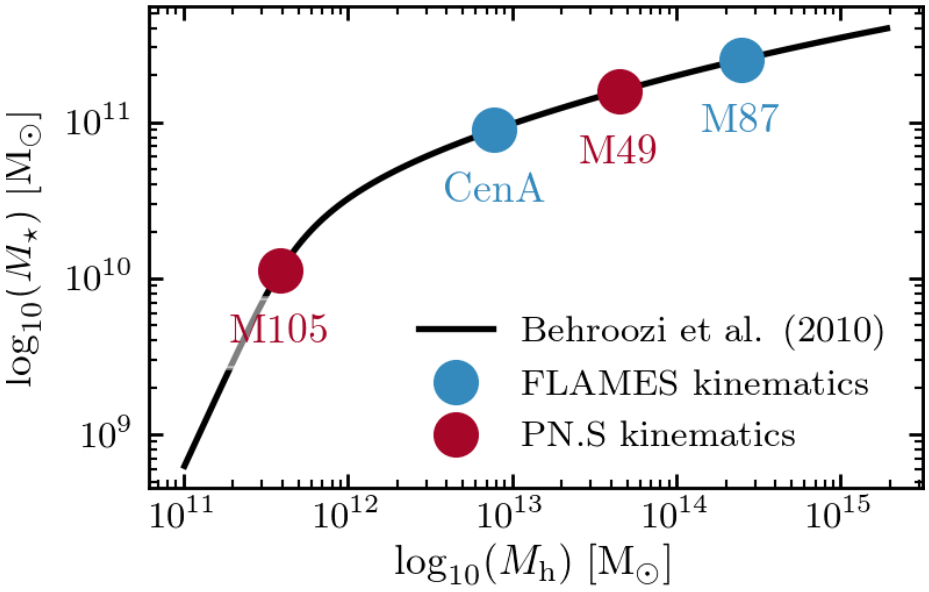

Figure 6.2: Stellar-mass function vs. halo-mass function from Behroozi et al. (2010). Red and blue circles denote the galaxies in my proposed survey and where they would lie on the stellar-to-halo-mass function according to their inferred halo masses from Das et al. (2010) and van den Bergh (2000).

blue and supposedly metal-poor halo is reflected in the planetary nebula (PN) population. Based on PN photometry, the variation in the planetary nebula luminosity function (PNLF) slope and α-parameter as function of radius can be studied. Combining these measurements with accurate PN kinematics, we can make inferences about the dynamic status of the galaxies' halos. We will develop a suite of Gaussian-mixture models (GMMs) in order to model the superposition of tracer populations with different density and line-of-sight (LOS) velocity distributions. By considering multiple targets in different group environments, we will also begin to see whether the origins of these halos are universal, or whether they depend on the size of the group in which they formed.

6.2 PN-abundances in M49 and VCC 1249

As detailed in Chapter 3, I have found evidence for PNe associated with the accretion of the dwarf irregular (dIrr) galaxy VCC 1249 into the halo of M49. We have successfully obtained telescope time to measure the oxygen abundances of individual PNe in M49's halo in order to follow-up the discovery of three distinct PN-populations in magnitude-velocity space. We plan to measure the line fluxes of the strong [O III]λ4959 and λ5007 lines, [O II]λ3727, Hβ λ4861 and Hα λ6563, as well as [Ne III]λ3868 in order to to estimate the effective nebular temperature and oxygen abundance. The measurement of oxygen abundances of the progenitor stars of the bright PNe in the dIrr galaxy and in M49's halo, will enable us to determine whether the two populations are of the same or of distinct origin and thus further improve our understanding of the late phases of halo build-up in giant ETGs.

6.3 Characterising the PNLF in ETGs with Integral-Field Spectrographs

Empirically it has been found that PNLFs steepen from star-forming to old metal-rich populations (e.g. Ciardullo et al. 2004; Ciardullo 2010; Longobardi et al. 2013, 2015a). In this thesis I have shown that this is also the case in the ETGs M49 and M105. Our excellent data furthermore revealed that bright and faint PN populations in M49 have distinct kinematics and spatial distributions (see Chapter 3) akin to the distinct kinematics of red and blue GCs (Côté et al. 2003). In order to interpret these results it is vital to better understand the PNLF and to reconcile the observations with the current state-of-art models of post-asymptotic giant branch (AGB) and PN evolution.

The classical PN studies using narrow-band or counter-dispersed imaging are "blind" in the central regions of the galaxy due to the presence of the strong stellar background light and can thus only detect very bright PNe. In distant galaxies, the central regions, however, are most accessible for the analysis of the integrated stellar population properties. The advance of integral-field spectroscopy (IFS) can overcome this limitation as the spectra in the bright central region can be decomposed into their respective stellar and nebular

contribution. This technique was first used by Sarzi et al. (2011) in order to characterise the PN population in the central regions of M32 with the SAURON instrument. With the newest-generation instruments like the Multi-Unit Spectroscopic Explorer (MUSE) only moderate exposure times are needed to cover the first two magnitudes of the PNLF. Furthermore, there is already an ample amount of archival MUSE data of the central regions of ETGs that could be exploited for this research.

With these data, I will be able to systematically quantify the variation of the PNLF with the age and metallicity of the different stellar populations, which will in turn contribute to a better understanding of the PNLF variations at large radii. Recent simulations of post-AGB evolution (Miller Bertolami 2016) predict different PNLF slopes depending on the age of the host stellar population (Zijlstra et al. 2016) and can, for the first time, reproduce the bright cut-off of the PNLF for intermediate-age stellar populations (Gesicki et al. 2018). In this context, a systematic observational study of the PNLF would therefore not only advance its use as a diagnostic tool to trace galaxy assembly, but will also provide important observational constraints for the most recent evolutionary tracks of post-AGB stars and central stars of PNe.

Appendix A

Improved co-addition of SuprimeCam images with Astromatic tools

A.1 Data processing

A.1.1 Reduction with SDFRED2

First, the data reduction is carried out with the standard Subaru SuprimeCam data reduction package SDFRED2[1]. This "pipeline" takes over after step 9 of SDFRED2.

A.1.2 Apply distortion correction to flat-fields

SDFRED2 applies a distortion and atmospheric dispersion correction (ADC) to correct for the geometric distortion due to the telescope optics and differential dispersion of light travelling through the Earth's atmosphere to all flat-fielded science frames. After the correction, the science frames have a slightly different number of pixels along the x- and y-axes. We want to apply the same correction to the flat-fields as well in order to keep the sizes of the science frames and flat-fields equal. This is vital for the use of the Astromatic tool `Weight Watcher` that will be described later in this document. The ADC is a function of airmass, therefore we create a copy of the flat-fields with the airmass keyword from the corresponding science exposure. The ADC also needs a number of other header parameters, that are all taken over from the science exposure. The python routine in Sect. A.3.1 can be used to create a copy of each flat-field with header parameters of the corresponding science exposure. It also writes out the input list for the SDFRED2 `distcorr` task. Then the correction can simply be run on the flat-fields: > `distcorr.sh flat_distcorr.lis` The resulting frames will have the letter `g` prepended to their file names.

[1] `https://www.naoj.org/Observing/Instruments/SCam/sdfred/sdfred2.html.en`

A.1.3 Creation of initial weight maps

I use the Astromatic software `weight watcher` for the creation of weight and flag maps. These maps are crucial for correctly weighting and combining the data from multiple chips and exposures. I use both the science images and their associated distortion-corrected flat fields as input images to construct the weight maps.

A.1.4 Building the mosaic

In order to combine the chips for all exposures, I use the astromatic tools `SExtractor`, `SCAMP` and `SWarp`. To automate the process, I use the python package `astromatic-wrapper`[2] to build a reduction pipeline. The pipeline consists of the following seven steps:

1. First the brightest sources on each chip are extracted with `SExtractor`.
2. Based on these sources, `SCAMP` calculates an astrometric solution for each chip with respect to the UCAC-4[3] and 2MASS[4] catalogues.
3. `SWarp` is used to resample the chips weighted by their input weight maps and taking into account the headers with the astrometric solution calculated in the previous step. The resampled images are then stacked and the corresponding weight map of the stack is calculated.
4. In order to calculate the point-spread function (PSF) across the image, first `SExtractor` is used to generate a catalogue with positions of objects in the stacked image.
5. This catalogue is then fed to `PSFex`, which calculates the PSF.
6. The resulting PSF can then be used by `SExtractor` to do PSF photometry on the image. *Note: this step was not needed for any project in this thesis, but was left in the pipeline for completeness.*
7. Finally, any remaining temporary files are cleaned up.

The pipeline is built such that each of the seven steps can be run individually.

A.2 Results

The following four figures show the impressive improvements after re-processing the SDFRED2 pipeline outputs with astromatic tools. The images are now astrometrised with respect to the UCAC-4 catalogue (red circles). Furthermore, dead pixel rows resulting from bleeding due to saturated stars have been reduced through the efficient use of weight maps. The images can be created with the python script included in Sect. A.3.3.

[2] `http://astromatic-wrapper.readthedocs.io/en/latest/`
[3] `http://www.usno.navy.mil/USNO/astrometry/optical-IR-prod/ucac`
[4] `https://www.ipac.caltech.edu/2mass/`

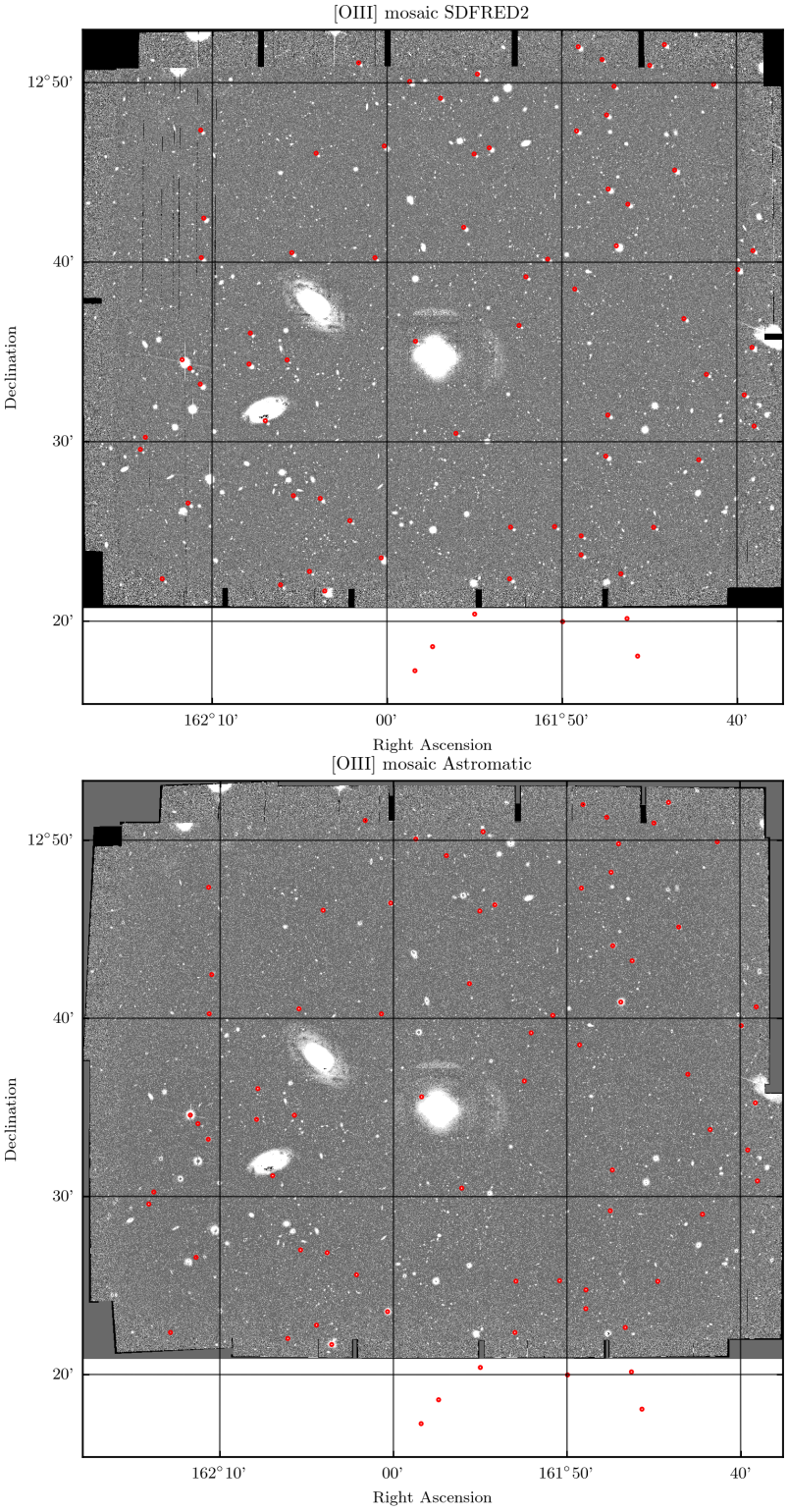

Figure A.1: [OIII] mosaic processed with the SDFRED2 pipeline (top) and after reprocessing with astromatic tools (bottom). In both images, red circles denote reference stars from the UCAC-4 catalog.

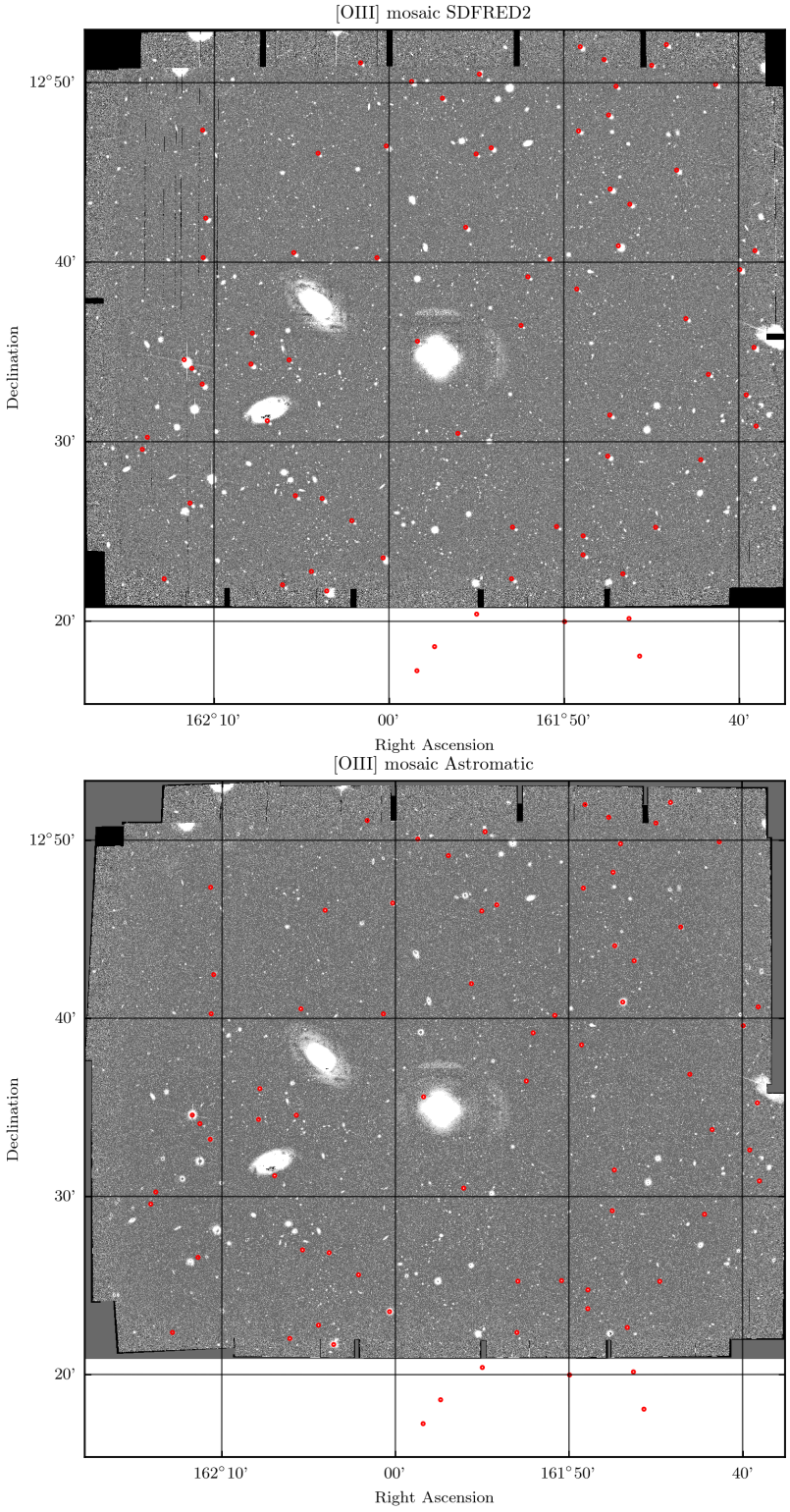

Figure A.2: V-band mosaic processed with the SDFRED2 pipeline (top) and after re-processing with astromatic tools (bottom). In both images, red circles denote reference stars from the UCAC-4 catalog.

A.3 Python routines

A.3.1 Apply distortion correction to flat-fields

```
# coding: utf-8
import numpy as np
import sys
import os
import subprocess

# directory structure
datadir = '/Volumes/Backup_Johanna/M105_MOS/'
filter = 'V'
filterdir = os.path.join(datadir, filter)
imagedir = os.path.join(filterdir, 'images')
flatdir = os.path.join(datadir, 'skyflat_' + filter)

# list of exposures
explist = np.loadtxt(os.path.join(filterdir, 'makemos.lis'), dtype = np.str)
# list of pre-corrected flat-fields
flatlist = np.loadtxt(os.path.join(flatdir, 'flat_distcorr.lis'),
                      dtype = np.str)
# prepend g to filename to use distortion-corrected fields
flatlist = np.array(['g' + flat for flat in flatlist])

# weight-watcher parameters
# path to parameter file
config = os.path.join(filterdir, 'config/default.ww')

# loop over all exposures and run weight watcher
for i,exp in enumerate(explist):
    obsname = exp.split('.')[0]
    args = {'config_file': config,
            'flats': os.path.join(flatdir, flatlist[i]),
            'images': os.path.join(imagedir, exp),
            'weights_out': os.path.join(imagedir, obsname + '.wtmap.fits'),
            'flags_out': os.path.join(imagedir, obsname + '.flag.fits')}
    print 'Running ww on ', obsname
    os.system('ww -c {config_file} -WEIGHT_NAMES {flats},
              {images} -OUTWEIGHT_NAME
              {weights_out} -OUTFLAG_NAME {flags_out}'.format(**args))
```

A.3.2 Building the mosaic

```
# coding: utf-8
# Modelled after the example here:
# http://astromatic-wrapper.readthedocs.io/en/latest/pipelines.html
import os
import datetime
import astromatic_wrapper as aw
from astropy.io import ascii
import numpy as np

# Get the current date and time
log_path = datetime.datetime.now().strftime('%Y-%m-%d_%H-%M-%S_test')

# Set defaults
base_path = r'/Volumes/Backup_Johanna/M105_MOS/OIII'
paths = {
    'temp': os.path.join(base_path, 'temp'),
#     'log': os.path.join(base_path, 'log', log_path),
    'config': os.path.join(base_path, 'config'),
    'catalogs': os.path.join(base_path, 'catalogs'),
    'stacks': os.path.join(base_path, 'stacks'),
    'images': os.path.join(base_path, 'images')
}

build_paths = {
    'SExtractor':'/opt/local/bin/sex',
    'SCAMP': '/usr/local/bin/scamp',
    'SWARP': '/usr/local/scisoft///bin/swarp',
    'PSFEx': '/opt/local/bin/psfex'
}

def build_pipeline(pipeline, exposures,
                   ref_catalog='UCAC-4',
                   ref_band = 'DEFAULT',
                   frames = [],
                   stack_name = 'OIII_stack.fits',
                   output_cat_name =   'OIII_final.ldac.fits'):
    # Generate catalogs from SExtractor
    catalog_names = []
    for files in exposures:
        # create names for the output catalogs for each image
        catalog_names.append(os.path.join(pipeline.paths['temp'],
```

```
                                        os.path.basename(files['image']).replace('.fits',
                                                                                 '.ldac')))
    kwargs  = {
        # image to SExtract
        'files': files,
        'api_kwargs':{
            # arguments to initialize Astromatic class
            'config': {'CATALOG_NAME': catalog_names[-1],
                       'CATALOG_TYPE': 'FITS_LDAC',
                       'DETECT_THRESH':'5.',
                       'ANALYSIS_THRESH':'5.',
                       'FILTER': 'N',
                       'GAIN': '3.3',
                       # as the exposures are the "pure counts"
                       'PARAMETERS_NAME':'default.param'},
            # frames to run Sextractor on
            'frames': frames,
            'config_file': os.path.join(pipeline.paths['config'],
                                        'SCAM_OIII_par.sex')
        }
    }
    # Add the step to the pipeline
    pipeline.add_step(aw.api.run_sex, ['step1', 'SExtractor'],
                      ignore_errors=True, ignore_exceptions=True,
                      **kwargs)

# Get astrometric solution from SCAMP
# Use SCAMP to get astrometric solutions
kwargs = {
    'catalogs': catalog_names,
    'api_kwargs': {
        'config': {
            'ASTREF_CATALOG': ref_catalog,
            'ASTREF_BAND': ref_band,
            'CATALOG_TYPE': 'FITS_LDAC',
            'SOLVE_PHOTOM': 'N',
            'CHECKPLOT_DEV': 'NULL',
            'NTHREADS':'2'
        },
        'config_file': os.path.join(pipeline.paths['config'],
                                    'default.scamp')
```

```
    }
}
pipeline.add_step(aw.api.run_scamp, ['step2', 'SCAMP'],**kwargs)

# Resample (rotate and scale) and combine (stack) images
stack_filename = os.path.join(pipeline.paths['temp'], stack_name)
kwargs = {
    'filenames': [exp['image'] for exp in exposures],
    'api_kwargs': {
        'config': {
            'WEIGHT_TYPE': 'MAP_WEIGHT',
            'WEIGHT_SUFFIX': '.wtmap.fits',
            'IMAGEOUT_NAME': stack_filename,
            'WEIGHTOUT_NAME': stack_filename.replace('.fits','.wtmap.fits'),
            'RESAMPLE_DIR': pipeline.paths['temp'],
        }
    },
    'frames': frames
}
pipeline.add_step(aw.api.run_swarp, ['step3', 'SWarp'], **kwargs)

# Get positions in stack for PSF photometry
kwargs = {
    'files': {
        'image': stack_filename,
        'wtmap': stack_filename.replace('.fits', '.wtmap.fits')
    },
    'api_kwargs': {
        'config': {
            'CATALOG_TYPE': 'FITS_LDAC',
            'FILTER': False,
            'WEIGHT_TYPE': 'MAP_WEIGHT',
            'NTHREADS':'2',
        },
        'params': ['NUMBER', 'EXT_NUMBER', 'XWIN_IMAGE', 'YWIN_IMAGE',
                   'ERRAWIN_IMAGE', 'ERRBWIN_IMAGE', 'ERRTHETAWIN_IMAGE',
                    'XWIN_WORLD', 'YWIN_WORLD', 'FLUX_APER(1)',
                    'FLUXERR_APER(1)', 'FLAGS', 'FLAGS_WEIGHT',
                    'FLUX_RADIUS', 'ELONGATION',
                    'VIGNET(20,20)', 'SNR_WIN'],
    },
    'frames': frames
}
```

```
pipeline.add_step(aw.api.run_sex, ['step4', 'SExtractor'], **kwargs)

# Calculate PSF
kwargs = {
    'catalogs': stack_filename.replace('.fits', '.cat'),
    'api_kwargs': {
        'config': {
            'CENTER_KEYS': 'XWIN_IMAGE,YWIN_IMAGE',
            'PSFVAR_KEYS': 'XWIN_IMAGE,YWIN_IMAGE',
            'CHECKPLOT_DEV': 'NULL',
            'PSF_SUFFIX': '.psf'
        },
    }
}
pipeline.add_step(aw.api.run_psfex, ['step5', 'PSFEx'], **kwargs)

# Calculate PSF photometry for stacked image
# Get positions in stack for PSF photometry
catalog_name = os.path.join(pipeline.paths['catalogs'], output_cat_name)
kwargs = {
    'files': {
        'image': stack_filename,
        'wtmap': stack_filename.replace('.fits', '.wtmap.fits')
    },
    'api_kwargs': {
        'config': {
            'PSF_NAME': os.path.join(stack_filename.replace('.fits', '.psf')),
            'CATALOG_TYPE': 'FITS_LDAC',
            'FILTER': False,
            'CATALOG_NAME': catalog_name,
            'WEIGHT_TYPE': 'MAP_WEIGHT',
            'NTHREADS':'2',
        },
        'params': ['NUMBER', 'EXT_NUMBER', 'XWIN_IMAGE',
                   'YWIN_IMAGE', 'ERRAWIN_IMAGE',
                   'ERRBWIN_IMAGE', 'ERRTHETAWIN_IMAGE',
                   'XWIN_WORLD', 'YWIN_WORLD', 'FLUX_AUTO',
                   'FLUXERR_AUTO', 'FLAGS', 'FLAGS_WEIGHT', 'FLUX_RADIUS',
                   'ELONGATION', 'MAG_AUTO', 'MAGERR_AUTO', 'ALPHAPSF_SKY',
                   'DELTAPSF_SKY','ERRX2PSF_WORLD','ERRY2PSF_WORLD',
                   'FLUX_PSF', 'FLUXERR_PSF', 'MAG_PSF', 'MAGERR_PSF'],
    },
    'frames': frames
```

```
    }
    pipeline.add_step(aw.api.run_sex, ['step6', 'SExtractor'], **kwargs)

    def save_output(pipeline, old_stack, new_stack, old_cat, new_cat):
            # Copy the final stack and catalog from the temp folder
            import shutil
            # Move the weight map if it exists
            if os.path.isfile(old_stack.replace('.fits', '.wtmap.fits')):
                shutil.move(old_stack.replace('.fits', '.wtmap.fits'),
                            new_stack.replace('.fits', '.wtmap.fits'))
            shutil.move(old_stack, new_stack)
            shutil.move(old_cat, new_cat)
            result = {
                'status': 'success'
            }
            return result

    kwargs = {
        'old_stack': stack_filename,
        'new_stack': os.path.join(pipeline.paths['stacks'], stack_name),
        'old_cat': catalog_name,
        'new_cat': os.path.join(pipeline.paths['catalogs'], output_cat_name)
    }
    pipeline.add_step(save_output, ['step7', 'save_output'], **kwargs)

    return pipeline

# load list of exposures
explist =  np.loadtxt(os.path.join(base_path,'makemos.lis'), dtype = 'str')

# Try running the pipeline without weight maps for one exposure
# Create the pipeline
pipeline = aw.utils.pipeline.Pipeline(paths, build_paths = build_paths)
frames = []
exposures = [{'image':os.path.join(pipeline.paths['images'],explist[0])}]
pipeline = build_pipeline(pipeline, exposures=exposures, frames=frames)

print exposures
pipeline.run(['step1'])
pipeline.run(['step2'])
pipeline.run(['step3'])

# It runs on one image, so now build the input list of all exposures
```

```
# Create the pipeline
pipeline = aw.utils.pipeline.Pipeline(paths, build_paths = build_paths)
frames = []
exposures = [{'image':os.path.join(pipeline.paths['images'],explist[i])}
             for i in xrange(len(explist))]
pipeline = build_pipeline(pipeline, exposures=exposures, frames=frames)

pipeline.run(['step1'])
pipeline.run(['step2'])
# copy header files into image directory
# %bash
# cp /Volumes/Backup_Johanna/M105_MOS/OIII/temp/*.head
# /Volumes/Backup_Johanna/M105_MOS/OIII/images/.
pipeline.run(['step3'])
pipeline.run(['step4'])
pipeline.run(['step5'])
pipeline.run(['step6'])
pipeline.run(['step7'])
```

A.3.3 Plotting the resulting images

```
# coding: utf-8
import astropy.coordinates as coords
import astropy.units as u
import numpy as np
from astropy.io import ascii
from astropy.table import Column, Table
import matplotlib.pyplot as plt
import matplotlib.patches as mpatches

from astropy.io import ascii
from astropy.io import fits
import astropy.units as u
import astropy.coordinates as coords
from astropy.wcs import WCS
from astropy.wcs import utils

import matplotlib

plt.style.use('publication')
from mpl_toolkits.axes_grid.inset_locator import inset_axes
from mpl_toolkits.axes_grid1 import ImageGrid
```

```
from matplotlib.colors import Normalize
from matplotlib.ticker import NullFormatter

from scipy import interpolate

from astroquery.simbad import Simbad
from astroquery.vizier import Vizier
import seaborn as sns
onecolumn = 8.8*0.393701 #in inches
twocolumn = 18.0*0.393701 #in inches
goldenratio = .5*(1. + np.sqrt(5))

Vizier.ROW_LIMIT = 2000
# load images
path = '/Users/jhartke/PhD/data/M105/Subaru/'
OIII_before, OIII_head_before = fits.getdata(path + 'Not_astrometrized/NGC3379_OIII.fits',
                                             header = True)
OIII_after, OIII_head_after = fits.getdata(path + 'Astromatic_Stack_skysub/OIII_stack.fits',
                                           header = True)
V_before, V_head_before = fits.getdata(path + 'Not_astrometrized/NGC3379_V.fits',
                                       header = True)
V_after, V_head_after = fits.getdata(path + 'Astromatic_Stack_skysub/V_stack.fits',
                                     header = True)

# load catalog
M105 = Simbad.query_object('M105')
M105_coords =coords.SkyCoord(M105['RA'], M105['DEC'], unit = (u.hourangle, u.deg))
cat_region = Vizier.query_region(M105_coords,
                                 width=0.6*u.deg, height=0.6*u.deg,
                                 catalog='UCAC4')

M105_cat = cat_region['I/322A/out']
M105_cat.colnames

# select useful reference stars (no high proper motions)
pmtot = np.sqrt(M105_cat['pmRA']**2 * M105_cat['pmDE']**2)
pmsel = pmtot < 500./15.

# Select stars which are not doubles or other weird objects
flags = np.logical_and(M105_cat['db'] == 0, M105_cat['of'] == 0)

# resulting catalogue
M105_alignment = M105_cat[np.logical_and(flags, pmsel)]
```

```
# plot
hdu = fits.open(path + 'Not_astrometrized/NGC3379_OIII.fits')[0]
wcs = WCS(hdu.header)
fig = plt.figure(figsize = (twocolumn, twocolumn))
ax1 = plt.subplot(111, projection=wcs)
ax1.imshow(hdu.data, vmin=-19.778765, vmax=19.214481, origin='lower')
ax1.grid(color='k', ls='solid', alpha = .7)
ax1.scatter(M105_alignment['RAJ2000'], M105_alignment['DEJ2000'],
            facecolors = 'none',
            edgecolors = 'r', transform=ax1.get_transform('fk5'), s = 3)
ax1.set_xlabel('Right Ascension')
ax1.set_ylabel('Declination')
ax1.set_title('[OIII] mosaic SDFRED2')
fig.savefig('plots/OIII_mosaic_before.png')

# plot
hdu = fits.open(path + 'Not_astrometrized/NGC3379_V.fits')[0]
wcs = WCS(hdu.header)
fig = plt.figure(figsize = (twocolumn, twocolumn))
ax1 = plt.subplot(111, projection=wcs)
ax1.imshow(hdu.data, vmin=-100, vmax=100, origin='lower')
ax1.grid(color='k', ls='solid', alpha = .7)
ax1.scatter(M105_alignment['RAJ2000'], M105_alignment['DEJ2000'],
            facecolors = 'none',
            edgecolors = 'r', transform=ax1.get_transform('fk5'), s = 3)
ax1.set_xlabel('Right Ascension')
ax1.set_ylabel('Declination')
ax1.set_title('$V$ mosaic SDFRED2')
fig.savefig('plots/V_mosaic_before.png')

hdu = fits.open(path + 'Astromatic_Stack_skysub/V_stack.fits')[0]
wcs = WCS(hdu.header)
fig = plt.figure(figsize = (twocolumn, twocolumn))
ax1 = plt.subplot(111, projection=wcs)
ax1.imshow(hdu.data, vmin=-100, vmax=100, origin='lower')
ax1.grid(color='k', ls='solid', alpha = .7)
ax1.scatter(M105_alignment['RAJ2000'], M105_alignment['DEJ2000'],
            facecolors = 'none',
            edgecolors = 'r', transform=ax1.get_transform('fk5'), s = 3)
ax1.set_xlabel('Right Ascension')
ax1.set_ylabel('Declination')
ax1.set_title('$V$ mosaic Astromatic')
```

```
fig.savefig('plots/V_mosaic_after.png')

# plot
hdu = fits.open(path + 'Astromatic_Stack_skysub/OIII_stack.fits')[0]
wcs = WCS(hdu.header)
fig = plt.figure(figsize = (twocolumn, twocolumn))
ax1 = plt.subplot(111, projection=wcs)
ax1.imshow(hdu.data, vmin=-47, vmax=47, origin='lower')
ax1.grid(color='k', ls='solid', alpha = .7)
ax1.scatter(M105_alignment['RAJ2000'], M105_alignment['DEJ2000'],
            facecolors = 'none',
            edgecolors = 'r', transform=ax1.get_transform('fk5'), s = 3)
ax1.set_xlabel('Right Ascension')
ax1.set_ylabel('Declination')
ax1.set_title('[OIII] mosaic Astromatic')
fig.savefig('plots/OIII_mosaic_after.png')
```

Bibliography

Abadi, M. G., Navarro, J. F., & Steinmetz, M. 2006, MNRAS, 365, 747

Abell, G. O. & Goldreich, P. 1966, Publications of the Astronomical Society of the Pacific, 78, 232

Agnello, A., Evans, N. W., Romanowsky, A. J., & Brodie, J. P. 2014, MNRAS, 442, 3299

Aguerri, J. A. L., Gerhard, O. E., Arnaboldi, M., et al. 2005, AJ, 129, 2585

Amorisco, N. C. 2015, MNRAS, 450, 575

Amorisco, N. C. 2017, MNRAS, 464, 2882

Amorisco, N. C. & Evans, N. W. 2012, MNRAS, 419, 184

Aniyan, S., Freeman, K. C., Arnaboldi, M., et al. 2018, MNRAS, 476, 1909

Arnaboldi, M., Aguerri, J. A. L., Napolitano, N. R., et al. 2002, AJ, 123, 760

Arnaboldi, M., Freeman, K. C., Gerhard, O., et al. 1998, ApJ, 507, 759

Arnaboldi, M., Freeman, K. C., Mendez, R. H., et al. 1996, ApJ, 472, 145

Arnaboldi, M., Freeman, K. C., Okamura, S., et al. 2003, AJ, 125, 514

Arnaboldi, M., Gerhard, O., Aguerri, J. A. L., et al. 2004, ApJ, 614, L33

Arnaboldi, M., Gerhard, O., Okamura, S., et al. 2007, Publications of the Astronomical Society of Japan, 59, 419

Arnaboldi, M., Pulsoni, C., Gerhard, O., & PN.S Consortium. 2017, in IAU Symposium, Vol. 323, Planetary Nebulae: Multi-Wavelength Probes of Stellar and Galactic Evolution, ed. X. Liu, L. Stanghellini, & A. Karakas, 279–283

Arnaboldi, M., Ventimiglia, G., Iodice, E., Gerhard, O., & Coccato, L. 2012, A&A, 545, A37

Arrigoni Battaia, F., Gavazzi, G., Fumagalli, M., et al. 2012, A&A, 543, A112

Awaki, H., Mushotzky, R., Tsuru, T., et al. 1994, Publications of the Astronomical Society of Japan, 46, L65

Balick, B. & Frank, A. 2002, Annual Review of Astronomy and Astrophysics, 40, 439

Barbosa, C. E., Arnaboldi, M., Coccato, L., et al. 2018, å, 609, A78

Barnes, J. E. 1992, ApJ, 393, 484

Beers, T. C. & Tonry, J. L. 1986, ApJ, 300, 557

Behroozi, P. S., Conroy, C., & Wechsler, R. H. 2010, ApJ, 717, 379

Belokurov, V., Evans, N. W., Irwin, M. J., et al. 2007, ApJ, 658, 337

Bender, R., Kormendy, J., Cornell, M. E., & Fisher, D. B. 2015, ApJ, 807, 56

Bender, R., Saglia, R. P., & Gerhard, O. E. 1994, MNRAS, 269, 785

Bernardi, M., Hyde, J. B., Sheth, R. K., Miller, C. J., & Nichol, R. C. 2007, AJ, 133, 1741

Bernardi, M., Renzini, A., da Costa, L. N., et al. 1998, ApJ, 508, L143

Bertin, E. 2006, in Astronomical Society of the Pacific Conference Series, Vol. 351, Astronomical Data Analysis Software and Systems XV, ed. C. Gabriel, C. Arviset, D. Ponz, & S. Enrique, 112

Bertin, E. & Arnouts, S. 1996, A&AS, 117, 393

Bertin, E., Mellier, Y., Radovich, M., et al. 2002, in Astronomical Society of the Pacific Conference Series, Vol. 281, Astronomical Data Analysis Software and Systems XI, ed. D. A. Bohlender, D. Durand, & T. H. Handley, 228

Bialas, D., Lisker, T., Olczak, C., Spurzem, R., & Kotulla, R. 2015, A&A, 576, A103

Binggeli, B., Popescu, C. C., & Tammann, G. A. 1993, A&AS, 98, 275

Binggeli, B., Sandage, A., & Tammann, G. A. 1988, Annual Review of Astronomy and Astrophysics, 26, 509

Binggeli, B., Tammann, G. A., & Sandage, A. 1987, AJ, 94, 251

Binney, J. & Tremaine, S. 1987, Galactic dynamics

Blakeslee, J. P., Jordán, A., Mei, S., et al. 2009, ApJ, 694, 556

Boardman, N. F., Weijmans, A.-M., van den Bosch, R., et al. 2017, MNRAS, 471, 4005

Boselli, A., Voyer, E., Boissier, S., et al. 2014, A&A, 570, A69

Broadhurst, T., Benítez, N., Coe, D., et al. 2005, ApJ, 621, 53

Bruzual, G. & Charlot, S. 2003, MNRAS, 344, 1000

Bullock, J. S. & Johnston, K. V. 2005, ApJ, 635, 931

Buzzoni, A. 1989, The Astrophysical Journal Supplement Series, 71, 817

Buzzoni, A. 2005, MNRAS, 361, 725

Buzzoni, A., Arnaboldi, M., & Corradi, R. L. M. 2006, MNRAS, 368, 877

Caon, N., Capaccioli, M., & D'Onofrio, M. 1994, A&AS, 106

Capaccioli, M., Held, E. V., Lorenz, H., & Vietri, M. 1990, AJ, 99, 1813

Capaccioli, M., Spavone, M., Grado, A., et al. 2015, A&A, 581, A10

Cappellari, M. 2016, ARA&A, 54, 597

Cappellari, M., Bacon, R., Bureau, M., et al. 2006, MNRAS, 366, 1126

Cappellari, M., Emsellem, E., Krajnović, D., et al. 2011, MNRAS, 413, 813

Cappellaro, E., Evans, R., & Turatto, M. 1999, A&A, 351, 459

Castro-Rodríguez, N., Aguerri, J. A. L., Arnaboldi, M., et al. 2003, A&A, 405, 803

Castro-Rodriguéz, N., Arnaboldi, M., Aguerri, J. A. L., et al. 2009, A&A, 507, 621

Chavez, M. & Bertone, E. 2011, Ap&SS, 335, 193

Churazov, E., Tremaine, S., Forman, W., et al. 2010, MNRAS, 404, 1165

Ciardullo, R. 2010, PASA, 27, 149

Ciardullo, R. 2012, Ap&SS, 341, 151

Ciardullo, R., Durrell, P. R., Laychak, M. B., et al. 2004, ApJ, 614, 167

Ciardullo, R., Feldmeier, J. J., Jacoby, G. H., et al. 2002, ApJ, 577, 31

Ciardullo, R., Gronwall, C., Wolf, C., et al. 2012, ApJ, 744, 110

Ciardullo, R., Jacoby, G. H., Feldmeier, J. J., & Bartlett, R. E. 1998, ApJ, 492, 62

Ciardullo, R., Jacoby, G. H., Ford, H. C., & Neill, J. D. 1989, ApJ, 339, 53

Ciardullo, R., Sigurdsson, S., Feldmeier, J. J., & Jacoby, G. H. 2005, ApJ, 629, 499

Coccato, L., Arnaboldi, M., & Gerhard, O. 2013, MNRAS, 436, 1322

Coccato, L., Gerhard, O., Arnaboldi, M., et al. 2009, MNRAS, 394, 1249

Colless, M., Ellis, R. S., Taylor, K., & Hook, R. N. 1990, MNRAS, 244, 408

Conroy, C., Wechsler, R. H., & Kravtsov, A. V. 2006, ApJ, 647, 201

Cook, B. A., Conroy, C., Pillepich, A., Rodriguez-Gomez, V., & Hernquist, L. 2016, ApJ, 833, 158

Cooper, A. P., D'Souza, R., Kauffmann, G., et al. 2013, MNRAS, 434, 3348

Correa, C. A., Wyithe, J. S. B., Schaye, J., & Duffy, A. R. 2015, MNRAS, 452, 1217

Cortesi, A., Arnaboldi, M., Coccato, L., et al. 2013a, A&A, 549, A115

Cortesi, A., Merrifield, M. R., Arnaboldi, M., et al. 2011, MNRAS, 414, 642

Cortesi, A., Merrifield, M. R., Coccato, L., et al. 2013b, MNRAS, 432, 1010

Côté, P., McLaughlin, D. E., Cohen, J. G., & Blakeslee, J. P. 2003, ApJ, 591, 850

Cowie, L. L. & Binney, J. 1977, ApJ, 215, 723

Crain, R. A., Schaye, J., Bower, R. G., et al. 2015, MNRAS, 450, 1937

Crnojević, D., Ferguson, A. M. N., Irwin, M. J., et al. 2013, MNRAS, 432, 832

Crnojević, D., Sand, D. J., Spekkens, K., et al. 2016, ApJ, 823, 19

Cui, W., Murante, G., Monaco, P., et al. 2014, MNRAS, 437, 816

Daddi, E., Renzini, A., Pirzkal, N., et al. 2005, ApJ, 626, 680

Das, P., Gerhard, O., Churazov, E., & Zhuravleva, I. 2010, MNRAS, 409, 1362

Davis, B. D., Ciardullo, R., Jacoby, G. H., Feldmeier, J. J., & Indahl, B. L. 2018, arXiv.org [1807.05279v1]

de Lorenzi, F., Debattista, V. P., Gerhard, O., & Sambhus, N. 2007, MNRAS, 376, 71

de Lorenzi, F., Gerhard, O., Coccato, L., et al. 2009, MNRAS, 395, 76

De Lucia, G. & Blaizot, J. 2007, MNRAS, 375, 2

De Lucia, G., Springel, V., White, S. D. M., Croton, D., & Kauffmann, G. 2006, MNRAS, 366, 499

de Vaucouleurs, G. 1948, Annales d'Astrophysique, 11, 247

de Vaucouleurs, G. 1961, ApJS, 5, 233

de Vaucouleurs, G. 1975a, Nearby Groups of Galaxies, 557

de Vaucouleurs, G. 1975b, ApJ, 202, 610

de Vaucouleurs, G. & Capaccioli, M. 1979, The Astrophysical Journal Supplement Series, 40, 699

Dekel, A. & Silk, J. 1986, ApJ, 303, 39

Dekel, A., Stoehr, F., Mamon, G. A., et al. 2005, Nature, 437, 707

DeMaio, T., Gonzalez, A. H., Zabludoff, A., Zaritsky, D., & Bradač, M. 2015, MNRAS, 448, 1162

DeMaio, T., Gonzalez, A. H., Zabludoff, A., et al. 2018, MNRAS, 474, 3009

Doherty, M., Arnaboldi, M., Das, P., et al. 2009, A&A, 502, 771

Dolag, K., Mevius, E., & Remus, R.-S. 2017, Galaxies, 5, 35

Dolag, K., Murante, G., & Borgani, S. 2010, MNRAS, 405, 1544

Dopita, M. A. & Evans, I. N. 1986, ApJ, 307, 431

Dopita, M. A., Jacoby, G. H., & Vassiliadis, E. 1992, ApJ, 389, 27

Dopita, M. A., Vassiliadis, E., Meatheringham, S. J., et al. 1996, ApJ, 460, 320

Dotter, A., Chaboyer, B., Jevremović, D., et al. 2008, The Astrophysical Journal Supplement Series, 178, 89

Douglas, N. G., Arnaboldi, M., Freeman, K. C., et al. 2002, PASP, 114, 1234

Douglas, N. G., Napolitano, N. R., Romanowsky, A. J., et al. 2007, ApJ, 664, 257

Douglas, N. G. & Taylor, K. 1999, MNRAS, 307, 190

Dressler, A. 1978, Lick Observatory Bulletin, 771, 1

Dressler, A. 1979, ApJ, 231, 659

Dressler, A. 1980, ApJ, 236, 351

Dressler, A. & Gunn, J. E. 1983, ApJ, 270, 7

Duc, P.-A., Cuillandre, J.-C., Karabal, E., et al. 2015, MNRAS, 446, 120

Duc, P.-A., Cuillandre, J.-C., Serra, P., et al. 2011, MNRAS, 417, 863

Dupraz, C. & Combes, F. 1986, A&A, 166, 53

Durrell, P. R., Ciardullo, R., Feldmeier, J. J., Jacoby, G. H., & Sigurdsson, S. 2002, ApJ, 570, 119

Durrell, P. R., Côté, P., Peng, E. W., et al. 2014, ApJ, 794, 103

Emsellem, E., Cappellari, M., Peletier, R. F., et al. 2004, MNRAS, 352, 721

Emsellem, E. & Sauron Team. 2002, Ap&SS, 281, 363

Faber, S. M. & Jackson, R. E. 1976, ApJ, 204, 668

Fabian, A. C. 1994, Annual Review of Astronomy and Astrophysics, 32, 277

Fasano, G. & Franceschini, A. 1987, MNRAS, 225, 155

Feldmeier, J. J., Ciardullo, R., & Jacoby, G. H. 1998, ApJ, 503, 109

Feldmeier, J. J., Ciardullo, R., Jacoby, G. H., & Durrell, P. R. 2003, ApJS, 145, 65

Feldmeier, J. J., Ciardullo, R., Jacoby, G. H., & Durrell, P. R. 2004, ApJ, 615, 196

Ferguson, A. M. N., Irwin, M. J., Ibata, R. A., Lewis, G. F., & Tanvir, N. R. 2002, AJ, 124, 1452

Ferguson, H. C., Tanvir, N. R., & von Hippel, T. 1998, Nature, 391, 461

Ferrarese, L., Côté, P., Cuillandre, J.-C., et al. 2012, ApJS, 200, 4

Forbes, D. A., Romanowsky, A. J., Pastorello, N., et al. 2016, MNRAS, 457, 1242

Ford, H. C. & Jenner, D. C. 1975, ApJ, 202, 365

Ford, H. C., Jenner, D. C., & Epps, H. W. 1973, ApJ, 183, L73

Foreman-Mackey, D., Hogg, D. W., Lang, D., & Goodman, J. 2013, PASP, 125, 306

Gal-Yam, A., Maoz, D., Guhathakurta, P., & Filippenko, A. V. 2003, AJ, 125, 1087

Gallazzi, A., Charlot, S., Brinchmann, J., White, S. D. M., & Tremonti, C. A. 2005, MNRAS, 362, 41

Gavazzi, R., Treu, T., Rhodes, J. D., et al. 2007, ApJ, 667, 176

Gawiser, E., Francke, H., Lai, K., et al. 2007, ApJ, 671, 278

Gebhardt, K., Richstone, D., Kormendy, J., et al. 2000, AJ, 119, 1157

Gerhard, O., Arnaboldi, M., Freeman, K. C., et al. 2005, ApJ, 621, L93

Gerhard, O., Arnaboldi, M., Freeman, K. C., et al. 2007, A&A, 468, 815

Gerhard, O., Kronawitter, A., Saglia, R. P., & Bender, R. 2001, AJ, 121, 1936

Gerhard, O. E. 1993, MNRAS, 265, 213

Gesicki, K. & Zijlstra, A. A. 2000, A&A, 358, 1058

Gesicki, K., Zijlstra, A. A., & Miller Bertolami, M. M. 2018, Nature Astronomy, 52

Gitti, M., Piffaretti, R., & Schindler, S. 2007, A&A, 472, 383

Gnedin, O. Y. 2003a, ApJ, 589, 752

Gnedin, O. Y. 2003b, ApJ, 582, 141

Gonzalez, A. H., Zabludoff, A. I., & Zaritsky, D. 2005, ApJ, 618, 195

Gregg, M. D. & West, M. J. 1998, Nature, 396, 549

Greggio, L. & Renzini, A. 2011, Stellar Populations. A User Guide from Low to High Redshift

Gronwall, C., Ciardullo, R., Hickey, T., et al. 2007, ApJ, 667, 79

Gunn, J. E. & Gott, III, J. R. 1972, ApJ, 176, 1

Hammer, F., Flores, H., Lilly, S. J., et al. 1997, ApJ, 481, 49

Hargis, J. R. & Rhode, K. L. 2014, ApJ, 796, 62

Hartke, J., Arnaboldi, M., Gerhard, O., et al. 2018, ArXiv e-prints [arXiv:1805.03092]

Hartke, J., Arnaboldi, M., Longobardi, A., et al. 2017, A&A, 603, A104 (H17)

Hausman, M. A. & Ostriker, J. P. 1978, ApJ, 224, 320

Helmi, A., Cooper, A. P., White, S. D. M., et al. 2011, ApJ, 733, L7

Henize, K. G. & Westerlund, B. E. 1963, ApJ, 137, 747

Hernquist, L. & Quinn, P. J. 1988, ApJ, 331, 682

Hernquist, L. & Quinn, P. J. 1989, ApJ, 342, 1

Hernquist, L., Spergel, D. N., & Heyl, J. S. 1993, ApJ, 416, 415

Hibbard, J. E. & Mihos, J. C. 1995, AJ, 110, 140

Hinshaw, G., Larson, D., Komatsu, E., et al. 2013, ApJS, 208, 19

Hoekstra, H., Yee, H. K. C., & Gladders, M. D. 2004, ApJ, 606, 67

Hogg, D. W., Cohen, J. G., Blandford, R., & Pahre, M. A. 1998, ApJ, 504, 622

Hoskin, M. 2014, Journal for the History of Astronomy, 45, 209

Hubble, E. P. 1926, ApJ, 64, 321

Huchra, J. P. & Geller, M. J. 1982, ApJ, 257, 423

Hui, X., Ford, H. C., Freeman, K. C., & Dopita, M. A. 1995, ApJ, 449, 592

Humphrey, P. J. & Buote, D. A. 2013, MNRAS, 436, 2879

Iodice, E., Capaccioli, M., Grado, A., et al. 2016, ApJ, 820, 42

Iodice, E., Spavone, M., Capaccioli, M., et al. 2017, ApJ, 839, 21

Irwin, J. A. & Sarazin, C. L. 1996, ApJ, 471, 683

Jacob, R., Schönberner, D., & Steffen, M. 2013, A&A, 558, A78

Jacoby, G. H. 1980, The Astrophysical Journal Supplement Series, 42, 1

Jacoby, G. H. 1989, ApJ, 339, 39

Jacoby, G. H. 1997, in Planetary Nebulae, Vol. 180, 448

Jacoby, G. H., Branch, D., Ciardullo, R., et al. 1992, Publications of the Astronomical Society of the Pacific, 104, 599

Jacoby, G. H., Ciardullo, R., & Ford, H. C. 1990, ApJ, 356, 332

Janowiecki, S., Mihos, J. C., Harding, P., et al. 2010, ApJ, 715, 972

Jiménez-Teja, Y., Dupke, R., Benítez, N., et al. 2018, ApJ, 857, 79

Jones, C. & Forman, W. 1984, ApJ, 276, 38

Kapferer, W., Schindler, S., Knollmann, S. R., & van Kampen, E. 2010, A&A, 516, A41

Kelson, D. D., Zabludoff, A. I., Williams, K. A., et al. 2002, ApJ, 576, 720

Kewley, L. J. & Dopita, M. A. 2002, The Astrophysical Journal Supplement Series, 142, 35

Kim, S., Rey, S.-C., Jerjen, H., et al. 2014, ApJS, 215, 22

Kirby, E. N., Cohen, J. G., Guhathakurta, P., et al. 2013, ApJ, 779, 102

Koopmans, L. V. E., Treu, T., Bolton, A. S., Burles, S., & Moustakas, L. A. 2006, ApJ, 649, 599

Kormendy, J. 1977, ApJ, 218, 333

Kormendy, J., Fisher, D. B., Cornell, M. E., & Bender, R. 2009, ApJS, 182, 216

Kreckel, K., Groves, B., Bigiel, F., et al. 2017, ApJ, 834, 174

Krick, J. E. & Bernstein, R. A. 2007, AJ, 134, 466

Krishna Kumar, C. & Thonnard, N. 1983, AJ, 88, 260

Kronawitter, A., Saglia, R. P., Gerhard, O., & Bender, R. 2000, Astronomy and Astrophysics Supplement Series, 144, 53

Kwok, S., Purton, C. R., & Fitzgerald, M. P. 1978, ApJ, 219, L125

Lauer, T. R., Postman, M., Strauss, M. A., Graves, G. J., & Chisari, N. E. 2014, ApJ, 797, 82

Leavitt, H. S. 1908, Annals of Harvard College Observatory, 60, 87

Lee, M. G. & Jang, I. S. 2016, ApJ, 822, 70

Li, H. & Gnedin, O. Y. 2014, ApJ, 796, 10

Lidman, C., Iacobuta, G., Bauer, A. E., et al. 2013, MNRAS, 433, 825

Limousin, M., Richard, J., Jullo, E., et al. 2007, ApJ, 668, 643

Lin, Y.-T. & Mohr, J. J. 2004, ApJ, 617, 879

Loewenstein, M. 1999, in Star Formation in Early Type Galaxies, Vol. 163, 153

Longobardi, A., Arnaboldi, M., Gerhard, O., et al. 2013, A&A, 558, A42 (L13)

Longobardi, A., Arnaboldi, M., Gerhard, O., & Hanuschik, R. 2015a, A&A, 579, A135 (L15a)

Longobardi, A., Arnaboldi, M., Gerhard, O., & Mihos, J. C. 2015b, A&A, 579, L3 (L15b)

Longobardi, A., Peng, E. W., Côté, P., et al. 2018, arXiv.org [1807.08750v1]

Lotz, J. M., Jonsson, P., Cox, T. J., & Primack, J. R. 2008, MNRAS, 391, 1137

Lotz, J. M., Koekemoer, A., Coe, D., et al. 2017, ApJ, 837, 97

Lynden-Bell, D. 1967, MNRAS, 136, 101

Ma, C.-P., Greene, J. E., McConnell, N., et al. 2014, ApJ, 795, 158

Magrini, L., Leisy, P., Corradi, R. L. M., et al. 2005, A&A, 443, 115

Mandelbaum, R., Hirata, C. M., Broderick, T., Seljak, U., & Brinkmann, J. 2006, MNRAS, 370, 1008

Marigo, P., Girardi, L., Weiss, A., Groenewegen, M. A. T., & Chiosi, C. 2004, A&A, 423, 995

Marmo, C. & Bertin, E. 2008, in Astronomical Society of the Pacific Conference Series, Vol. 394, Astronomical Data Analysis Software and Systems XVII, ed. R. W. Argyle, P. S. Bunclark, & J. R. Lewis, 619

Martel, H., Robichaud, F., & Barai, P. 2014, AJ, 786, 79

Martínez-Delgado, D., Gabany, R. J., Crawford, K., et al. 2010, AJ, 140, 962

Matthews, T. A., Morgan, W. W., & Schmidt, M. 1964, ApJ, 140, 35

Mayer, L., Mastropietro, C., Wadsley, J., Stadel, J., & Moore, B. 2006, MNRAS, 369, 1021

McCarthy, J. K., Mould, J. R., Mendez, R. H., et al. 1990, ApJ, 351, 230

McConnachie, A. W., Irwin, M. J., Ibata, R. A., et al. 2009, Nature, 461, 66

McNamara, B. R. & O'Connell, R. W. 1989, AJ, 98, 2018

McNamara, B. R., Sancisi, R., Henning, P. A., & Junor, W. 1994, AJ, 108, 844

McNeil, E. K., Arnaboldi, M., Freeman, K. C., et al. 2010, A&A, 518, A44

Mei, S., Blakeslee, J. P., Côté, P., et al. 2007, ApJ, 655, 144

Melnick, J., Giraud, E., Toledo, I., Selman, F., & Quintana, H. 2012, MNRAS, 427, 850

Melnick, J. & Sargent, W. L. W. 1977, ApJ, 215, 401

Mendez, R. H. 2016, ArXiv e-prints [arXiv:1610.08625]

Méndez, R. H., Riffeser, A., Kudritzki, R.-P., et al. 2001, ApJ, 563, 135

Mendez, R. H. & Soffner, T. 1997, A&A, 321, 898

Merrett, H. R., Merrifield, M. R., Douglas, N. G., et al. 2006, MNRAS, 369, 120

Merritt, D. 1985, ApJ, 289, 18

Michel-Dansac, L., Duc, P.-A., Bournaud, F., et al. 2010, ApJ, 717, L143

Mihos, J. C., Harding, P., Feldmeier, J., & Morrison, H. 2005, ApJ, 631, L41

Mihos, J. C., Harding, P., Feldmeier, J. J., et al. 2017, ApJ, 834, 16

Mihos, J. C., Harding, P., Rudick, C. S., & Feldmeier, J. J. 2013, ApJ, 764, L20

Miller Bertolami, M. M. 2016, A&A, 588, A25

Miyazaki, S., Komiyama, Y., Sekiguchi, M., et al. 2002, PASJ, 54, 833

Montes, M. & Trujillo, I. 2018, MNRAS, 474, 917

Moore, B., Katz, N., Lake, G., Dressler, A., & Oemler, A. 1996, Nature, 379, 613

Moore, B., Lake, G., & Katz, N. 1998, ApJ, 495, 139

Moore, B., Lake, G., Quinn, T., & Stadel, J. 1999, MNRAS, 304, 465

Morgan, W. W. 1958, Publications of the Astronomical Society of the Pacific, 70, 364

Morgan, W. W. 1959, Publications of the Astronomical Society of the Pacific, 71, 394

Morgan, W. W. 1961, Proceedings of the National Academy of Science, 47, 905

Morishita, T., Abramson, L. E., Treu, T., et al. 2017a, ApJ, 846, 139

Morishita, T., Abramson, L. E., Treu, T., et al. 2017b, ApJ, 835, 254

Mould, J., Kennicutt, Robert C., J., & Freedman, W. 2000, Reports on Progress in Physics, 63, 763

Murante, G., Arnaboldi, M., Gerhard, O., et al. 2004, ApJ, 607, L83

Murante, G., Giovalli, M., Gerhard, O., et al. 2007, MNRAS, 377, 2

Naab, T., Johansson, P. H., & Ostriker, J. P. 2009, ApJ, 699, L178

Navarro, J. F., Frenk, C. S., & White, S. D. M. 1996, ApJ, 462, 563

Navarro, J. F., Frenk, C. S., & White, S. D. M. 1997, ApJ, 490, 493

Newville, M., Stensitzki, T., Allen, D. B., & Ingargiola, A. 2014, LMFIT: Non-Linear Least-Square Minimization and Curve-Fitting for Python

O'Connell, R. W. & McNamara, B. R. 1989, AJ, 98, 180

Oegerle, W. R. & Hill, J. M. 2001, AJ, 122, 2858

Oser, L., Naab, T., Ostriker, J. P., & Johansson, P. H. 2012, ApJ, 744, 63

Oser, L., Ostriker, J. P., Naab, T., Johansson, P. H., & Burkert, A. 2010, ApJ, 725, 2312

Ostriker, J. P. & Tremaine, S. D. 1975, ApJ, 202, L113

Peacock, J. A. 1983, MNRAS, 202, 615

Pedregosa, F., Varoquaux, G., Gramfort, A., et al. 2011, Journal of Machine Learning Research, 12, 2825

Peebles, P. J. E. 1978, A&A, 68, 345

Peebles, P. J. E. 1980, The large-scale structure of the universe

Peebles, P. J. E. 1982, ApJ, 258, 415

Peng, C. Y., Ho, L. C., Impey, C. D., & Rix, H.-W. 2010, AJ, 139, 2097

Peng, E. W., Jordán, A., Côté, P., et al. 2006, ApJ, 639, 95

Perlmutter, S., Aldering, G., Goldhaber, G., et al. 1999, ApJ, 517, 565

Pierce, M. J. & Tully, R. B. 1985, AJ, 90, 450

Pillepich, A., Madau, P., & Mayer, L. 2015, ApJ, 799, 184

Pillepich, A., Springel, V., Nelson, D., et al. 2018, MNRAS, 473, 4077

Planck Collaboration, Ade, P. A. R., Aghanim, N., et al. 2016, A&A, 594, A13

Pop, A.-R., Pillepich, A., Amorisco, N., & Hernquist, L. 2017, Galaxies, 5, 34

Postman, M., Coe, D., Benítez, N., et al. 2012, The Astrophysical Journal Supplement Series, 199, 25

Pota, V., Forbes, D. A., Romanowsky, A. J., et al. 2013, MNRAS, 428, 389

Press, W. H., Teukolsky, S. A., Vetterling, W. T., & Flannery, B. P. 2007, Numerical Recipes 3rd Edition: The Art of Scientific Computing, 3rd edn. (New York, NY, USA: Cambridge University Press)

Puchwein, E., Springel, V., Sijacki, D., & Dolag, K. 2010, MNRAS, 406, 936

Pulsoni, C., Gerhard, O., Arnaboldi, M., et al. 2017, ArXiv e-prints [arXiv:1712.05833]

Quinn, P. J. 1984, ApJ, 279, 596

Read, J. I., Wilkinson, M. I., Evans, N. W., Gilmore, G., & Kleyna, J. T. 2006, MNRAS, 366, 429

Rejkuba, M., Greggio, L., Harris, W. E., Harris, G. L. H., & Peng, E. W. 2005, ApJ, 631, 262

Rejkuba, M., Harris, W. E., Greggio, L., et al. 2014, ApJ, 791, L2

Rejkuba, M., Mouhcine, M., & Ibata, R. 2009, MNRAS, 396, 1231

Remus, R.-S., Dolag, K., & Hoffmann, T. 2017, Galaxies, 5, 49

Renaud, F., Agertz, O., & Gieles, M. 2017, MNRAS, 465, 3622

Renzini, A. 1983, in Planetary Nebulae, Vol. 103, 267–280

Renzini, A. & Buzzoni, A. 1986, in Astrophysics and Space Science Library, Vol. 122, Spectral Evolution of Galaxies, ed. C. Chiosi & A. Renzini, 195–231

Richardson, J. C., Ferguson, A. M. N., Johnson, R. A., et al. 2008, AJ, 135, 1998

Richtler, T., Dirsch, B., Gebhardt, K., et al. 2004, AJ, 127, 2094

Riess, A. G., Filippenko, A. V., Challis, P., et al. 1998, AJ, 116, 1009

Rodriguez-Gomez, V., Pillepich, A., Sales, L. V., et al. 2016, MNRAS, 458, 2371

Romanowsky, A. J., Douglas, N. G., Arnaboldi, M., et al. 2003, Science, 301, 1696

Rood, H. J. & Williams, B. A. 1984, ApJ, 285, L5

Rood, H. J. & Williams, B. A. 1985, ApJ, 288, 535

Rubin, V. C., Ford, Jr., W. K., & Thonnard, N. 1980, ApJ, 238, 471

Rudick, C. S., Mihos, J. C., Frey, L. H., & McBride, C. K. 2009, ApJ, 699, 1518

Rudick, C. S., Mihos, J. C., Harding, P., et al. 2010, ApJ, 720, 569

Rudick, C. S., Mihos, J. C., & McBride, C. 2006, ApJ, 648, 936

Rudick, C. S., Mihos, J. C., & McBride, C. K. 2011, ApJ, 732, 48

Sambhus, N., Gerhard, O., & Méndez, R. H. 2006, AJ, 131, 837

Sarazin, C. L. 1986, Reviews of Modern Physics, 58, 1

Sarzi, M., Mamon, G. A., Cappellari, M., et al. 2011, MNRAS, 415, 2832

Schaye, J., Crain, R. A., Bower, R. G., et al. 2015, MNRAS, 446, 521

Schechter, P. 1976, ApJ, 203, 297

Schindler, S., Binggeli, B., & Böhringer, H. 1999, A&A, 343, 420

Schneider, S. 1985, ApJ, 288, L33

Schneider, S. E., Helou, G., Salpeter, E. E., & Terzian, Y. 1983, ApJ, 273, L1

Schombert, J. M. 1986, The Astrophysical Journal Supplement Series, 60, 603

Schönberner, D., Jacob, R., & Steffen, M. 2005, A&A, 441, 573

Sérsic, J. L. 1963, Boletin de la Asociacion Argentina de Astronomia La Plata Argentina, 6, 41

Shapiro, K. L., Cappellari, M., de Zeeuw, T., et al. 2006, MNRAS, 370, 559

Skrutskie, M. F., Cutri, R. M., Stiening, R., et al. 2006, AJ, 131, 1163

Somerville, R. S., Hopkins, P. F., Cox, T. J., Robertson, B. E., & Hernquist, L. 2008, MNRAS, 391, 481

Somerville, R. S., Lee, K., Ferguson, H. C., et al. 2004, ApJ, 600, L171

Sommer-Larsen, J. 2006, MNRAS, 369, 958

Spavone, M., Capaccioli, M., Napolitano, N. R., et al. 2017, A&A, 603, A38

Spiniello, C., Napolitano, N. R., Arnaboldi, M., et al. 2018, MNRAS, 477, 1880

Starkenburg, E., Helmi, A., Morrison, H. L., et al. 2009, ApJ, 698, 567

Statler, T. S. & Smecker-Hane, T. 1999, AJ, 117, 839

Steinmetz, M. & Navarro, J. F. 2002, New A, 7, 155

Stewart, K. R., Bullock, J. S., Wechsler, R. H., Maller, A. H., & Zentner, A. R. 2008, ApJ, 683, 597

Teplitz, H. I., Malkan, M. A., Steidel, C. C., et al. 2000, ApJ, 542, 18

Theuns, T. & Warren, S. J. 1997, MNRAS, 284, L11

Thomas, J., Saglia, R. P., Bender, R., et al. 2005, MNRAS, 360, 1355

Tolstoy, E., Hill, V., & Tosi, M. 2009, Annual Review of Astronomy and Astrophysics, 47, 371

Tonry, J. & Schneider, D. P. 1988, AJ, 96, 807

Tonry, J. L., Dressler, A., Blakeslee, J. P., et al. 2001, ApJ, 546, 681

Toomre, A. 1977, in Evolution of Galaxies and Stellar Populations, 401

Toomre, A. & Toomre, J. 1972, in Bulletin of the American Astronomical Society, Vol. 4, 214

Tortora, C., Napolitano, N. R., Romanowsky, A. J., & Jetzer, P. 2010, ApJ, 721, L1

Tortora, C., Napolitano, N. R., Saglia, R. P., et al. 2014, MNRAS, 445, 162

Tremaine, S., Henon, M., & Lynden-Bell, D. 1986, MNRAS, 219, 285

Tremonti, C. A., Heckman, T. M., Kauffmann, G., et al. 2004, ApJ, 613, 898

Treu, T. & Koopmans, L. V. E. 2004, ApJ, 611, 739

Tully, R. B. 1987, ApJ, 321, 280

Tully, R. B., Courtois, H., Hoffman, Y., & Pomarède, D. 2014, Nature, 513, 71

Umetsu, K., Broadhurst, T., Takada, M., & Kong, X. 2005, Journal of Korean Astronomical Society, 38, 191

Umetsu, K. & Diemer, B. 2017, ApJ, 836, 231

Usher, C., Forbes, D. A., Brodie, J. P., et al. 2012, MNRAS, 426, 1475

van den Bergh, S. 2000, AJ, 119, 609

van den Bosch, F. C., Weinmann, S. M., Yang, X., et al. 2005, MNRAS, 361, 1203

van der Marel, R. P. & Franx, M. 1993, ApJ, 407, 525

van der Wel, A., Holden, B. P., Zirm, A. W., et al. 2008, ApJ, 688, 48

van Dokkum, P. G., Franx, M., Kriek, M., et al. 2008, ApJ, 677, L5

van Zee, L., Barton, E. J., & Skillman, E. D. 2004, AJ, 128, 2797

Vassiliadis, E. & Wood, P. R. 1994, The Astrophysical Journal Supplement Series, 92, 125

Veale, M., Ma, C.-P., Greene, J. E., et al. 2018, MNRAS, 473, 5446

Veale, M., Ma, C.-P., Thomas, J., et al. 2017, MNRAS[arXiv:1609.00391]

Venn, K. A., Irwin, M., Shetrone, M. D., et al. 2004, AJ, 128, 1177

Ventimiglia, G., Arnaboldi, M., & Gerhard, O. 2008, Astronomische Nachrichten, 329, 1057

Ventimiglia, G., Arnaboldi, M., & Gerhard, O. 2011, A&A, 528, A24

Vikhlinin, A., Markevitch, M., Murray, S. S., et al. 2005, ApJ, 628, 655

Vilchez-Gomez, R., Pello, R., & Sanahuja, B. 1994, A&A, 283, 37

Vogelsberger, M., Genel, S., Springel, V., et al. 2014, MNRAS, 444, 1518

Von Der Linden, A., Best, P. N., Kauffmann, G., & White, S. D. M. 2007, MNRAS, 379, 867

Walker, M. G. & Peñarrubia, J. 2011, ApJ, 742, 20

Walsh, J. R., Rejkuba, M., & Walton, N. A. 2015, A&A, 574, A109

Watkins, A. E., Mihos, J. C., Harding, P., & Feldmeier, J. J. 2014, ApJ, 791

Watkins, L. L., van de Ven, G., den Brok, M., & van den Bosch, R. C. E. 2013, MNRAS, 436, 2598

Wechsler, R. H., Zentner, A. R., Bullock, J. S., Kravtsov, A. V., & Allgood, B. 2006, ApJ, 652, 71

Weijmans, A.-M., Cappellari, M., Bacon, R., et al. 2009, MNRAS, 398, 561

White, S. D. M. & Frenk, C. S. 1991, ApJ, 379, 52

White, S. D. M. & Rees, M. J. 1978, MNRAS, 183, 341

Williams, B. F., Ciardullo, R., Durrell, P. R., et al. 2007, ApJ, 656, 756

Willman, B., Governato, F., Wadsley, J., & Quinn, T. 2004, MNRAS, 355, 159

Wilson, G., Kaiser, N., & Luppino, G. A. 2001, ApJ, 556, 601

Worthey, G. 1994, ApJS, 95, 107

Zabludoff, A. I., Huchra, J. P., & Geller, M. J. 1990, The Astrophysical Journal Supplement Series, 74, 1

Zacharias, N., Finch, C. T., Girard, T. M., et al. 2012, VizieR Online Data Catalog

Zahid, H. J., Kudritzki, R.-P., Conroy, C., Andrews, B., & Ho, I. T. 2017, ApJ, 847, 18

Zhang, Z., Xu, H., Wang, Y., et al. 2007, ApJ, 656, 805

Zibetti, S., White, S. D. M., Schneider, D. P., & Brinkmann, J. 2005, MNRAS, 358, 949

Zijlstra, A. A., Gesicki, K., & Bertolami, M. M. M. 2016, Proceedings of the International Astronomical Union, 12, 184–187

Zwicky, F. 1937, ApJ, 86, 217

Zwicky, F. 1951, PASP, 63, 61

Acknowledgements

This thesis would have never been possible without the support of a number of people. Dear Magda and Ortwin, many thanks for offering this great PhD opportunity to me. Thank you for letting me explore my research project independently, but guiding me back onto the right track when it was time for it. Magda, I would like to especially like to thank you for the joint observing run with the PN.S that has really shaped my professional vision for the coming years!

Marina, thank you for being part of my thesis advisory committee, for your advice and encouragement. I would also like to thank the members of my thesis examination committee. Adriano, I could not have asked for a better fellow mentor! Thank you for the support and encouragement, and for letting me shadow you during one of your duty trips to Paranal (and for making me go full-Bayesian).

Lodo, thank you for helping me to not completely lose my mind over the PN.S data reduction. Ken, 6 years ago my journey in astronomy started with a small internship project on stellar streams. I am still very grateful for this opportunity and happy that we are still collaborating now. I also would like to express my sincere gratitude to my collaborators as well as to my mentors and previous supervisors from Jacobs University and Rijksuniversiteit Groningen. Andra and Chiara, thank you for all the advice and help that you provided during the last 3+ years. Stefan, vielen Dank für die schöne Zeit in Office E3.39, die mehrmalige Umzugshilfe und den tollen Ausflug zum Rodeln nach Österreich. Ich hoffe unsere Couch bekommt nun einen Ehrerplatz im MPA!

Dear current and former Dynamics Group, thank you for all your for solicited and unsolicited advice, help, and company. Special thanks go to the 'Elliptical Girls' (for the record, I did not come up with this name): without your relentless support and encouragement especially the final weeks of writing this thesis would have been much tougher! Isabella, thank you for diving into the NMagic archive countless times while you were busy with wrapping up your own thesis!

A big thank you also goes to the ESO Office for Science. Eric, Gaitee, Stella, Nelma, Pam, and Hildegarde, many thanks for making sure that I could make the most out of the ESO experience. My thanks also extend to Annette, Veronika, and Werner from the IMPRS office.

Dear former and current IMPRS representatives, thank you for all the fun meetings, symposia, parties, BBQs and excursions that we organised together. Keep up the great work and enjoy the upcoming excursion!

Staying for three years at ESO means that one sees a lot of students and fellows passing through. Each summer was marked by the departure of friends and colleagues, but also with the arrival of friendly new faces. I guess now it is my turn to say goodbye (or rather *Auf Wiedersehen*). I honestly think that the student and fellow community at ESO is truly amazing! Unfortunately, individually naming all of you would extend the page-count of my thesis significantly, so here are some joint acknowledgements: I would especially like to thank those that made me survive the legendary group-bonding "easy hike", the code-coffee goers, the post-proposal Erding crew, and my swim- and boulder mates. If somebody had told me at the beginning of my PhD that I would one day voluntarily hang off a 3m tall wall, I would have proclaimed them insane.

To my friends from outside of Munich, thank you for encouraging me from afar. Thank you for distracting me, answering my calls in the dead of night, and welcoming me to your homes when I needed to escape Bavaria for a weekend! As you were always invited to Munich, I hope that you will visit me in Chile as well!

Lieber Daniel, vielen Dank dass ich mich zu Beginn meiner Promotion nicht gleich mit dem Münchner Wohnungsmarkt abkämpfen musste. Anna und Martin, vielen Dank für die schöne Zeit in Haidhausen. Andra and Victor, thank you in advance for making sure that I won't go insane while preparing for the defense.

Liebe Tonspur, vielen Dank für die schönen Stunden die wir gemeinsam singend (und essend) verbracht haben! Auch beim Münchner Motettenchor, und besonders bei Magdalena und Elisabeth, möchte ich mich für die tollen Proben, Konzerte, Projekte und Reisen bedanken.

Abschließend möchte ich mich bei meiner Familie bedanken! Vielen Dank, dass ihr mich auf meinem Weg immer unterstützt und gefördert habt, mir vertraut und mich ermutigt habt und dass ihr mir meine Liebe zur Musik in die Wiege gelegt habt!

Music expresses that which cannot be said and on which it is impossible to be silent.
Die Musik drückt das aus, was nicht gesagt werden kann und worüber zu schweigen unmöglich ist.
Victor Hugo